Site U1390[1]

Expedition 339 Scientists[2]

Chapter contents

Background and objectives

Integrated Ocean Drilling Program (IODP) Site U1390 (36°19.110′N, 7°43.078′W, 992 m water depth) is located southeast of the Guadalquivir Bank and the Guadalquivir contourite channel (Fig. F1, F2) over the large sheeted drifts from the northwest part of Sector 3 of the contourite depositional system (CDS) (channel and ridge sector defined by Hernández-Molina et al., 2003, and Llave et al., 2007a). This site represents an opportunity for identifying the recent tectonic influence on the architecture and evolution of the CDS and how it affected Mediterranean Ocean Water (MOW) distribution. It was selected to recover an early Pleistocene to present sedimentary record as well as date several prominent unconformities (Fig. F2) that can be traced regionally across the dense seismic grid.

This area, located in the central middle slope of the Gulf of Cádiz, has been affected by recent tectonic activity, which controlled the major morphostructural features and its recent evolution (Maldonado et al., 1999; Maestro et al., 2003; Terrinha et al., 2003, 2006, 2009; Medialdea et al., 2004, 2009; Fernández-Puga et al., 2007; Zitellini et al., 2009; Duarte et al., 2010; Roque et al., 2012) and determined a complex pattern of different erosive features, such as contourite moats, contourite channels, marginal valleys, and large isolated furrows (Hernández-Molina et al., 2003, 2006; Llave et al., 2007a; García et al., 2009) (see Fig. F4 in the "Site U1389" chapter [Expedition 339 Scientists, 2013g]). A general background about the area of Site U1390 has been included in **"Background and objectives"** in the "Site U1389" chapter (Expedition 339 Scientists, 2013g), although we summarize some new important local aspects here.

Charting the chronology of neotectonic activity that has had significant effect on development and architecture of the CDS is essential to a more complete understanding of the margin system in this region. Margin evolution anywhere is controlled by complex interaction of many different forcing variables, most importantly sea level and climate, sediment supply, and tectonics.

In the Gulf of Cádiz, it is theorized that by the end of the early Pliocene subsidence decreased and the continental margin was evolving toward its present, more stable conditions (Maldonado et al., 1999; Lopes et al., 2006; Medialdea et al., 2004; Roque et al., 2012). Nevertheless some neotectonic activity is also evident, as expressed by changes in the submarine topography, the occur-

[1] Expedition 339 Scientists, 2013. Site U1390. *In* Stow, D.A.V., Hernández-Molina, F.J., Alvarez Zarikian, C.A., and the Expedition 339 Scientists, *Proc. IODP,* 339: Tokyo (Integrated Ocean Drilling Program Management International, Inc.). doi:10.2204/iodp.proc.339.108.2013
[2] **Expedition 339 Scientists' addresses.**

doi:10.2204/iodp.proc.339.108.2013

rence of mud volcanoes and diapiric ridges (Somoza et al., 2003; Pinheiro et al., 2003; Terrinha et al., 2009; Fernández-Puga et al., 2007; Duarte et al., 2010), and fault reactivation (Alves et al., 2003; Medialdea et al., 2004, 2009; Zitellini et al., 2009; Terrinha et al., 2006, 2009). In addition, some studies have reported how the tectonics have exerted strong control on the pathways of MOW and, therefore, on the architecture of the CDS (Llave et al., 2001, 2007b, 2011; García et al., 2009; Roque et al., 2012). Llave et al. (2007b) and Stow et al. (2011) postulate that this tectonic activity has controlled the change from a tabular MOW flow regime to separate flows forming distinct cores of MOW in the Gulf of Cádiz. Although some tectonic unconformities were previously considered by these authors, no drilling or dating has been carried out. The location of Site U1390, close to the Guadalquivir Bank and Guadalquivir contourite channel, was planned in order to better determine the timing and effects of tectonic activity during the Quaternary.

The Guadalquivir Bank represents a structural high in which Paleozoic and Mesozoic rocks of the Iberian margin have been uplifted (Gràcia et al., 2003; Medialdea et al., 2004, 2009; Terrinha et al., 2003, 2006; Roque et al., 2012) from the Neogene through the present. This morphostructure is associated with a cluster of earthquake epicenters showing a dominant reversed motion (Borges et al., 2001; Buforn et al., 2004).

The Guadalquivir Bank has played an important role in this area, affecting the hydrodynamic system and accommodation space for the Pliocene–Quaternary sedimentation (Figs. **F1**, **F2**). The Guadalquivir contourite channel, crossing the southeastern boundary, is the second largest contourite channel in this sector being >90 km long (García et al., 2009). The Guadalquivir contourite channel is located between the Guadalquivir diapiric ridge and the Guadalquivir Bank and corresponds to Channel 3 identified by Kenyon and Belderson (1973). This channel has two almost parallel east-west–oriented branches that merge near the Guadalquivir Bank, the southern and northern branches of the Guadalquivir contourite channel. After merging, the unique channel is parallel to the Guadalquivir Bank. Widths range from 1 to 12 km, with the minimum values in the distal reaches. Vertical incision depths reach 130 m, and transverse profiles are asymmetrical, U- or V-shaped, with generally steeper northern flanks. The average axial gradient is 0.37° on the northern branch and 0.44° on the southern branch.

The contourite channels were created by erosive processes. In their alongslope-trending zones, the present-day MOW has medium to low velocities of 10–50 cm/s in a southeast–northwest direction. In contrast, in the downslope-trending zones MOW shows velocities of 50–90 cm/s in a northeast–southwest direction (Madelain, 1970; Kenyon and Belderson, 1973; Melières, 1974; Zenk, 1975; Nelson et al., 1999; Hernández-Molina et al., 2006; García et al., 2009; Stow et al., in press). Hanquiez et al. (2007) suggest a similar intensification of the current velocity in the downslope-trending sectors, based on estimated transport velocity values and the orientation of bedforms. As a result of Coriolis effect, when the lower core of MOW reaches the Guadalquivir Bank, the lower section of the flow is affected by the topography, which increases the flow's velocity and erosive capability while it is deflected toward the southwest and is constricted by the topography. Coriolis effect forces the trend of the flow toward the right, enhancing the erosive capability of the flow along the northwest flank. The flow in contourite channels is strong enough to erode both the northwest and southeast flanks, but no associated generation of mounded contourite drifts occurs. A similar effect of salt walls and diapirs has been interpreted to cause the acceleration of deep currents in the Brazilian margin (Viana, 2001; Viana et al., 2002).

Objectives

The major objective for Site U1390 is to recover a sedimentary contourite record for the Quaternary (Stow et al., 2011), deposited under the influence of the lower core of MOW, and determine the synsedimentary neotectonic control on architecture and evolution of the CDS. A careful dating of the principal unconformities throughout the region is proposed, followed by correlation with the seismic reflection framework already established (see Fig. **F19** in the "Expedition 339 summary" chapter [Expedition 339 Scientists, 2013a]). Specific objectives for Site U1390 include:

- Drilling through the drift succession and into Quaternary sediments deposited by the lower core of MOW in the medial part of the CDS;
- Charting the chronology of recent tectonic activity that has had significant effect on development and architecture of the CDS and identifying the principal morphological changes that have resulted from this tectonic activity;
- Calibrating the three main stages of drift evolution recently identified and understanding the timing and formation of the buried relict drifts in the central part of the middle slope of the Gulf of Cádiz (Llave et al., 2007a, 2007b, 2011; Hernández-Molina et al., 2006; García et al., 2009);

- Evaluating the direct influence of recent diapiric activity on evolution of the CDS, particularly with regard to the erosion of channels and moats through the softer cores of diapir strings. An excellent opportunity exists to determine the rate of diapiric movement and its change through time;
- Obtaining a more accurate picture of the relationship between recent tectonics and paleoceanographic changes by combining the above data, and, in particular, elucidating the influence of the Guadalquivir Bank, diapirs, and diapiric ridges on MOW pathways and hence on changes in mixing between MOW and surrounding waters. This will in turn influence the nature of erosion and entrainment by currents;
- Determining the sedimentary stacking pattern of a sheeted drift in relation to changes in sea level and other forcing mechanisms; and
- Evaluating periods of drift construction, nondeposition (hiatuses), and erosion.

Operations

The vessel departed for Site U1390, the sixth site of the expedition, at 1930 h on 2 January 2012. The 22 nmi transit from Site U1389 was covered in just over 2 h. The vessel was positioned on the new coordinates at 2145 h.

Three holes were drilled at Site U1390 (Table T1). Hole U1390A was cored using the advanced piston corer (APC) to 76.7 meters below seafloor (mbsf) and then with the extended core barrel (XCB) to 350 mbsf. Hole U1390B was cored with the APC to 194.1 mbsf. Hole U1390C was cored with the APC to 175.4 mbsf. Downhole logging was carried out in Hole U1390A using the triple combination (triple combo) and Formation MicroScanner (FMS)-sonic tool strings (see **"Downhole logging at Site U1390"**). Overall recovery at Site U1390 was 437.95 m (98.2%) with the APC and 248.32 m (90.9%) with the XCB. Total cored interval at Site U1390 was 719.5 m and total recovery was 686.27 m (95.4%).

Hole U1390A

The APC/XCB bottom-hole assembly (BHA) and the drill string were deployed with the underwater camera. A survey of the seafloor was conducted using a 30 m grid pattern. Other than one large rock, no significant obstructions were observed. Hole U1390A was spudded with the APC at 0520 h on 3 January. Seafloor depth was established at 1005.1 meters below rig floor (mbrf; 993.4 mbsl), which was 3.1 m deeper than the corrected precision depth recorder value of 1002 mbrf. Piston coring was only able to advance to 76.7 mbsf. The decision was made to switch to the XCB when the last APC core (339-U1390A-9H) required ~3 h to extract from the core barrel. Recovery for the piston-cored interval was 102%. Cores were oriented starting with Core 4H. The advanced piston corer temperature tool (APCT-3) was deployed to measure temperature at 32.1 (Core 4H) and 60.6 (Core 7H) mbsf. XCB coring deepened the hole to the depth objective of 350 mbsf by 1700 h on 4 January. Recovery for the 273.3 m XCB interval was 91%. The overall recovery in Hole U1390A was 93%.

Hole U1390B

With the scientific objective of finding a target horizon on the seismic line at a shallower depth than at Hole U1390A, the vessel was offset 200 m north of Hole U1390A. The underwater camera was deployed and the seafloor monitored during the movement of the vessel. Once the vessel was in position, Hole U1390B was spudded with the APC at 1002 mbrf at 1700 h. The calculated seafloor depth was 1002.4 mbrf (990.7 mbsl). Piston coring advanced to 194.1 mbsf, where Core 21H could not be recovered with the coring line. When the orientation tool was retrieved to the surface using the coring line, it was discovered that the bulkhead lock pin between the male and female sections that connect the nonmagnetic sinker bars to the core barrel had parted in two places (possible metal fatigue). After several fishing attempts failed to grasp the female section that remained downhole with the core barrel, the BHA was recovered and the core barrel extracted at the surface. The bit was at the rotary table at 2120 h on 6 January. Piston coring recovered 189.9 m, which represented 98% of the cored interval. Cores were oriented starting with Core 3H. Temperature measurements were obtained with the APCT-3 at 18.6 (Core 2H), 47.1 (Core 5H), and 75.6 (Core 8H) mbsf. All cores were obtained with nonmagnetic core barrels.

Hole U1390C

The drill string was redeployed for the second time on site and the vessel offset 20 m east of Hole U1390B. Hole U1390C was spudded with the APC at 0240 h on 7 January and established seafloor depth at 1004.1 mbrf (992.4 mbsl). Piston coring proceeded to the depth objective of 174.5 mbsf by 2200 h on 7 January. Stuck core barrels for Cores 2H through 4H required an extra coring line round trip to pull the orientation tool before it was possible to recover the core barrel. Cores were oriented starting with Core 4H and then followed by Cores 9H through 19H (last core). APCT-3 measurements were obtained at 23.4

(Core 3H), 51.9 (Core 6H), 80.4 (Core 9H), and 108.9 (Core 12H) mbsf. Nonmagnetic core barrels were used to obtain all cores. The bit was pulled free of the seafloor at 2300 h and cleared the rotary table at 0115 h on 8 January, ending operations at Site U1390. The vessel departed for the last site of the expedition at 0230 h that morning. Total time on site was 5.2 days.

Downhole logging at Site U1390

Instead of logging the third hole at the site, it was decided to log Hole U1390A. The hole was subjected to routine conditioning procedures, including a wiper trip, mud flushes, and displacement with 124 bbl of 10.5 ppg mud before the bit was placed at 96.6 mbsf. The logging program consisted of the triple combo and FMS-sonic tool strings. The triple combo tool string was deployed at 2400 h on 4 January and recovered at 0330 h. The FMS-sonic tool string was run in at 0600 h and recovered at 1000 h on 5 January. Both tools successfully covered the open hole to 350 mbsf. After the FMS-sonic tool string was rigged down, the bit was pulled clear of the seafloor at 1155 h on 5 January.

Lithostratigraphy

Drilling at Site U1390 recovered a 351 m thick section of sediment (Figs. **F3, F4**). The shipboard lithostratigraphic program at Site U1390 involved detailed visual logging of all archive sections, visual assessment of sediment color, petrographic analysis of smear slides, and X-ray diffraction (XRD) analyses of powdered bulk samples. We sampled regularly for smear slides during visual core description in Hole U1390A (n = 96); these results were used to provide detailed sediment description, to identify major components, and to apply a more detailed descriptive sediment classification. Smear slides were selected from specific intervals in Holes U1390B (n = 29) and U1390C (n = 4) to investigate lithologies and features of specific interest and to identify any differences from Hole U1390A. Thirty-eight samples were selected from Hole U1390A for powder XRD analysis in order to obtain a general indication of bulk mineral composition (Fig. **F5;** Table **T2**). Ten of these samples were processed to identify clay mineralogy (Fig. **F6**).

The age at the bottom of Hole U1390A is between 1.2 and 1.6 Ma (see **"Biostratigraphy"**). Two minor hiatuses are recognized at 228.68 and 293.68 mbsf, with durations of 0.26 to >0.6 m.y. and of 0.9 to 1.2 m.y., respectively.

The sedimentary succession at Site U1390 is classified as one major lithologic unit divided into two subunits (IA and IB) (Fig. **F4;** Table **T3**). Overall, Unit I is dominated by calcareous mud and silty mud with biogenic carbonate. Sandy mud with biogenic carbonate is a subordinate lithology.

Total carbonate content based on carbonate analyses in Hole U1390A ranges from 21 to 34.5 wt% with an average of 27 wt% (Table **T4**). These results are consistent with abundances of biogenic carbonate and detrital carbonate estimated from smear slides. Thus, the lithologic names determined from smear slide analyses have been used without modification through this text, the summary diagrams, and the visual core description sheets.

The character of sediment physical properties, including natural gamma radiation (NGR), magnetic susceptibility, color reflectance parameters, and density records the distribution of these various lithologies and sediment components (see **"Physical properties"**). Characteristics of the sedimentary sequence cored at Site U1390, together with some of these additional properties, are summarized in Figure **F7.**

Unit I description

Intervals: 339-U1390A-1H-1, 0 cm, through 38X-CC, 37 cm; 339-U1390B-1H-1, 0 cm, through 21H-CC, 6 cm; 339-U1390C-1H-1, 0 cm, through 19H-CC, 35 cm

Depths: Hole U1390A = 0–351.26 mbsf (bottom of hole [BOH]), Hole U1390B = 0–189.64 mbsf (BOH), Hole U1390C = 0–175 mbsf (BOH)

Age: Holocene–Pleistocene

Unit I sediment is composed of varying amounts of terrigenous and biogenic components (mainly clay minerals, nannofossils, detrital and biogenic carbonate, and quartz) (Table **T5**). Calcareous mud, silty mud with biogenic carbonate, sandy mud with biogenic carbonate, and silty sand with biogenic carbonate are common lithologies in Unit I.

Unit I is divided into Subunits IA and IB on the basis of the composition of the muddy deposits (Table **T5**) and the thickness of the sandy deposits (i.e., silty sand with biogenic carbonate and sandy mud with biogenic carbonate). The lithology of Subunit IA is dominated by mud. In contrast, sand beds in Subunit IB are thicker than those in Subunit IA.

Subunit IA

Intervals: 339-U1390A-1H-1, 0 cm, through 32X-CC, 29 cm; 339-U1390B-1H-1, 0 cm, through

21H-CC, 6 cm; 339-U1390C-1H-1, 0 cm, through 19H-CC, 35 cm

Depths: Hole U1390A = 0–293.78 mbsf; Hole U1390B = 0–189.64 mbsf (BOH), Hole U1390C = 0–175 mbsf (BOH)

Age: Holocene–Pleistocene

Lithologies and bedding

The major lithologies in Subunit IA are calcareous mud, silty mud with biogenic carbonate, sandy mud with biogenic carbonate, and silty sand with biogenic carbonate (Fig. **F4**). An important feature of these lithologies is that increased grain size corresponds to increased detrital content and decreased abundance of biogenic carbonate. The downhole variations in the number of beds of these major lithologies, except for calcareous mud, are shown in Figure **F4.** Within Subunit IA in Hole U1390A, overall downhole changes in the number of silty sand, sandy mud, and silty mud beds appear to show three cycles in Cores 339-U1390A-1H through 13X, 13X through 19X, and 19X through 32X. A similar cyclic change is also recognized at the previous sites (Unit I at Sites U1386, U1387, and U1389). These cycles might be controlled by the changes of sediment supply, bottom water current velocity, relative sea level, or neotectonic activity.

Almost all the intervals composed of calcareous mud are characterized by indistinct bedding (Fig. **F8**). Thus, features that might be beds are distinguished by subtle changes in color, bioturbation intensity, or silt/clay ratio. The coarser sediments (i.e., silty sand with biogenic carbonate, sandy mud with biogenic carbonate, and silty mud with biogenic carbonate) are intercalated in the calcareous mud and show two distinctive bedding patterns, bi-gradational grading and normal grading (Figs. **F9, F10**). The bi-gradational sequence is typically characterized by coarsening upward from calcareous mud to silty mud with biogenic carbonate to sandy mud with biogenic carbonate (or silty sand with biogenic carbonate) and subsequent fining upward from silty mud with biogenic carbonate to calcareous mud. Some of the bi-gradational sequences in Subunit IA lack sandy intervals (i.e., muddy sand with biogenic carbonate and silty sand with biogenic carbonate). Thicknesses of the bi-gradational sequences are commonly a few decimeters to several meters. In contrast, the normally graded sequence is characterized by fining upward, generally from sandy mud with biogenic carbonate or silty sand with biogenic carbonate to silty mud with biogenic carbonate to calcareous mud. The thickness of the normally graded sequences is generally <1 m. Inversely graded sequences are rare (Fig. **F11**) and show lithologic changes from calcareous mud to silty mud with biogenic carbonate to sandy mud with biogenic carbonate with a sharp upper contact.

Contacts between all lithologies, and between subjacent beds of calcareous mud, are mainly gradational or bioturbated but do also occur as sharp basal contacts, particularly with the normal graded sequences.

No distinctive features suggesting tectonic influence (e.g., microfaults, slumping, or sediment gravity flow deposits) are recognized in Subunit IA.

Structures and texture

For the most part, primary sedimentary structures were not observed in Subunit IA, except for faint lamination in parts of the calcareous mud (e.g., Sections 339-U1390B-2H-2 through 2H-5; Fig. **F12**). The preserved laminations suggest especially rapid sedimentation rates for the calcareous mud in these intervals.

Bioturbation is the most evident postdepositional sedimentary structure in Subunit IA and is present throughout the observed section. Most of the bioturbation and individual burrows are recognized as centimeter to millimeter scale, dispersed, and gray to black color mottling and pyritic burrow fills. In some intervals, the relative frequency of the mottling seems to be greater and the mottles darker than those of the previous sites (U1386–U1389). Some of the black mottling appears to be associated with high values of natural remanent magnetization (NRM) intensity in shipboard paleomagnetic measurements (see **"Paleomagnetism"**). The bioturbation intensity is slight to sparse on the basis of the observation of beds with slight color changes.

Composition

Mineral compositions based on smear slide observations show no clear differences between the two subunits (Fig. **F13**). The results show that almost all lithologies at Site U1390 are dominated by siliciclastic minerals including clay minerals, quartz, feldspars, mica, dolomite, and detrital carbonate (Fig. **F14;** Table **T5**). The biogenic fraction is mainly composed of nannofossils, with a few foraminifers present. A few beds are also characterized by rare to abundant diatoms, some radiolarians, and few to common sponge spicule fragments (e.g., Sections 339-U1390A-19X-3 and 339-U1390B-18H-3; Fig. **F15**). Authigenic components are dominated by dolomite and pyrite (Fig. **F16**). Abundances of terrigenous components, as estimated from smear slides (Table **T5**), are 45%–63% (average = 51%) siliciclastics (including quartz,

heavy minerals, opaques, micas, and feldspars) and 13%–35% (average = 24%) detrital carbonate. No discrete volcanic ash layers and no dropstones were observed. Abundances of biogenic components, as estimated from smear slides, are 10%–38% (average = 23%) biogenic carbonate (primarily nannofossils, plus foraminifers for the sandy mud and silty sand lithology) and 1%–22% (average = 0.4%) biogenic silica (primarily diatoms and radiolarians). Siliceous microfossils (≤20%) were estimated only in intervals 339-U1390A-19X-3, 108 cm (163.94 mbsf) and 19X-4, 10 cm (164.15 mbsf). Total carbonate contents (assuming all inorganic carbon to be $CaCO_3$) range from 21.15 to 34.51 wt% (average 27.04 wt%; Table T4). Abundances of other minerals, as estimated from smear slides, are <5% pyrite (usually classified as opaque mineral grains) and <5% authigenic dolomite (mostly observed by its rhombic shape). A limited number of glauconite grains are also present (interval 339-U1390A-1H-2, 80 cm; 2.3 mbsf).

Macrofossil fragments and sparse nearly whole specimens are visible throughout Subunit IA at Site U1390. Recognizable fragments include gastropods, bivalves, echinoids, cold-water corals, and *Arenaria* (Fig. F17).

Color

A downhole color change from olive-gray (5Y 4/2) to dark gray (5Y 4/1) occurs at Sections 339-U1390A-3H-1 (~13 mbsf), 339-U1390B-1H-6 (8.2 mbsf) and 339-U1390C-2H-4 (9.03 mbsf). Subsequently, below 32 mbsf, sediments become slightly more greenish (dark greenish gray) (10Y 4/1). Very dark greenish gray intervals are moderately well developed, which is consistent with relatively low values of L*.

The principal colors of the lithologies in Subunit IA, as noted during visual description of the core, range from dark greenish gray (56.36% of Subunit IA) to dark gray (13.94%) to greenish gray (12.12%) and very dark greenish gray (8.28%). The remaining colors of Subunit IA are olive-gray (3.84%), gray (2.22%), greenish gray (1.21%), reddish gray (1.01%), dark olive-gray (0.81%), and dark grayish brown (0.20%).

Bulk mineralogies

The bulk mineral composition of 18 sediment samples in Subunit IA was analyzed by XRD. Diffraction peaks from silicate minerals such as quartz, plagioclase, and illite and carbonate minerals such as calcite and dolomite contribute most of the measured total diffraction peak intensity (Fig. F5; Table T2).

Subunit IB

Interval: 339-U1390A-32X-CC, 29 cm, through 38X-CC, 37 cm
Depth: 293.78–351.26 mbsf (BOH)
Age: Pleistocene

Lithologies and bedding

Subunit IB comprises the lower part of Unit I and is characterized by more thick sands than were observed Subunit IA. In particular, bi-gradational contourite sequences from several to at least 7 m thick are well preserved in Subunit IB (Fig. F18). One bi-gradational sequence ~10 m thick was recovered in Cores 339-U1390A-33X and 34X, if we assume that both cores recovered parts of the same bed. The observation that thick sands are present in Subunit 1B is consistent with downhole logging results (see "Downhole measurements").

No distinctive features that suggest tectonic influence (e.g., microfaults, slumping, or sediment gravity flow deposits) are recognized in Subunit IB.

Structures and texture

For the most part, primary sedimentary structures were not observed in Subunit IB, although bioturbation occurs as a common postdepositional sedimentary structure throughout. Individual burrows are recognized as centimeter to millimeter scale, dispersed, gray to black color mottling and pyritic burrow fills. The bioturbation intensity is slight to sparse based on the observation of beds with slight color changes.

Composition

The features of the main lithologies in Subunit IB are the same as those in Subunit IA. Abundances of terrigenous components in Subunit IB (Hole U1390A) are also similar to those in Subunit IA (Table T5), with 40%–70% (average = 57%) siliciclastics (including quartz, heavy minerals, opaques, micas, and feldspars) and 20%–30% (average = 22%) detrital carbonate. No discrete volcanic ash layers and no dropstones were observed. Abundances of biogenic components are 10%–30% (average = 21%) biogenic carbonate (primarily nannofossils, plus foraminifers for the sandy mud and silty sand lithology), and biogenic silica is absent.

Color

The principal colors of the lithologies in Subunit IB range from greenish gray (69.05% of Subunit IB) to light greenish gray (21.43%). The remaining colors

of Subunit IB are gray (5.95%), reddish gray (1.19%), light greenish gray (1.19%), and dark gray (1.19%).

Bulk mineralogy

The bulk mineral composition of six sediment samples from Subunit IB was analyzed by XRD. Diffraction peaks from silicate minerals such as quartz, plagioclase, and illite and carbonate minerals such as calcite and dolomite contribute most of the measured total diffraction peak intensity (Fig. **F5;** Table **T2**).

Discussion

Contourite depositional system

Given the physical setting of Site U1390, several lines of evidence support the interpretation of Unit I as a sequence of contourite deposits and thus evidence for current transport and changing current velocities. Among these lines of evidence are that

- This site is located on the sheeted drift related to the Guadalquivir contourite channel;
- Bi-gradational graded successions are abundant;
- Interbedded normal graded sequences with sharp base contacts and inversely graded sequences with sharp top contacts are occasionally observed; and
- Obvious primary sedimentary structures, commonly observed in sediment gravity flow deposits, have not been recognized in these sediments.

Subunit IA (293.68 m thick) is a typical example of a muddy/silty contourite succession, similar to that defined by Stow and Faugères (2008) as a conceptual contourite facies model (Figs. **F4, F8, F9, F10, F11**), whereas Subunit IB (over 57.58 m thick) is a typical example of a sandy contourite succession (Figs. **F4, F18**). Very thick bi-gradational sequences are interpreted to indicate rapid sedimentation caused by high sediment supply from the Guadalquivir Channel. Some faint laminations observed at the top of Hole U1390B (Fig. **F12**) also support the interpretation of rapid sedimentation. The differences observed between Subunits IA and IB are most likely associated with a change from a sand-dominated CDS to a mud-dominated CDS.

Relationship between the observed hiatuses and the lithologic features

Two hiatuses are recognized on the basis of the micropaleontological data. In Hole U1390A, one hiatus is at 228.68 mbsf, which extends from 0.26 to >0.6 Ma, and the other is at 293.68 mbsf, which extends from 0.9 to 1.2 Ma (see **"Biostratigraphy"**). The older hiatus apparently corresponds to the boundary between Subunits IA and IB. It is difficult to observe the contact clearly because the boundary is in the core catcher of Core 339-U1390A-32X. However, the total thicknesses of the sandy deposits (i.e., silty sand with biogenic carbonate and sandy mud with biogenic carbonate) within each core show clear differences across the Subunit 1A/1B boundary (Fig. **F4**). Thus, it is suggested that some of the controlling factors for the deposition of the contourites (e.g., bottom water current velocity, sediment supply, or relative sea level) changed during the hiatus.

In contrast, the younger hiatus can be located precisely at the downhole color change from darker greenish gray to lighter greenish gray at interval 339-U1390A-26X-2, 19 cm (228.7 mbsf), based on nannofossil dates of 0.26 Ma at 228.65 mbsf and >0.6 Ma at 228.73 mbsf (Fig. **F19;** see **"Biostratigraphy"**). No major lithologic change is observed across this hiatus, as calcareous mud is present both above and below that level. The only compositional change is a decrease in the abundance of the siliciclastic fraction, from 38% above the hiatus to 55% below (Table **T5**). Further detailed examination (e.g., composition or grain size) will be necessary to better understand the hiatus in relation to the changes in depositional environment.

Biostratigraphy

Sediment at Site U1390 dates from the Holocene to the mid-Pleistocene (Fig. **F20;** Table **T6**), with the base age of Hole U1390A estimated at younger than 1.4 Ma. The absence of relevant and characteristic calcareous nannofossil bioevents in the micropaleontological succession allows us to define two hiatuses covering the interval between 0.3–0.6 and 0.9–1.2 Ma. The older hiatus is, furthermore, indicated by the co-occurrence of the "*Stilostomella* extinction" event (0.58–0.7 Ma) and the top of the paracme of *Neogloboquadrina pachyderma* (sinistral) (1.21 Ma) between Samples 339-U1390A-31X-CC and 32X-CC (Table **T6**).

A sedimentation rate of ~75 cm/k.y. has been estimated for the upper part of the site, whereas intervals below the younger hiatus are close to 85 cm/k.y., although the absence of precise age control prevents an accurate calculation (Fig. **F20**).

The microfossil content of sediment recovered at Site U1390 was usually high. The samples are rich in planktonic and benthic foraminifers as well as calcareous nannofossils (Tables **T7, T8, T9**). Pteropod fragments were found in several samples and in Sample 339-U1390A-2H-CC, their occurrence is even common. Ostracods were not studied at Site U1390.

Pollen and spores are abundant in the seven samples analyzed in Hole U1390A, ranging from ~6,000 to 60,000 grains/cm^3. These figures are similar to those found at the previous sites in the Gulf of Cádiz. However, they are 10 to 50 times lower than the values observed in Holocene sediment from the Guadiana estuary (Fletcher et al., 2007), located 100 km north on the Portuguese coast. The preservation of the grains is mostly good to moderate. The proportion of unidentifiable grains progressively increases toward the bottom of the sequence, as is the case at Sites U1387 and U1389 (Fig. F26 in the "Site U1387" chapter [Expedition 339 Scientists, 2013e] and Fig. F22 in the "Site U1389" chapter [Expedition 339 Scientists, 2013g]). Microcharcoal particles and dinocysts were also observed.

Calcareous nannofossils

We examined all core catcher samples from Holes U1390A–U1390C for calcareous nannofossil biostratigraphy. The assemblages are abundant to very abundant. The preservation is good to moderate, with weak dissolution in some samples. Small- and medium-sized placolith species (<3 and 3–5.5 µm, respectively) dominate most of the assemblages (Table T7). Two possible hiatuses were detected (see above) at this site.

Six Pleistocene nannofossil events defined and/or calibrated by Raffi et al. (2006 and references therein) and Flores et al. (2010) were identified in Hole U1390A (Table T6). In this site the LO of *Gephyrocapsa omega* (0.57 Ma; Maiorano and Marino, 2004, and references therein) was considered to better constrain the younger hiatus. The deepest samples in Holes U1390B and U1390C are younger than the first occurrence (FO) of *Emiliania huxleyi* (0.26 Ma) and thus precede the first hiatus recognized in Hole U1390A.

The change in abundance of large *E. huxleyi* (>4 µm) that characterizes Termination 1 in mid-latitude water masses in the Atlantic Ocean has been proven as a useful event by Flores et al. (2010). This change in abundance was recorded in Hole U1390A between Samples 339-U1390A-2H- 3, 75 cm, and 2H-4, 75 cm (7.37–8.87 mbsf). The FO of *E. huxleyi* (0.26 Ma), which marks the base of Zone NN21, was placed in Hole U1390A between Samples 22X-1, 70 cm, and 22X-2, 20 cm (189.50–190.50 mbsf). However, this event should be taken with caution because of dissolution effects and the low proportion of this species.

A possible hiatus was detected between Samples 339-U1390A-26X-2, 15 cm, and 26X-2, 23 cm (228.65–228.73 mbsf), characterized by a variation in the composition of calcareous nannofossil assemblages. The concomitant presence of *Pseudoemiliania lacunosa* (last occurrence [LO] at 0.46 Ma) and *G. omega* (LO at 0.57 Ma; Maiorano and Marino, 2004) in the latter sample allows us to place the hiatus within Zones NN20 and NN19 (i.e., between 0.26 and 0.57 Ma).

Reticulofenestra asanoi was not identified at this site. In general, the *R. asanoi* biohorizon (0.90–1.07 Ma) is considered a useful and globally recognized event in Pleistocene sediment. The subsequent event recognized is the LO of large *Gephyrocapsa* spp. (>5.5 µm) (1.24 Ma), placed between Samples 339-U1390A-32X-5, 138 cm, and 32X-6, 23 cm (292.08–292.43 mbsf), and pointing to a second hiatus at this site that covers the interval between 0.9 and 1.24 Ma.

The LO of *Helicosphaera sellii* (1.25 Ma) was identified between Samples 339-U1390A-36X-CC and 37X-1, 72 cm (332.63–333.02 mbsf). This event is considered diachronous (Raffi et al., 1993; Wei, 1993). However, its occurrence at this site is consistent with the ages provided by Raffi et al. (2006) for the Mediterranean Sea when compared with other calibrated events.

Planktonic foraminifers

Planktonic foraminifers were studied in all core catcher samples from Holes U1390A–U1390C. To better constrain the older hiatus and the paracme of *N. pachyderma* (sinistral), additional samples were analyzed from Core 339-U1390A-34X. Foraminifer abundance is, in general, abundant to dominant, and preservation is very good to good (Table T8). Lesser abundance was observed in Core 339-U1390A-34X and Samples 339-U1390A-36X-CC and 37X-CC, which consist of detrital sands (see **"Lithostratigraphy"**).

The planktonic foraminifer assemblages are typical for subtropical to temperate surface waters. The presence of *Globigerinoides ruber* (pink), *Globigerinoides trilobus,* and *Globigerinoides sacculifer* indicate warmer conditions and thus interglacial or interstadial conditions. Samples 339-U1390A-1H-CC and 339-U1390C-1H-CC are attributed to the Holocene, and Samples 339-U1390A-14X-CC, 339-U1390B-13H-CC, and 339-U1390C-13H-CC most likely correlate with marine isotope stage (MIS) 5e. In several samples, especially from the interval between Cores 3H and 9H in all three holes and Samples 339-U1390C-16H-CC through 19H-CC, *Globigerina bulloides* and *N. pachyderma* (dextral) dominate the fauna, indicating glacial conditions. Deep-dwelling foraminifers, typically *Globorotalia truncatulinoides* and/or *Globorotalia crassaformis,* were found in nearly every sample and can even reach abundances of 5%–10% (few).

Samples 339-U1390A-30X-CC; 31X-CC; 33X-CC; 34X-1, 59–61 cm; 34X-3, 59–61 cm; and 37X-CC contain few specimens of reworked Pliocene or Miocene planktonic foraminifer species, (i.e., *Globorotalia margaritae, Globorotalia puncticulata, Globorotalia miotumida,* and *Sphaeroidinellopsis seminulina*). Generally, each species is represented by just one specimen.

The only biostratigraphic event, the top of the paracme of *N. pachyderma* (sinistral) defined by the reappearance of this species in MIS 36 (1.21 Ma; Lourens et al., 2004; Raymo et al., 1989; Sierro et al., 2009), was observed between Samples 339-U1390A-31X-CC and 32X-CC (284.61–293.68 mbsf).

Large, heavily encrusted specimens of *Neogloboquadrina atlantica* (dextral) were observed in Samples 339-U1390A-36X-CC and 37X-CC (332.63–335.27 mbsf). This event was observed at other sites of this expedition, occurring at ~1.3 Ma and always within the paracme of *N. pachyderma* (sinistral).

Benthic foraminifers

All core catcher samples from Hole U1390A were analyzed for benthic foraminiferal assemblages (Table **T9**). Benthic foraminifers are generally abundant and well preserved. As at previous sites, the abundance and preservation of benthic foraminifers are related to lithology, and less abundant, moderately preserved benthic foraminiferal assemblages are associated with coarser sediments.

Most of the samples above the younger hiatus (Samples 339-U1390A-1H-CC through 25X-CC) are dominated by *Brizalina dilatata, Bulimina striata* gr., *Cassidulina teretis, Melonis barleeanus,* and *Uvigerina* spp., species that characterize environments with elevated organic matter flux and reduced ventilation (van Morkhoven et al., 1986; Leckie and Olson, 2003; Murray, 2006). Sample 339-U1390A-19X-CC possesses a unique composition with a very high abundance of *Eubuliminella exilis* (>75%), a species rarely observed in other samples from this and previous sites. Its high abundance might be related to a change in the source and the quality of the organic matter delivered to the seafloor, as this species proliferates in environments rich in fresh phytodetritus (Caralp, 1989). Strong bottom currents are indicated by elevated abundances of *Trifarina angulosa* in Samples 339-U1390A-17X-CC, 20X-CC, and 22X-CC through 25X-CC. In most of these samples, a parallel decrease in *B. dilatata* is observed.

Below the hiatus, *Cibicides*/*Cibicidoides* spp. occurs more commonly, with the highest abundances between Samples 339-U1390A-33X-CC and 38X-CC. In parallel, the abundances of *Brizalina, Bulimina, Melonis,* and *Uvigerina* species significantly decrease, pointing to improved ventilation.

The "epibenthos group," which has been suggested as an indicator for MOW intensity in the area (Schönfeld, 1997, 2002; Schönfeld and Zahn, 2000), has generally low abundances of <5% and is most common between Samples 339-U1390A-26X-CC and 32X-CC. In contrast to previous sites, *Discanomalina coronata* is a regular component besides *Cibicides lobatulus, Planulina* spp., and *Textularia pseudogramen*.

The last frequent occurrence of nodosariids, pleurostomellids, and stilostomellids was recorded in Sample 339-U1390A-32X-CC. Above this level (i.e., above the older hiatus), individual shells of *Siphonodosaria* were identified in Samples 339-U1390A-31X-CC, 29X-CC, 28X-CC, 16X-CC, and 15X-CC. These single shells are considered allochthonous, as the corresponding planktonic foraminifers indicate reworking (Table **T8**). After careful consideration and comparison with age estimates from the other microfossil groups, the *Stilostomella* extinction (0.58–0.7 Ma) (Hayward, 2002; Kawagata et al., 2005) is placed between Samples 339-U1390A-31X-CC and 32X-CC (284.61–293.68 mbsf).

Palynology

Seven samples from Hole U1390A (Samples 1H-CC, 6H-CC, 12X-CC, 18X-CC, 24X-CC, 30X-CC, and 36X-CC) were analyzed. The lowest pollen and spore concentrations correspond to samples characterized by the highest proportion of sand (Samples 12X-CC and 36X-CC; see **"Lithostratigraphy"**), although the preservation is good to moderate.

The very low resolution pollen record reflects the alternating dominance of the four main plant ecological groups that characterize this region, *Pinus,* Mediterranean forest, semidesert, and grasslands (Fig. **F21**), as already documented at the previous sites for the last 1.5 m.y (see "Biostratigraphy" in the **"Site U1385,"** **"Site U1386,"** **"Site U1837,"** **"Site U1388,"** and **"Site U1389"** chapters [Expedition 339 Scientists, 2013c, 2013d, 2013e, 2013f, 2013g). Interestingly, the floristic composition and the proportion of each palynomorph in the uppermost sample (339-U1390A-1H-CC) is similar to those found in the levels dated between ~7.3 and 4.4 calendar k.y. BP in the Guadiana estuary (Fletcher et al., 2007). These levels are characterized by the abundance of *Quercus, Taraxacum*-type, Poaceae, and *Isoetes* spores; the low concentrations of *Pinus;* and the virtual absence of Ericaceae. Therefore, an age of ~6 calendar k.y. BP was assigned to 3.63 mbsf, indicating a high sedimentation rate for the mid–late Holocene interval of this sequence (Fig. **F20**).

Paleomagnetism

Paleomagnetic investigation of the 78 APC and XCB cores collected at Site U1390 included the measurement of magnetic susceptibility of whole-core and archive-half split-core sections and the NRM of archive-half split-core sections. NRM was measured before and after alternating field (AF) demagnetization with 20 mT peak field for all studied cores of the site. The FlexIt tool was used to orient 29 cores in the APC sections of Holes U1390A and U1390B starting with Core 4H and in Hole U1390C starting with Core 9H. However, as was the case at Site U1389, the tool failed to properly orient the cores in Hole U1390A. The technical issue was resolved subsequently and the APC core orientations for Holes U1390B and U1390C are provided in Table **T11** and used for APC core reorientation (Fig. **F22**). We processed data extracted from the Laboratory Information Management System database by removing all measurements collected from disturbed and void intervals, which are listed in Table **T12** (see **"Stratigraphic correlation"**), and all measurements that were made within 10 cm of the section ends, which are slightly biased by measurement edge effects. The processed NRM inclination, declination (including the FlexIt tool corrected declination), and intensity data after 20 mT peak field AF demagnetization are listed in Tables **T13, T14,** and **T15.**

Natural remanent magnetization and magnetic susceptibility

The intensity of NRM after 20 mT demagnetization is similar in magnitude in the overlapping parts of Holes U1390A, U1390B, and U1390C, ranging from ~10^{-5} to ~10^{-2} A/m (Fig. **F22,** third panel). Sediment from the uppermost ~20 mbsf exhibits the highest NRM intensities, on the order of 10^{-2} A/m, with a mean of ~0.017 A/m. Below 20 mbsf, magnetic intensities are variable (mean value is ~0.0046 A/m) but generally lower than those in the top part of the section. NRM intensity data also show a few spikes where black or gray color mottling (burrows) is present (see **"Lithostratigraphy"**). The high values of NRM intensity could be related to diagenetic growth of fine-grained magnetic minerals (possibly iron sulfides) in the burrows.

Despite the coring disturbance and drill string overprint in the XCB-cored sections, a relatively stable magnetic component was preserved in sediment from all holes, allowing for the determination of magnetic polarity for most parts of the recovered sedimentary sequences. The XCB sections in Hole U1390A are often heavily biscuited and frequently contain as much of the disturbed matrix as the intact material, compromising the quality of the resulting paleomagnetic data.

Magnetic susceptibility measurements were made on whole cores from all three holes as part of the Whole-Round Multisensor Logger (WRMSL) analysis and on archive-half split-core sections using the Section Half Multisensor Logger (SHMSL) (see **"Physical properties"**). The WRMSL-acquired susceptibility was stored in the database in raw meter units. These were multiplied by a factor of 0.68 × 10^{-5} to convert to the dimensionless volume SI unit (Blum, 1997). A factor of (67/80) × 10^{-5} was multiplied by the SHMSL-acquired susceptibility stored in the database. Magnetic susceptibility is consistent between the two instruments and, in general, parallels the intensity of magnetic remanence. Magnetic susceptibility varies between 5 × 10^{-5} and 40 × 10^{-5} SI (Fig. **F22,** fourth panel). Note that in Figure **F22,** a constant of 25 × 10^{-5} SI was added to the SHMSL measurements (gray lines) to facilitate the comparison with the WRMSL measurements (black lines).

Magnetostratigraphy

We use magnetic inclinations and FlexIt tool corrected declinations when available to interpret magnetostratigraphy for the APC-cored sediment sequences. The lack of core orientation and the significant coring disturbance, as well as drill string overprint in the XCB cores, limit our magnetostratigraphic interpretation for the XCB-cored sediment in Hole U1390A to relying on magnetic inclination changes. The geomagnetic field at the latitude of Site U1390 (36.32°N) has an expected inclination of 55.78°, assuming a geocentric axial dipole field model, which is sufficiently steep to determine magnetic polarity in cores that lack horizontal orientation.

NRM inclination data (after 20 mT peak field AF demagnetization) in all three holes indicate that the Brunhes (C1n) normal polarity chron is recorded in the uppermost ~230 m of sediment (Fig. **F22**). This interpretation is consistent with the LO of *G. omega* (0.6 Ma) at 228.69 mbsf. Biostratigraphic evidence (see **"Biostratigraphy"**) suggests the existence of two hiatuses in Hole U1390A, with the older one at ~290 mbsf (0.7–1.2 Ma) and the younger one at ~230 mbsf (0.6–0.47 Ma), which makes a straightforward magnetostratigraphic interpretation difficult. Although a very clear normal and reversed magnetic polarity pattern seems to exist (Fig. **F22**), an assignment of the normal and reversed polarity intervals to known parts of the geomagnetic polarity timescale is impossible without additional constraints from discrete sample measurements.

Physical properties

Physical properties at Site U1390 were determined in Holes U1390A–U1390C. High-resolution scanning on whole-round sections was performed with the WRMSL at 2.5 cm intervals. NGR was determined for all holes at a high resolution of ~10 cm with two positions of the detector array and occasionally at lower resolution (~20 cm) with one position of the detector. The Special Task Multisensor Logger (STMSL) was only used for Holes U1390B and U1390C, for stratigraphic correlation purposes, at a scanning interval of 2.5 cm. Thermal conductivity probes were applied on Section 3 downhole to Core 339-U1390A-8H and from Core 339-U1390C-9H to 19H. *P*-wave velocity on split-core segments (working half) was obtained for APC Core 339-U1390A-1H through Section 5H-1. Moisture and density (MAD) measurements were determined for every second section of each core in Hole U1390A. Color reflectance analysis and split-core point-magnetic measurements were performed for every segment at 5 cm intervals.

Based on the physical property data, three main units were defined at Site U1390 (Figs. **F23, F24, F25**). Physical properties Unit I spans from 0 to 70 mbsf (base of Core 339-U1390A-8H), physical properties Unit II from 70 to 295 mbsf, and physical properties Unit III from 295 mbsf to the base of Hole U1390A at 350 mbsf.

At this site, the general trends in physical properties show consistent relationships with lithology over the uppermost 220 mbsf. In particular, beds of coarser grain size correspond to higher gamma ray attenuation (GRA) density, magnetic susceptibility, and a* (i.e., more reddish color) (Figs. **F23, F24**). From 220 to 295 mbsf, the relationship between measured parameters and lithology is inconsistent. Varying correlations between physical properties and lithology occur below 295 mbsf.

Physical properties Unit I shows a positive correlation between GRA density, magnetic susceptibility, NGR, and a*. An exception is the uppermost 20 mbsf, where a negative correlation between GRA density and NGR with respect to magnetic susceptibility and a* is apparent (Figs. **F23, F24**). This interval is also marked by a rapid decline in porosity and moisture content caused by consolidation in the upper ~20 m (Fig. **F25**).

Physical properties Unit II is characterized by cyclic high-amplitude changes in magnetic susceptibility, GRA density, a*, and L* (Figs. **F23, F24**). The general trends of this cyclicity show consistent positive correlation between GRA density, magnetic susceptibility, NGR, and a* downhole to ~220 mbsf. At small scale, excursions are more complex; GRA density correlates negatively with magnetic susceptibility and a* does not correlate with any other physical property. Below 220 mbsf, the correlation between sandy layers and GRA density is no longer clear and, in general, the relationship between lithology and physical properties is inconsistent. The hiatus noted at 230 mbsf (see **"Biostratigraphy"**) appears to correlate with this change in the physical property characteristics within physical properties Unit II.

Physical properties Unit III corresponds to lithologic Subunit IB (see **"Lithostratigraphy"**) and is generally marked by a decrease in magnetic susceptibility and NGR and by a change in the frequency and amplitude of the cycles observed in most of the physical properties (Figs. **F23, F24**). Downhole logging also indicates a more distinct variability in the standard (total) gamma ray (HSGR) data in this interval (see **"Downhole measurements"**), interpreted as an increase in the abundance of thick sandy layers. The discontinuity previously defined by Llave et al. (2001, 2007, 2011) and Hernández-Molina et al. (2006) as the mid-Pleistocene revolution discontinuity is estimated at 295 mbsf and correlates with the physical properties Units II/III boundary. Therefore, a good correlation seems to exist between climatic changes and cyclical changes in the lithology reflected by physical properties, but further detailed work is required for confirmation.

Whole-Round Multisensor Logger and Special Task Multisensor Logger measurements

The STMSL was not used in Hole U1390A because no immediate acquisition of data for stratigraphic correlation was necessary, but its use was resumed in Holes U1390B and U1390C. Temperature equilibration before starting with the WRMSL was at least 3 h.

Gamma ray attenuation bulk density

GRA density at Site U1390 shows highly variable values between 1.6 and 2.1 g/cm^3, with a general increase downhole (Fig. **F23**). In the upper 220 mbsf, the natural variations in grain size and sediment texture are clearly reflected in the GRA density record, in which increases in grain size commonly correspond to increases in GRA density. This matches the observation that sandy beds are generally poorly sorted (see **"Lithostratigraphy"**), leaving less open pore space than well-sorted sand and therefore increasing bulk density. Below 220 mbsf, the relation between density and grain size deteriorates. Long-term variations in GRA density show three different trends:

1. High values and medium-amplitude cycles in physical properties Unit I,
2. High-amplitude cyclicity in physical properties Unit II, and
3. Highly scattered values of GRA density with high-frequency variations in physical properties Unit III.

Magnetic susceptibility

Magnetic susceptibility data in Hole U1390A show a cyclic pattern, especially from 70 to 295 mbsf within physical properties Unit II, and declining oscillations between 5×10^{-5} and 40×10^{-5} SI in the lower part of the hole (Fig. F23). As discussed above, a remarkable coherence of susceptibility and GRA density can be observed for the coarse-grained layers, mainly in physical properties Units I and II, suggesting a relatively high content of magnetite or other magnetic minerals in the fine fraction of the sand layers. In Unit III, the magnetic susceptibility does not appear to vary with sand content.

P-wave velocity

The WRMSL was used to gather sonic velocities for all holes at Site U1390, and an attempt was made to determine *P*-wave velocities on split cores in each section of Hole U1390A (Fig. F23). Because of poor sediment to liner coupling, reasonable results from the WRMSL could only be obtained for the upper ~30 m of cores retrieved with the APC. The *P*-wave velocity profile can be extended downhole to 35 mbsf by using the *P*-wave determinations on split cores in Hole U1390A. Although the sediment surface appeared to be smooth and should have provided adequate coupling to the transducers, no clear acoustic signal could be obtained greater depth. The formation of small cracks in the relatively stiff and brittle sediment might have negatively affected signal propagation through the sediment.

P-wave velocities follow GRA densities in the upper 30 mbsf, with values close to 1600 m/s in the uppermost 20 mbsf and then decreasing to 1450 m/s (Fig. F23). Because 1450 m/s is lower than the sonic speed in water, such low values are most likely an underestimation of the true speed, caused by cracks and voids in the sediment. The same problem occurs when measuring split cores. The pressure needed to provide a good contact for the transducers on the upper and lower sides of the sediment specimen leads in some cases to small cracks that increase the traveltime of the acoustic signal through the sediment. Sonic velocities measured for the same intervals by the continuous WRMSL are lower than those obtained individually by selective measurements on split cores. These latter velocities seem to be more reliable from 20 to 30 mbsf (Fig. F23).

Natural gamma radiation

NGR scanning was performed in all holes at Site U1390. NGR counts fluctuate mostly between 20 and 45 cps, exhibiting cyclic patterns for the cores retrieved with the APC and XCB (Fig. F24). These patterns are also consistent with the logging data (see "Downhole measurements"). At 70 mbsf, a peak of 50 cps is observed, and a notable positive correlation of NGR with GRA density, magnetic susceptibility, and a* is present between 70 and 220 mbsf, where the cyclicity is more evident and oscillates between 30 and 45 cps (Fig. F24). Below 295 mbsf, the correlation with the other studied parameters is less consistent as the amplitude of the variations increases. The relation of the sandy layers and NGR data is complex, with high NGR counts in physical properties Unit I and potentially also in Unit II (upper part) and low NGR values in Unit III. A possible explanation could be that the sands within physical properties Unit III appear to have lower clay content than those above (see "Lithostratigraphy").

Moisture and density

Determination of MAD on discrete sediment samples was performed on every section in Hole U1390A (Figs. F23, F25). Generally, GRA density and MAD measurements give consistent results when taken on APC and XCB cores.

Grain densities in the uppermost 20 mbsf of Hole U1390A oscillate between 2.75 and 2.8 g/cm^3 and between 2.8 and 2.65 g/cm^3 downhole.

Moisture and porosity show parallel variations downhole. Porosity decreases rapidly from 70% to 50% in the uppermost 20 mbsf and then to values around 40% at 295 mbsf, overprinted by wide oscillations. Below 295 mbsf, no further porosity decrease is observed (Fig. F25). Moisture content decreases from 40% to 30% in the uppermost 20 mbsf and from 30% to 20% with broad oscillations over the next 270 m, with no further systematic downhole change.

Thermal conductivity

Thermal conductivity was measured once per core in all cores in Hole U1390A using the full-space probe, usually in Section 3, near the middle of the section (see "Downhole measurements"). Because cores retrieved with the XCB are severely disturbed and affected by biscuiting, thermal conductivity measurements were only taken on APC Cores 339-U1390A-

1H through 11H. Thermal conductivity varies between 1.0 and 2.1 W/(m·K), which is in the range of thermal conductivity values observed at the other sites. No clear trend is apparent. A relation to moisture content and porosity is also not evident, although pore water content should have an effect on thermal conductivity.

Summary of main results

The physical property data allow us to define three main units at Site U1390, with boundaries at 70 and 295 mbsf. In general, a coherent relation exists between high magnetic susceptibility, NGR, and GRA density correlating with coarser intervals downhole to ~220 mbsf. These intervals are mainly composed of contourites, which are believed to be exclusively responsible for the formation of these coarse-grained layers. This would explain the more uniform relation between lithology and physical properties noted in this section. The boundary between physical properties Units II and III corresponds to a hiatus determined by biostratigraphy, with a duration between 0.60 and 0.47 m.y. Color reflectance indicates that sandy layers are mostly more reddish in color, whereas muddy intervals tend to be more greenish.

Geochemistry

Volatile hydrocarbons

Headspace gas analysis was performed as a part of the standard protocol required for shipboard safety and pollution prevention monitoring. In total, 37 headspace samples from Hole U1390A (sampling resolution of one per core) were analyzed (Fig. **F26;** Table **T16**), spanning the entire depth range of the site. In Hole U1390A, methane (C_1), ethane (C_2), ethene ($C_{2=}$), propane (C_3), and propene ($C_{3=}$) were detected. Methane ranged from 2.9 ppmv near the seafloor to a maximum of 63,991 ppmv at 49.2 mbsf (Section 339-U1390A-6H-6). At the base of Hole U1390A, methane is 9,830.5 ppmv. Both ethane and ethene were detected starting at 31.60 mbsf, but concentrations remain low. Ethane reached a maximum value of 46.3 ppmv, and ethene reaches a maximum of 2.5 ppmv. Propene and propane concentrations at Site U1390 are also low; their concentrations are below 1 ppmv except for the last sample measured (Section 339-U1390A-38X-4), in which propane reaches 11.52 ppmv.

Sedimentary geochemistry

Sediment samples were collected for analysis of solid-phase geochemistry (inorganic and organic carbon) at a resolution of approximately one sample per core in Hole U1390A (Table **T4**), thereby spanning the full depth of the site. $CaCO_3$ varies from 21.1 to 34.5 wt% (Fig. **F27**), and no discernible downhole trends appear. Organic carbon is low, generally <1 wt%, and varies between 0.4 and 1.12 wt% (Fig. **F28A**).

Nitrogen (Fig. **F28B**) was measured downhole to 351 mbsf in Hole U1390A. Measured nitrogen ranges from 0.05 to 0.11 wt%. We did not observe any notable trends in nitrogen content with depth. The C/N ratio, used to distinguish the origin of organic matter (marine versus terrestrial) in sediment (Emerson and Hedges, 1988; Meyers, 1997), varies between 6 and 13 and indicates that the organic carbon is mainly of marine origin (Fig. **F28C**). Samples with C/N ratios exceeding 10 indicate some terrestrial input. Total organic carbon and C/N ratios are generally positively correlated, which is in agreement with the relationships observed at Sites U1385–U1388 but is in contrast with the relationship between total organic carbon and C/N at Site U1389.

Interstitial water chemistry

Major cations and anions

Whole-round samples were taken for interstitial water analysis at a resolution of one per core downhole to 346 mbsf in Hole U1390A. Sulfate concentrations drop to zero in the uppermost 20 mbsf (Fig. **F29A;** Table **T17**). Ammonium concentrations steadily increase downhole from 1,200 µM at the seafloor to 15,500 µM at 170 mbsf (Fig. **F29B**). From 170 to 295 mbsf, ammonium concentrations oscillate around 14,000 µM, reaching a minimum of 11,842 µM and maximum of 15,321 µM followed by a small increase at ~300 mbsf to values between 16,000 and 17,000 µM at the base of the hole. Alkalinity varies between 10.9 and 15.4 meq/L in the upper 70 mbsf and decreases to 5.67 meq/L at 107 mbsf (Fig. **F29C**). After a slight increase to 7.97 meq/L at 137 mbsf, alkalinity decreases again downhole to 290 mbsf and averages ~2 meq/L downhole to the base of the hole.

Calcium and magnesium display similar patterns of variation (Fig. **F30A, F30B**). Both decline in the upper 20.6 mbsf in the sulfate reduction zone, from 7.7 to 3 mM and 51.6 to 35.9 mM, respectively. The ratio of magnesium to calcium decreases from ~6.7 to 3.3, which indicates that both dolomite and calcite are precipitating. Calcium and magnesium remain roughly constant from 20 to 58.4 mbsf, after which they increase to17.3 and 85.1 mM, respectively at 194.7 mbsf. Between 194.7 and 290.6 mbsf, calcium continues to increase and reaches a maximum value of 31.6 mM, whereas magnesium oscillates between 83 and 87 mM before decreasing slightly to 81 mM

at 244 mbsf and increasing to 86.1 mM at 290.6 mbsf. Between 290.6 mbsf and the base of the hole, calcium and magnesium drop slightly to 14.2 and 80.5 mM, respectively.

Potassium decreases from 10.7 to 8.9 mM in the sulfate reduction zone between the seafloor and 20.6 mbsf (Fig. F30C). Potassium then remains constant until 39.3 mbsf, after which it increases gradually to 14.2 mM at the base of the hole.

Sodium and chloride concentrations have almost identical trends; however, the magnitude of changes in chloride is greater than that in sodium, which can be identified in the Na/Cl ratio. Sodium remains close to its core-top value of 479 mM downhole until 47.7 mbsf and increases to 1249 mM at 290.6 mbsf (Fig. F31B). After remaining constant for ~20 m, sodium increases to 1309 mM at 328.9 mbsf and decreases to 1169 mM at the base of the hole. The maximum sodium value is 2.7 times greater than its concentration at the top of the hole. Chloride is approximately constant and close to its core-top value of 586 mM in the upper 47.7 mbsf, after which it increases to 1745 mM at 290.6 mbsf (Fig. F31A). From 290.6 to 317.3 mbsf, chloride is roughly constant. The concentration increases to 1788 mM at 328.9 mbsf and decreases to 1604 mM at the base of the hole. The maximum chloride concentration is three times greater than its value in the top of the hole. Na/Cl ratios are all below the modern seawater value of 0.86, except at 81.1 mbsf (Fig. F31C). In the upper ~80 mbsf, Na/Cl varies around 0.8 but shows no significant trend. From 81.1 to 253.7 mbsf, Na/Cl decreases to a minimum value of 0.694. The ratio increases to ~0.73 from 253.7 mbsf to the base of the hole.

Minor elements

Barium concentration in the upper 11 mbsf is ~2 µM and increases to 27.3 µM at 20.6 mbsf (Fig. F32A). From 20.6 to 107 mbsf, barium varies between 13.6 and 24 µM. Between 107 and 118 mbsf, barium concentration increases to 40.9 µM. Barium increases between 118 and 290.6 mbsf to a maximum of 1131.2 µM. The concentration then decreases to 470.4 µM at the base of the hole, except for an excursion at 329 mbsf to 894.6 µM.

Boron increases from 493.6 to 558.8 µM in the sulfate reduction zone (upper 20.6 mbsf; Fig. F32B). The concentration is constant between 20.6 and 39.3 mbsf, after which it decreases to 346 µM at 118 mbsf. The concentration oscillates slightly until 156 mbsf and then decreases to 256.5 µM at 214 mbsf. After a slight positive excursion to 325.7 µM at 223.4 mbsf, boron concentration continues to decrease to the base of the hole, reaching a minimum of 242.3 µM.

Iron increases from 27.4 to 53.9 µM between 2.85 and 11.1 mbsf (Fig. F32C). The concentration of iron then decreases to ~2.3 µM at 67.8 mbsf and remains low until an increase to 60.2 µM at 162.8 mbsf. Iron concentration oscillates over a large range between 162.8 mbsf and the base of the hole, with the most significant jump being between 3.64 and 122.3 µM at 223.4 mbsf. At the base of the hole, the concentration of iron is ~32 µM.

Lithium decreases from 25.7 to 16 µM in the upper 20.6 mbsf (Fig. F33A). It then remains approximately constant until 107.1 mbsf, after which it increases to 69.3 µM at 253.7 mbsf. Between 253.7 and 280.9 mbsf, lithium increases more rapidly with depth to 156.9 µM. The lithium concentration decreases very slightly from 280.9 mbsf to a value of 134.3 µM at 328.9 mbsf. Lithium then increases to a value of 170 µM at the base of the hole.

Silicon concentration is highly variable and has no significant trend in the upper 156 mbsf, varying between a minimum of 270 µM and a maximum of 413.4 µM (Fig. F33B). The concentration increases to 805.1 µM at 162.8 mbsf. Silicon then decreases to 307.5 µM at 213.8 mbsf and increases to 544.9 µM at 223.4 mbsf. From 223.4 to 271.7 mbsf, silicon decreases to 292.5 µM. The concentration increases to 414.3 µM at 309.8 mbsf. After decreasing again to ~295 µM, silicon concentration increases to 561.8 at the base of the hole.

Strontium is variable in the top part of the hole, with values ranging between 57.5 and 97.9 µM (Fig. F33C). At 107.1 mbsf, strontium starts increasing monotonically and reaches a maximum of 2793 µM at 262.3 mbsf. The concentration of strontium decreases from 271.7 mbsf to 1925 µM at the base of the hole.

Stable isotopes

Oxygen and hydrogen isotopes are ~0.9‰ and 5.8‰, respectively, at the seafloor, reflecting MOW (Fig. F34A, F34B; Table T18). Oxygen isotopes are variable, with generally lower values between 100 and 200 mbsf and higher values above and below this interval. Maximum $\delta^{18}O$ values of ~1.4‰ are found at the base of the hole.

Hydrogen isotope values average ~7‰ in the upper 107 mbsf. Below this level, δD decreases markedly, reaching minimum values of –6.5‰ at 300 mbsf and increasing slightly toward the base of the hole. The very high concentrations of chloride and sodium are not associated with increases in $\delta^{18}O$ and δD. In fact, δD and chloride are highly negatively correlated (Fig. F35), with the lowest δD values recorded in the interval of highest chloride concentrations (Fig. F34B,

F34C). The low δD signature is characteristic of clay mineral dehydration reactions (Kastner et al., 1991; Dählmann and de Lange, 2003). As clay dehydration requires higher temperatures than those inferred from the downhole temperature trend (see "Downhole measurements"), we speculate that the isotopic and elemental composition of interstitial water at Site U1390 are a product of the upward movement of interstitial water from the deep subsurface, which has been affected by clay dehydration reactions and dissolved salt layers at greater depth.

Summary

At Site U1390, organic sediment analysis shows that organic carbon is generally low. $CaCO_3$ content varies between 21 and 34 wt%. C/N ratios indicate that the source of organic carbon to this site is primarily of marine origin. We did not observe notable trends with depth in any of the organic or inorganic carbon indexes.

In Hole U1390A, the most distinctive feature of the interstitial water concentration profiles is the relatively high values as compared to those measured at other sites during Expedition 339. The maximum interstitial water concentrations of ammonium and strontium are an order of magnitude greater than those at any other previous site (U1385–U1388), and the maximum barium concentration is two orders of magnitude higher than concentrations at other sites in the Gulf of Cádiz and an order of magnitude higher than concentrations measured at Site U1385. The maximum values of chloride and sodium concentrations at Site U1390 are approximately double those at Site U1389. Maximum strontium concentrations are higher by an order of magnitude than values measured at other sites. Calcium and magnesium concentrations are elevated as well with respect to maximum values at other sites, although only by ~1.5–2 times.

All the alkali earth elements (Ca, Mg, Sr, and Ba) have very similar downhole patterns, suggesting that the same process controls their concentrations.

The downhole increases of sodium and chloride are quite notable. Chloride is 3 times the bottom water value and sodium is 2.75 times the bottom water value. Although the sodium and chloride concentrations reach high values, the Na/Cl ratios decrease to significantly less than the modern seawater value of 0.86. It is possible that part of the trend in Na/Cl ratios is false, as the reliability of the sodium measurements at high concentration has not been verified. However, the high chloride and sodium concentrations are associated with low δD values, and no evidence exists for evaporite deposits in the sediment (see "Lithostratigraphy"). This indicates that high salinity may not be the result of in situ salt dissolution. Instead, we suggest that salts were dissolved at depth by interstitial water that was altered by clay mineral dehydration reactions, which can also the affect water sodium concentration.

Downhole measurements

Logging operations

After the last core from Hole U1390A arrived on deck, the hole was prepared for logging. The wiper trip found no fill. A go-devil was pumped to lock open the lockable float valve, and the hole was flushed with 20 bbl of sepiolite mud. The hole was then displaced with 124 bbl of barite-weighted heavy mud (10.5 ppg), and the pipe was set at 96.6 mbsf. Two tool strings were deployed in Hole U1390A, the triple combo and FMS-sonic (Fig. F36; see also "Downhole measurements" and Table T6 in the "Methods" chapter [Expedition 339 Scientists, 2013b] for tool acronym definitions).

The triple combo tool string started downhole at 0000 h on 5 January 2012. The Hostile Environment Natural Gamma Ray Sonde (HNGS), High-Resolution Laterolog Array (HRLA), and Hostile Environment Litho-Density Sonde (HLDS) were included; the Accelerator Porosity Sonde (APS) was omitted because it allowed the HNGS to be placed at the bottom of the tool string to record the sand-rich beds at the base of the hole. The tool string reached the base of the hole at 350 mbsf, and a 70 m repeat pass was taken before the main pass up to seafloor. FMS-sonic tool string rig-up started at 0430 h. Sonic logs were taken on the descent, and two upward passes were made from the bottom of the hole (350 mbsf).

Maximum ship heave during logging was higher than at previous sites, ~1.5 m maximum peak-to-peak for the triple combo run and 1.7 m for the FMS-sonic run. The tide was falling during the triple combo run (+0.5 to –0.1 m) and rising during the FMS-sonic run (–0.5 to +0.1 m) (Fig. F37). The wireline heave compensator was used to counter ship heave during logging.

Log data quality

In Hole U1390A, the quality of the log data is good because of the generally narrow and smooth borehole. In the upper 270 mbsf, the borehole diameter generally ranges from 9.5 to 12 inches and varies smoothly except for some thin washouts, which generally do not exceed 14 inches (Fig. F38). Below 270 mbsf, the borehole quality decreases but is still reasonable, with more washouts and an increase in

borehole diameter to >12 inches, exceeding 16 inches in very few places.

Resistivity, sonic velocity, and NGR logs are robust to the moderate changes in hole diameter. As for previous sites, the NGR log (HSGR) correlates well with the NGR values measured on cores (Fig. F39). The density log values match the MAD bulk density values (Fig. F38), and the downhole patterns correlate well with the GRA bulk density values, except for small offsets in depth and value (GRA underestimates density slightly). The photoelectric effect log has anomalously high values (>10 b/e$^-$) because of barium in the logging mud. FMS resistivity images are of good quality because of good contact with the borehole wall in most of the borehole.

Logging units

The logged intervals at Site U1390 were assigned to one logging unit (Fig. F38) because no major baselevel changes in log data are apparent. In this unit, density and sonic velocity have a steadily increasing downhole trend reflecting downhole compaction. Resistivity has a curious curve, declining to low values downhole rather than showing a normal downhole compaction trend (see below). The unit is divided into two subunits mostly on the basis of an increasing proportion of low NGR values below 293 mbsf (Figs. F38, F40).

Logging Subunit 1A: base of drill pipe to 293 mbsf

Logging Subunit 1A is characterized by medium-amplitude alternations in bulk density, NGR (and its uranium, thorium, and potassium components), density, and sonic velocity values (Fig. F38). Several orders of cycles are observed in the NGR curves, varying from one to several tens of meters in thickness (Fig. F40). Potassium and thorium concentrations co-vary closely, suggesting that clay content controls these logs. The uranium concentrations correlate to potassium and thorium at some depths or vary independently at others. As expected from downhole compaction, the density and sonic velocity logs have an increasing downhole trend and are generally well correlated with each other. These logs also correlate well with the resistivity curve at a medium scale (several tens of meters). At the borehole scale, the resistivity curves show an opposite trend, decreasing downhole, that we relate to the increase in interstitial water salinity (see "Geochemistry"), because the amount of ions in the interstitial water solution lowers the apparent formation resistivity. Below ~160 mbsf, the resistivity curves display clearer medium-scale alternations than in the upper part of logging Subunit IA (Fig. F38).

Logging Subunit 1A at Site U1390 resembles logging Subunit 1A observed at Site U1389 (see "Downhole measurements" in the "Site U1389" chapter [Expedition 339 Scientists, 2013g]). Both of the subunits are Pleistocene in age, although their lower boundaries are diachronous (see "Biostratigraphy" in the "Site U1389" chapter [Expedition 339 Scientists, 2013g]).

Logging Subunit 1B: 293–350 mbsf

Logging Subunit 1B is distinguished from the subunit above by its higher amplitude variability and by the presence of lower NGR values (Figs. F38, F40). The potassium and thorium logs contain drops to below 0.6% and 4 ppm, respectively. This suggests that Subunit 1B contains some several-meter thick sandy intervals, which is in agreement with the observations on cores (e.g., see "Lithostratigraphy" and thick sandy packages in Cores 339-U1390A-33X, 34X, 36X, and 37X). In Subunit 1B, uranium is closely correlated to the potassium and thorium curves. The NGR and *P*-wave velocity curves are anticorrelated in the upper part of this subunit, downhole to ~315 mbsf.

The upper part of logging Subunit 1B is in accord with the upper part of lithologic Subunit IB, recognized in Hole U1390A at 293.78 mbsf and characterized by thicker sand-rich beds than the lithologic unit above (see "Lithostratigraphy"). This boundary is also seen in petrophysical properties (upper boundary of physical properties Unit III) as a decrease in magnetic susceptibility and NGR and also by a change in the frequency and amplitude of the observed cycles (see "Physical properties"). The transition between logging Subunits 1A and 1B also corresponds to a minor hiatus recognized between 292.08 and 292.43 mbsf based on micropaleontological analysis, and covering an interval between 0.9 and 1.2 Ma (see "Biostratigraphy").

Formation MicroScanner images

Because of the good borehole conditions in Hole U1390A, the quality of the FMS resistivity data allows the resistivity of the borehole formation to be interpreted at several scales. At the scale of the borehole, a downhole trend of increasing conductivity is observed, which correlates well with the resistivity logs. The interval above ~160 mbsf is characterized by relatively high resistivity (light-colored upper interval in the FMS image in Fig. F41), becoming less resistive downhole to ~220 mbsf and reaching mini-

mum values between 220 and 320 mbsf (dark color in the FMS image). We relate this general downhole increase in conductivity to the progressive downhole increase in pore water salinity (see "Geochemistry"). At a finer scale, the FMS images reveal numerous resistive and conductive intervals, whose thickness ranges from several tens of centimeters to a few meters. Both gradual and sharp transitions between alternations are observed. In some places, most of these alternations correlate well with other logs. As an example, the conductive interval extending from 220 to 228 mbsf on the FMS images correlates with lower values in NGR, bulk density, *P*-wave velocity, and resistivity logs (Fig. F41) and corresponds to coarse-grained intervals (sands and silts). These intervals contrast with muddy intervals appearing as less conductive on the FMS images and correlating with higher values in the NGR, bulk density, *P*-wave, and resistivity logs (see for example the 10 m thick, light-colored interval extending from 228 to 238 mbsf in Fig. F41). The above relation between lithologies and FMS image resistivity is, however, not observed throughout the borehole, especially in Subunit 1B (e.g., see the clay interval located at ~300 mbsf [NGR peak] correlating with a conductive interval on the FMS image in Fig. F41). FMS resistivity images also reveal stratigraphic information at a finer spatial resolution than the standard logs. In Figure F42 (240–253 mbsf), a series of resistive (light colored) layers, with thicknesses ranging from 0.2 to 1 m, correlates with lower values in the NGR log and higher values in the high-resolution bulk density log. We correlate some of these resistive layers with silty sand layers in cores. Some other layers may be related to more subtle changes in clay content or in sediment hardness that have not been visually recognized in cores. Inclined bedding (appearing as sinusoids) at slight angles is observed at some depths. It will be possible to map their occurrence and measure dip directions and angle.

Sonic velocity and two-way traveltime

Sonic velocity logs in Hole U1390A help to establish depth in two-way traveltime (TWT) conversions and link the borehole logs to the seismic section, in the absence of a vertical seismic profile at this site. Sonic velocity repeats well from Pass 1 to Pass 2, and data from the uppermost 20 mbsf are provided by core *P*-wave logger results (Fig. F43). Sonic traveltimes were calculated from sonic log velocities and give TWTs for the base of the hole (350 mbsf) of ~395 ms below seafloor and ~1705 ms below sea level, assuming a velocity of 1.58 km/s just below the seafloor (Fig. F43). The seafloor reflection peak is at 1310 ms in the seismic section, and precision depth recorder measurements put the seafloor at 1314 ms.

Heat flow

Nine APCT-3 downhole temperature measurements in Holes U1390A–U1390C ranged from 13.6°C at 18.6 mbsf to 16.5°C at 108.9 mbsf (Table T19), giving a geothermal gradient of 32.0°C/km (Fig. F44). The measurements increase linearly with depth, and the trend line intersects the seafloor at 13.03°C. Some scatter and minor differences between the three holes is evident. These differences are probably caused by (1) uncertainty in fitting to the APCT-3 temperature equilibration curves to obtain the formation temperature and (2) lateral heterogeneity in heat flow leading to small temperature differences between the holes. Readings at shallower depths have more uncertainty because the APC barrel has more freedom of movement in the hole where the sediment is soft. Similar to previous sites, the bottom water temperature was difficult to determine accurately from the APCT-3 temperature profiles (Fig. F45). The intersection of the linear temperature trend with the seafloor probably gives the best estimate here.

Thermal conductivity under in situ conditions was estimated from laboratory-determined thermal conductivity using the method of Hyndman et al. (1974) (see "Physical properties" in the "Methods" chapter [Expedition 339 Scientists, 2013b]). The calculated in situ values average 1.5% higher than the measured laboratory values. Thermal resistance was then calculated by integrating the inverse of the in situ thermal conductivity over depth (Fig. F44). A heat flow of 42.5 mW/m^2 was obtained from the linear fit between temperature and thermal resistance (Pribnow et al., 2000). This value is mid-range for the Gulf of Cádiz area (Grevemeyer et al., 2009).

Stratigraphic correlation

The meters composite depth (mcd) scale for Site U1390 was based on correlation of magnetic susceptibility and NGR data between Holes U1390A–U1390C. The correlation is relatively straightforward downhole to 195 mcd (~175 mbsf, which is the base of Cores 339-U1390B-19H and 339-U1390C-19H), with only a few exceptions where the gaps between cores from all three holes nearly align (Fig. F46). These gaps occur at approximately 92, 102, and 142 mcd. In all three cases, it is likely that little (a few

tens of centimeters) or no material is missing. Even if no gap exists, the overlap of underlying cores with those above is too short and/or the susceptibility and NGR anomalies too indistinct to establish a firm correlation. Similarly, the quality of the correlations from 195 mcd to the base of the multicored interval at ~210 mcd is relatively poor, mainly because of lower core recovery and higher coring disturbance within this interval.

Overall, the three holes cored at Site U1390 provide enough material to produce a composite stratigraphic section that is complete with little or no gaps from seafloor downhole to the base of Core 339-U1390A-22X at 214.87 mcd (198.4 mbsf) (Table T20). The section below this depth is cored only in Hole U1390A to a total depth of 350 mbsf, with short gaps inevitably occurring between cores and larger gaps occurring where core recovery is low.

Although the exact amount of material missing cannot be determined precisely for the gaps between cores in single-cored intervals, estimates can be made in two ways. First, prior construction of mcd scales have shown repeatedly that expansion between mcd and mbsf scales is ~7%–15%. Hence, a similar expansion should be expected. In fact, we observed that a moderately accurate mcd scale could be constructed by merely expanding the mbsf depth scale by ~10%. Ultimately, detailed correlation is necessary, but where correlative features do not exist, using a ~10% expansion factor serves as a useful guide and provides rough estimates for the amount of material that might have been missed in the coring gaps. Second, Site U1390 susceptibility, density, and NGR records can be correlated to other nearby Expedition 339 sites, particularly in the upper 150 mbsf. Furthermore, logging NGR data (HSGR) in Holes U1390A and U1390C correlate well with NGR data from the cores (Fig. F39).

Offsets and composite depths are listed in Table T21. A growth factor of 1.099 is calculated by linear regression for the multicored intervals in all three holes, indicating a 9.9% expansion of mcd values relative to mbsf values (Fig. F47). Because of the very linear nature of the expansion, the mcd scale can readily be compressed by dividing by 1.099 to produce a modified depth scale (mbsf*) that corresponds more closely to true coring depths while retaining the between-hole correlations. For the single-cored interval, we retained roughly the same growth factor by adding 1 m to the total offset at the top of each core from Core 339-U1390A-23X downhole.

Spliced records are provided for magnetic susceptibility (Table T22) and NGR (Table T23) data, which were first cleaned by removing data affected by section- and core-edge artifacts or that occurred in disturbed intervals or gaps, as listed in Table T12. Additional anomalous magnetic susceptibility data were excluded from the splice, as listed in Table T24.

References

Alves, T.M., Gawthorpe, R.L., Hunt, D.W., and Monteiro, J.H., 2003. Cenozoic tectono-sedimentary evolution of the western Iberian margin. *Mar. Geol.*, 195(1–4):75–108. **doi:10.1016/S0025-3227(02)00683-7**

Blum, P., 1997. Physical properties handbook: a guide to the shipboard measurement of physical properties of deep-sea cores. *ODP Tech. Note,* 26. **doi:10.2973/odp.tn.26.1997**

Borges, J.F., Fitas, A.J.S., Bezzeghoud, M., and Teves-Costa, P., 2001. Seismotectonics of Portugal and its adjacent Atlantic area. *Tectonophysics*, 331(4):373–387. **doi:10.1016/S0040-1951(00)00291-2**

Buforn, E., Bezzeghoud, M., Udías, A., and Pro, C., 2004. Seismic sources on the Iberia-African plate boundary and their tectonic implications. *Pure Appl. Geophys.* 161(3):623–646. **doi:10.1007/s00024-003-2466-1**

Caralp, M.H., 1989. Abundance of *Bulimina exilis* and *Melonis barleeanum:* relationship to the quality of marine organic matter. *Geo-Mar. Lett.,* 9(1):37–43. **doi:10.1007/BF02262816**

Dählmann, A., and de Lange, G.J., 2003. Fluid–sediment interactions at eastern Mediterranean mud volcanoes: a stable isotope study from ODP Leg 160. *Earth Planet. Sci. Lett.,* 212(3–4):377–391. **doi:10.1016/S0012-821X(03)00227-9**

Duarte, J.C., Terrinha, P., Rosas, F.M., Valadares, V., Pinheiro, L.M., Matias, L., Magalhães, V., and Roque, C., 2010. Crescent-shaped morphotectonic features in the Gulf of Cádiz (offshore SW Iberia). *Mar. Geol.,* 271(3–4):236–249. **doi:10.1016/j.margeo.2010.02.017**

Egbert, G.D., and Erofeeva, S.Y., 2002. Efficient inverse modeling of barotropic ocean tides. *J. Atmos. Oceanic Technol.,* 19(2):183–204. **doi:10.1175/1520-0426(2002)019<0183:EIMOBO>2.0.CO;2**

Emerson, S., and Hedges, J.I., 1988. Processes controlling the organic carbon content of open ocean sediments. *Paleoceanography,* 3(5):621–634. **doi:10.1029/PA003i005p00621**

Expedition 339 Scientists, 2013a. Expedition 339 summary. *In* Stow, D.A.V., Hernández-Molina, F.J., Alvarez Zarikian, C.A., and the Expedition 339 Scientists, *Proc. IODP,* 339: Tokyo (Integrated Ocean Drilling Program Management International, Inc.). **doi:10.2204/iodp.proc.339.101.2013**

Expedition 339 Scientists, 2013b. Methods. *In* Stow, D.A.V., Hernández-Molina, F.J., Alvarez Zarikian, C.A., and the Expedition 339 Scientists, *Proc. IODP,* 339: Tokyo (Integrated Ocean Drilling Program Management International, Inc.). **doi:10.2204/iodp.proc.339.102.2013**

Expedition 339 Scientists, 2013c. Site U1385. *In* Stow, D.A.V., Hernández-Molina, F.J., Alvarez Zarikian, C.A.,

and the Expedition 339 Scientists, *Proc. IODP,* 339: Tokyo (Integrated Ocean Drilling Program Management International, Inc.). **doi:10.2204/iodp.proc.339.103.2013**

Expedition 339 Scientists, 2013d. Site U1386. *In* Stow, D.A.V., Hernández-Molina, F.J., Alvarez Zarikian, C.A., and the Expedition 339 Scientists, *Proc. IODP,* 339: Tokyo (Integrated Ocean Drilling Program Management International, Inc.). **doi:10.2204/iodp.proc.339.104.2013**

Expedition 339 Scientists, 2013e. Site U1387. *In* Stow, D.A.V., Hernández-Molina, F.J., Alvarez Zarikian, C.A., and the Expedition 339 Scientists, *Proc. IODP,* 339: Tokyo (Integrated Ocean Drilling Program Management International, Inc.). **doi:10.2204/iodp.proc.339.105.2013**

Expedition 339 Scientists, 2013f. Site U1388. *In* Stow, D.A.V., Hernández-Molina, F.J., Alvarez Zarikian, C.A., and the Expedition 339 Scientists, *Proc. IODP,* 339: Tokyo (Integrated Ocean Drilling Program Management International, Inc.). **doi:10.2204/iodp.proc.339.106.2013**

Expedition 339 Scientists, 2013g. Site U1389. *In* Stow, D.A.V., Hernández-Molina, F.J., Alvarez Zarikian, C.A., and the Expedition 339 Scientists, *Proc. IODP,* 339: Tokyo (Integrated Ocean Drilling Program Management International, Inc.). **doi:10.2204/iodp.proc.339.107.2013**

Fernández-Puga, M.C., Vázquez, J.T., Somoza, L., Díaz del Rio, V., Medialdea, T., Mata, M.P., and León, R., 2007. Gas-related morphologies and diapirism in the Gulf of Cádiz. *Geo-Mar. Lett.*, 27(2–4):213–221. **doi:10.1007/s00367-007-0076-0**

Fletcher, W.J., Boski, T., and Moura, D., 2007. Palynological evidence for environmental and climatic change in the lower Guadiana Valley, Portugal, during the last 13,000 years. *Holocene,* 17(4):481–494. **doi:10.1177/0959683607077027**

Flores, J.-A., Colmenero-Hidalgo, E., Mejía-Molina, A.E., Baumann, K.-H., Hendericks, J., Larsson, K., Prabhu, C.N., Sierro, F.J., and Rodrigues, T., 2010. Distribution of large *Emiliania huxleyi* in the central and northeast Atlantic as a tracer of surface ocean dynamics during the last 25,000 years. *Mar. Micropaleontol.,* 76(3–4):53–66. **doi:10.1016/j.marmicro.2010.05.001**

García, M., Hernández-Molina, F.J., Llave, E., Stow, D.A.V., León, R., Fernández-Puga, M.C., Díaz del Río, V., and Somoza, L., 2009. Contourite erosive features caused by the Mediterranean Outflow Water in the Gulf of Cádiz: Quaternary tectonic and oceanographic implications. *Mar. Geol.*, 257(1–4):24–40 **doi:10.1016/j.margeo.2008.10.009**

Gràcia, E., Dañobeitia, J., Vergés, J., Bartolomé, R., and Córdoba, D., 2003. Crustal architecture and tectonic evolution of the Gulf of Cádiz (SW Iberian margin) at the convergence of the Eurasian and African plates. *Tectonics,* 22(4):1033. **doi:10.1029/2001TC901045**

Grevemeyer, I., Kaul, N., and Kopf, A., 2009. Heat flow anomalies in the Gulf of Cadiz and off Cape San Vincente, Portugal. *Mar. Pet. Geol.,* 26(6):795–804. **doi:10.1016/j.marpetgeo.2008.08.006**

Hanquiez, V., Mulder, T., Lecroart, P., Gonthier, E., Marchès, E., and Voisset, M., 2007. High-resolution seafloor images in the Gulf of Cádiz, Iberian margin. *Mar. Geol.,* 246(1):42–59. **doi:10.1016/j.margeo.2007.08.002**

Hayward, B.W., 2002. Late Pliocene to middle Pleistocene extinctions of deep-sea benthic foraminifera ("*Stilostomella* extinction") in the southwest Pacific. *J. Foraminiferal Res.,* 32(3):274–307. **doi:10.2113/32.3.274**

Hernández-Molina, F.J., Llave, E., Somoza, L., Fernández-Puga, M.C., Maestro, A., León, R., Medialdea, T., Barnolas, A., García, M., Díaz del Río, V., Fernández-Salas, L.M., Vázquez, J.T., Lobo, F., Alveirinho Dias, J.M., Rodero, J., and Gardner, J., 2003. Looking for clues to paleoceanographic imprints: a diagnosis of the Gulf of Cádiz contourite depositional systems. *Geology,* 31(1):19–22. **doi:10.1130/0091-7613(2003)031<0019:LFCTPI>2.0.CO;2**

Hernández-Molina, F.J., Llave, E., Stow, D.A.V., García, M., Somoza, L., Vázquez, J.T., Lobo, F.J., Maestro, A., Díaz del Río, V., León, R., Medialdea, T., and Gardner, J., 2006. The contourite depositional system of the Gulf of Cádiz: a sedimentary model related to the bottom current activity of the Mediterranean Outflow Water and its interaction with the continental margin. *Deep-Sea Res., Part II,* 53(11–13):1420–1463. **doi:10.1016/j.dsr2.2006.04.016**

Hyndman, R.D., Erickson, A.J., and Von Herzen, R.P., 1974. Geothermal measurements on DSDP Leg 26. *In* Davies, T.A., Luyendyk, B.P., et al., *Init. Repts. DSDP,* 26: Washington, DC (U.S. Govt. Printing Office), 451–463. **doi:10.2973/dsdp.proc.26.113.1974**

Kastner, M., Elderfield, H., and Martin, J.B., 1991. Fluids in convergent margins: what do we know about their composition, origin, role in diagenesis and importance for oceanic chemical fluxes? *Philos. Trans. R. Soc. London, Ser. A,* 335(1638):243–259. **doi:10.1098/rsta.1991.0045**

Kawagata, S., Hayward, B.W., Grenfell, H.R., and Sabaa, A., 2005. Mid-Pleistocene extinction of deep-sea foraminifera in the North Atlantic Gateway (ODP Sites 980 and 982). *Palaeogeogr., Palaeoclimatol., Palaeoecol.,* 221(3–4):267–291. **doi:10.1016/j.palaeo.2005.03.001**

Kenyon, N.H., and Belderson, R.H., 1973. Bed forms of the Mediterranean undercurrent observed with side-scan sonar. *Sediment. Geol.,* 9(2):77–99. **doi:10.1016/0037-0738(73)90027-4**

Leckie, R.M., and Olson, H.C., 2003. Foraminifera as proxies of sea-level change on siliciclastic margins. *In* Olson, H.C., and Leckie, R.M. (Eds.), *Micropaleontologic Proxies of Sea-Level Change and Stratigraphic Discontinuities*. Spec. Publ.—SEPM (Soc. Sediment. Geol.), 75:5–19.

Llave, E., Hernández-Molina, F.J., Somoza, L., Díaz del Río, V., Stow, D.A.V., Maestro, A., and Alveirinho Dias, J.M., 2001. Seismic stacking pattern of the Faro-Albufeira contourite system (Gulf of Cádiz): a Quaternary record of paleoceanographic and tectonic influences. *Mar. Geophys. Res.*, 22(5–6):487–508. **doi:10.1023/A:1016355801344**

Llave, E., Hernández-Molina, F.J., Somoza, L., Stow, D.A.V., and Díaz Del Río, V., 2007a. Quaternary evolution of the contourite depositional system in the Gulf of Cádiz. *Geol. Soc. Spec. Publ.,* 276:49–79. **doi:10.1144/GSL.SP.2007.276.01.03**

Llave, E., Hernández-Molina, F.J., Stow, D.A.V., Fernández-Puga, M.C., García, M., Vázquez, J.T., Maestro, A., Somoza, L., and Díaz del Río, V., 2007b. Reconstructions of the Mediterranean Outflow Water during the Quaternary based on the study of changes in buried mounded drift stacking pattern in the Gulf of Cádiz. *Mar. Geophys. Res.,* 28(4):379–394. **doi:10.1007/s11001-007-9040-7**

Llave, E., Matias, H., Hernández-Molina, F.J., Ercilla, G., Stow, D.A.V., and Medialdea, T., 2011. Pliocene–Quaternary contourites along the northern Gulf of Cadiz margin: sedimentary stacking pattern and regional distribution. *Geo-Mar. Lett.,* 31(5–6):377–390. **doi:10.1007/s00367-011-0241-3**

Lopes, F.C., Cunha, P.P., and Le Gall, B., 2006. Cenozoic seismic stratigraphy and tectonic evolution of the Algarve margin (offshore Portugal, southwestern Iberian Peninsula). *Mar. Geol.*, 231(1–4):1–36. **doi:10.1016/j.margeo.2006.05.007**

Lourens, L., Hilgen, F., Shackleton, N.J., Laskar, J., and Wilson, D., 2004. The Neogene period. *In* Gradstein, F.M., Ogg, J.G., and Smith, A. (Eds.), *A Geologic Time Scale 2004:* Cambridge (Cambridge Univ. Press), 409–440.

Madelain, F., 1970. Influence de la topographie du fond sur l`écoulement méditerranéen entre le Détroit de Gibraltar et le Cap Saint-Vincent. *Cah. Océanogr.,* 22:43–61.

Maestro, A., Somoza, L., Medialdea, T., Talbot, C.J., Lowrie, A., Vázquez, J.T., and Díaz del Río, V., 2003. Large-scale slope failure involving Triassic and middle Miocene salt and shale in the Gulf of Cádiz (Atlantic Iberian margin). *Terra Nova*, 15(6):380–391. **doi:10.1046/j.1365-3121.2003.00513.x**

Maiorano, P., and Marino, M., 2004. Calcareous nannofossil bioevents and environmental control on temporal and spatial patterns at the early–middle Pleistocene. *Mar. Micropaleontol.*, 53(3–4):405–422. **doi:10.1016/j.marmicro.2004.08.003**

Maldonado, A., Somoza, L., and Pallarés, L., 1999. The Betic orogen and the Iberian–African boundary in the Gulf of Cádiz: geological evolution (central North Atlantic). *Mar. Geol.*, 155(1–2):9–43. **doi:10.1016/S0025-3227(98)00139-X**

Medialdea, T., Somoza, L., Pinheiro, L.M., Fernández-Puga, M.C., Vázquez, J.T., León, R., Ivanov, M.K., Magalhaes, V., Díaz del Río, V., and Vegas, R., 2009. Tectonics and mud volcano development in the Gulf of Cádiz. *Mar. Geol.*, 261(1–4):48–63. **doi:10.1016/j.margeo.2008.10.007**

Medialdea, T., Vegas, R., Somoza, L., Vázquez, J.T., Maldonado, A., Díaz-del-Río, V., Maestro, A., Córdoba, D., and Fernández-Puga, M.C., 2004. Structure and evolution of the "Olistostrome" complex of the Gibraltar Arc in the Gulf of Cádiz (eastern Central Atlantic): evidence from two long seismic cross-sections. *Mar. Geol.,* 209(1–4):173–198. **doi:10.1016/j.margeo.2004.05.029**

Melières, F., 1974. Recherches sur la dynamique sédimentaire du golfe de Cádiz (Espagne) [Thèse Doctorat d'Etat]. Univ. Paris.

Meyers, P.A., 1997. Organic geochemical proxies of paleoceanographic, paleolimnologic, and paleoclimatic processes. *Org. Geochem.,* 27(5–6):213–250. **doi:10.1016/S0146-6380(97)00049-1**

Murray, J.W., 2006. *Ecology and Applications of Benthic Foraminifera*: Cambridge (Cambridge Univ. Press).

Nelson, C.H., Baraza, J., Maldonado, A., Rodero, J., Escutia, C., and Barber, J.H., Jr., 1999. Influence of the Atlantic inflow and Mediterranean outflow currents on late Quaternary sedimentary facies of Gulf of Cádiz continental margin. *Mar. Geol.*, 155(1–2):99–129. **doi:10.1016/S0025-3227(98)00143-1**

Pinheiro, L.M., Ivanov, M.K., Sautkin, A., Akhmanov, G., Magalhães, V.H., Volkonskaya, A., Monteiro, J.H., Somoza, L., Gardner, J., Hamouni, N., and Cunha, M.R., 2003. Mud volcanism in the Gulf of Cádiz: results from the TTR-10 cruise. *Mar. Geol.,* 195(1–4):131–151. **doi:10.1016/S0025-3227(02)00685-0**

Pribnow, D., Kinoshita, M., and Stein, C., 2000. *Thermal Data Collection and Heat Flow Recalculations for Ocean Drilling Program Legs 101–180:* Hanover, Germany (Inst. Joint Geosci. Res., Inst. Geowiss. Gemeinschaftsauf. [GGA]). **http://www-odp.tamu.edu/publications/heatflow/ODPReprt.pdf**

Raffi, I., Backman, J., Fornaciari, E., Pälike, H., Rio, D., Lourens, L., and Hilgen, F., 2006. A review of calcareous nannofossil astrobiochronology encompassing the past 25 million years. *Quat. Sci. Rev.,* 25(23–24):3113–3137. **doi:10.1016/j.quascirev.2006.07.007**

Raffi, I., Backman, J., Rio, D., and Shackleton, N.J., 1993. Plio–Pleistocene nannofossil biostratigraphy and calibration to oxygen isotope stratigraphies from Deep Sea Drilling Project Site 607 and Ocean Drilling Program Site 677. *Paleoceanography,* 8(3):387–408. **doi:10.1029/93PA00755**

Raymo, M.E., Ruddiman, W.F., Backman, J., Clement, B.M., and Martinson, D.G., 1989. Late Pliocene variation in Northern Hemisphere ice sheets and North Atlantic deep water circulation. *Paleoceanography,* 4(4):413–446. **doi:10.1029/PA004i004p00413**

Roque, C., Duarte, H., Terrinha, P., Valadares, V., Noiva, J., Cachão, M., Ferreira, J., Legoinha, P., and Zitellini, N., 2012. Pliocene and Quaternary depositional model of the Algarve margin contourite drifts (Gulf of Cádiz, SW Iberia): seismic architecture, tectonic control, and paleoceanographic insights. *Mar. Geol.,* 303–306:42–62. **doi:10.1016/j.margeo.2011.11.001**

Schönfeld, J., 1997. The impact of the Mediterranean Outflow Water (MOW) on benthic foraminiferal assemblages and surface sediments at the southern Portuguese continental margin. *Mar. Micropaleontol.*, 29(3–4):211–236. **doi:10.1016/S0377-8398(96)00050-3**

Schönfeld, J., 2002. Recent benthic foraminiferal assemblages in deep high-energy environments from the Gulf of Cádiz (Spain). *Mar. Micropaleontol.*, 44(3–4):141–162. **doi:10.1016/S0377-8398(01)00039-1**

Schönfeld, J., and Zahn, R., 2000. Late glacial to Holocene history of the Mediterranean outflow. Evidence from benthic foraminiferal assemblages and stable isotopes at the Portuguese margin. *Palaeogeogr., Palaeoclimatol., Palaeoecol.*, 159(1–2):85–111. **doi:10.1016/S0031-0182(00)00035-3**

Sierro, F.J., Hernandez-Almeida, I., Alonso-Garcia, M., and Flores, J.A., 2009. Data report: Pliocene–Pleistocene planktonic foraminifer bioevents at IODP Site U1313. *In* Channell, J.E.T., Kanamatsu, T., Sato, T., Stein, R., Alvarez Zarikian, C.A., Malone, M.J., and the Expedition 303/306 Scientists, *Proc. IODP,* 303/306: College Station, TX (Integrated Ocean Drilling Program Management International, Inc.). **doi:10.2204/iodp.proc.303306.205.2009**

Somoza, L., Díaz-del-Rio, V., León, R., Ivanov, M., Fernández-Puga, M.C., Gardner, J.M., Hernández-Molina, F.J., Pinheiro, L.M., Rodero, J., Lobato, A., Maestro, A., Vázquez, J.T., Medialdea, T., and Fernández-Salas, L.M., 2003. Seabed morphology and hydrocarbon seepage in the Gulf of Cádiz mud volcano area: acoustic imagery, multibeam and ultra-high resolution seismic data. *Mar. Geol.*, 195(1–4):153–176. **doi:10.1016/S0025-3227(02)00686-2**

Stow, D., Hernández-Molina, F.J., Hodell, D., and Alvarez Zarikian, C.A., 2011. Mediterranean outflow: environmental significance of the Mediterranean Outflow Water and its global implications. *IODP Sci. Prosp.,* 339. **doi:10.2204/iodp.sp.339.2011**

Stow, D.A.V., and Faugères, J.-C., 2008. Contourite facies and the facies model. *Dev. Sedimentol.,* 60:223–256. **doi:10.1016/S0070-4571(08)10013-9**

Stow, D.A.V., Hernández-Molina, F.J., Llave, E., García, M., Díaz del Río, V., Somoza, L., and Bruno, M., in press. The Cádiz contourite channel: sandy contourites, bedforms and dynamic current interaction. *Mar. Geol.*

Terrinha, P., Matias, L., Valadares, V., Roque, C., Duarte, J., Rosas, F., Iribarren, L., Silva, S., Cunha, T., Batista, L., Duarte, H., Neves, M.C., Carrara, G., Zitellini, N., Grácia, E., Gutscher, M.A., Lourenço, N., and Pinto de Abreu, M., 2006. A margem sul portuguesa profunda. *In* Dias, R., Araújo, A., Terrinha, P., and Kullberg, J.C. (Eds.), *Geologia de Portugal No Contexto da Ibéria,* Sociedade Geológica de Portugal y Universidade de Évora.

Terrinha, P., Matias, L., Vicente, J., Duarte, J., Luís, J., Pinheiro, L., Lourenço, N., Diez, S., Rosas, F., Magalhães, V., Valadares, V., Zitellini, N., Roque, C., Mendes Víctor, L., and MATESPRO Team, 2009. Morphotectonics and strain partitioning at the Iberia-Africa plate boundary from multibeam and seismic reflection data. *Mar. Geol.,* 267(3–4):156–174. **doi:10.1016/j.margeo.2009.09.012**

Terrinha, P., Pinheiro, L.M., Henriet, J.-P., Matias, L., Ivanov, M.K., Monteiro, J.H., Akhmetzhanov, A., Volkonskaya, A., Cunha, T., Shaskin, P., and Rovere, M., 2003. Tsunamigenic-seismogenic structures, neotectonics, sedimentary processes and slope stability on the southwest Portuguese margin. *Mar. Geol.*, 195(1–4):55–73. **doi:10.1016/S0025-3227(02)00682-5**

van Morkhoven, F.P.C.M., Berggren, W.A., and Edwards, A.S., 1986. *Cenozoic Cosmopolitan Deep-Water Benthic Foraminifera*. Bull. Cent. Rech. Explor.—Prod. Elf-Aquitaine, 11.

Viana, A.R., 2001. Seismic expression of shallow- to deep-water contourites along the southeastern Brazilian margin. *Mar. Geophys. Res.,* 22(5–6):509–521. **doi:10.1023/A:1016307918182**

Viana, A.R., Hercos, C.M., De Almeida, W., Jr., Magalhães, J.L., and De Andrade, S.B., 2002. Evidence of bottom current influence on the Neogene to Quaternary sedimentation along the northern Campos Slope, SW Atlantic margin. *In* Stow, D.A.V., Pudsey, C.J., Howe, J.A., Faugères, J.-C., and Viana, A.R. (Eds.), *Deep-Water Contourite Systems: Modern Drifts and Ancient Series, Seismic and Sedimentary Characteristics*. Mem.—Geol. Soc. London, 22(1):249–259. **doi:10.1144/GSL.MEM.2002.022.01.18**

Wei, W., 1993. Calibration of upper Pliocene–lower Pleistocene nannofossil events with oxygen isotope stratigraphy. *Paleoceanography,* 8(1):85–99. **doi:10.1029/92PA02504**

Zenk, W., 1975. On the Mediterranean outflow west of Gibraltar. *"Meteor" Forschungsergeb., Reihe A,* 16:23–34.

Zitellini, N., Gràcia, E., Matias, L., Terrinha, P., Abreu, M.A., DeAlteriis, G., Henriet, J.P., Dañobeitia, J.J., Masson, D.G., Mulder, T., Ramella, R., Somoza, L., and Diez, S., 2009. The quest for the Africa–Eurasia plate boundary west of the Strait of Gibraltar. *Earth Planet. Sci. Lett.*, 280(1–4):13–50. **doi:10.1016/j.epsl.2008.12.005**

Publication: 17 June 2013
MS 339-108

Figure F1. 3-D sketch showing the location of Site U1390 southeast of the Guadalquivir Bank and the Guadalquivir contourite channel and over the sheeted drifts from the northwest part of Sector 3 of the contourite depositional system in the Gulf of Cádiz (made by H. Pereira, Escola Secundária de Loulé, Portugal, using Mirone and iView4D software).

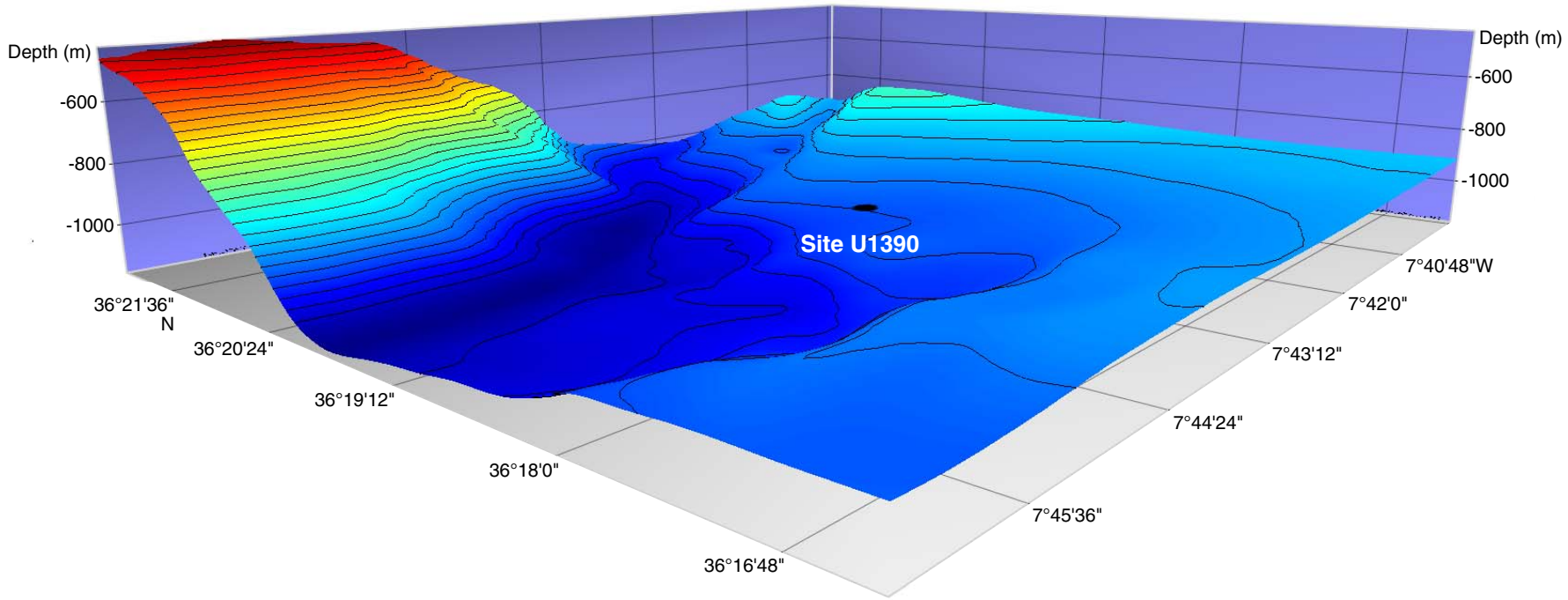

Figure F2. Bathymetric sketch with Site U1390 location over the sheeted drifts in the northwest part of Sector 3 of the contourite depositional system of the Gulf of Cádiz (base map made by Dr. R. León, Geological Survey, IGME, Spain).

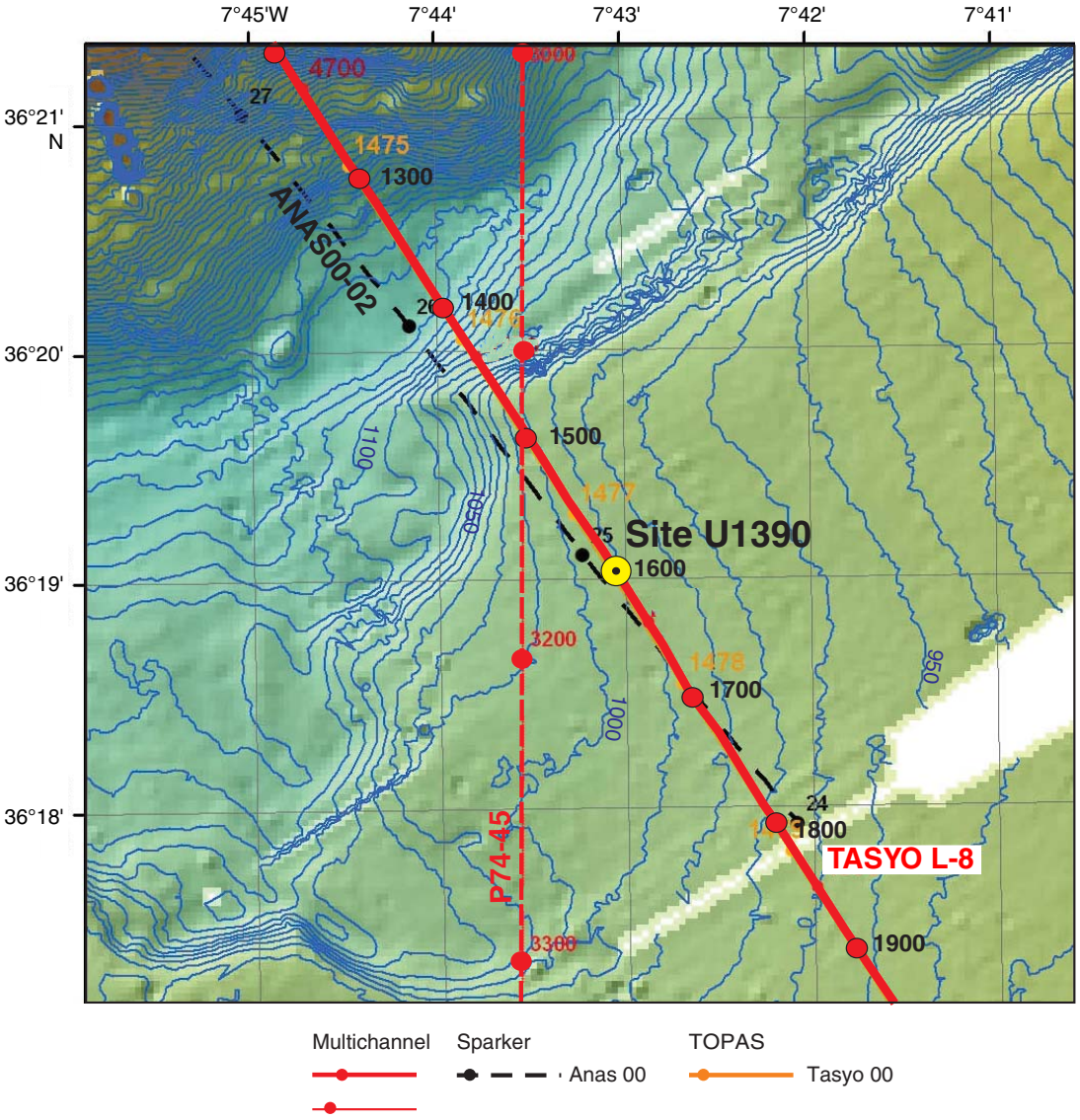

Figure F3. Graphic lithology summary logs, Site U1390.

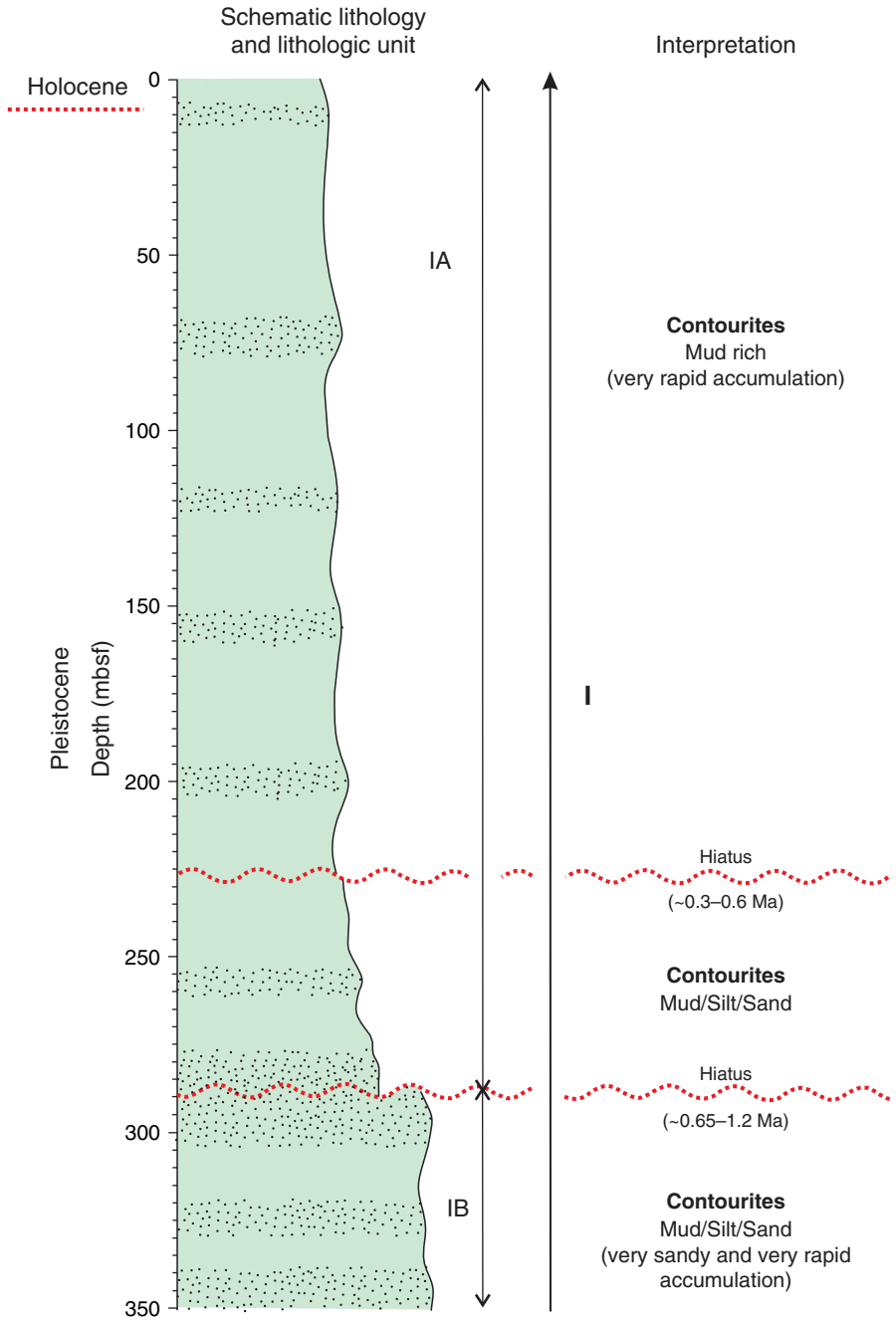

Figure F4. Plots of downhole variations in lithology, Site U1390.

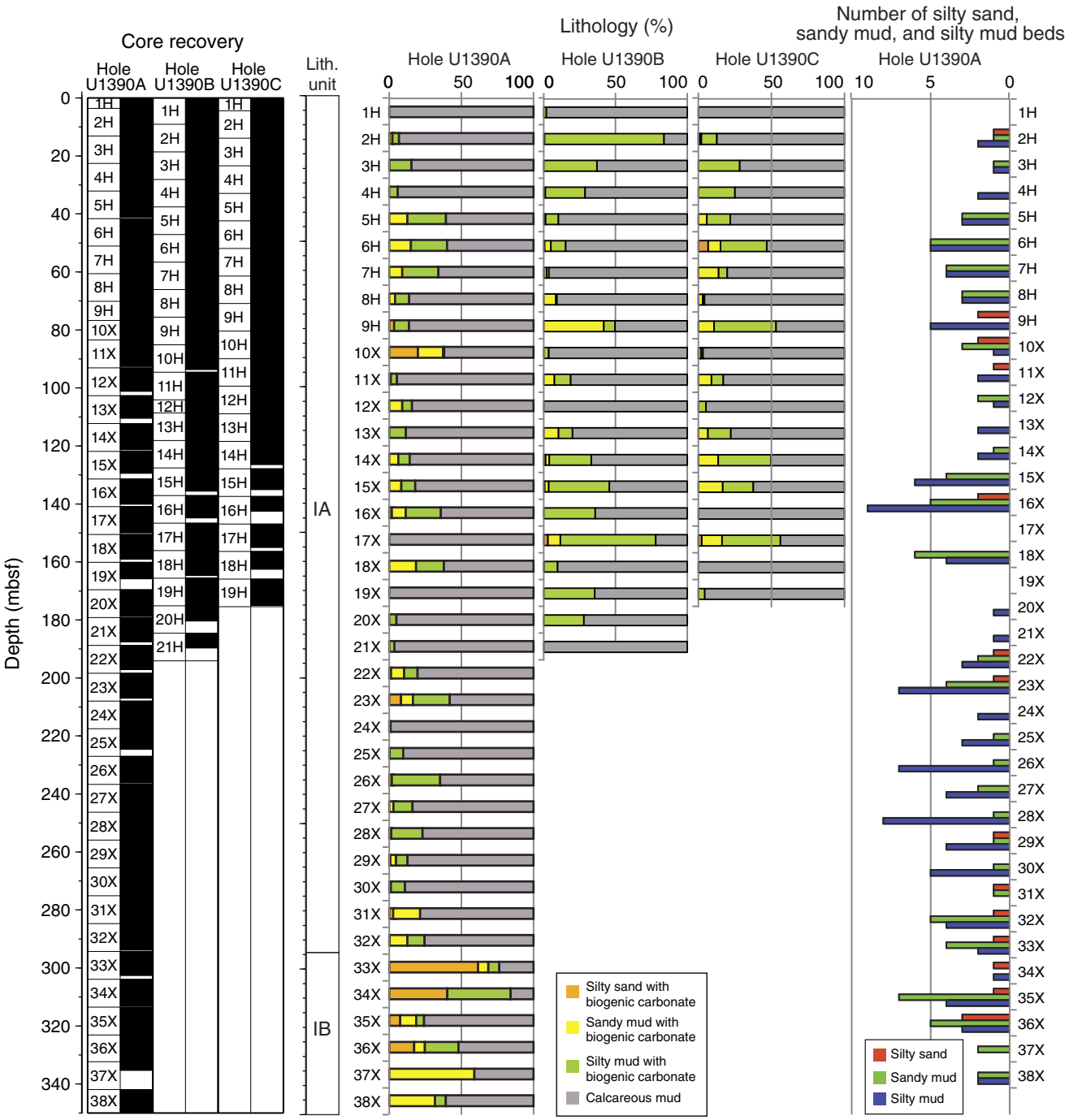

Figure F5. XRD peak intensity profiles, Site U1390.

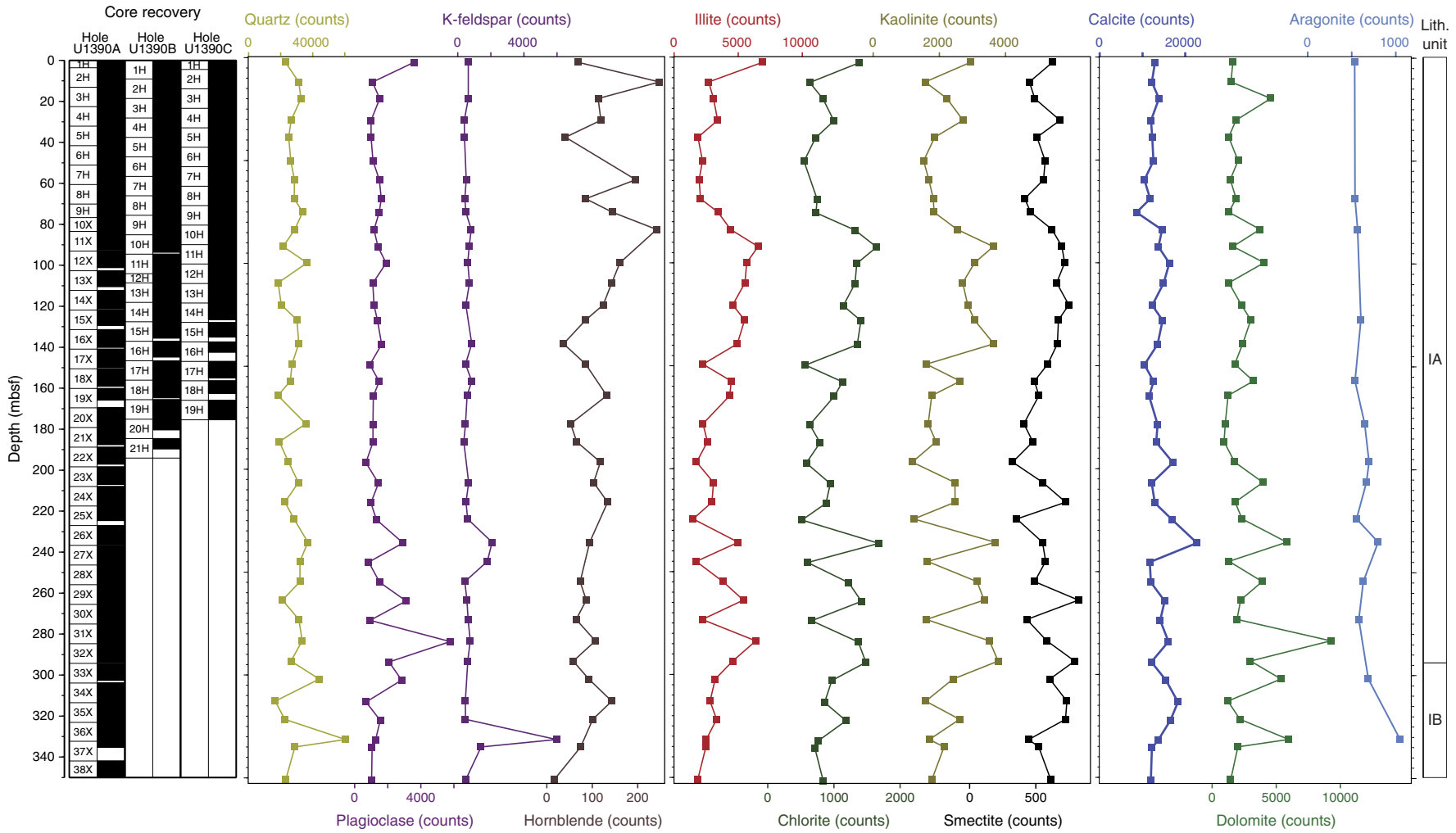

Figure F6. A, B. XRD patterns of bulk (black) and ethylene-glycolated (red) sediment samples, Site U1390. (Continued on next page.)

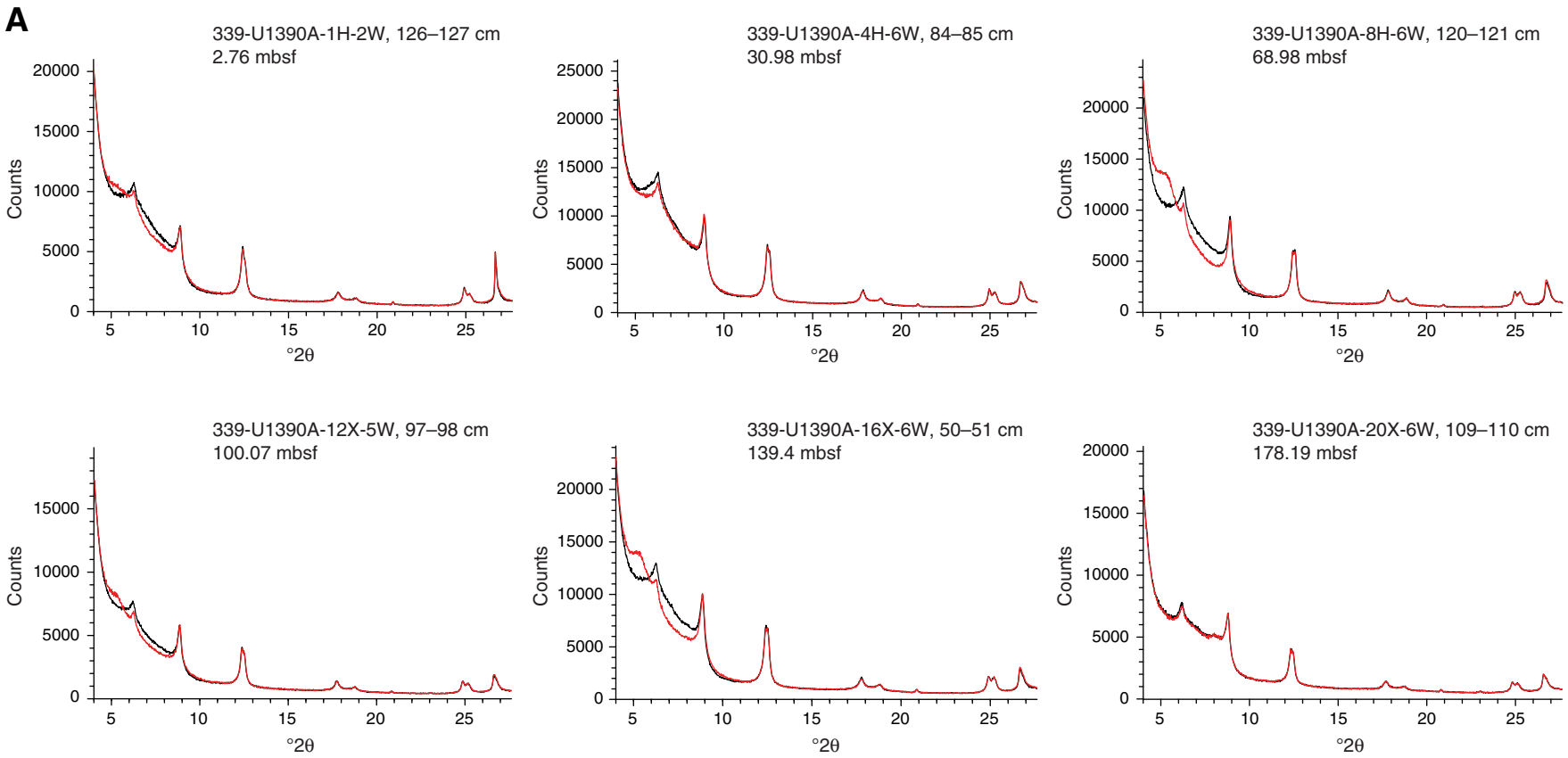

Figure F6 (continued).

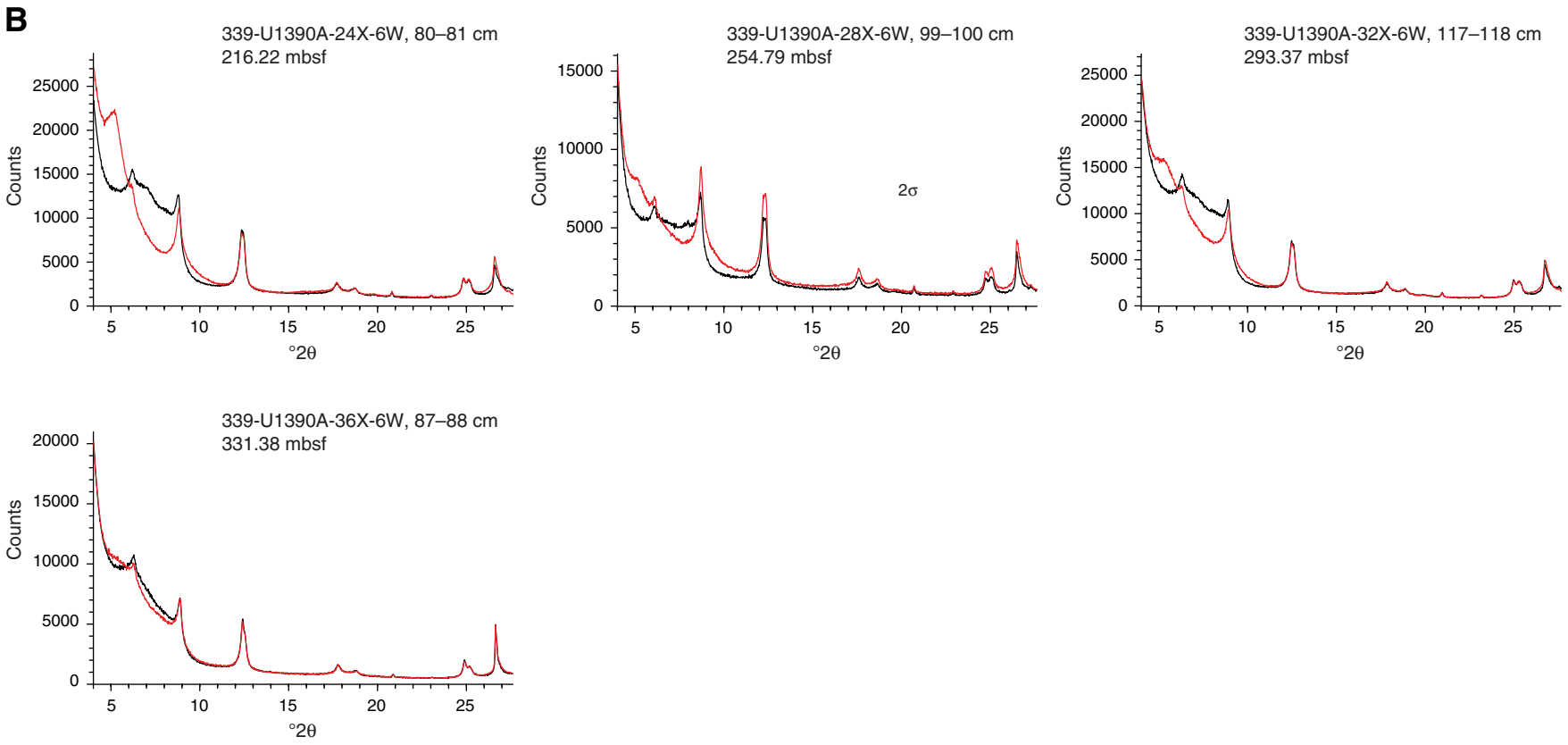

Figure F7. Graphic lithology summaries. **A.** Hole U1390A. (Continued on next two pages.)

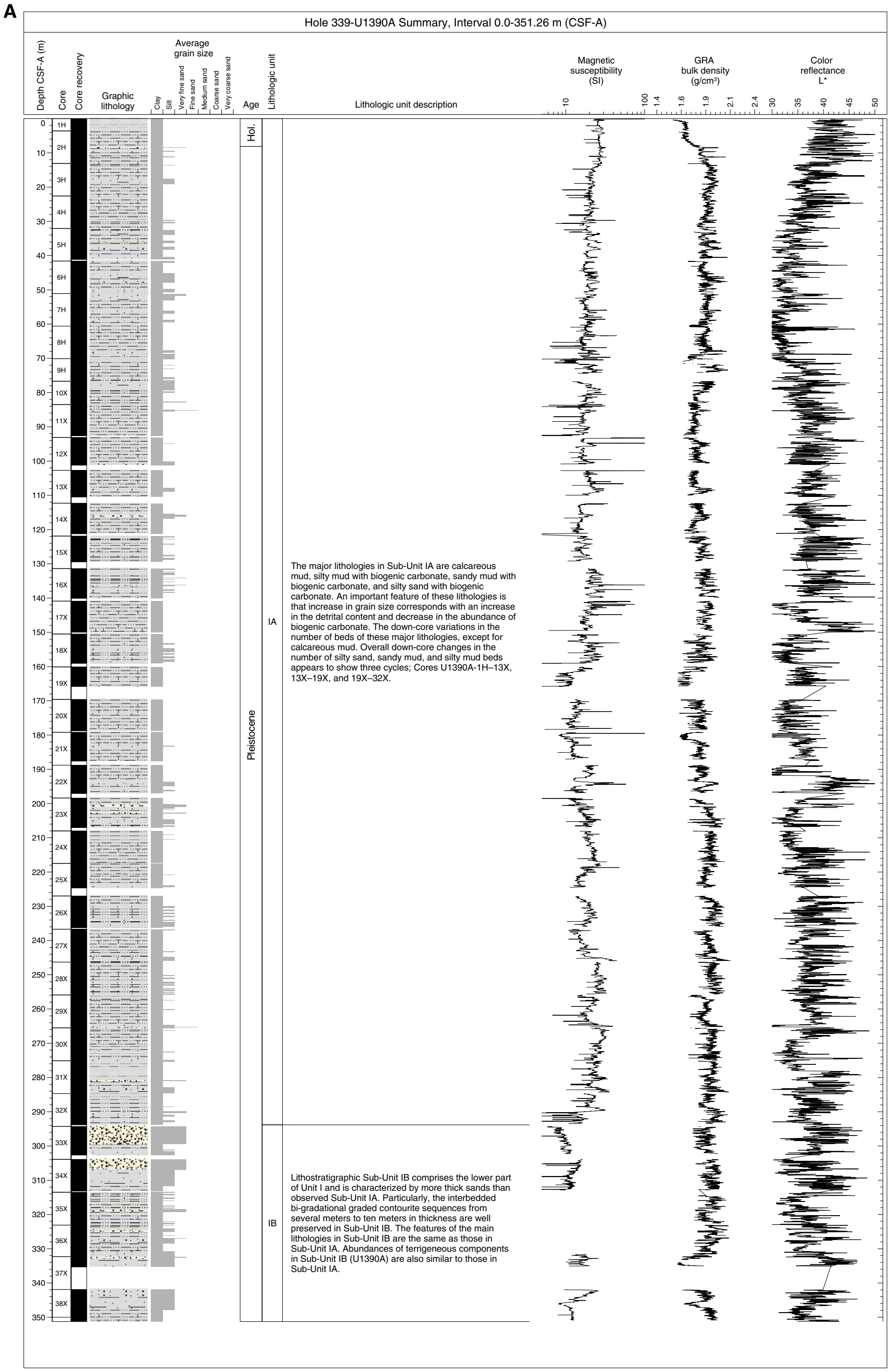

Figure F7 (continued). B. Hole U1390B. (Continued on next page.)

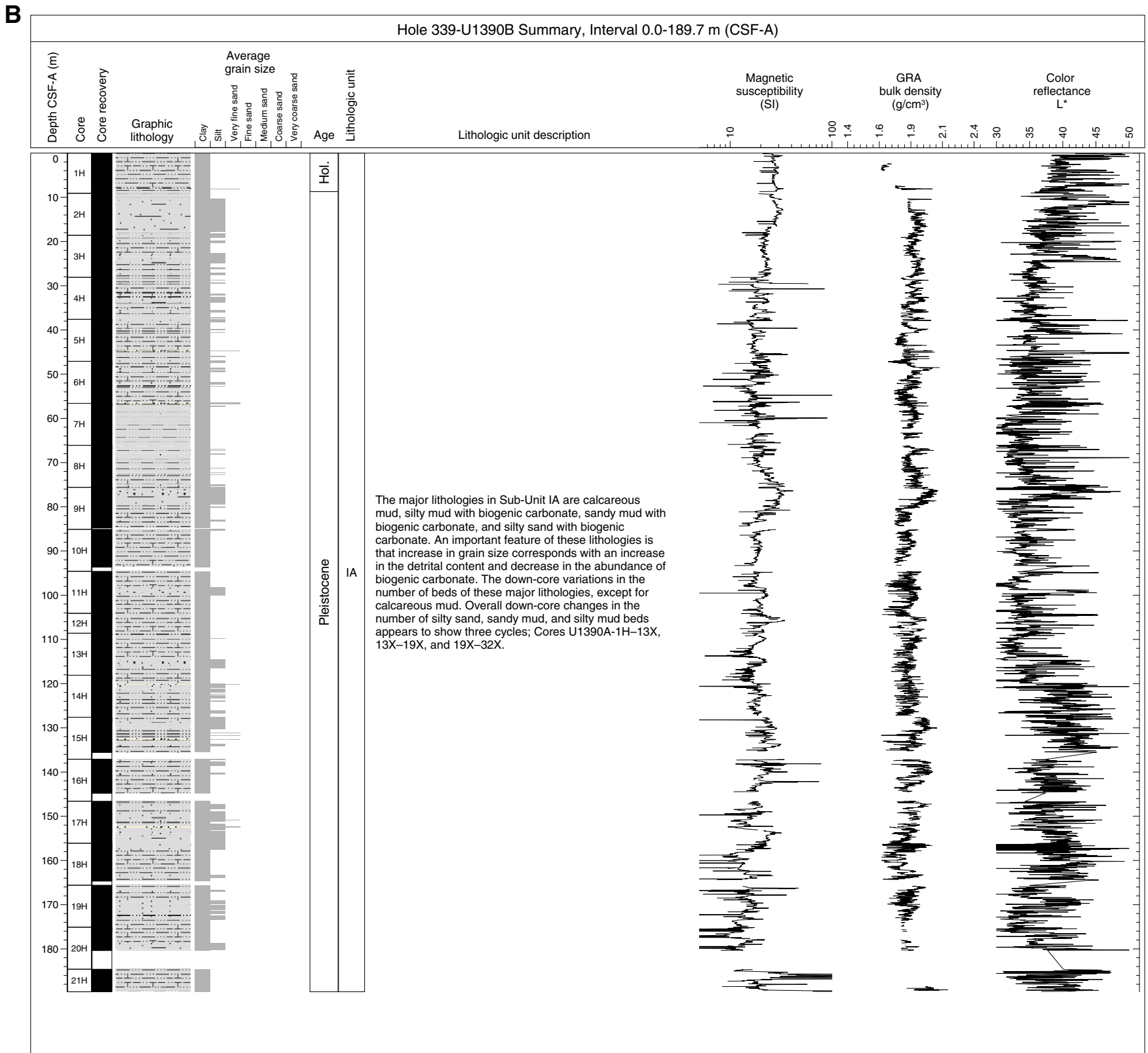

Figure F7 (continued). C. Hole U1390C.

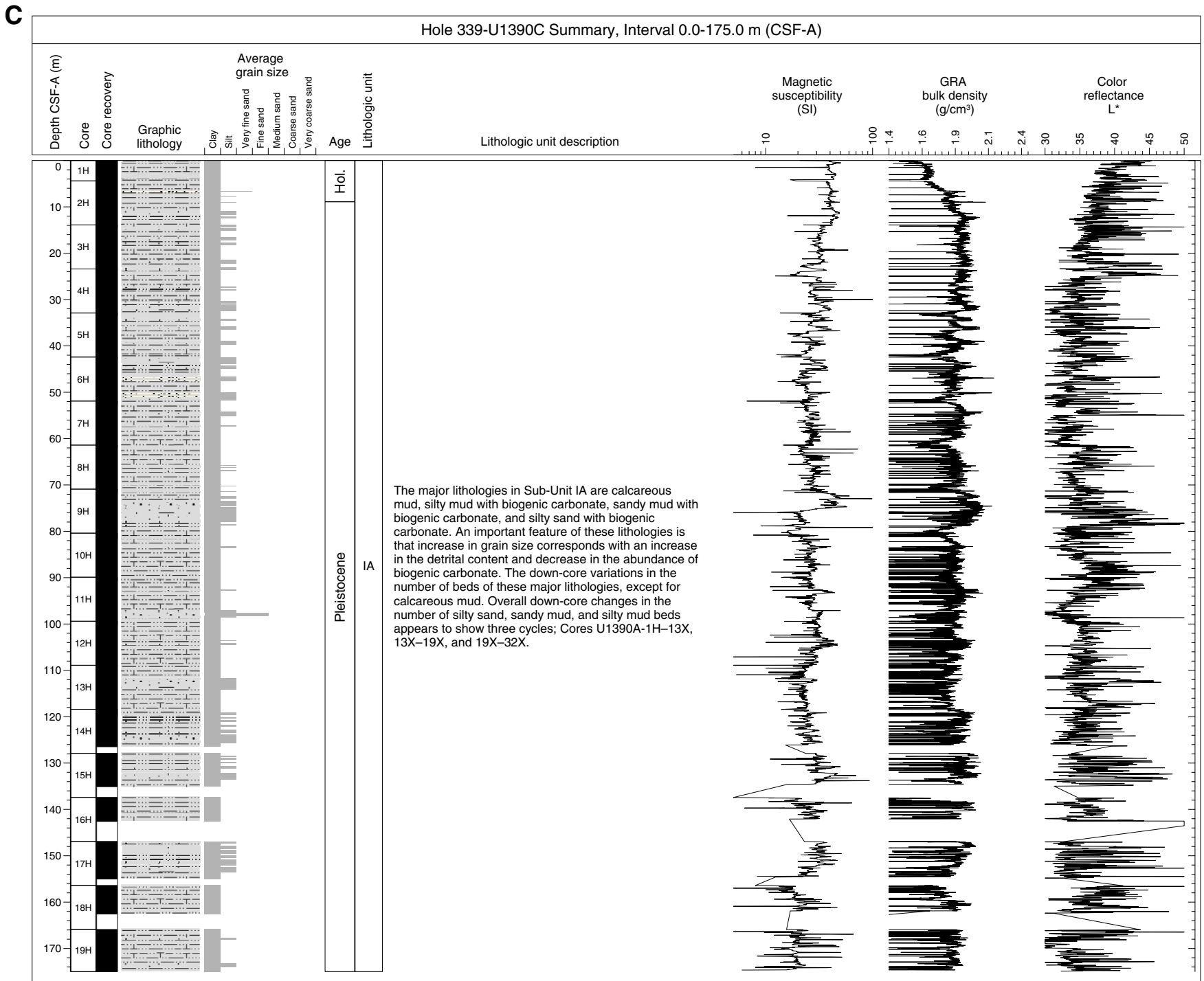

Figure F8. Core images of calcareous mud from Subunit IA (Section 339-U1390A-2H-3A).

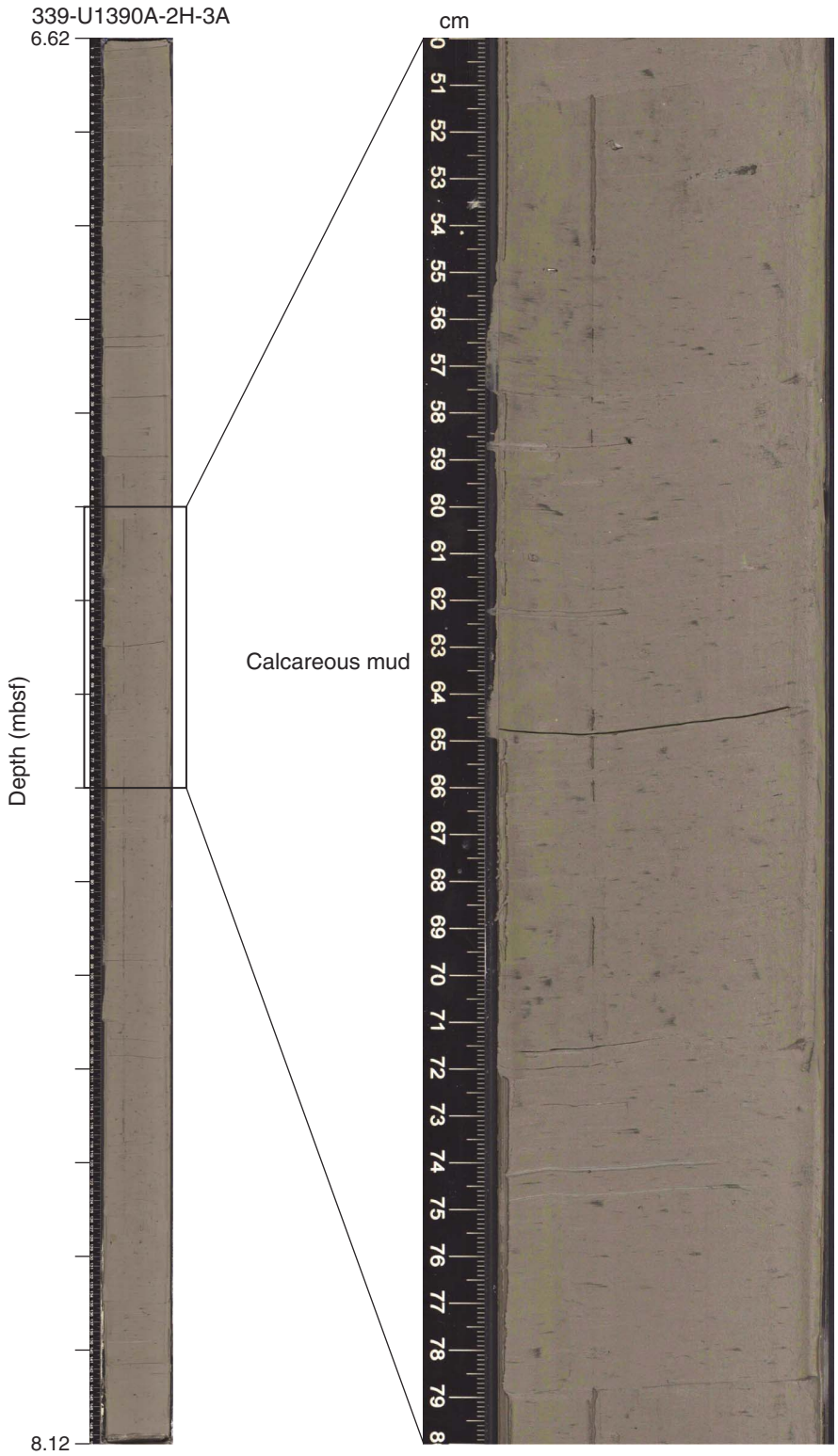

Figure F9. Core images of bi-gradational sequence composed of calcareous mud, silty mud with biogenic carbonate, and sandy mud with biogenic carbonate from Subunit IA (Section 339-U1390A-8H-6A).

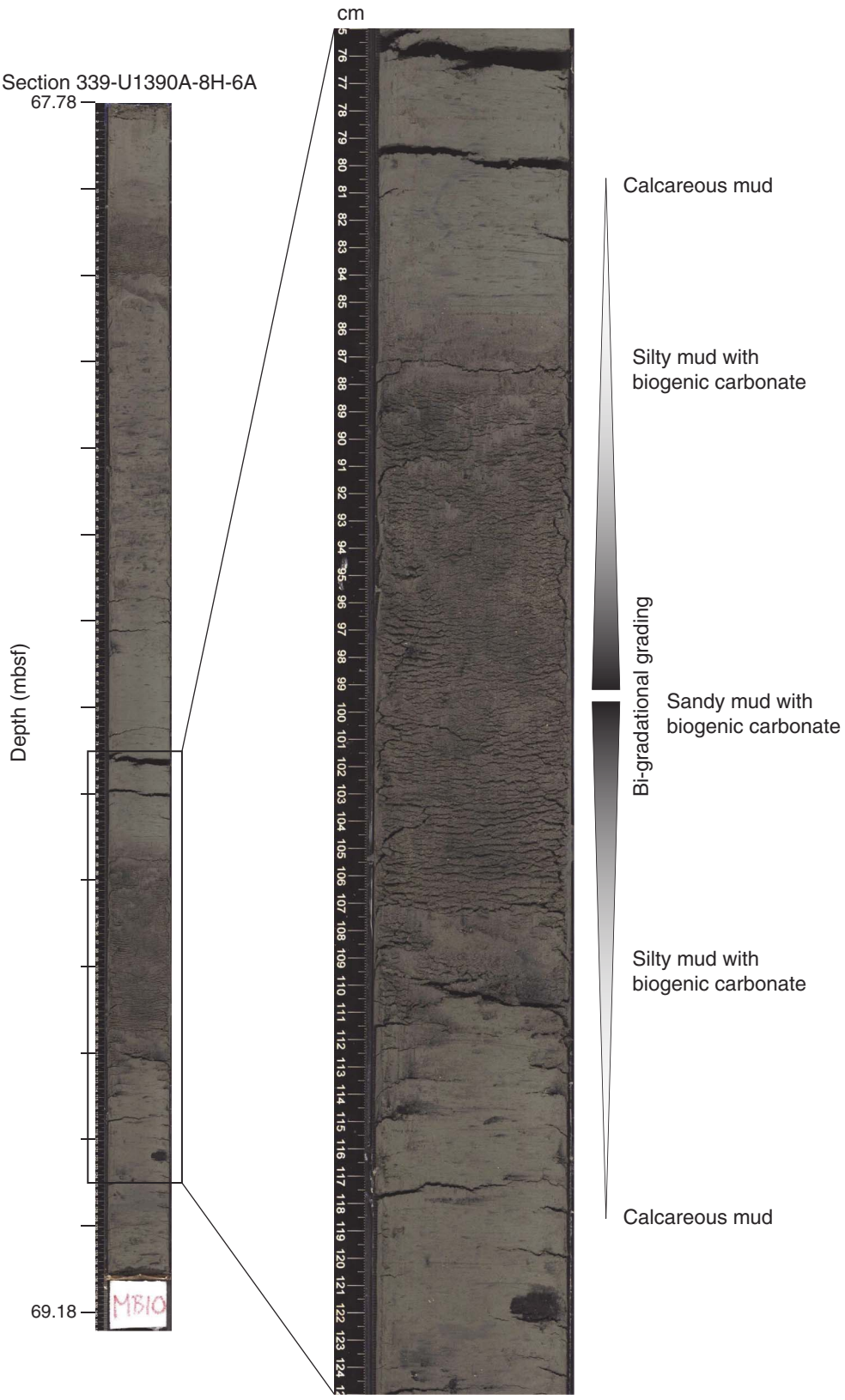

Figure F10. Core image of normal-graded sequence composed of sandy mud with biogenic carbonate and silty mud with biogenic carbonate from Subunit IA (Section 339-U1390A-8H-6A).

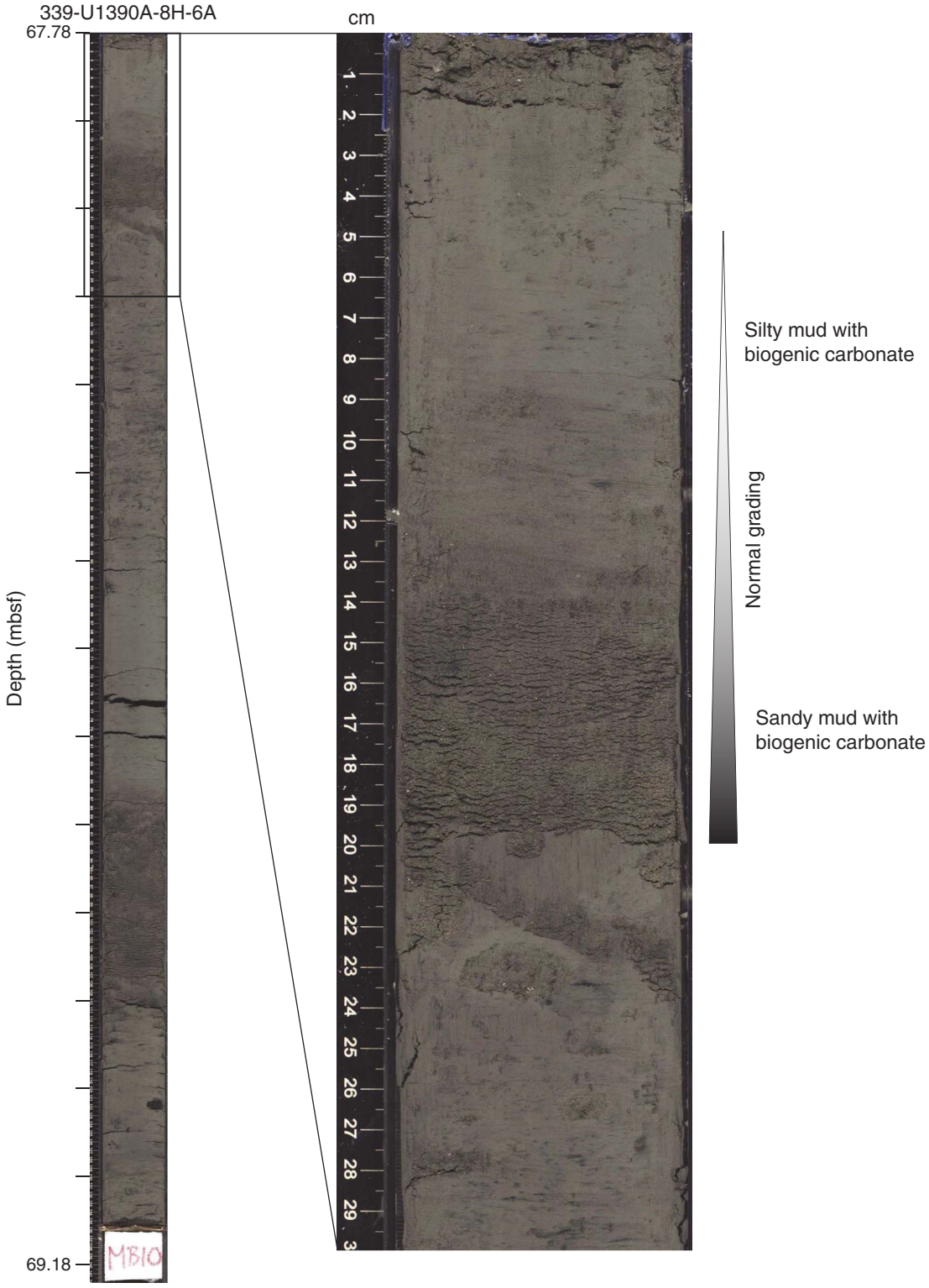

Figure F11. Core images of inverse-graded (top-cut-out) sequence composed of calcareous mud, silty mud with biogenic carbonate, and sandy mud with biogenic carbonate from Subunit IA (Sections 339-U1390A-18H-2A and 18H-3A).

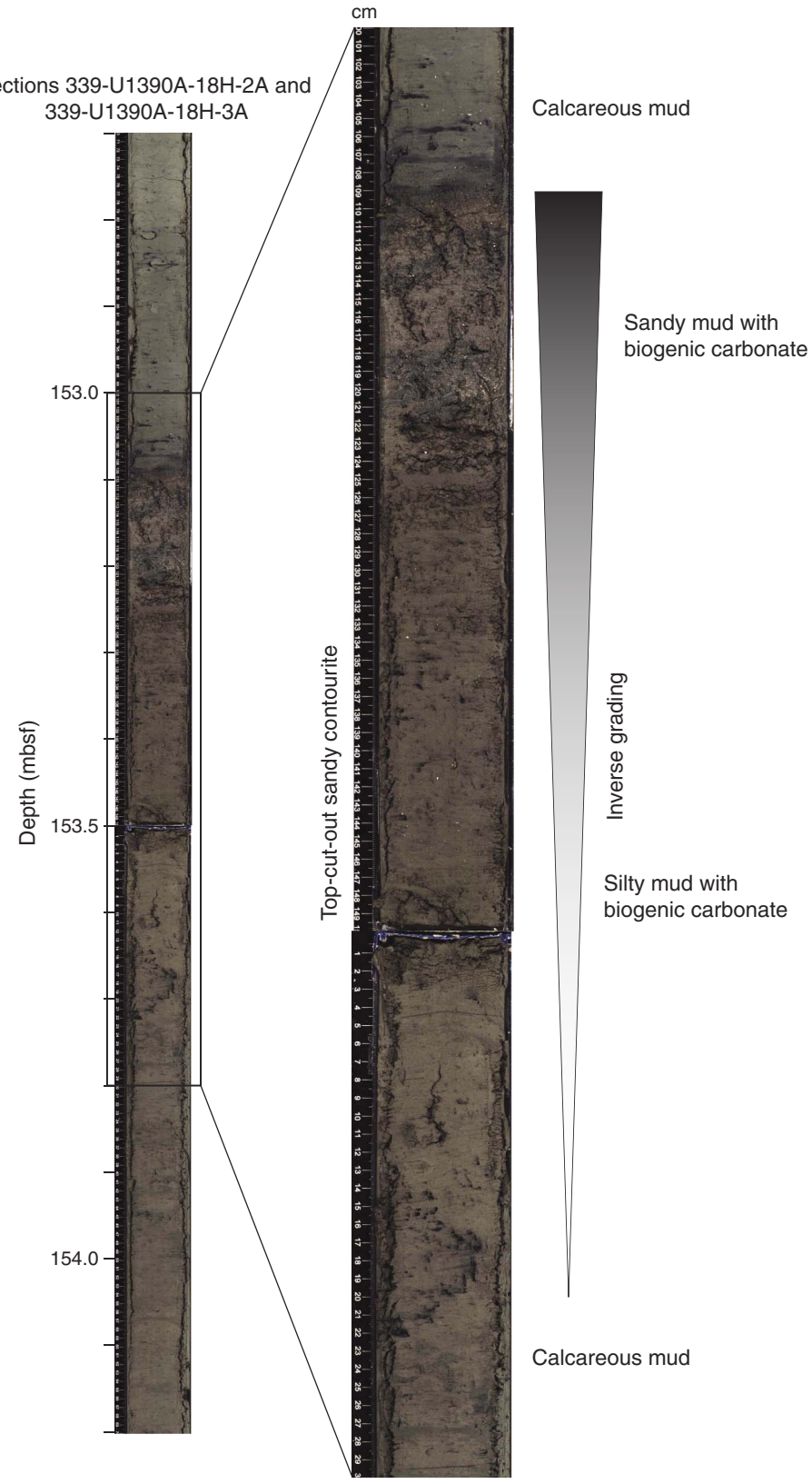

Figure F12. Core images of calcareous mud associated with faint lamination and few burrows from Subunit IA (Section 339-U1390B-2H-4A). Right image is processed for brightness and contrast.

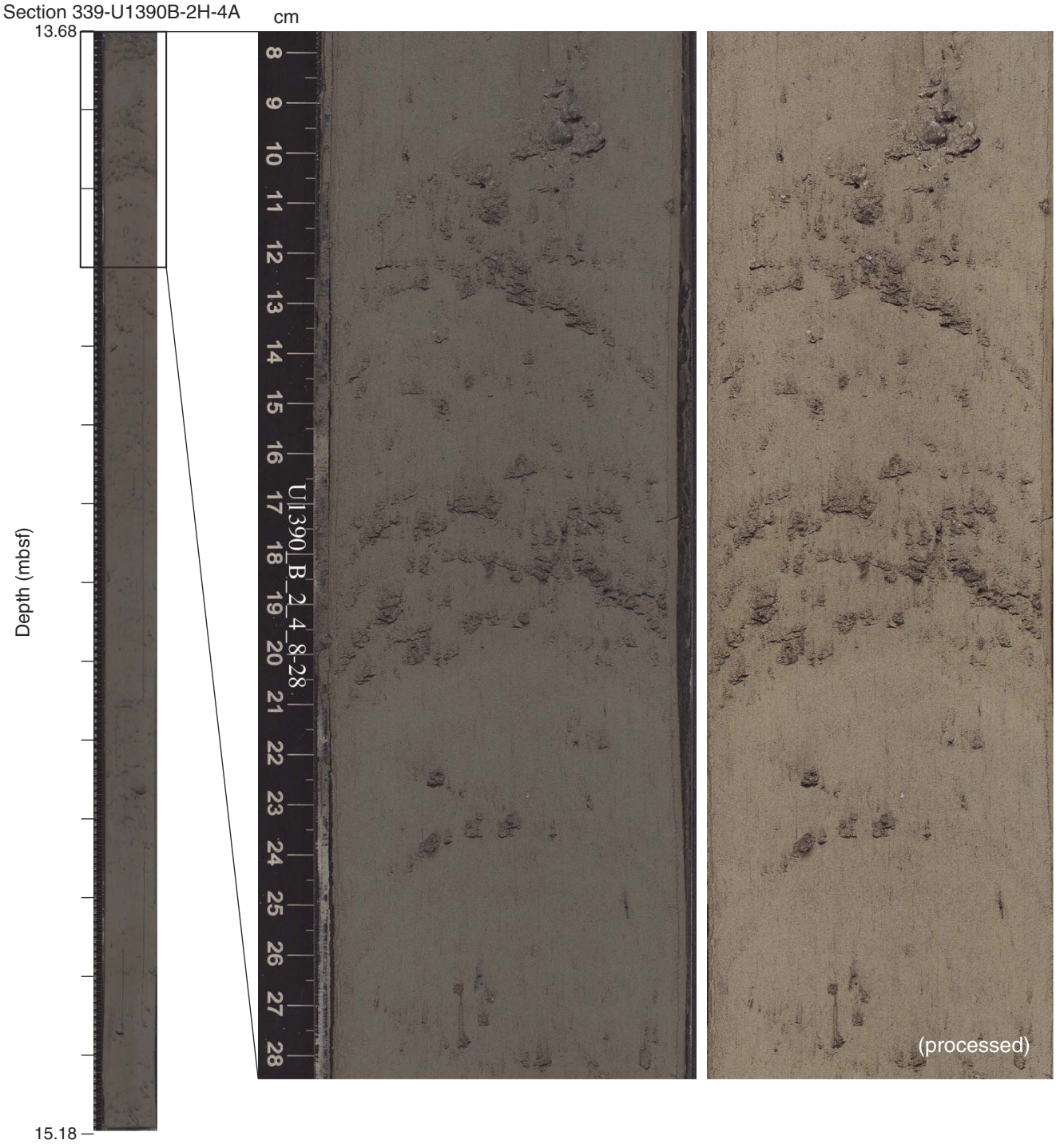

Figure F13. Plots of downhole changes in sediment composition based on smear slide observations, Site U1390.

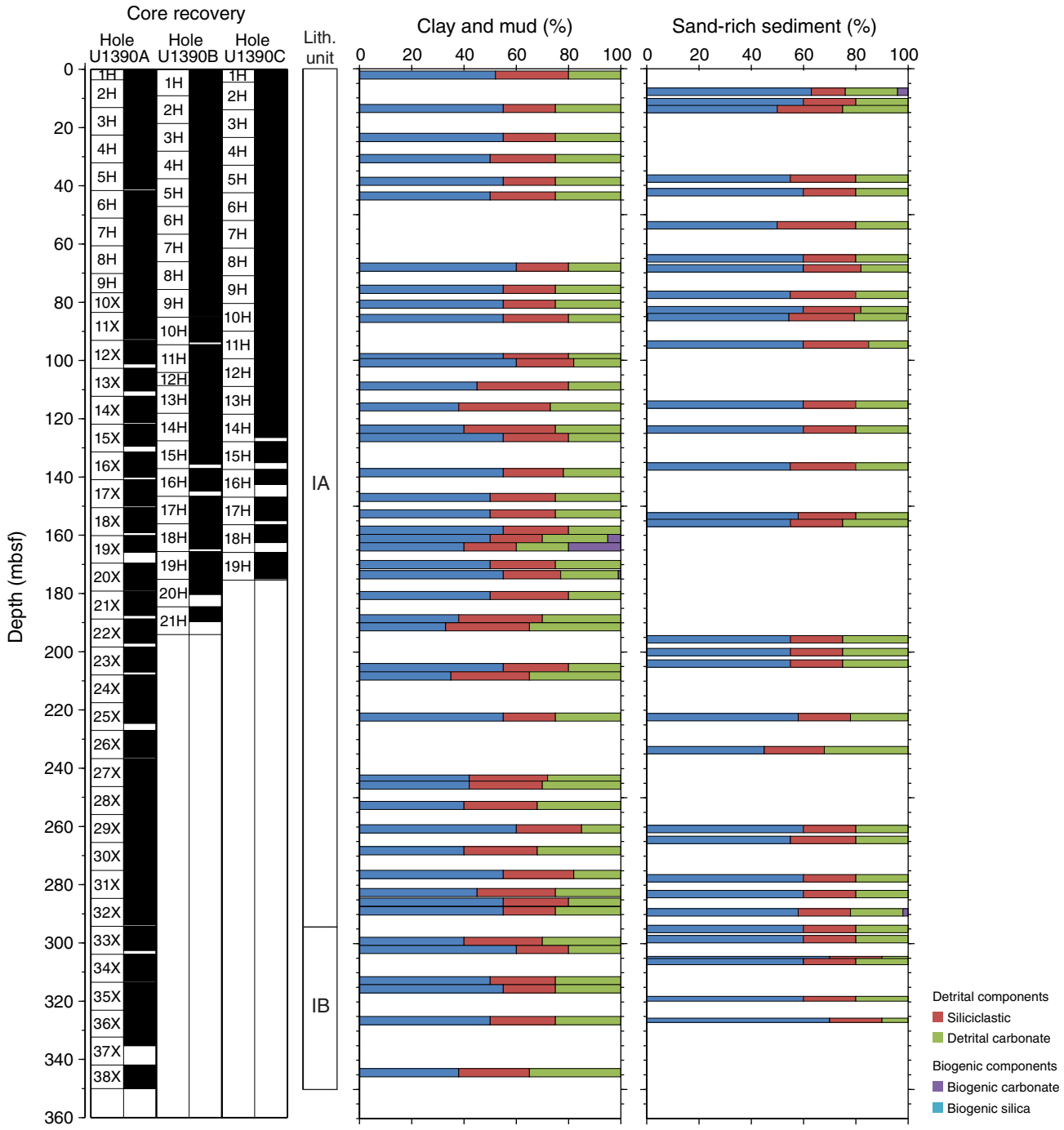

Figure F14. Photomicrographs of smear slide samples from Subunit IA. **A.** Calcareous mud (Sample 339-U1390A-21X-2A, 112 cm). **B.** Silty mud with biogenic carbonate (Sample 339-U1390A-21X-3A, 104 cm). **C.** Silty sand (Sample 339-U1390C-2H-2A, 80 cm). Left panels taken under plane-polarized light; right panels taken under cross-polarized light.

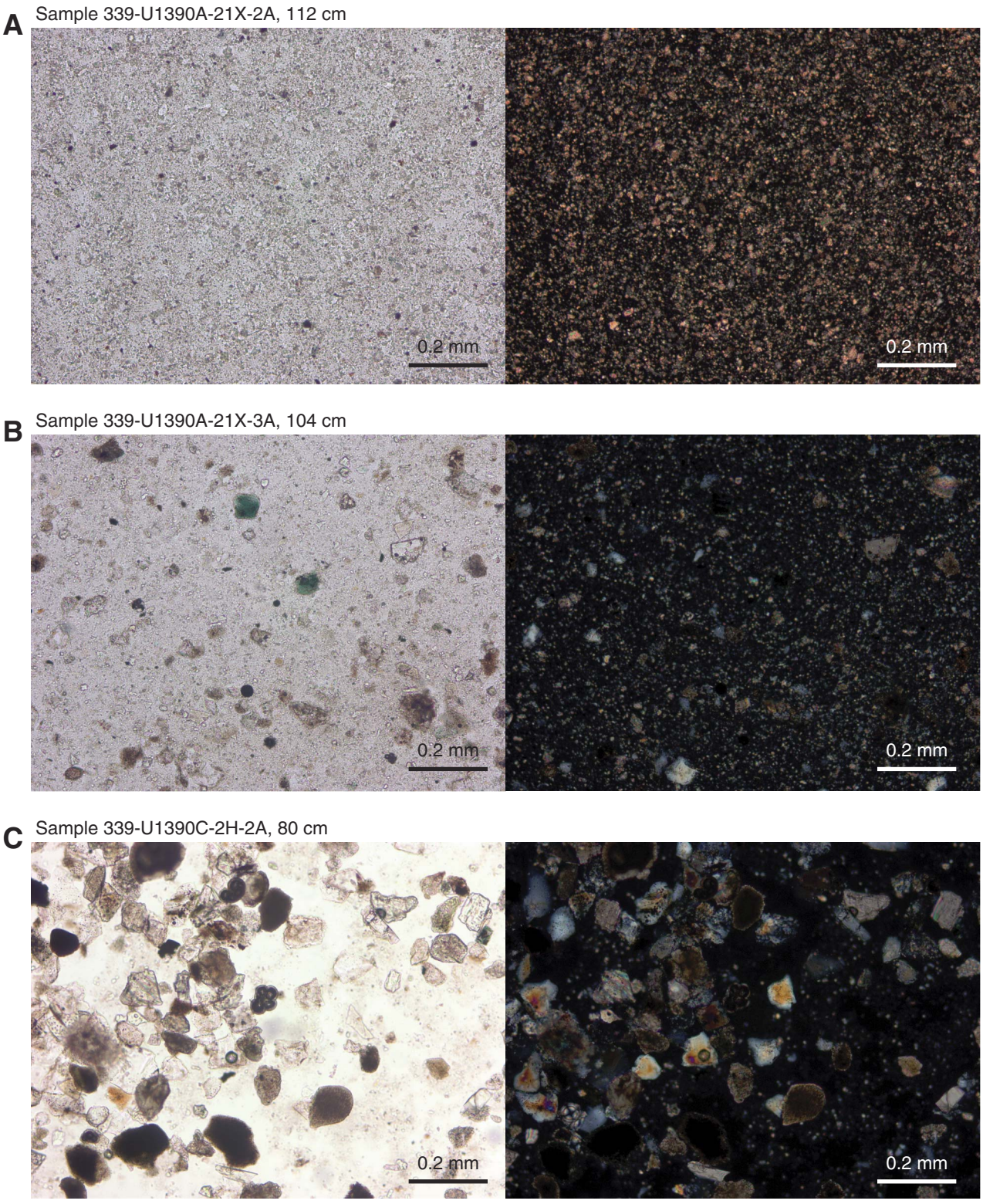

Figure F15. Photomicrographs of biogenic mud composed of siliceous fractions from Subunit IA. **A, B.** Sample 339-U1390A-19X-3A, 108 cm. **C.** Sample 339-U1390A-19X-4A, 10 cm. Left panels taken under plane-polarized light; right panels taken under cross-polarized light.

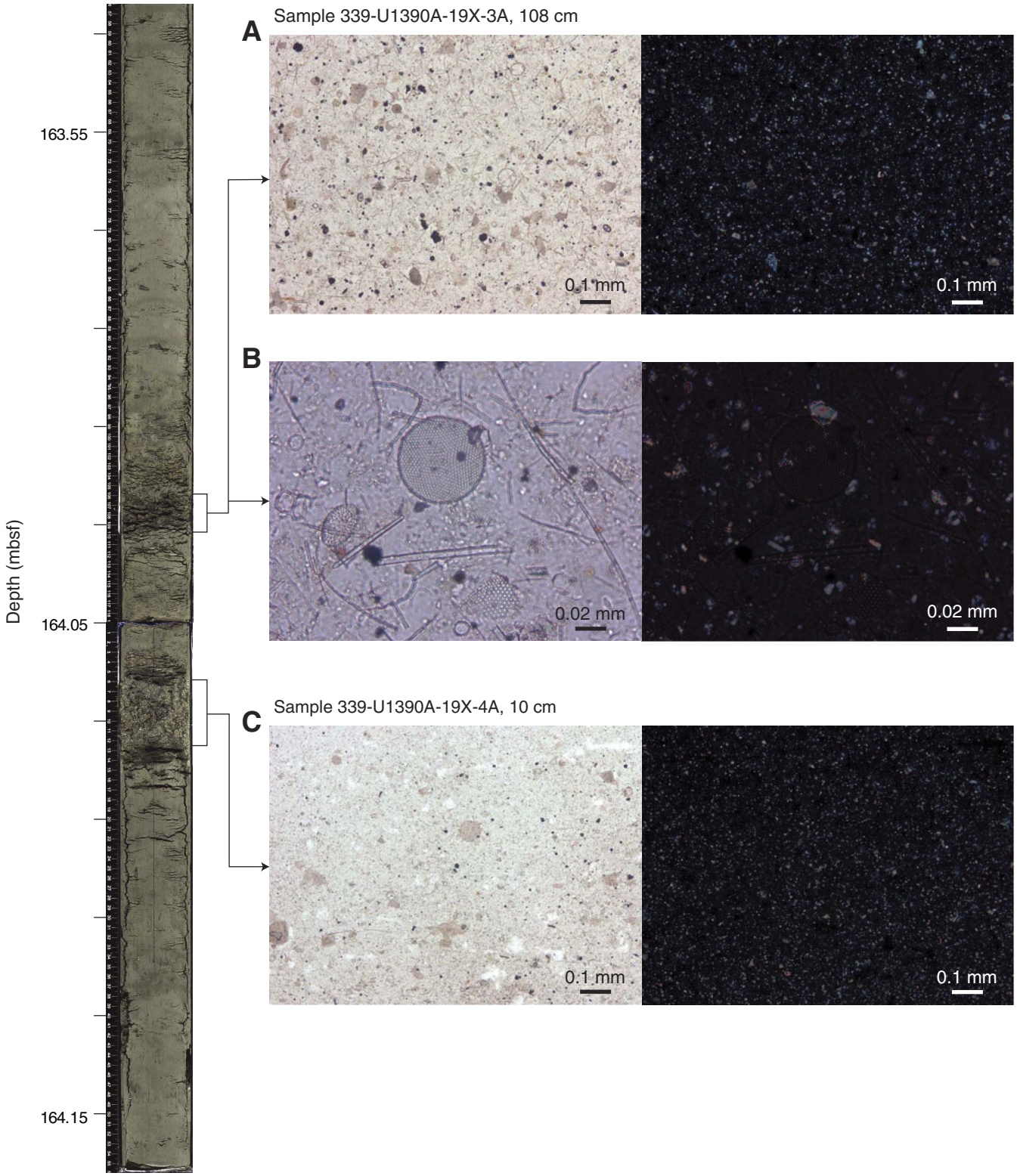

Figure F16. Photomicrographs of opaques from Subunit IA (Sample 339-U1390A-4H-3A, 85 cm). Left panel taken under plane-polarized light; right panel taken under cross-polarized light.

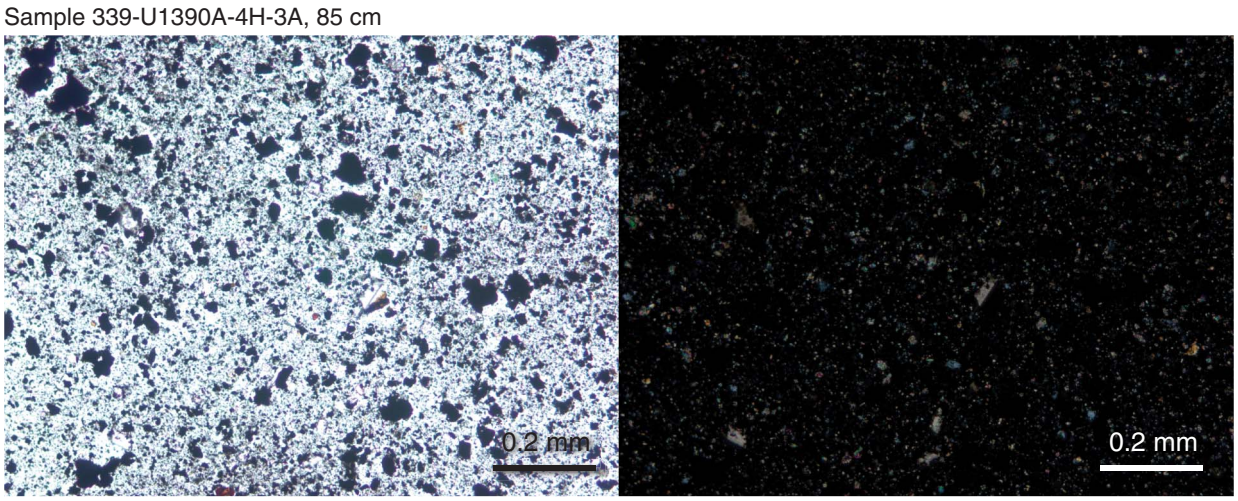

Figure F17. Photographs of macrofossils, Site U1390. **A.** Cold-water coral. **B.** Gastropods.

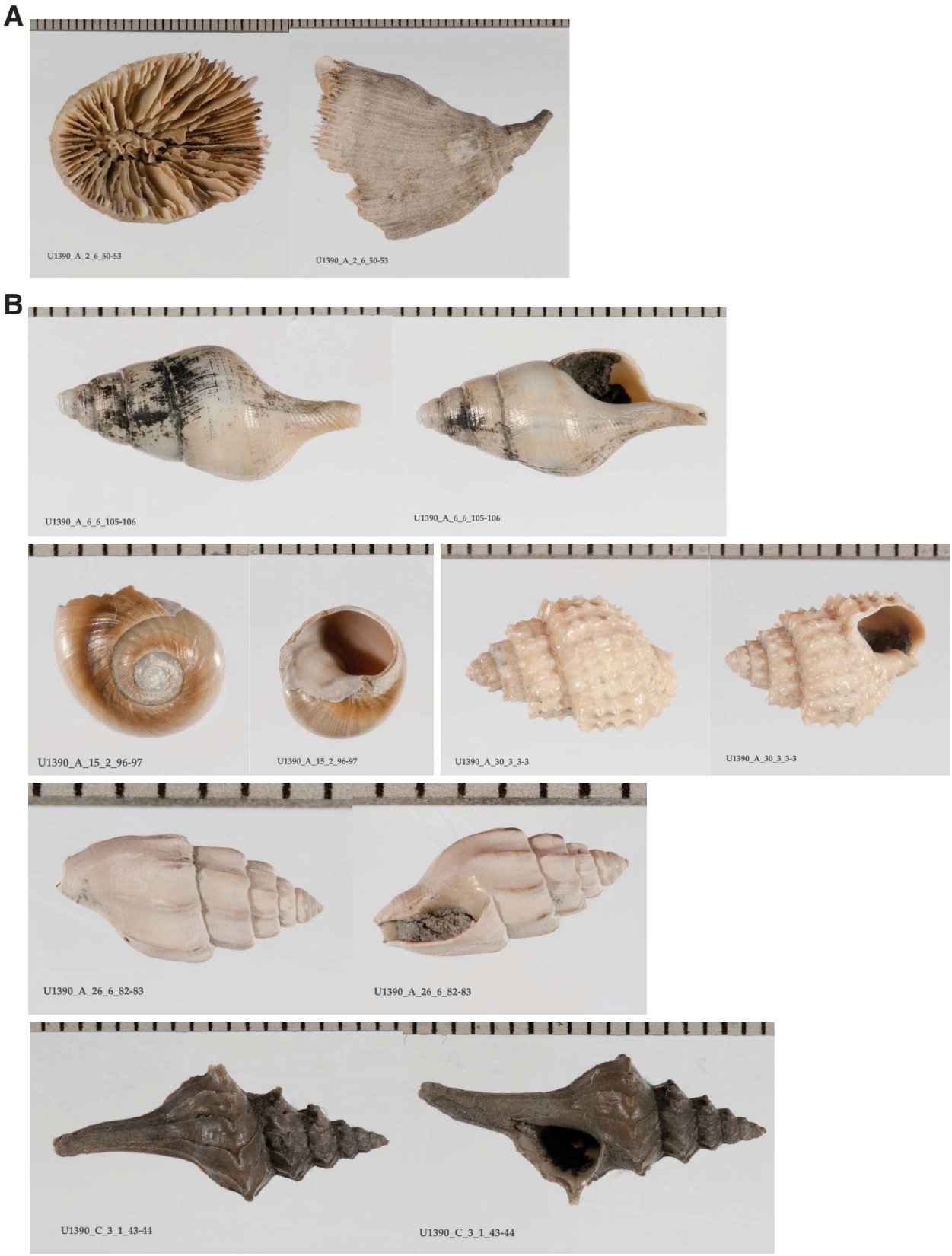

Figure F18. Core images of a thick bi-gradational sequence from Subunit IB (Sections 339-U1390A-33X-6A through 34X-3A).

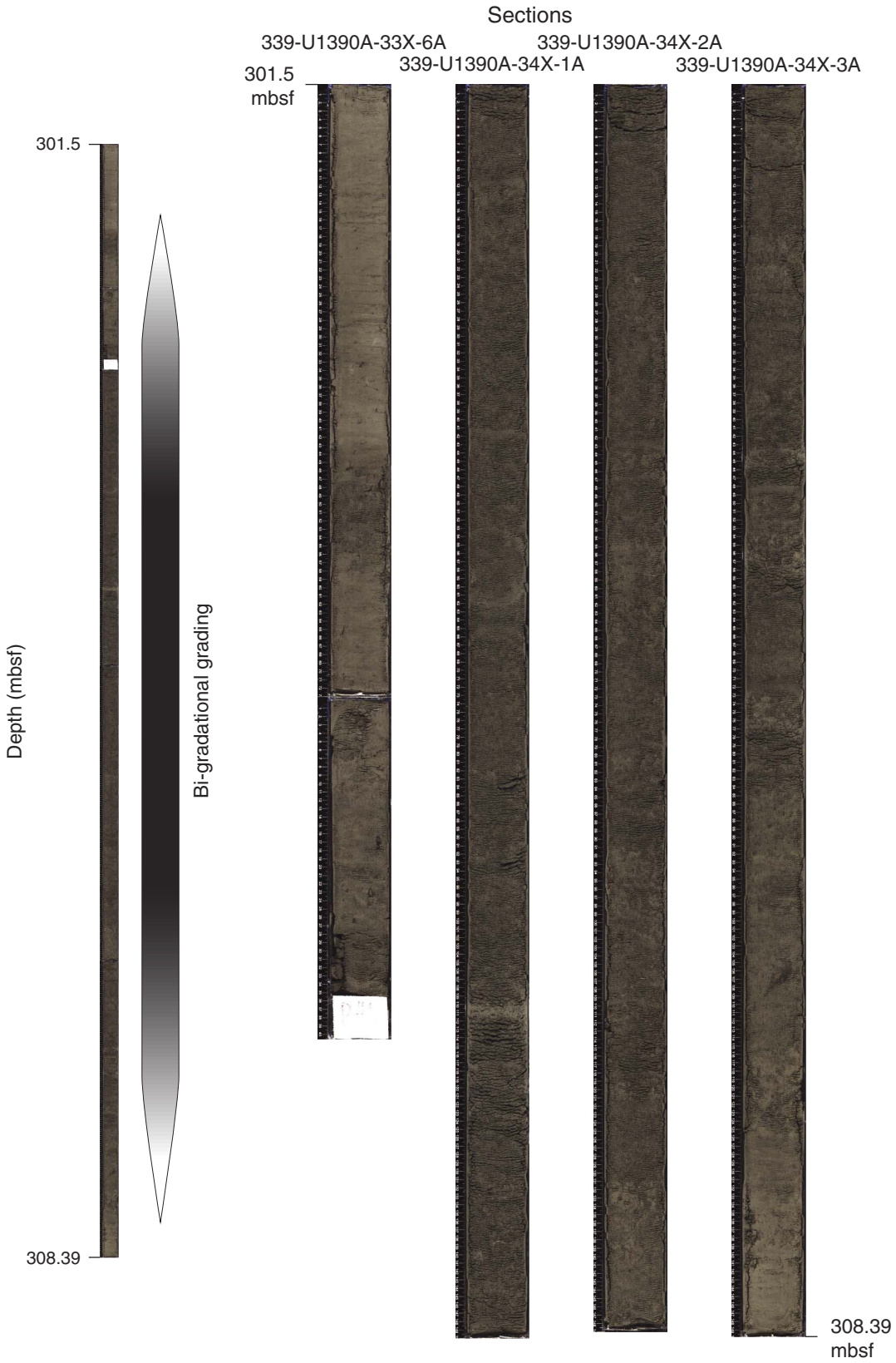

Figure F19. Core images of clear color contact of calcareous mud corresponding to upper hiatus in Subunit IA (Section 339-U1390A-26X-2A).

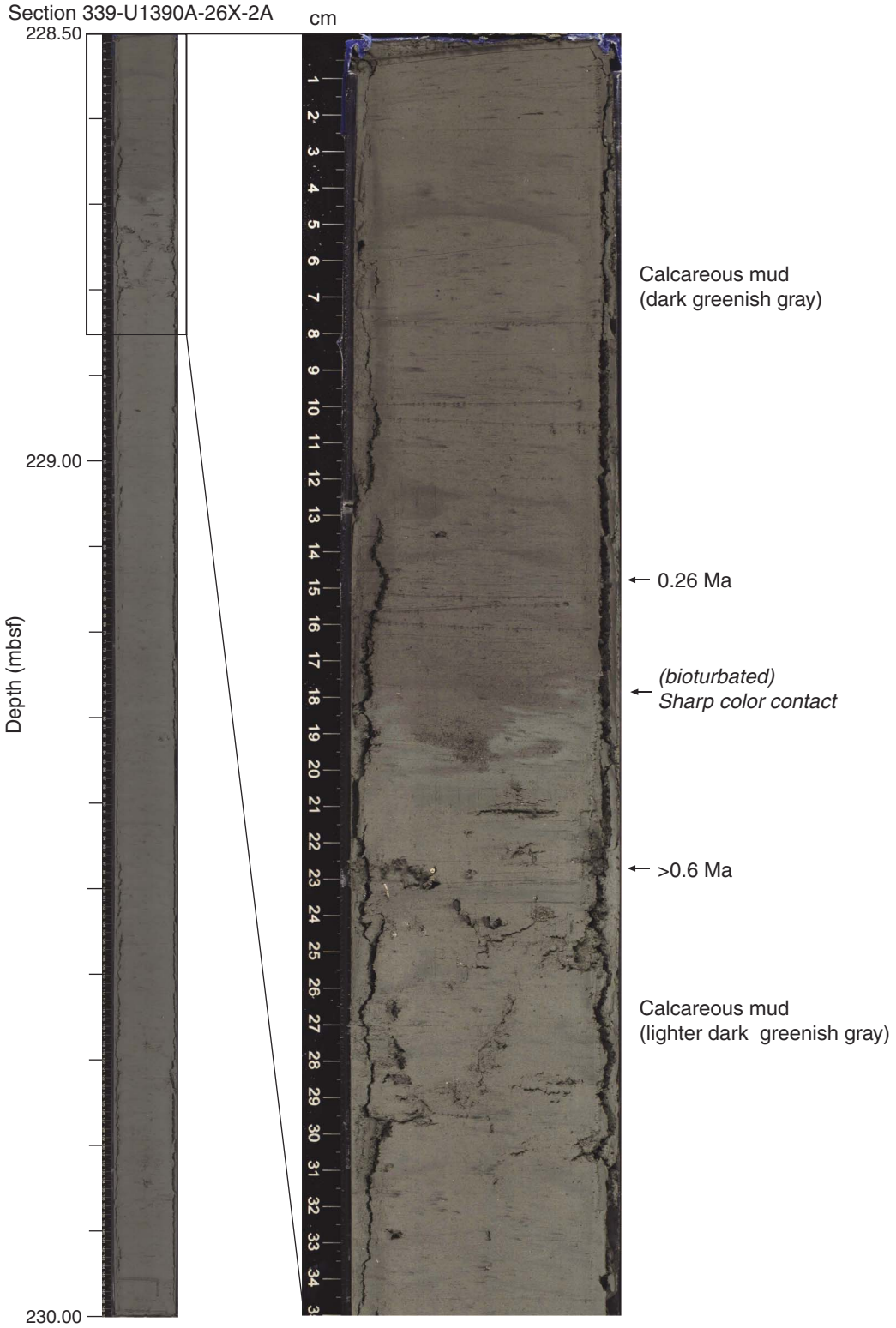

Figure F20. Biostratigraphic events vs. depth, Site U1390. Events are plotted at their mean depth (Table T6). Wavy lines = hiatus positions.

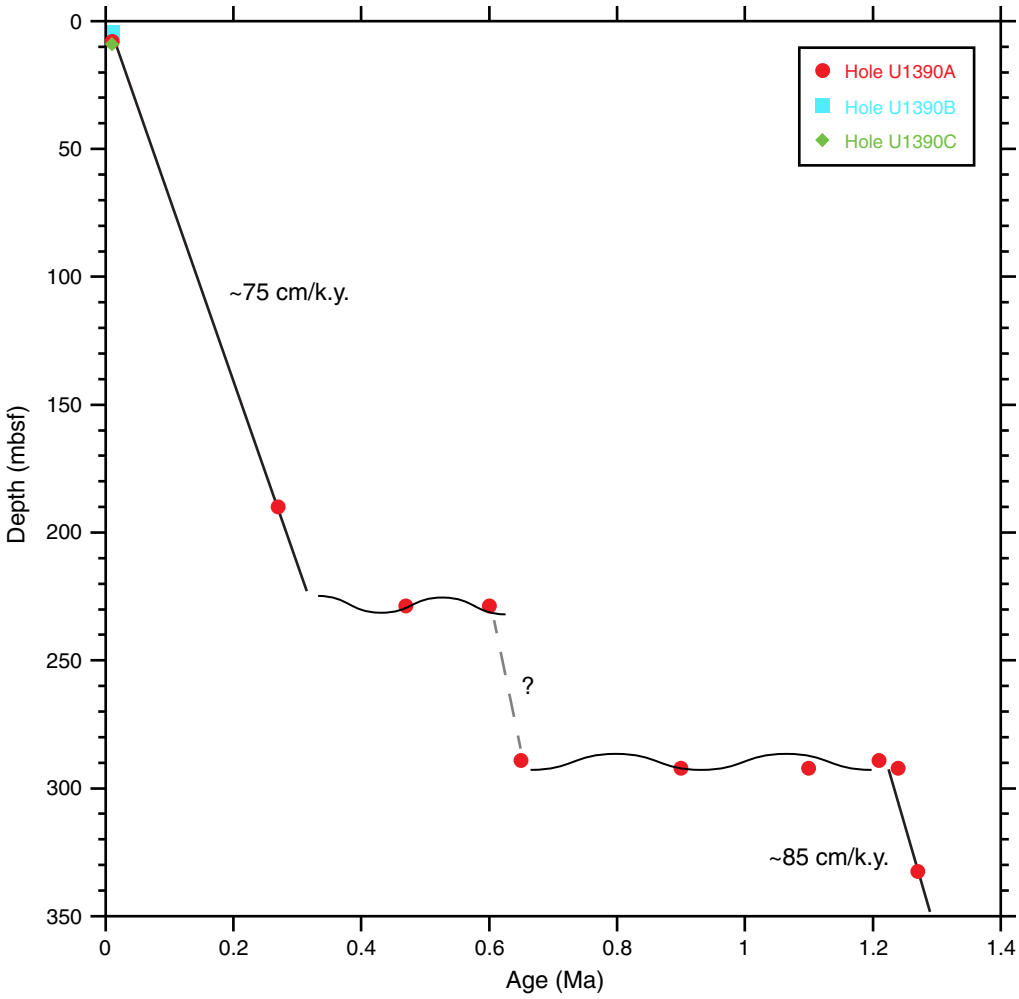

Figure F21. Preliminary pollen results from the analysis of seven samples in Hole U1390A. Mediterranean forest is mainly deciduous and evergreen *Quercus* and *Olea*. TPS = total pollen and spores. Preservation: G = good, M = moderate, P = poor.

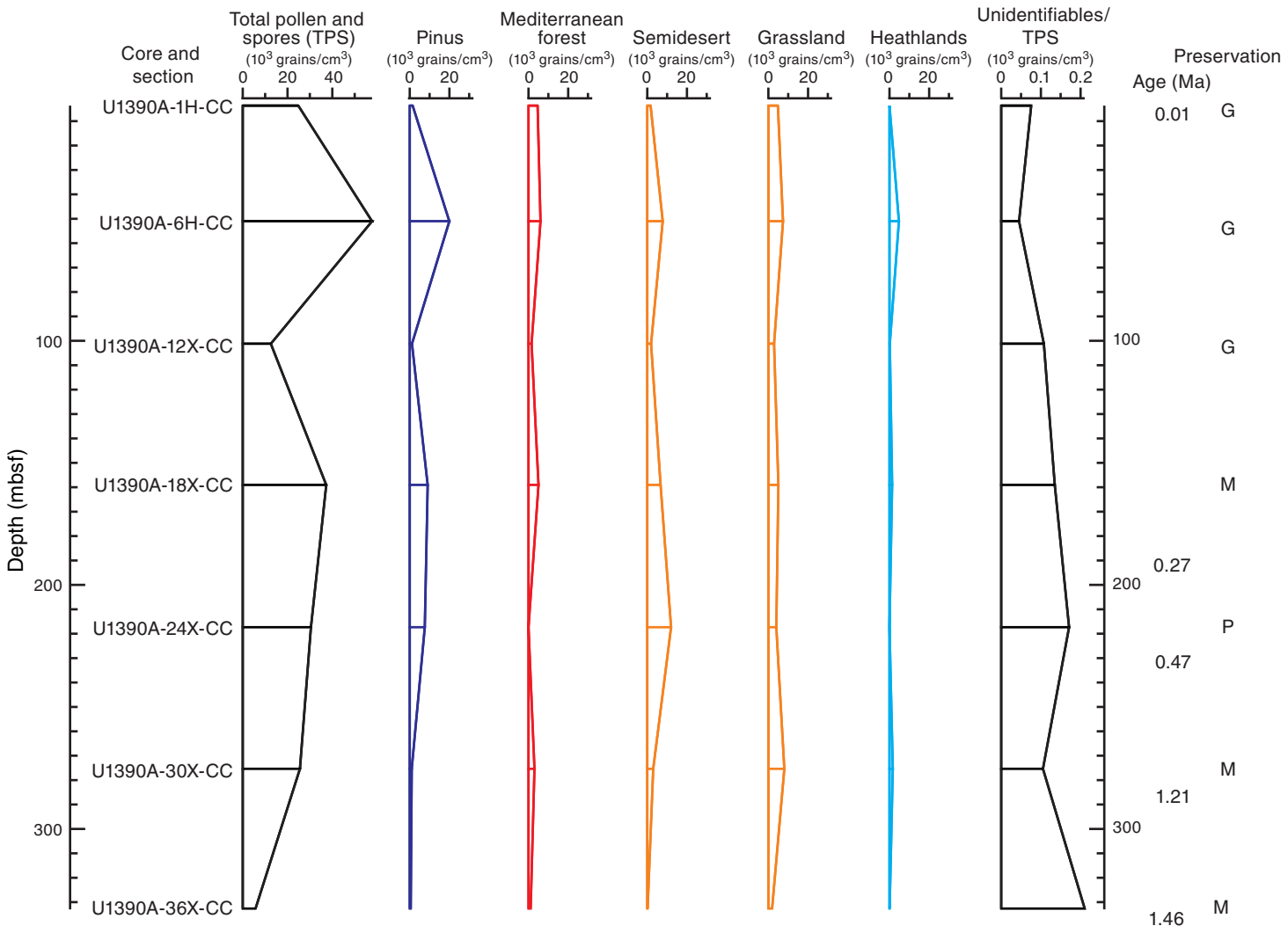

Figure F22. Paleomagnetism after 20 mT AF demagnetization, Site U1390. In the Chron columns, black = normal polarity, white = reversed polarity, and gray = zones or polarity boundaries without a clear magnetostratigraphic interpretation. In Inclination columns, blue dashed lines = expected geocentric axial dipole inclinations at the site latitude during reversed (left) and normal (right) polarities. In Declination columns, light blue circles = measured declinations and dark blue circles = FlexIt tool–corrected declinations. In Susceptibility columns, gray lines represent SHMSL susceptibility plus 25×10^{-5} volume SI to better show the comparison with WRMSL susceptibility (black lines). (Figure shown on next three pages.)

Figure F22 (continued). A. Hole U1390A. (Caption shown on previous page.) (Continued on next page.)

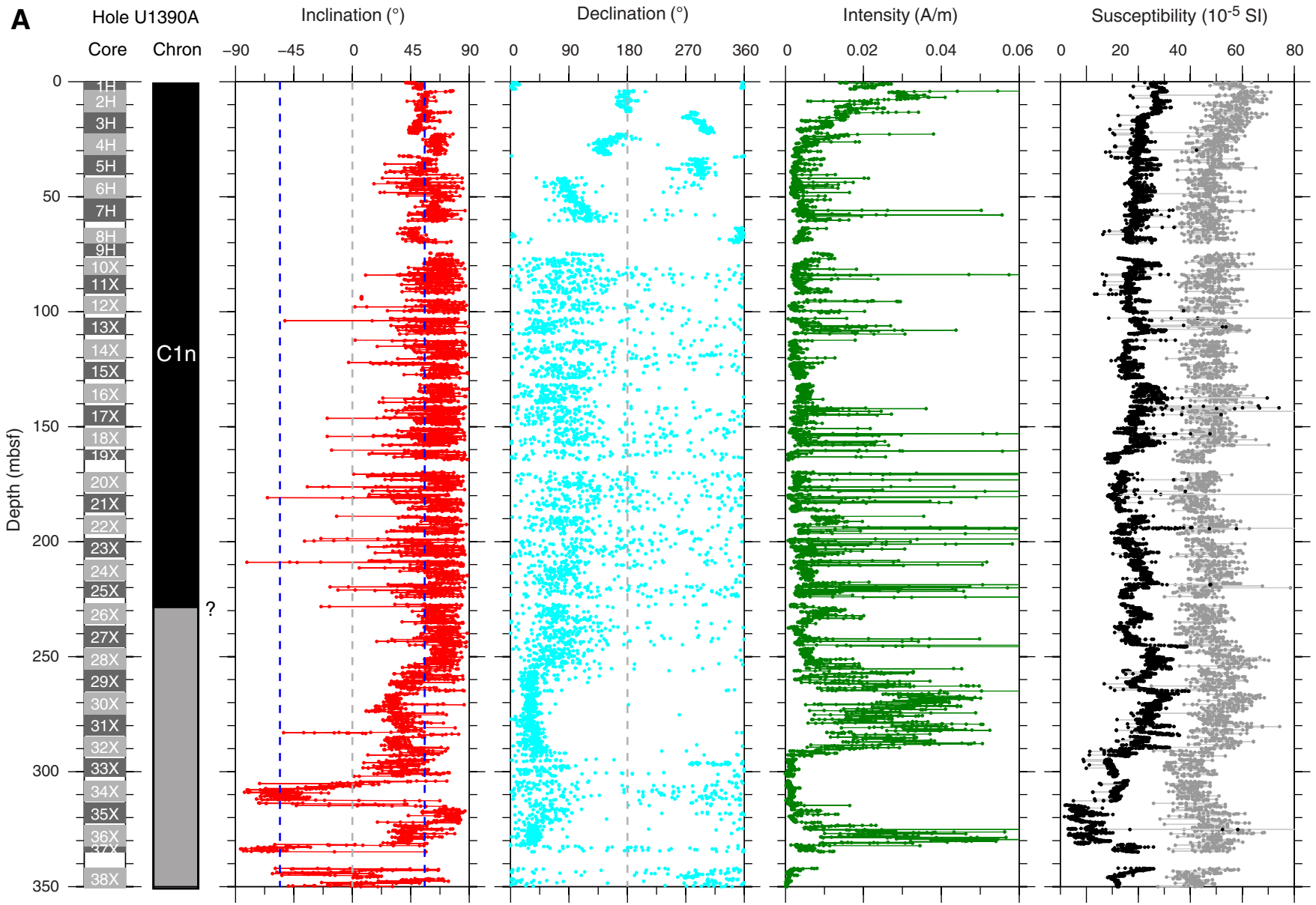

Figure F22 (continued). B. Hole U1390B. (Continued on next page.)

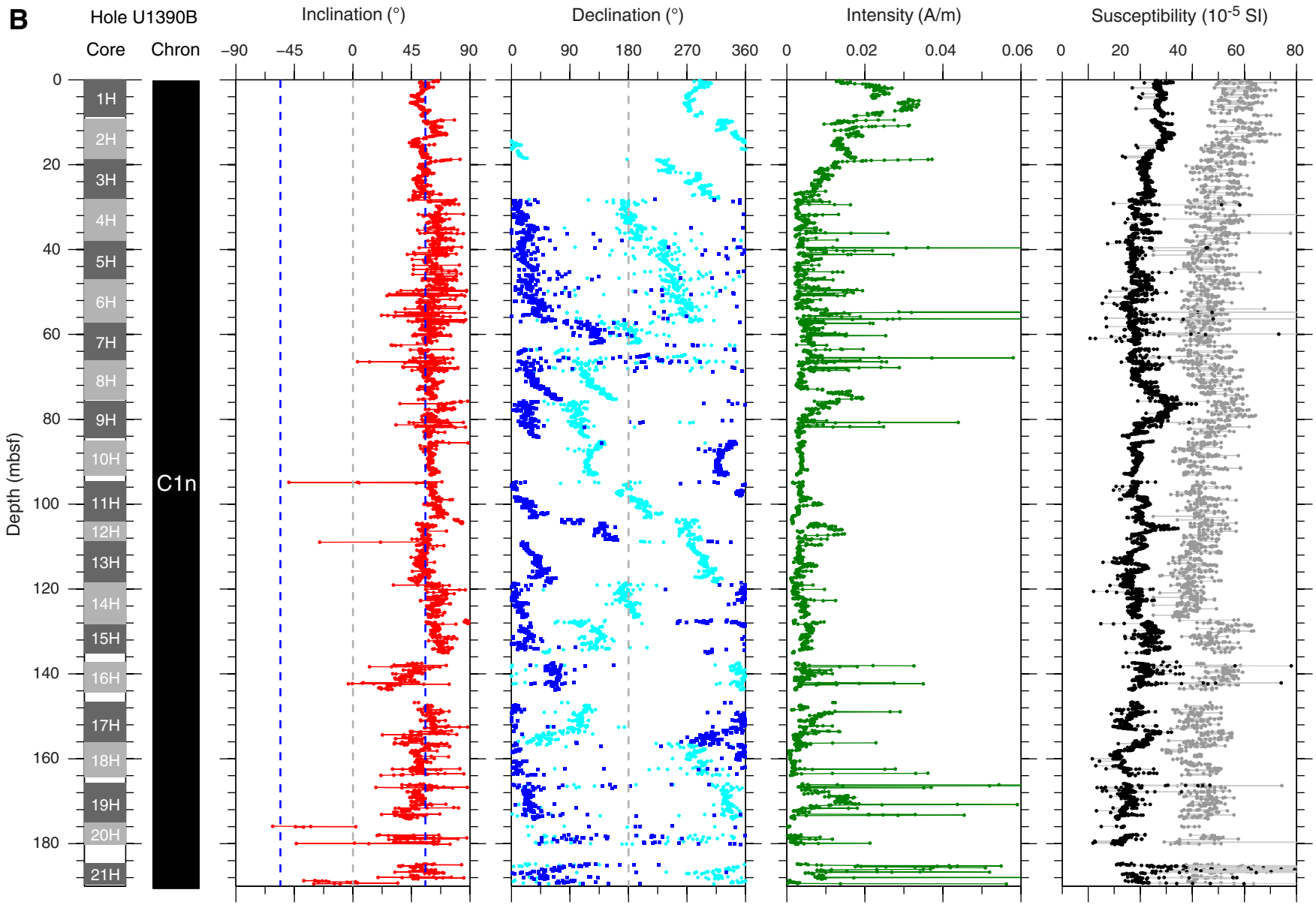

Figure F22 (continued). C. Hole U1390C.

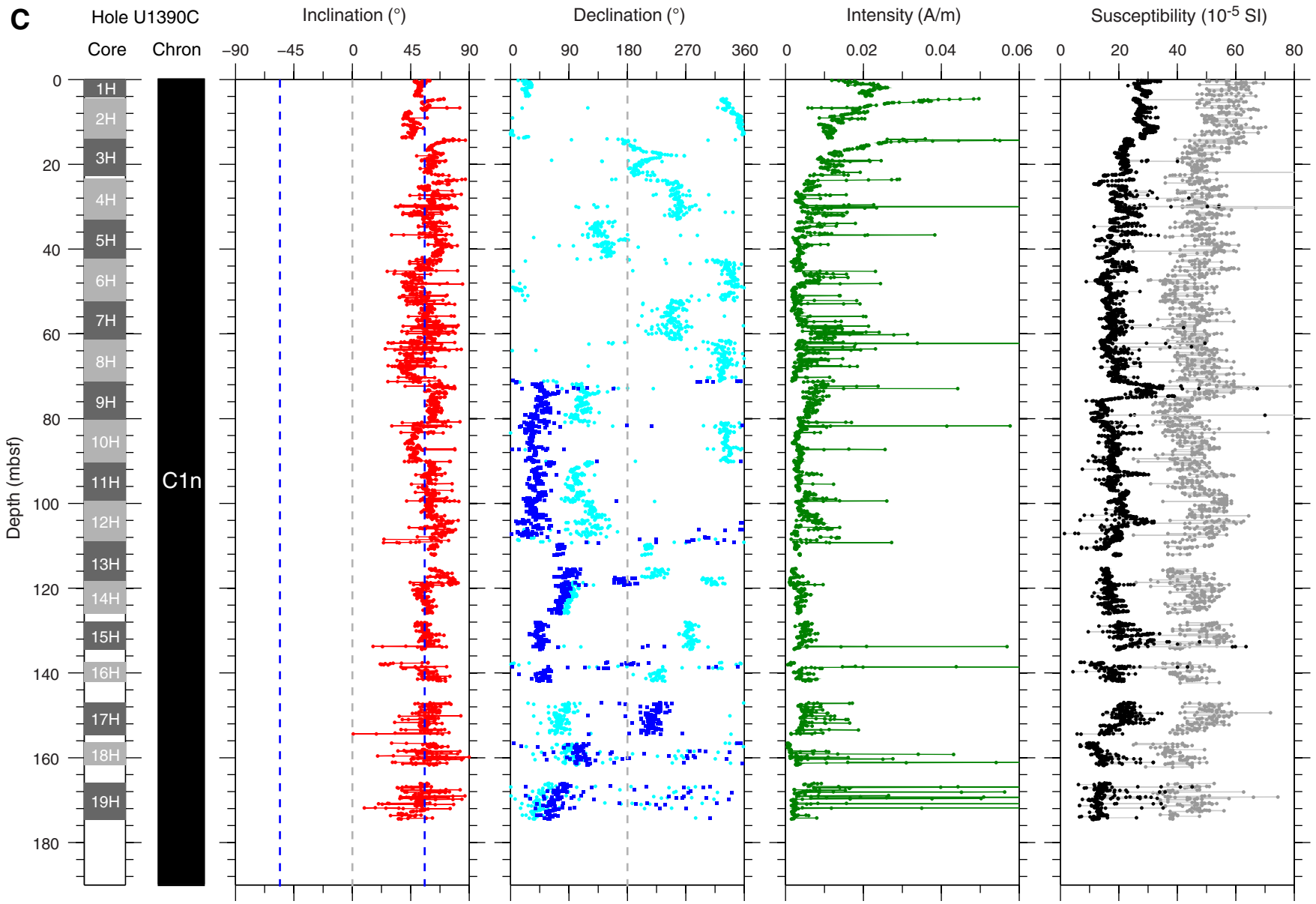

Figure F23. Plots of *P*-wave velocity (PWV) measured in Hole U1390A on the Whole-Round Multisensor Logger (WRMSL; green line) and Section Half Measurement Gantry (discrete samples) set to automatic (solid circles) and manual (open circles) mode, wet bulk density (red diamonds) on discrete samples and gamma ray attenuation density measured on the WRMSL (black line), magnetic susceptibility (MS) measured on the WRMSL (black line) and on split cores (green points). Gray lines for magnetic susceptibility (Cores 339-U1390A-35X and 36X) are measurements obtained with incorrect zero calibration (offset of -30×10^{-5} SI from standard) that have been corrected by adding 30×10^{-5} SI, in agreement with magnetic susceptibility determined on split cores. Note that records were cleaned for outliers and bad data at sections ends. PP = physical property.

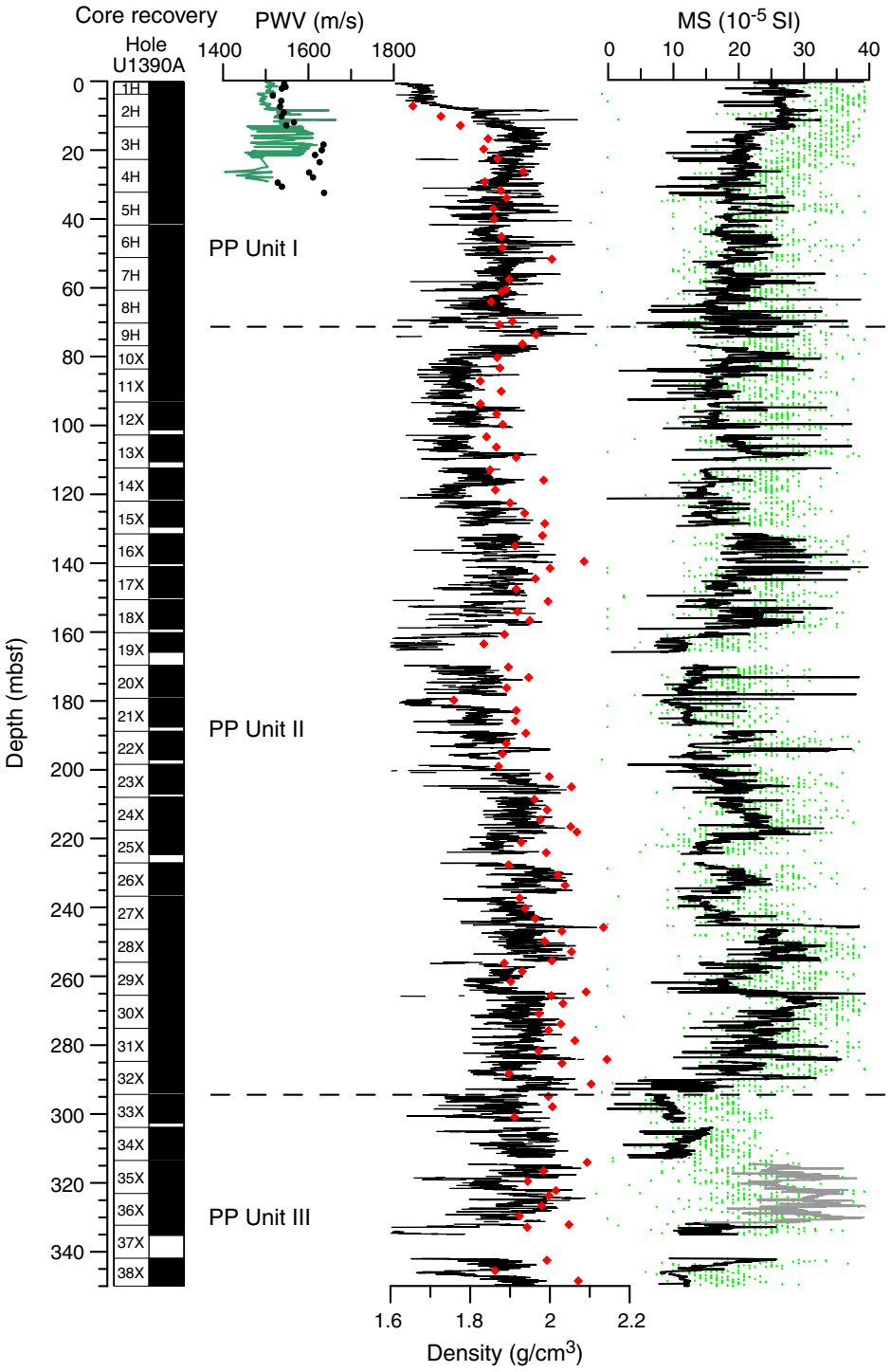

Figure F24. Plot of color reflectance (L*, a*) and natural gamma ray (NGR) measurements in Hole U1390A. Note that data were cleared for outliers and bad data at section ends. Reflectance data were smoothed with a 10-point running mean. PP = physical property.

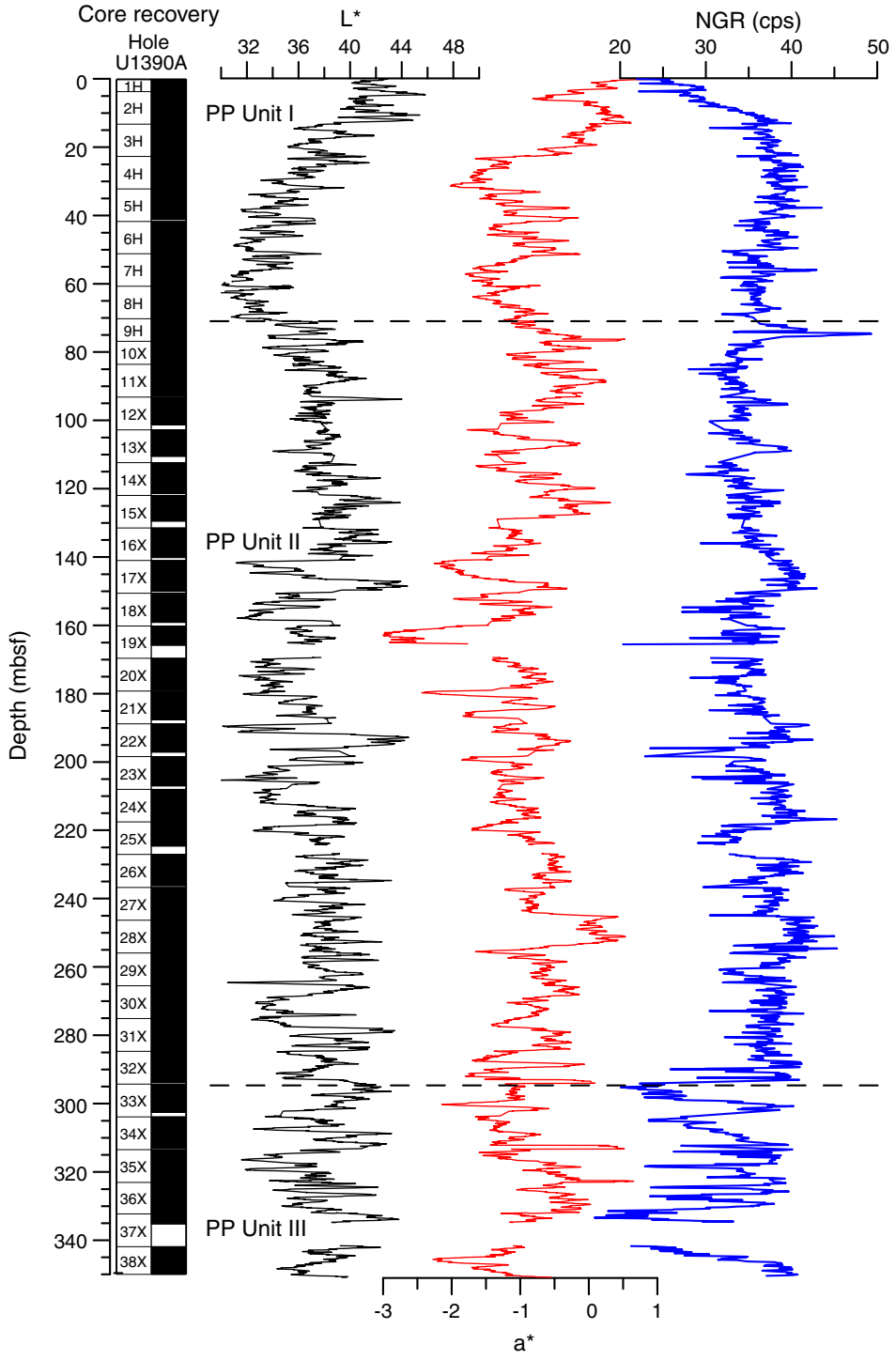

Figure F25. Plots of grain density, moisture content, and porosity, Hole U1390A. PP = physical property.

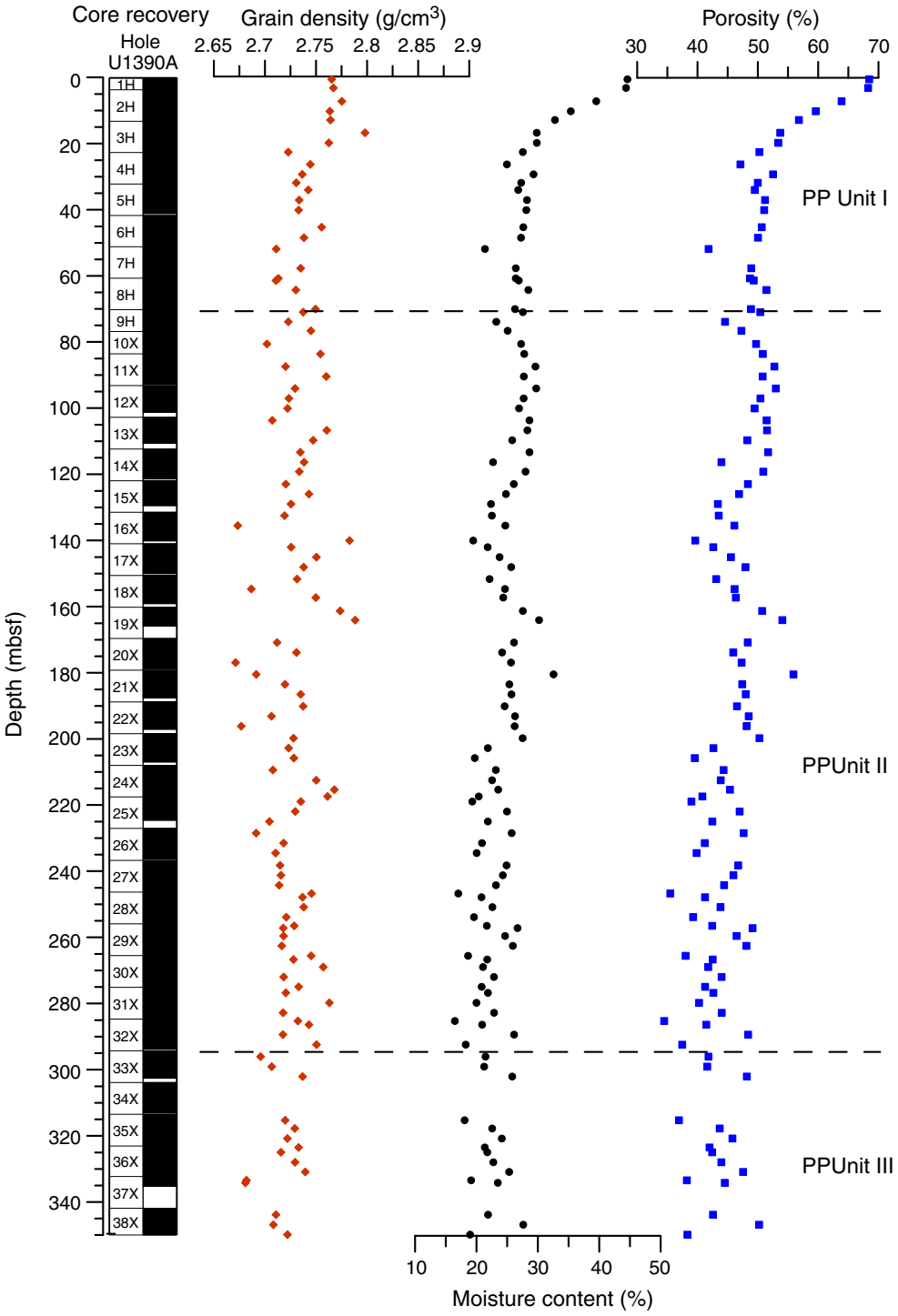

Figure F26. Plot of headspace gas analyses for volatile hydrocarbons, Hole U1390A.

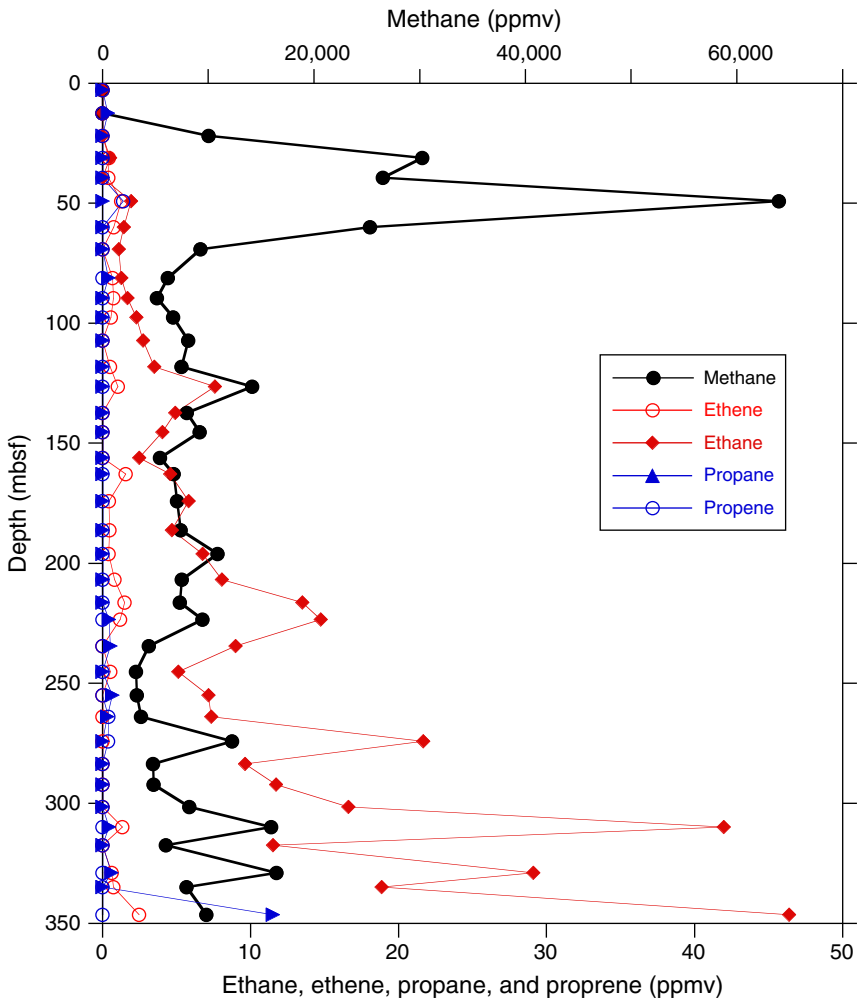

Figure F27. Plot of calcium carbonate vs. depth, Hole U1390A.

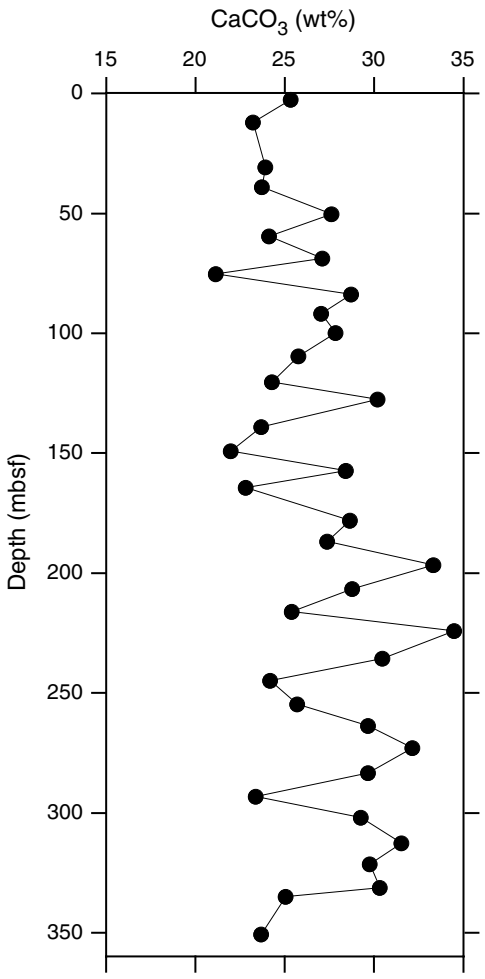

Figure F28. A–C. Plots of calculated total organic carbon (TOC), total nitrogen (TN), and C/N ratio, Hole U1390A.

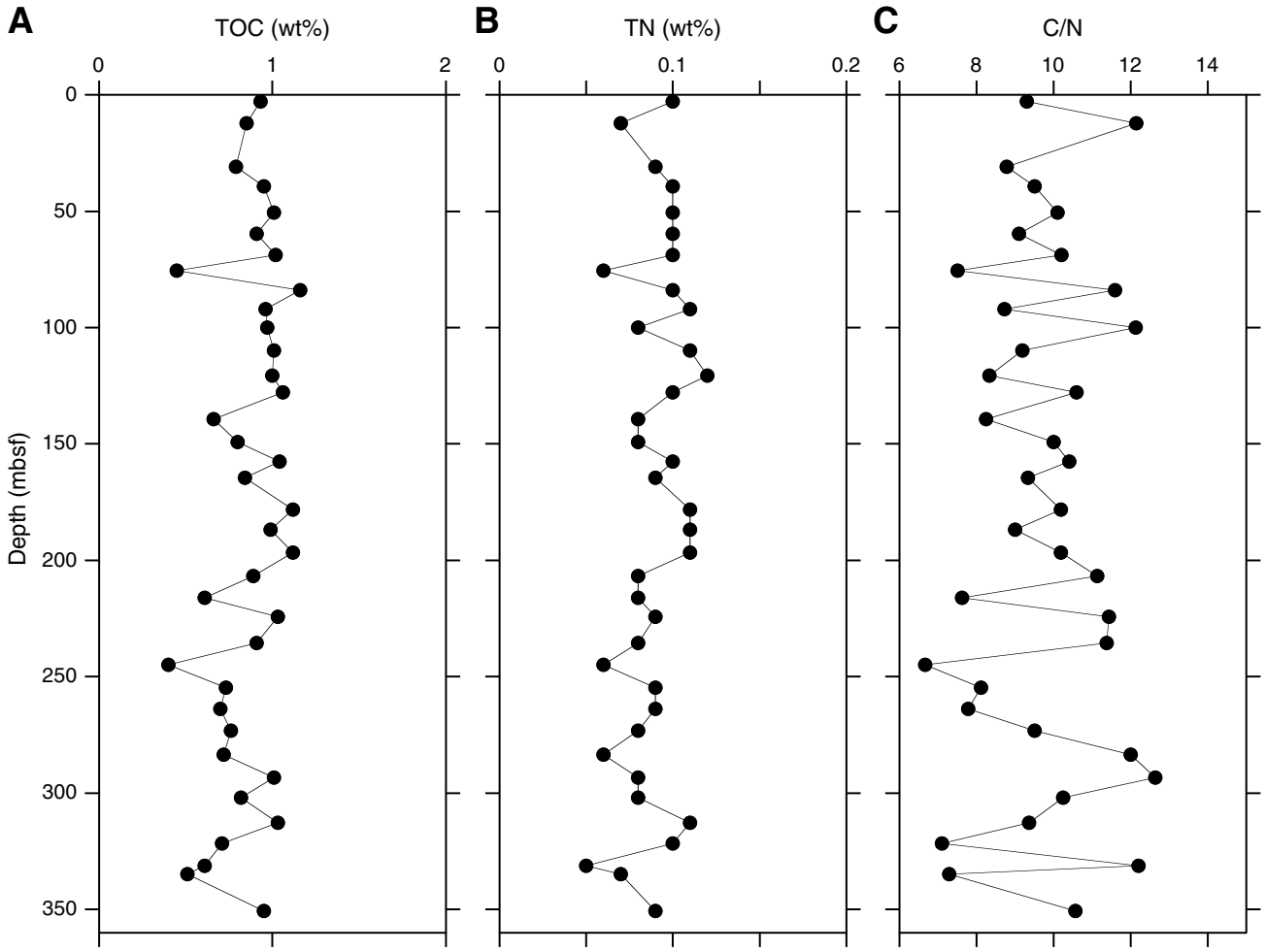

Figure F29. A–C. Plots of interstitial water sulfate, ammonium, and alkalinity, Hole U1390A.

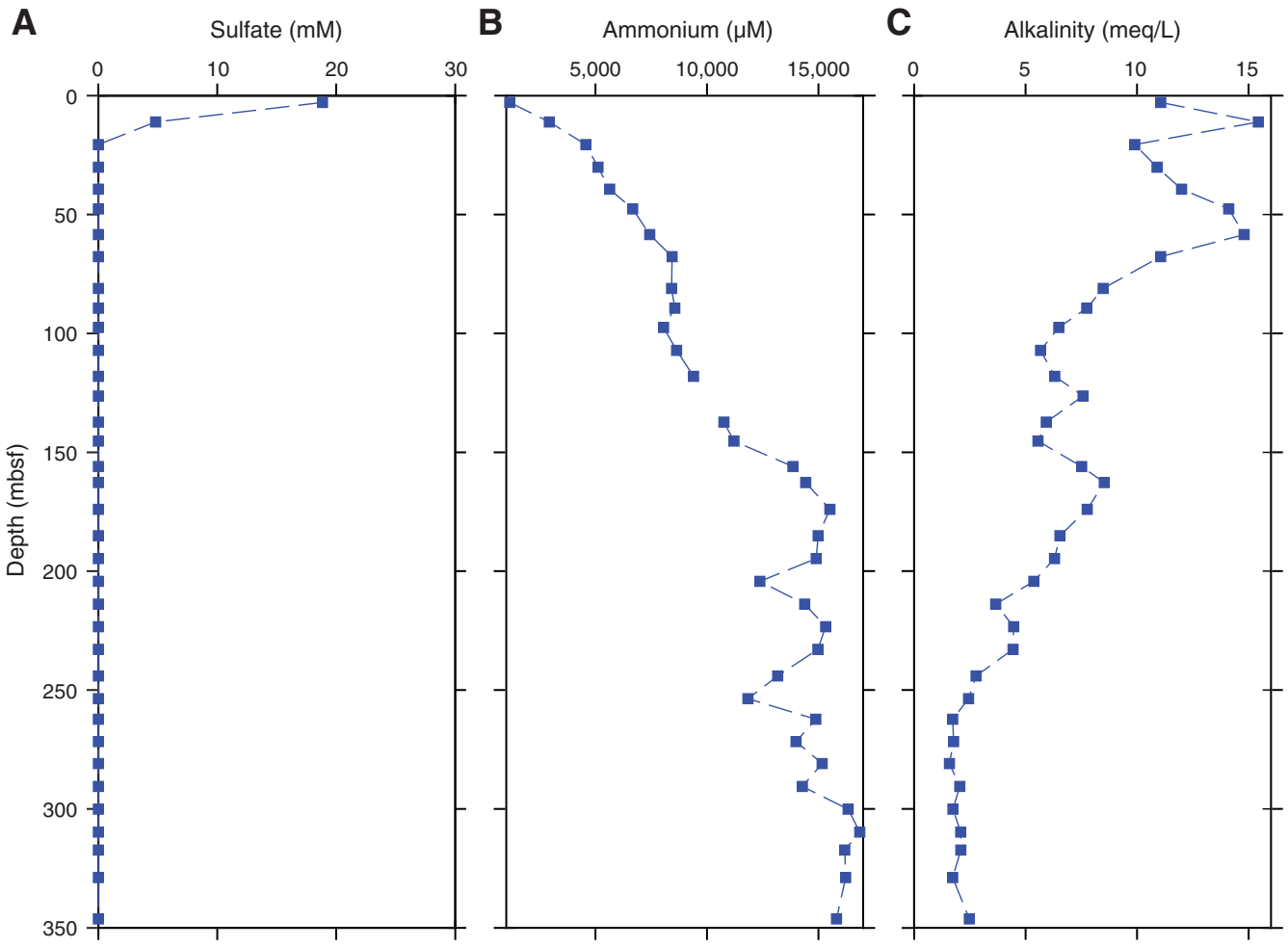

Figure F30. A–C. Plots of interstitial water calcium, magnesium, and potassium, Hole U1390A.

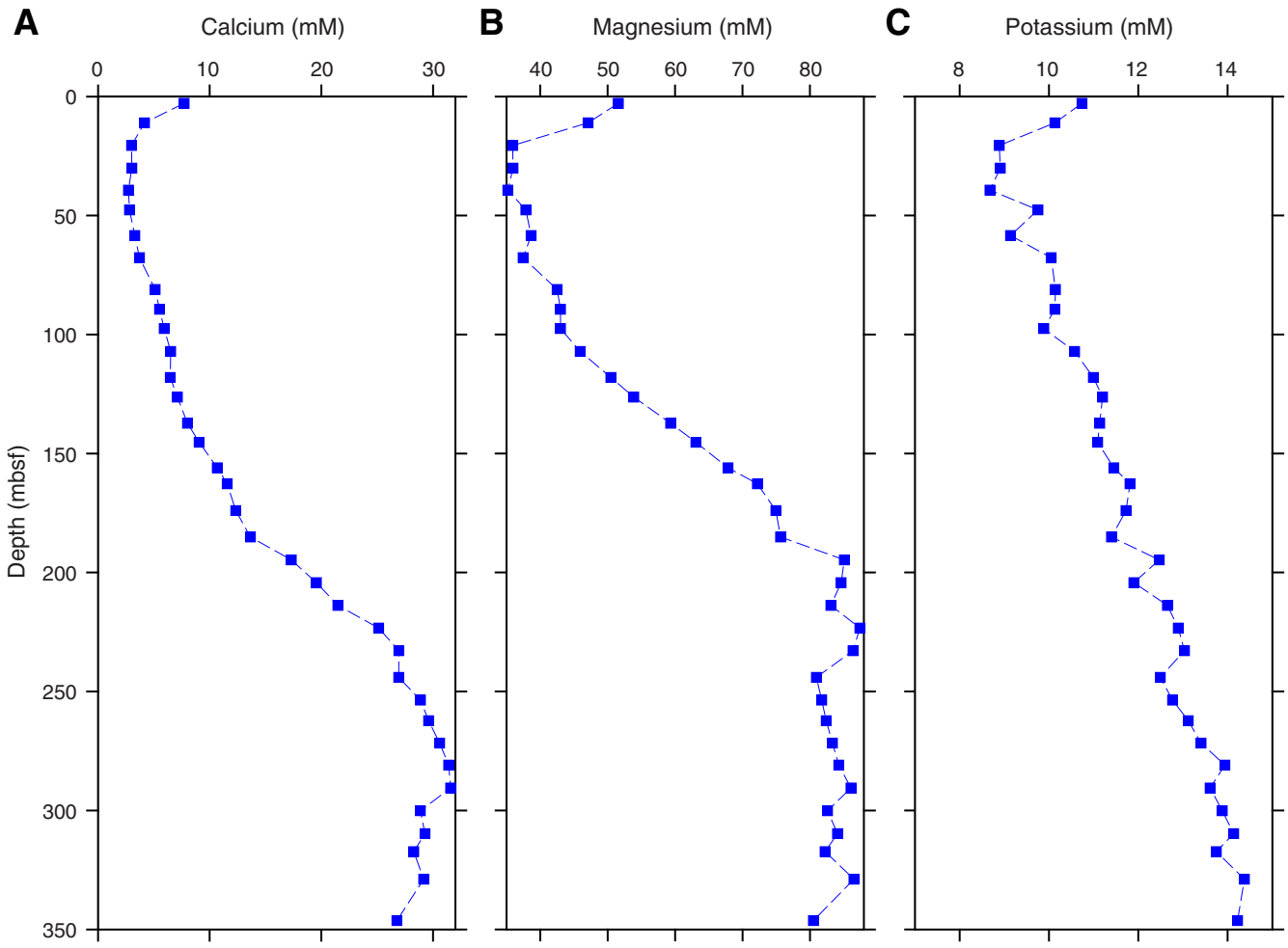

Figure F31. A–C. Plots of interstitial water chloride, sodium, and Na^+/Cl^- ratio, Hole U1390A.

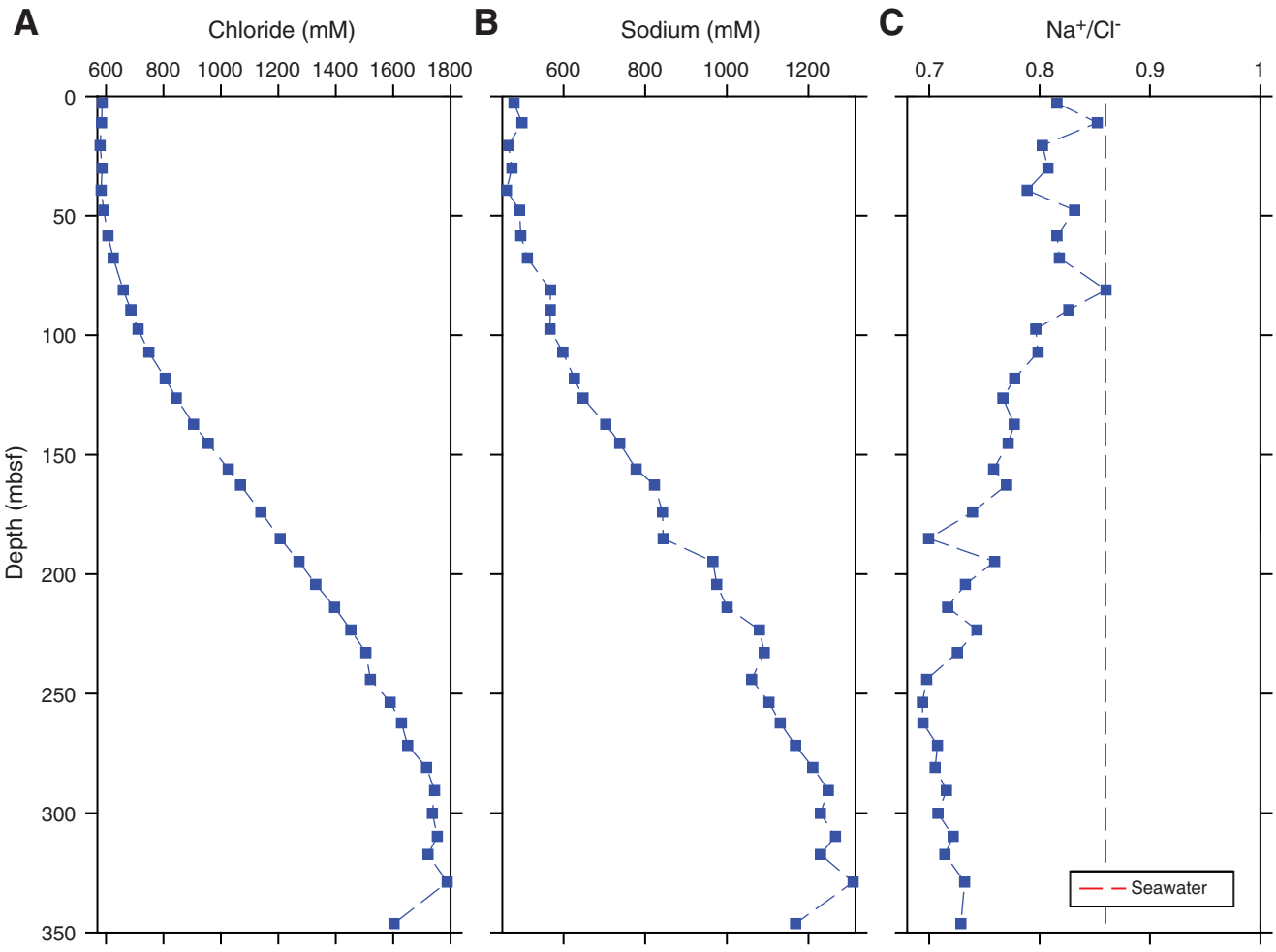

Figure F32. A–C. Plots of interstitial water barium, boron, and iron, Hole U1390A.

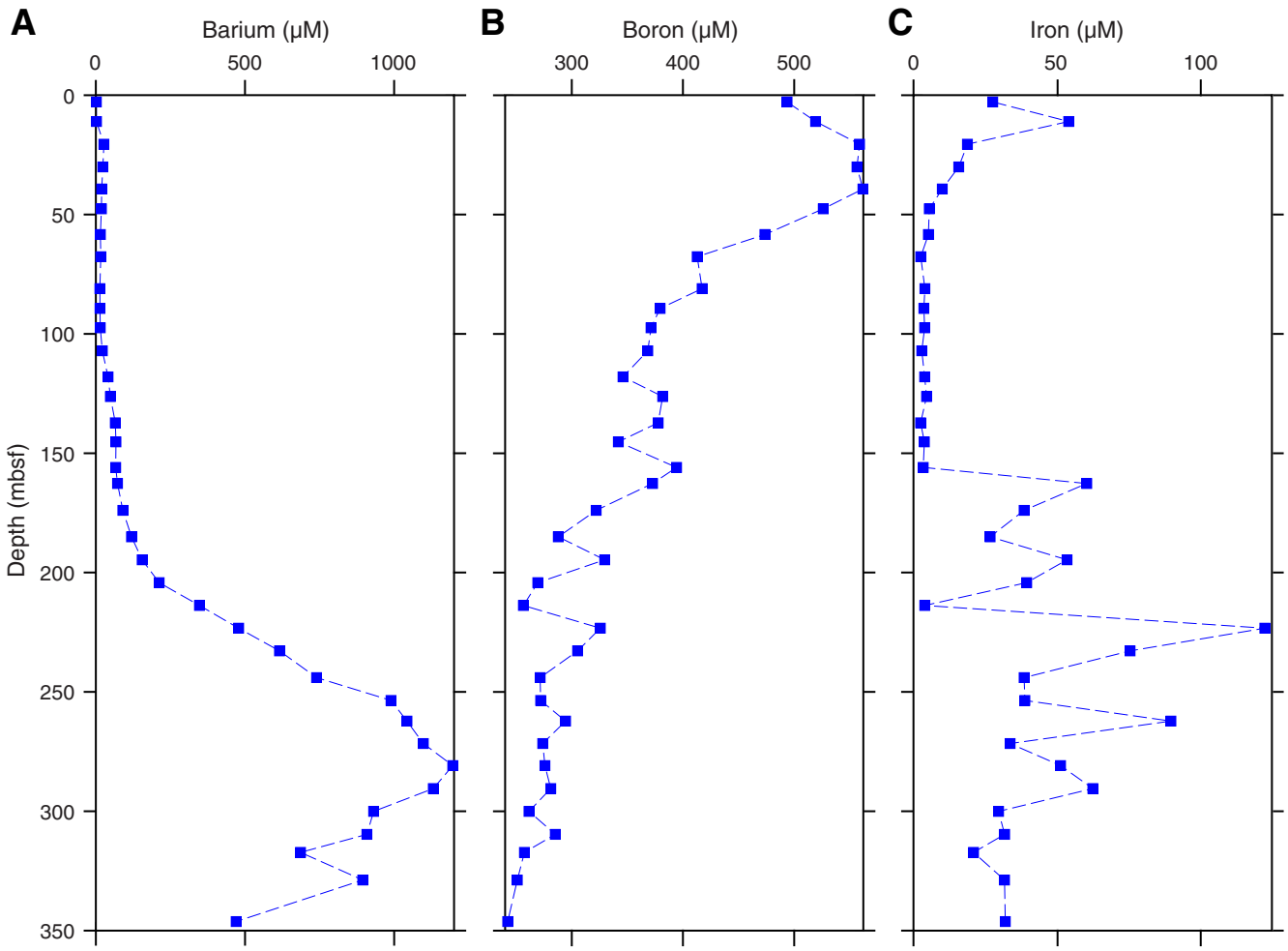

Figure F33. A–C. Plots of interstitial water lithium, silicon, and strontium, Hole U1390A.

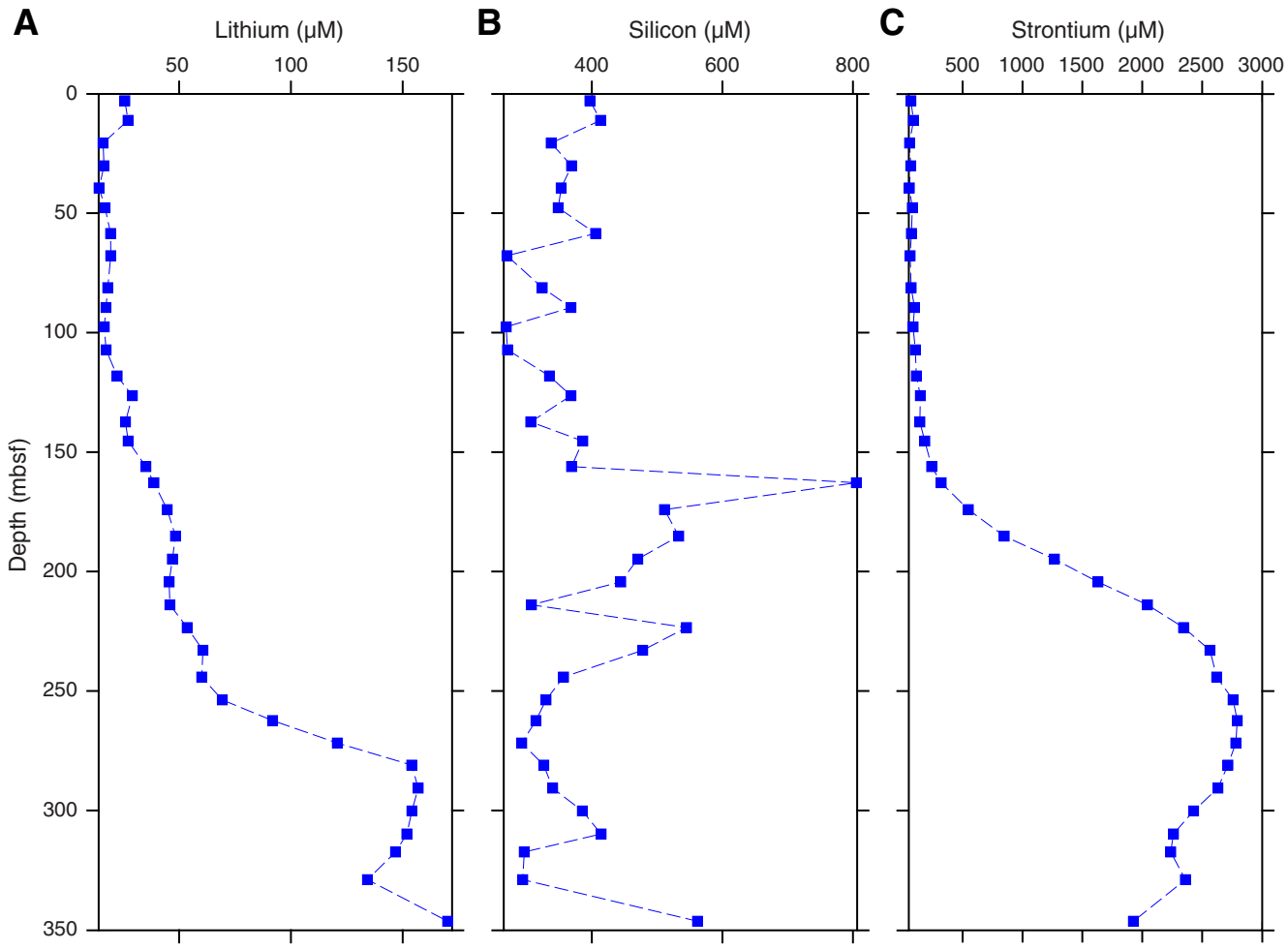

Figure F34. A–C. Plots of interstitial water stable isotopes and chloride concentration, Site U1390. VSMOW = Vienna Standard Mean Ocean Water.

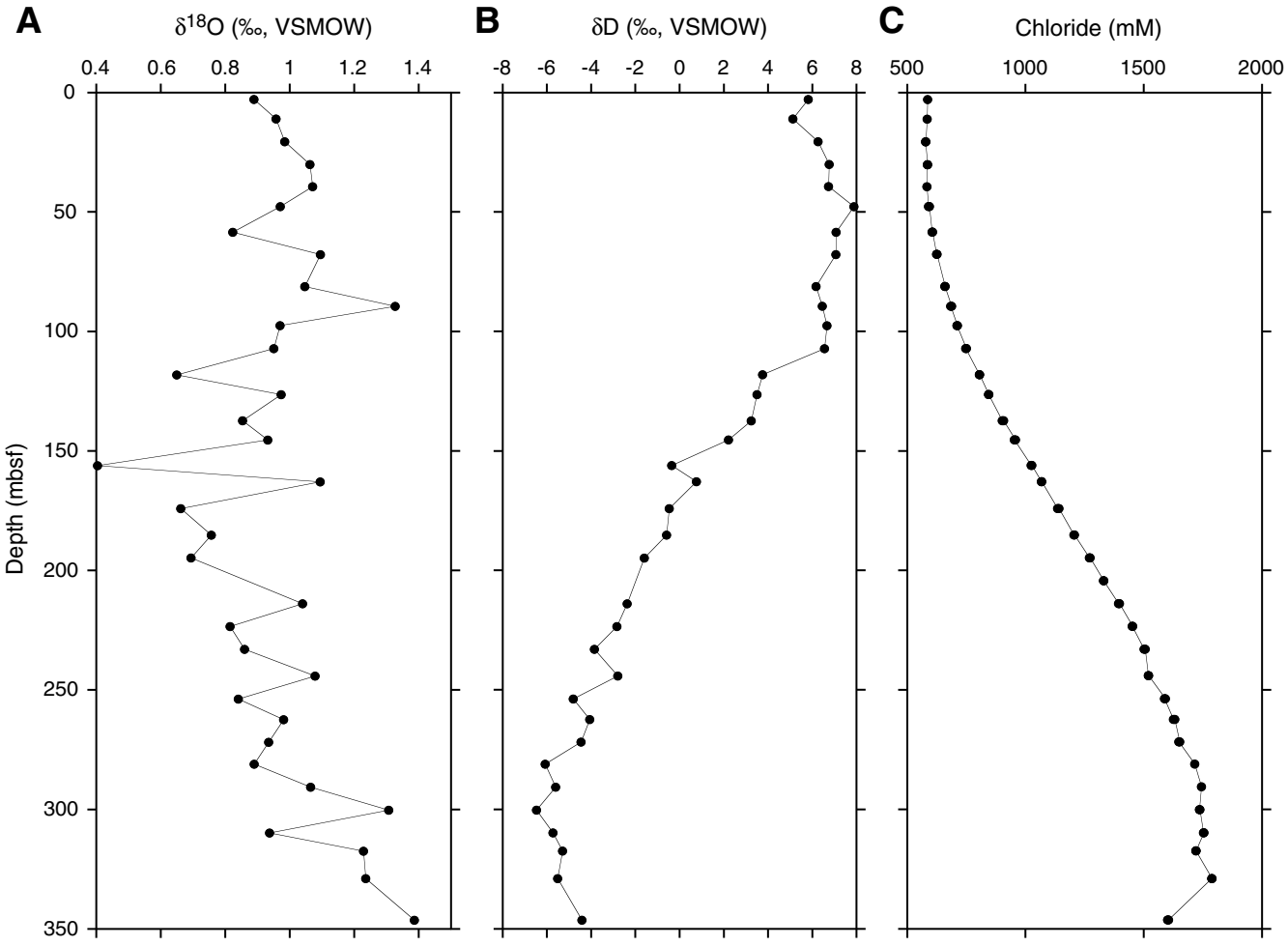

Figure F35. Plot of chloride vs. δD, Site U1390. VSMOW = Vienna Standard Mean Ocean Water.

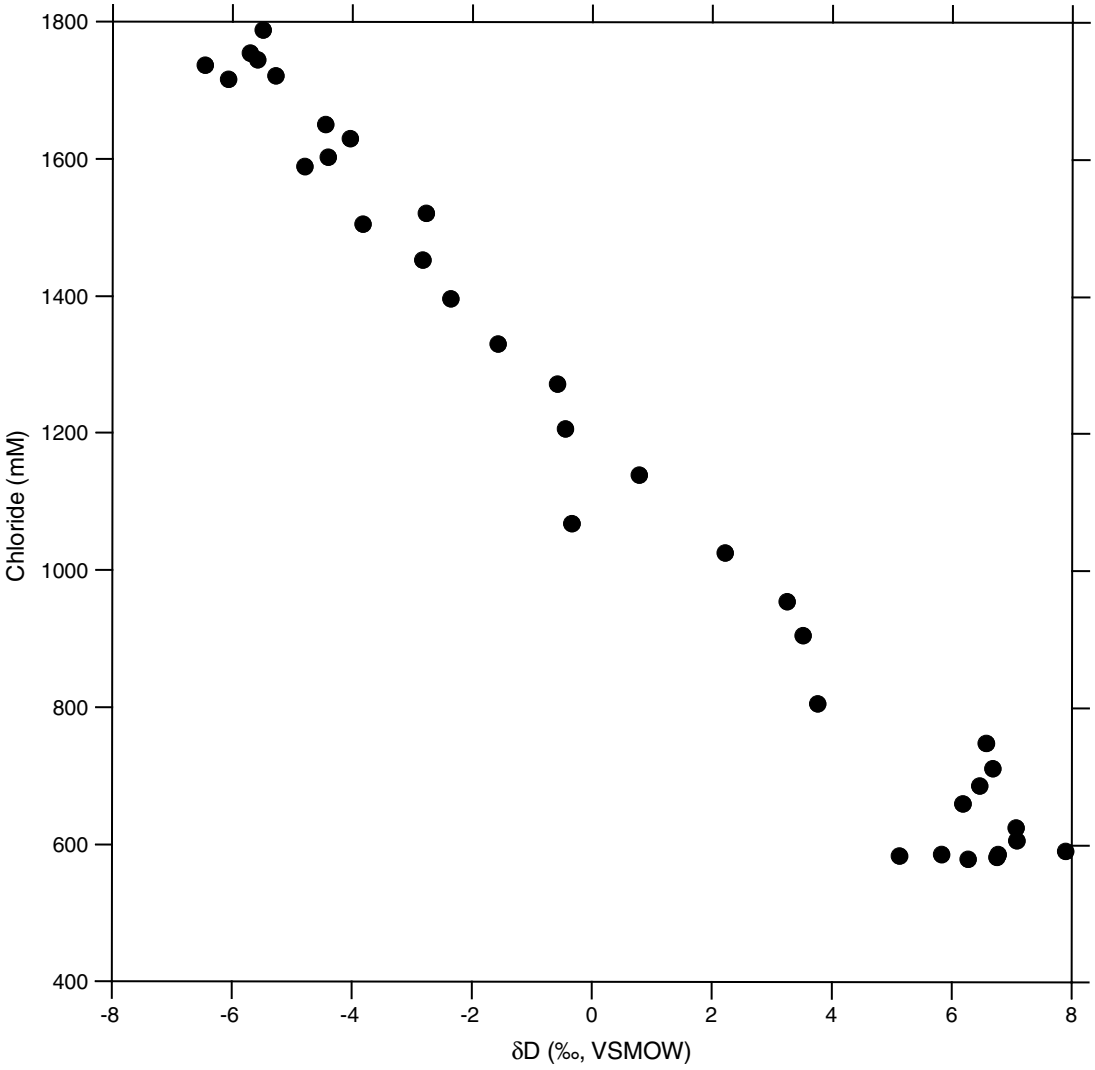

Figure F36. Logging operations summary diagram, Hole U1390A. FMS = Formation MicroScanner.

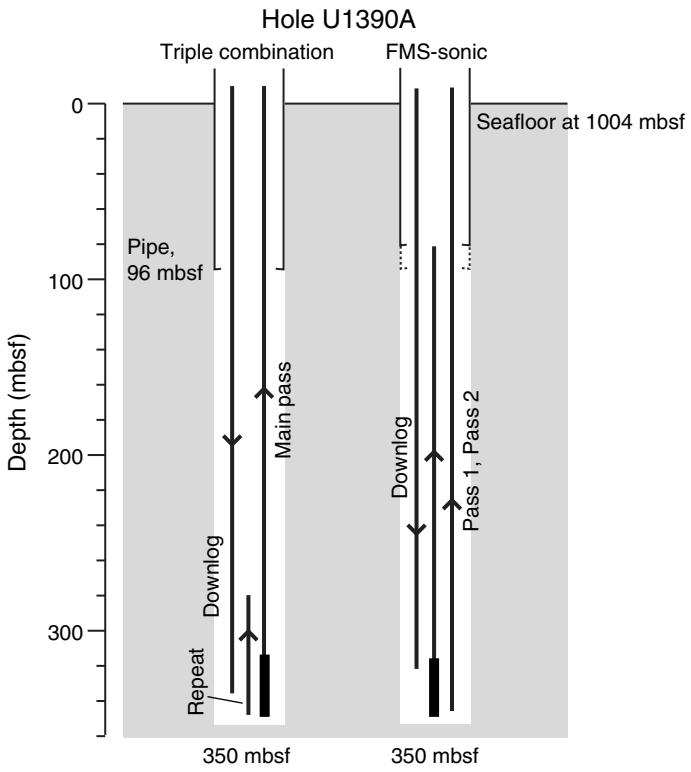

Figure F37. Plots of tides and ship heave, Site U1390. Tides were calculated using Tide Model Driver, a Matlab front-end for the Oregon State University Tidal Data Inversion (Egbert and Erofeeva, 2002). Ship heave was derived from acceleration measured by the motion reference unit in the moon pool area. FMS = Formation MicroScanner, APCT-3 = advanced piston corer temperature tool. RMS = root-mean square.

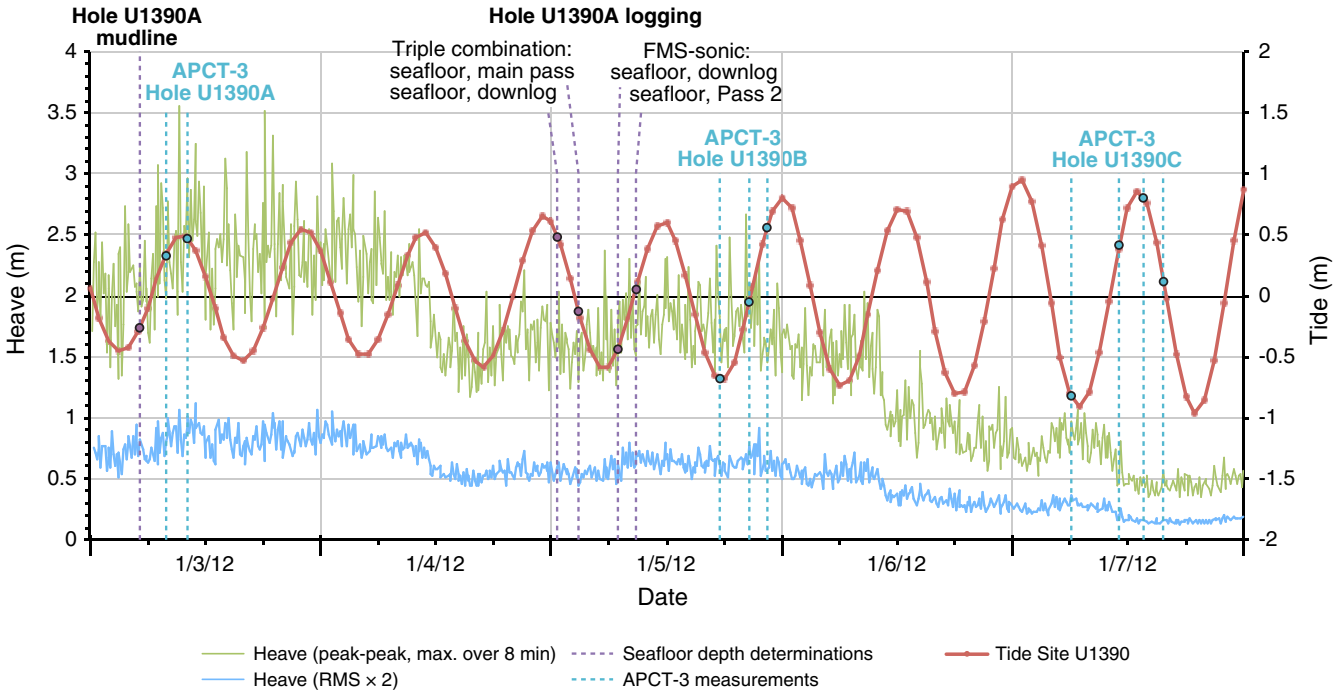

Figure F38. Downhole logs, lithologic units, and logging units, Hole U1390A. HSGR = standard (total) gamma radiation, NGR = natural gamma radiation, RHOM = bulk density, MAD = moisture and density discrete samples, GRA = gamma ray attenuation density, RT = "true" resistivity, PWL = *P*-wave logger.

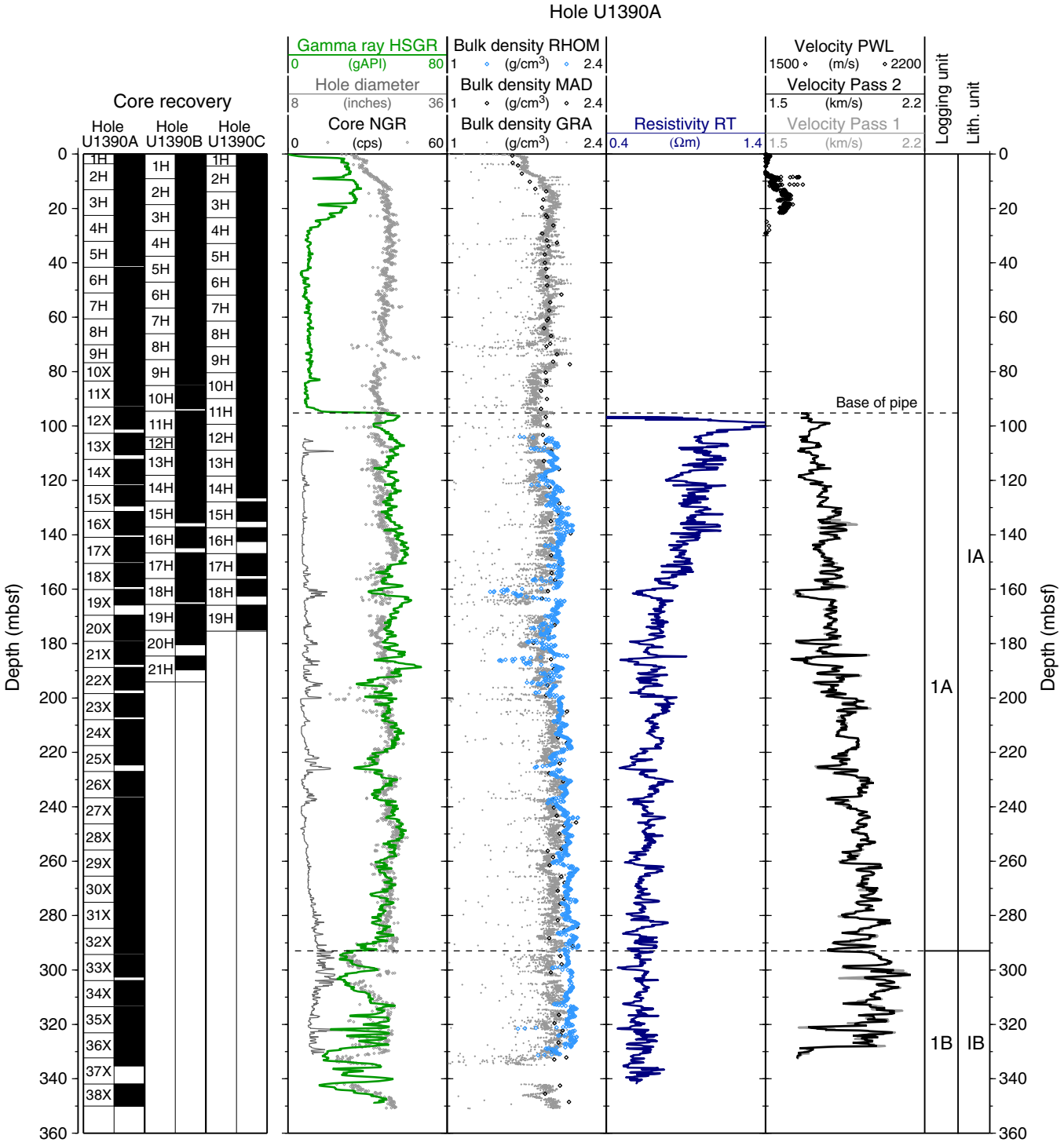

Figure F39. Plot of comparison between the logging standard (total) gamma ray (HSGR) data in Holes U1390A and U1390C and the (five-point average) natural gamma ray (NGR) data in Holes U1390A–U1390C vs. depth. HSGR data has been normalized separately for the interval below and above the end of the drill string.

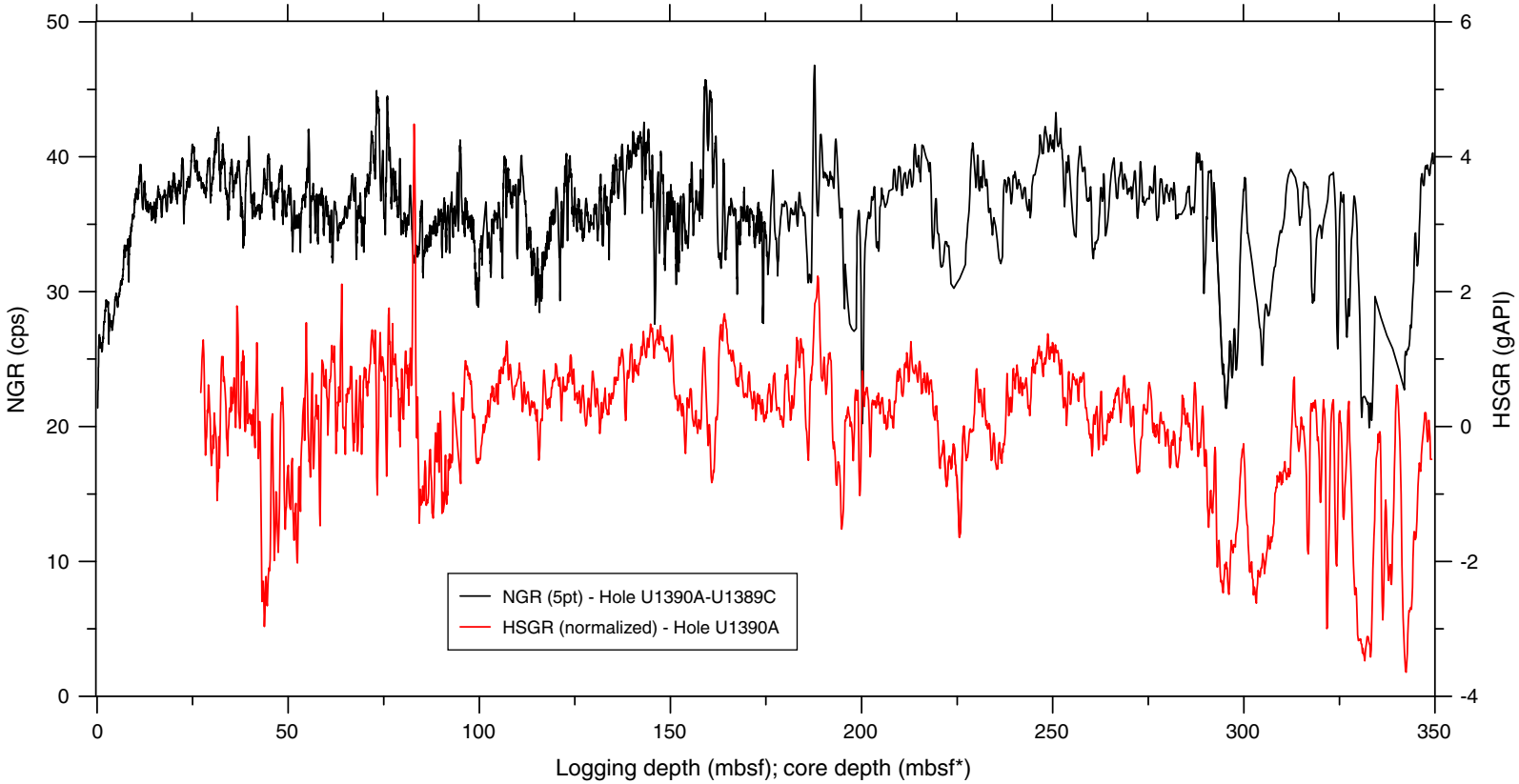

Figure F40. Natural gamma radiation (NGR) logs, lithologic units, and logging units, Hole U1390A. HSGR = standard (total) gamma radiation.

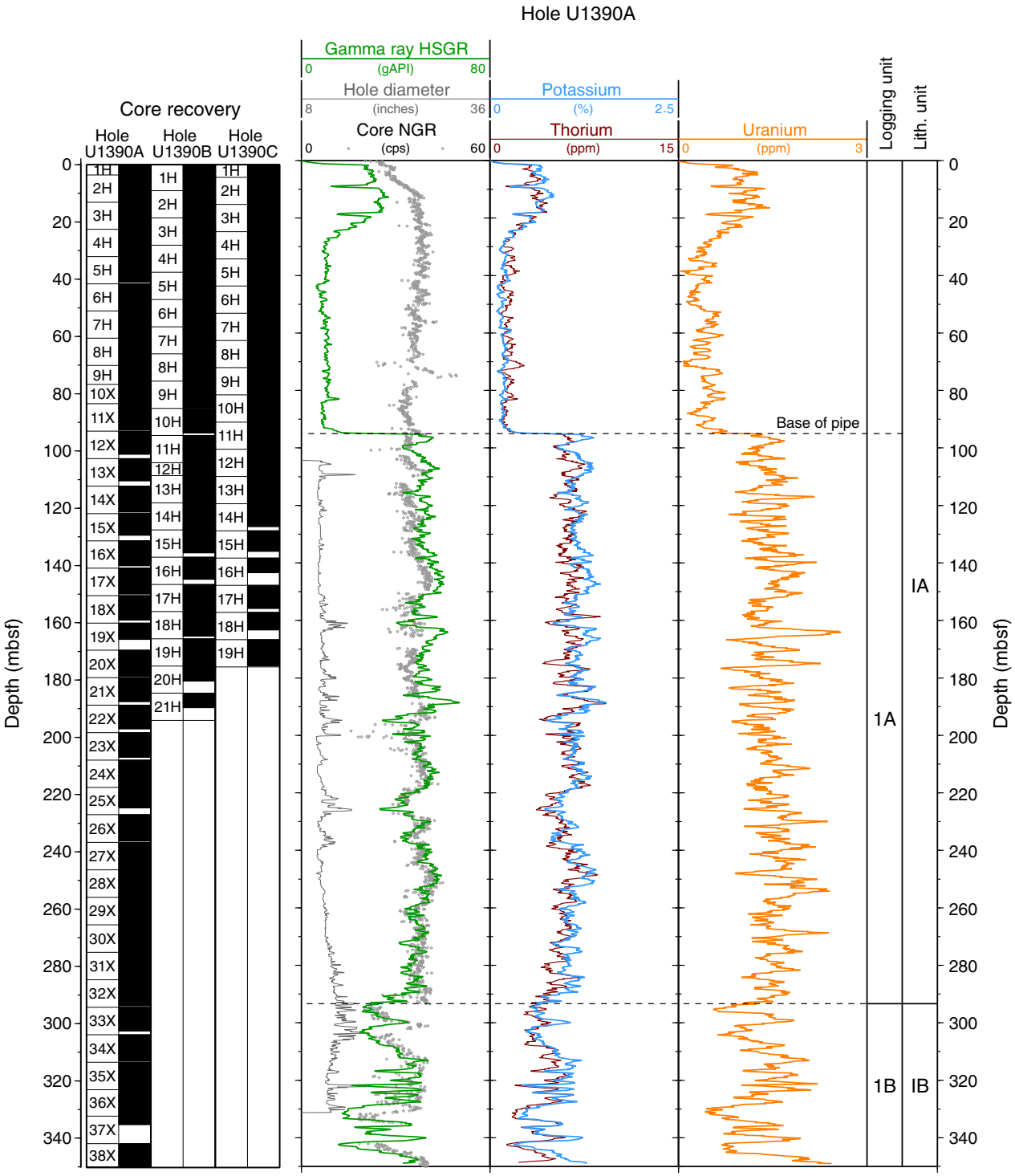

Figure F41. Comparison of downhole logs, Hole U1390A. Note increase of formation conductivity with depth. In logging Subunit 1A, some of the low–standard (total) gamma radiation (HSGR) (~sandier) intervals are less resistive than neighboring clay-rich beds. RHOM = bulk density, RT = "true" resistivity, FMS = Formation MicroScanner.

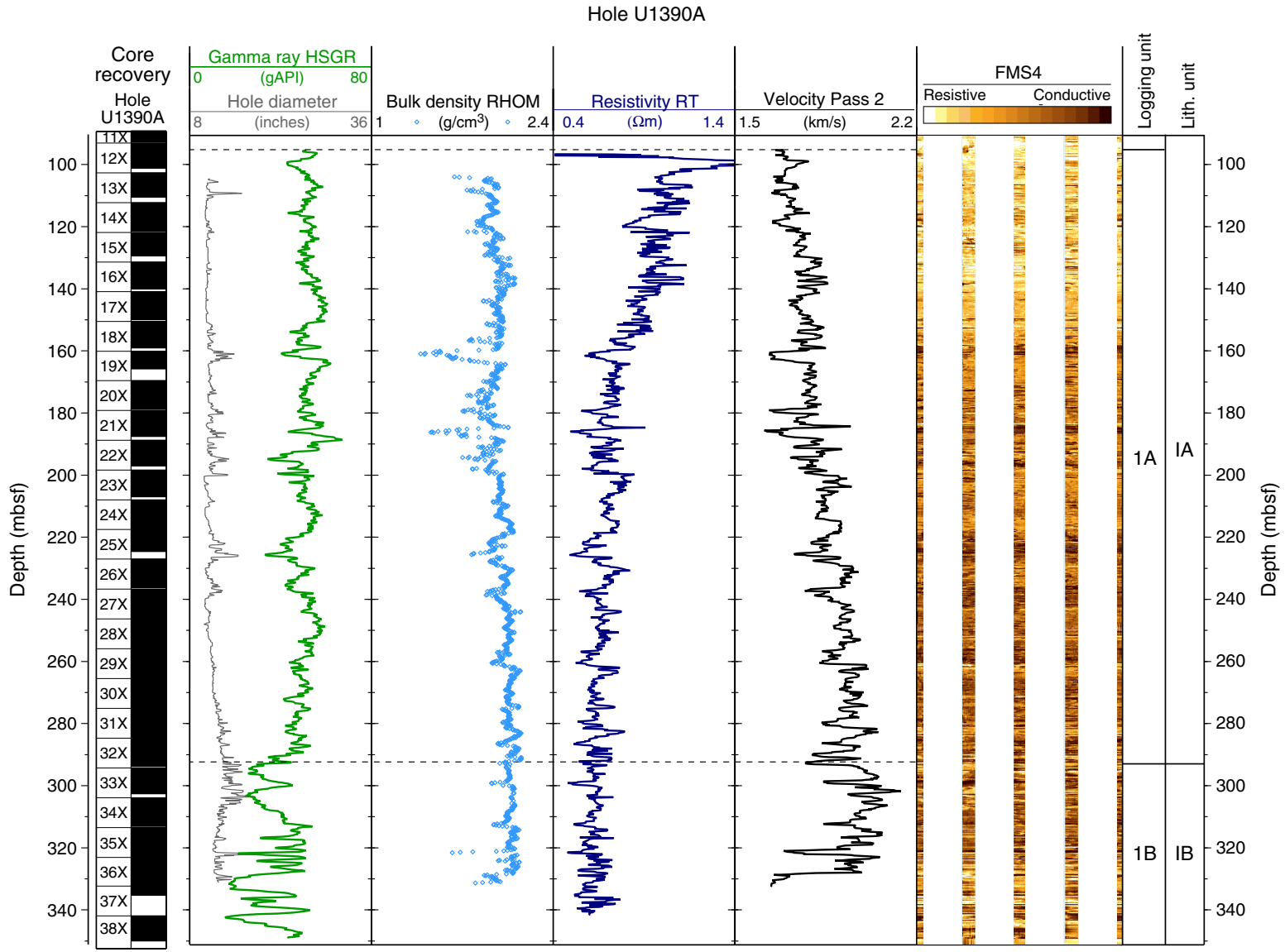

Figure F42. Correlation of downhole logs and lithology (240–253 mbsf) in Hole U1390A indicates that sand-rich layers have lower natural gamma radiation (NGR) and are more resistive than neighboring clay-rich beds (in contrast to some of the low–standard (total) gamma radiation [HSGR] layers in Subunit 1A). WRMSL = Whole-Round Multisensor Logger, HROM = high-resolution bulk density log, RT = "true" resistivity, FMS = Formation MicroScanner.

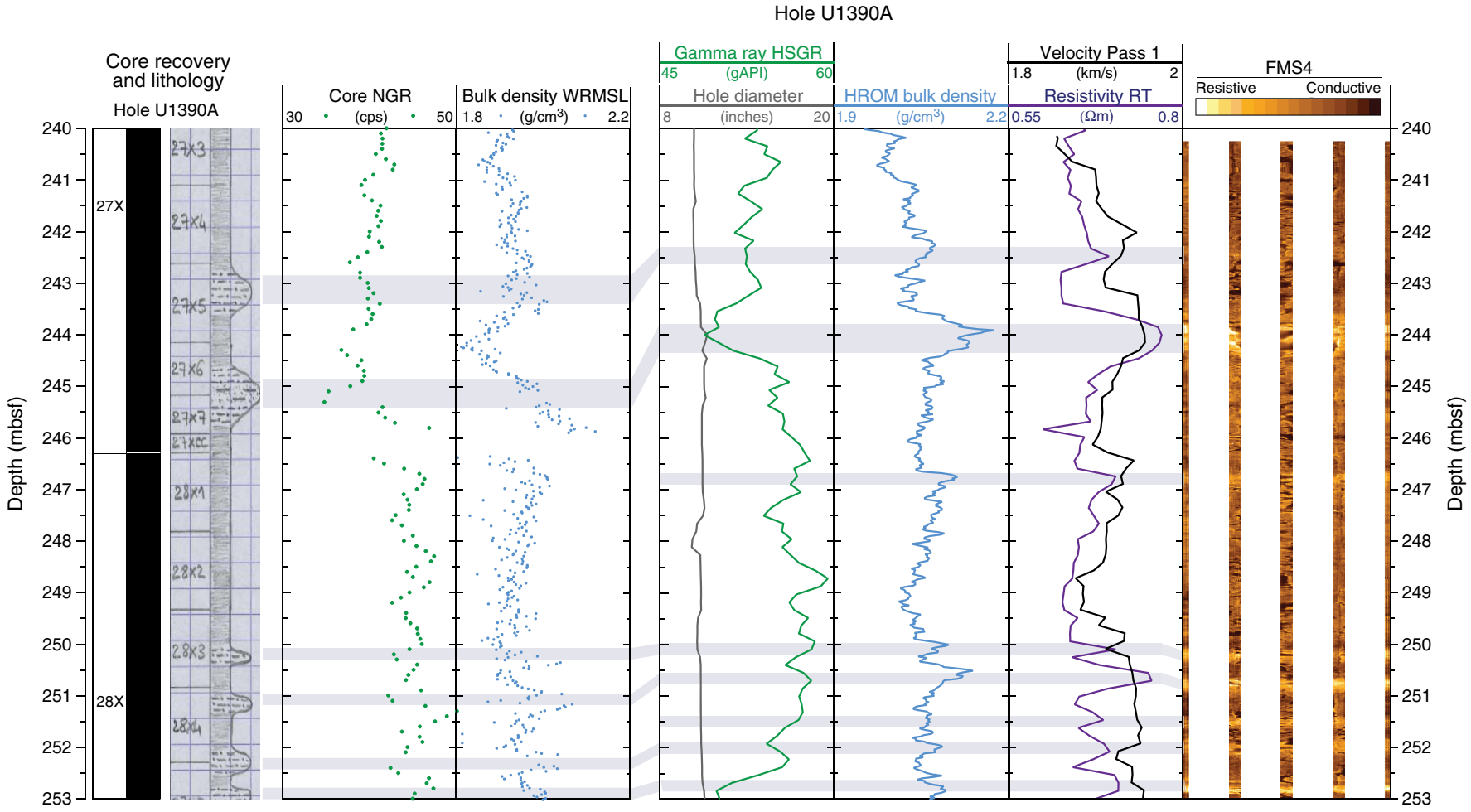

Figure F43. Plots of sonic velocity and two-way traveltime (TWT) data, Hole U1390A. TWT was calculated from Pass 2 sonic velocity data and extended upward to the seafloor using a linear trend between 0 and 96 mbsf.

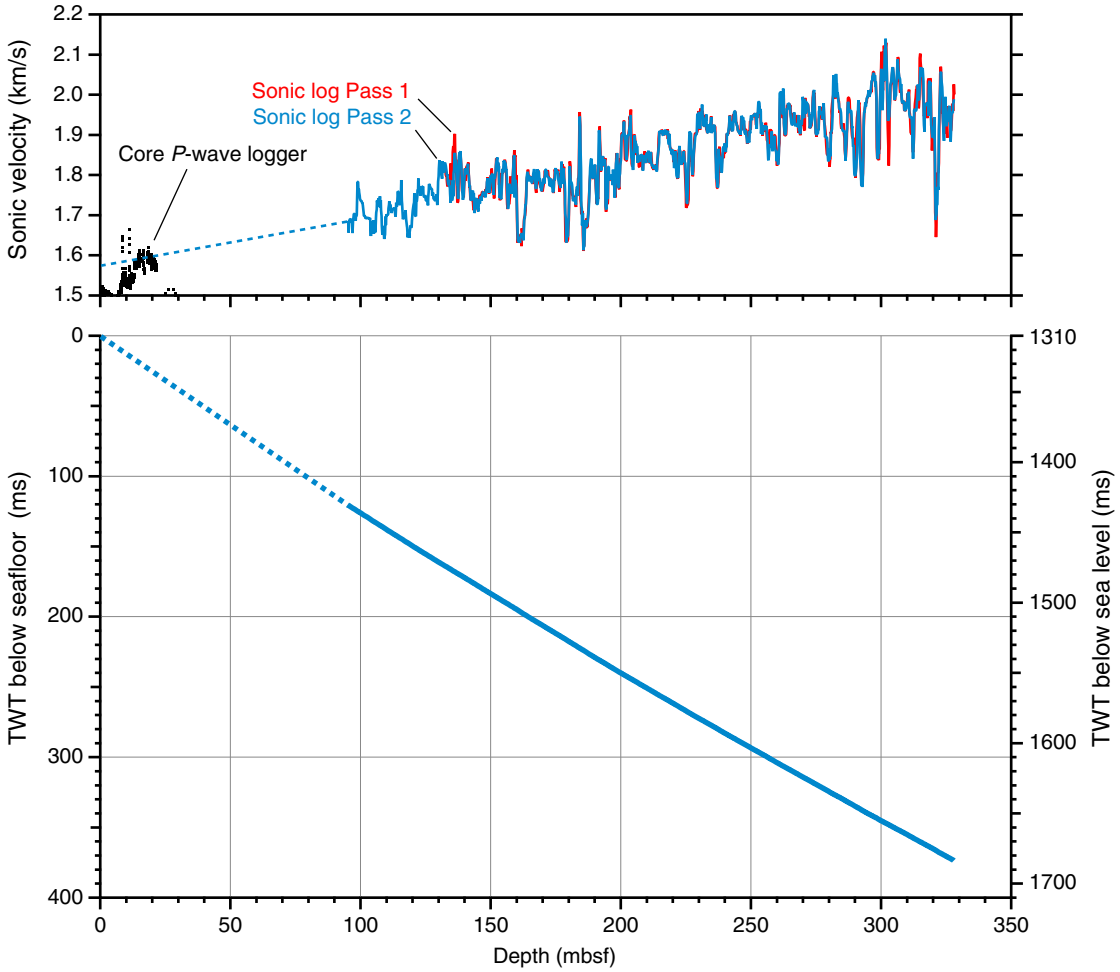

Figure F44. Plots of heat flow calculations, Site U1390. **A.** Sediment temperatures in Holes U1390A (blue), U1390B (yellow), and U1390C (purple). **B.** Thermal conductivity data from Hole U1390A (circles) with calculated thermal resistance (solid line). **C.** Bullard plot of heat flow calculated from a linear fit of the temperature data.

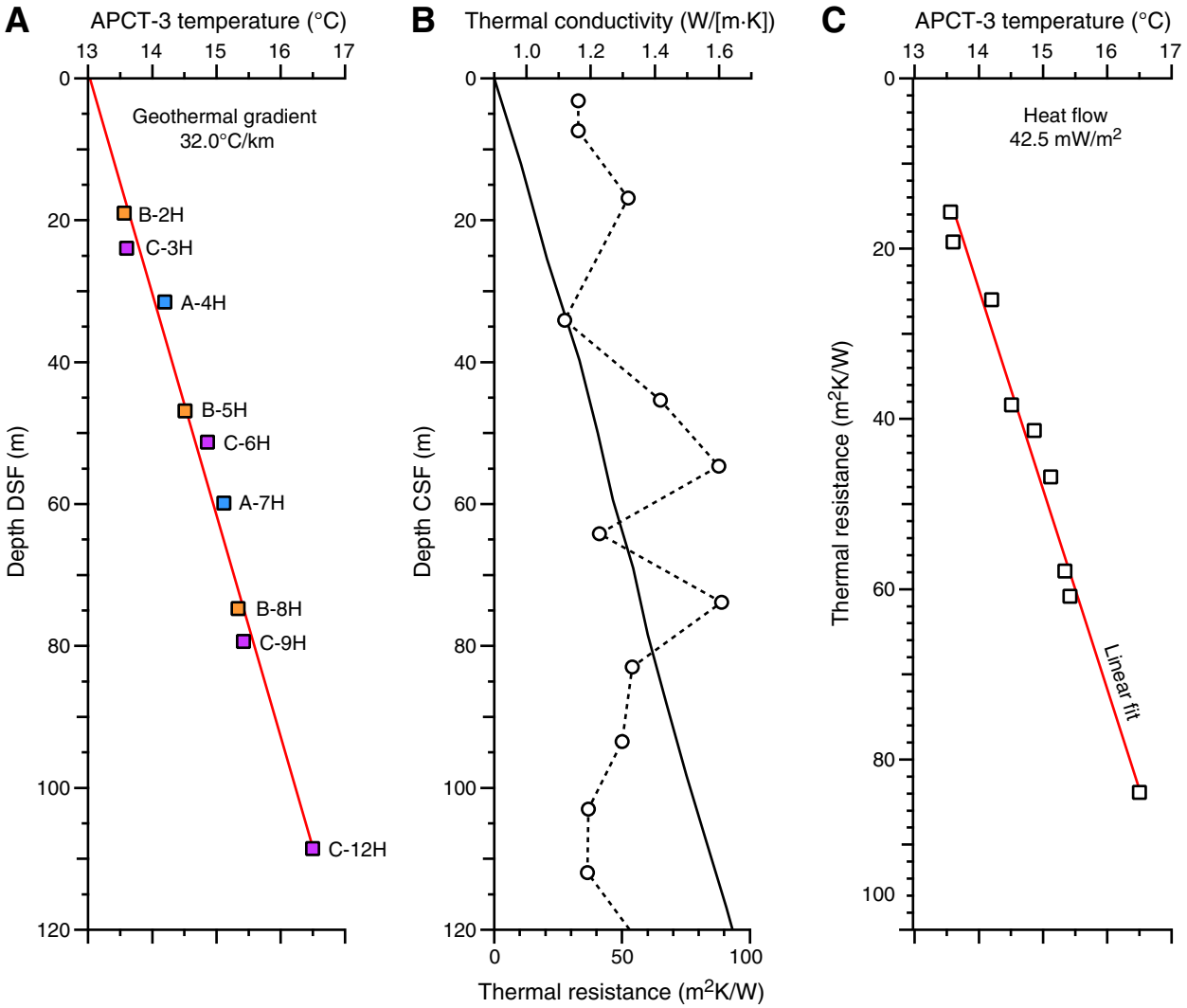

Figure F45. Plot of advanced piston corer temperature tool (APCT-3) temperature-time series with extrapolated formation temperature estimates, Site U1390. APC = advanced piston corer.

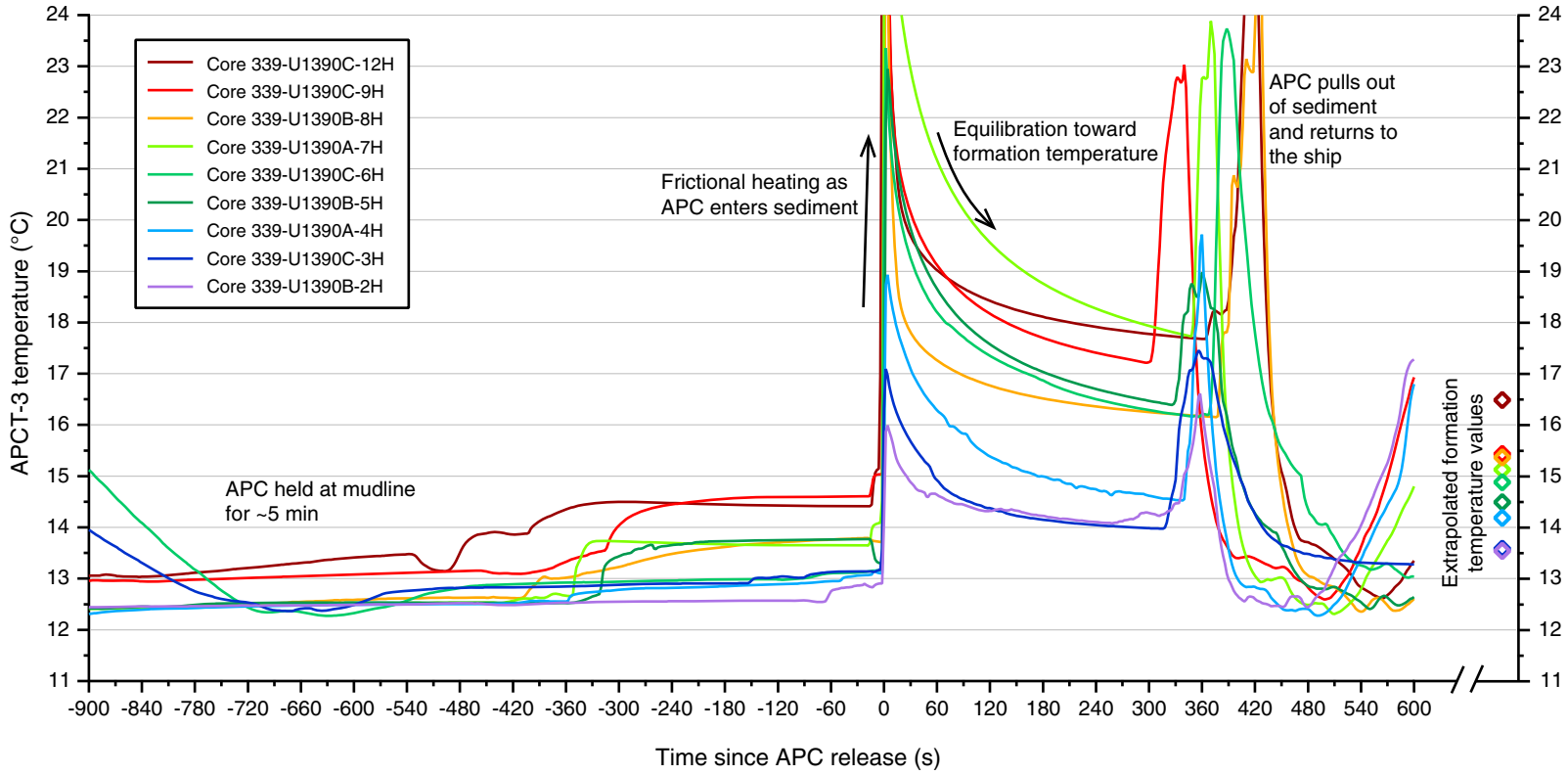

Figure F46. Plots of magnetic susceptibility vs. meters composite depth, Site U1390. In the lower panel, susceptibility values for Holes U1390B and U1390C are shifted for display purposes. **A.** 0–40 mcd. (Continued on next nine pages.)

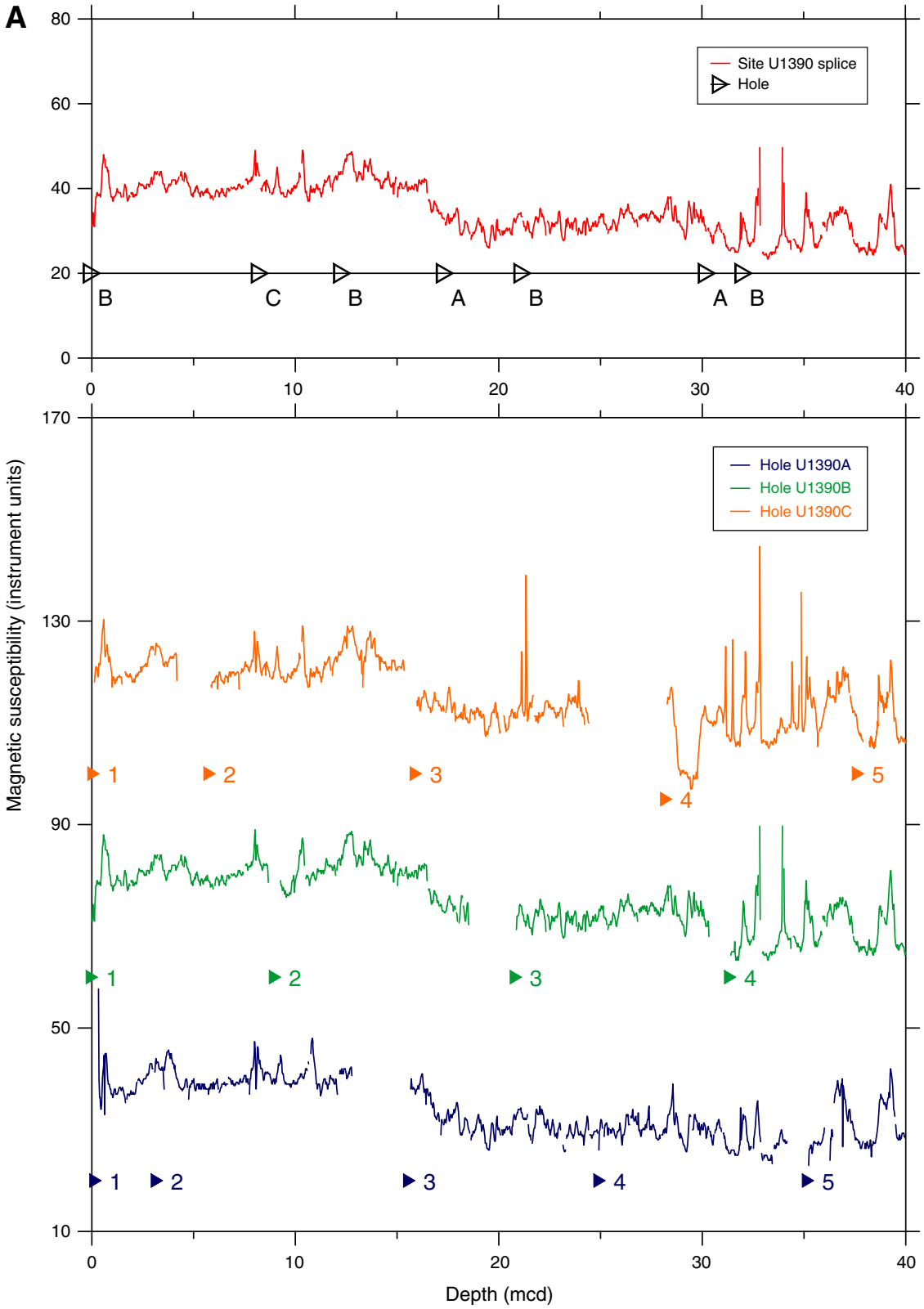

Figure F46 (continued). B. 40–80 mcd. (Continued on next page.)

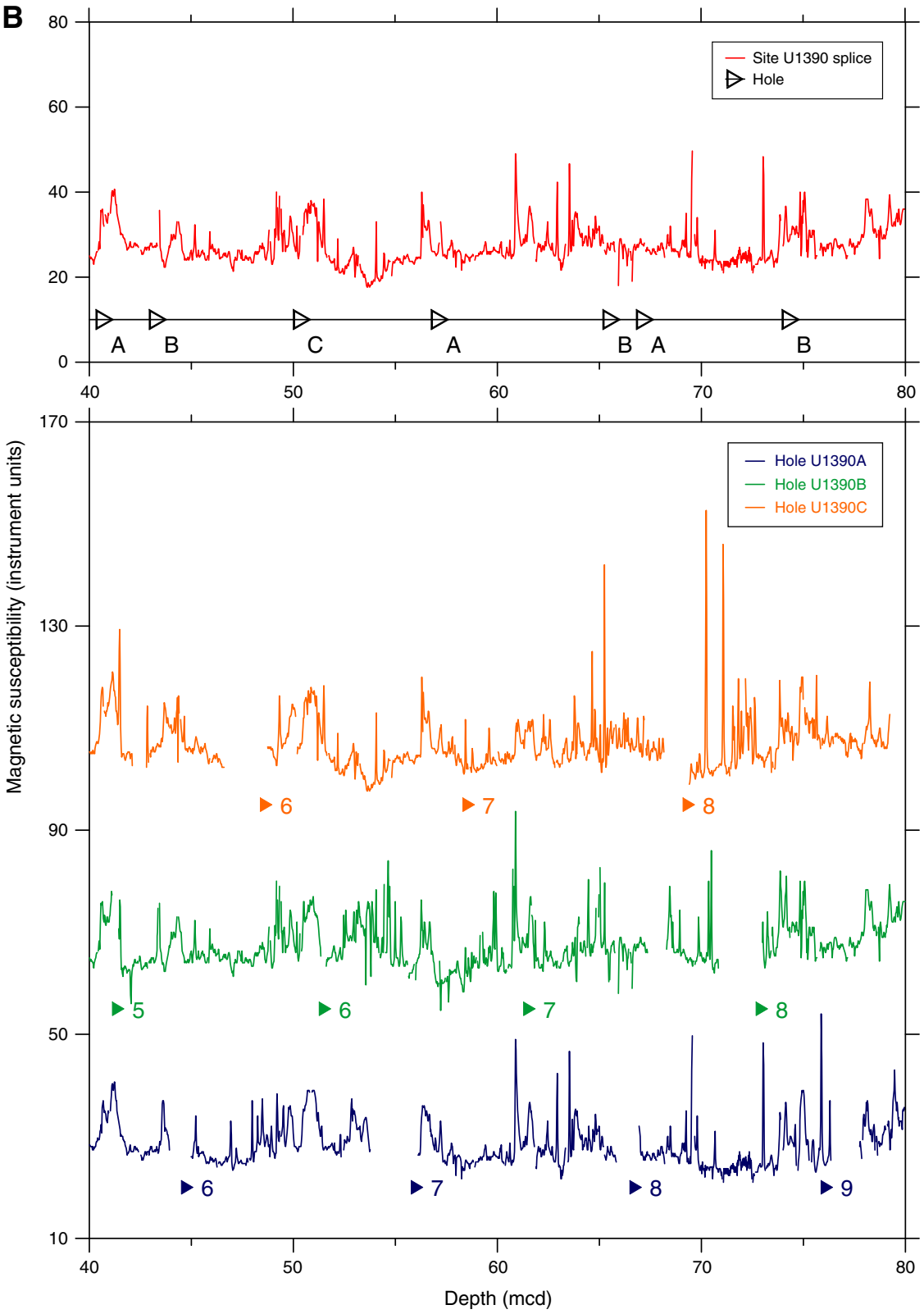

Figure F46 (continued). C. 80–120 mcd. (Continued on next page.)

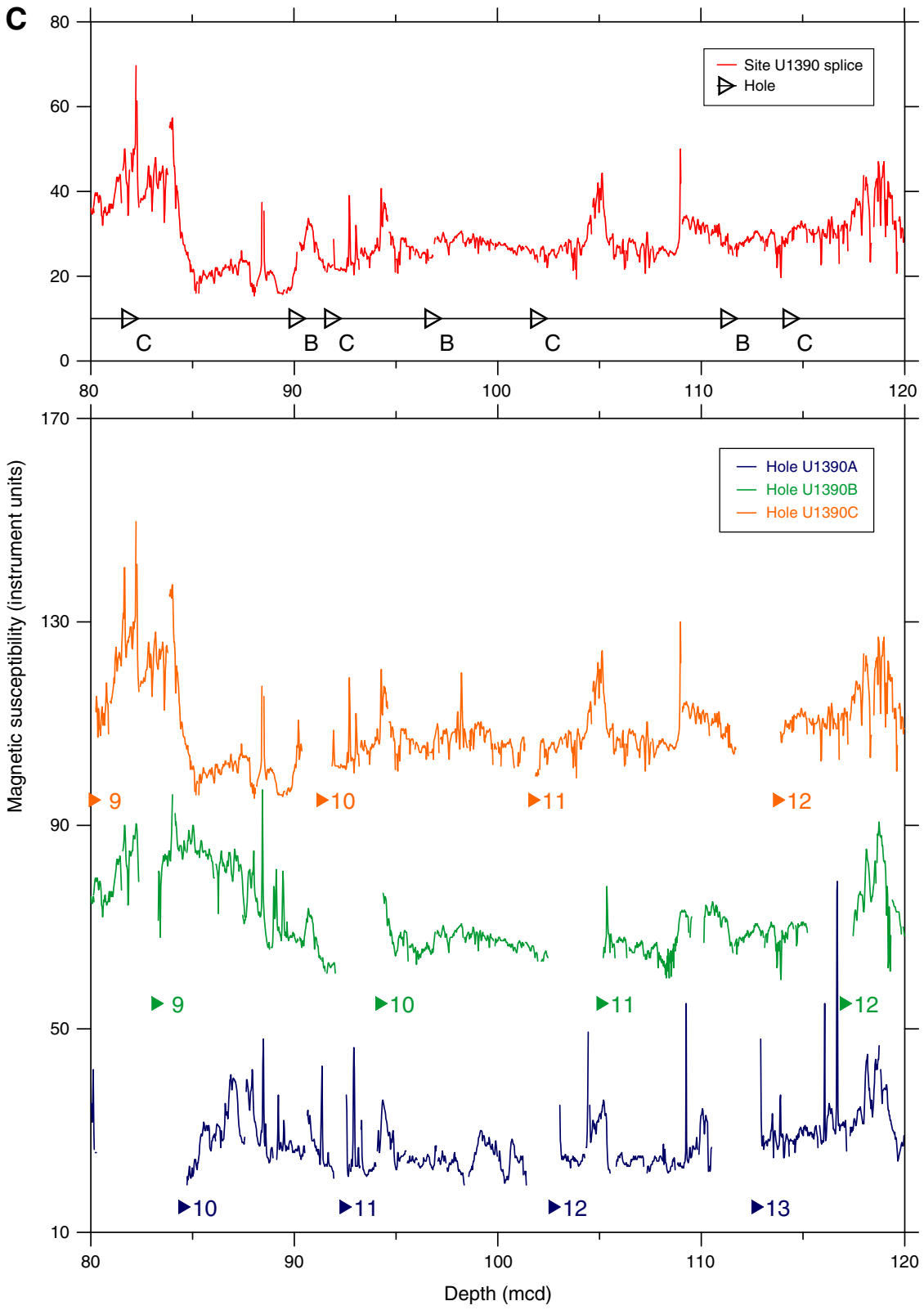

Figure F46 (continued). D. 120–160 mcd. (Continued on next page.)

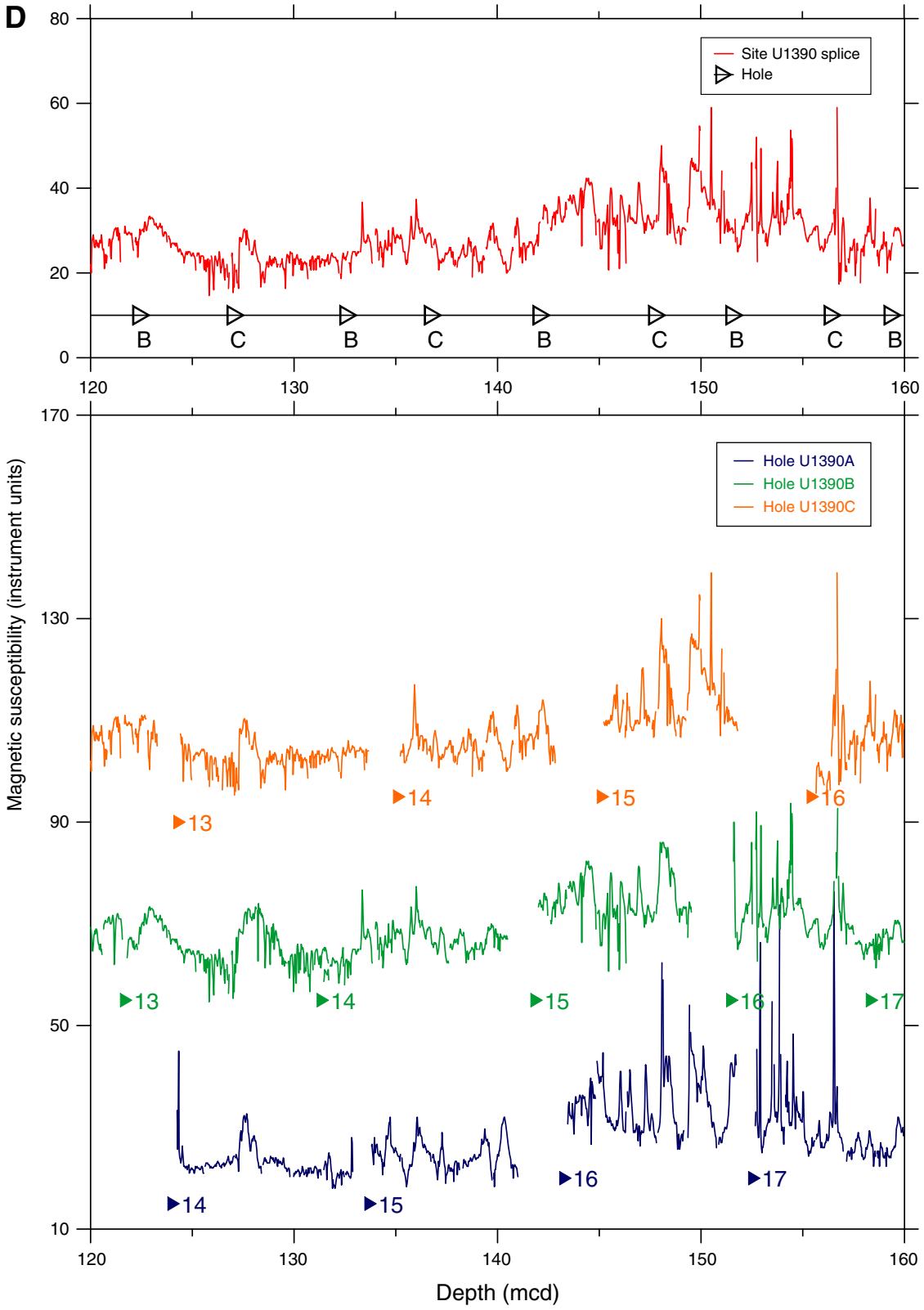

Figure F46 (continued). E. 160–200 mcd. (Continued on next page.)

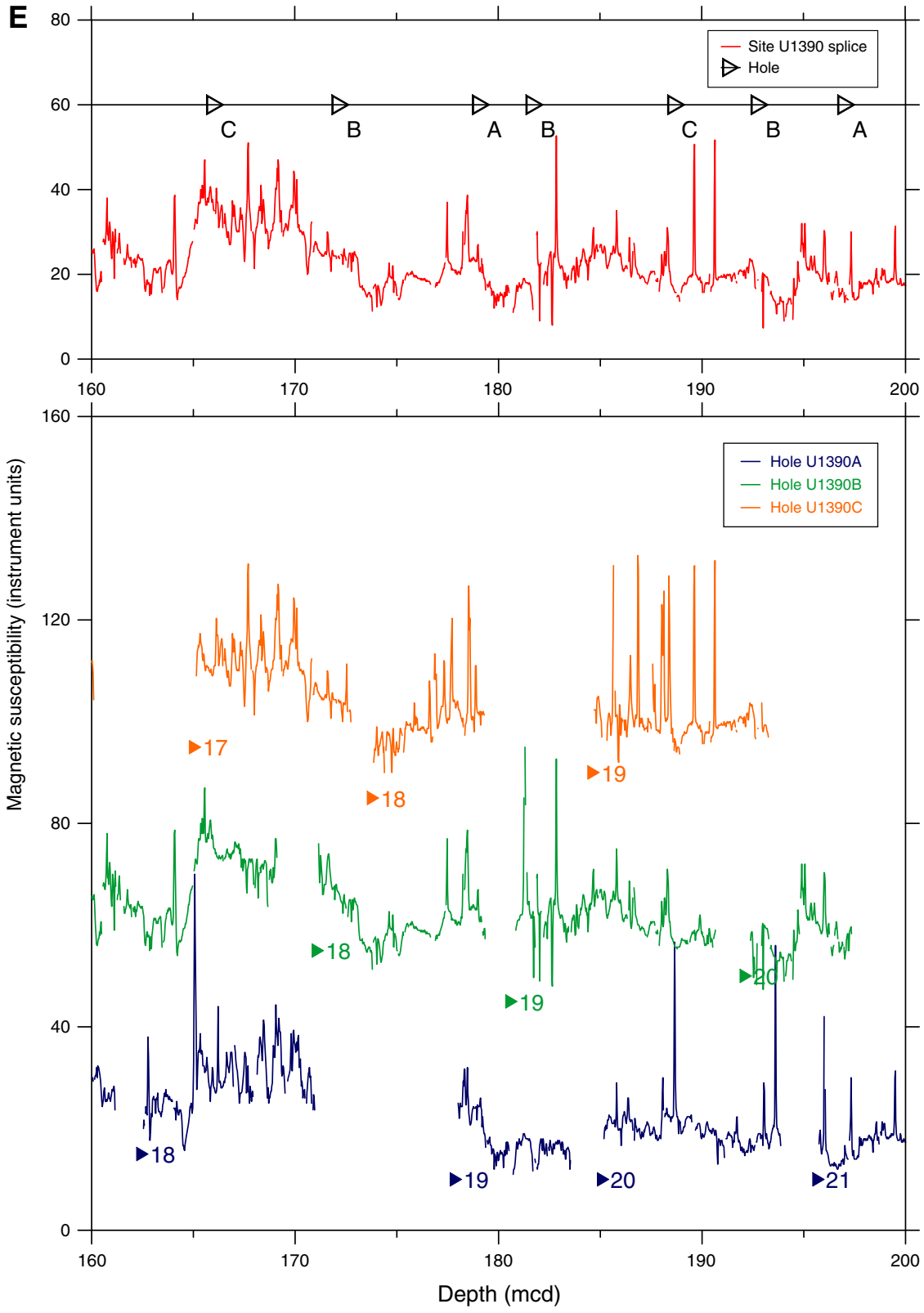

Figure F46 (continued). F. 200–240 mcd. (Continued on next page.)

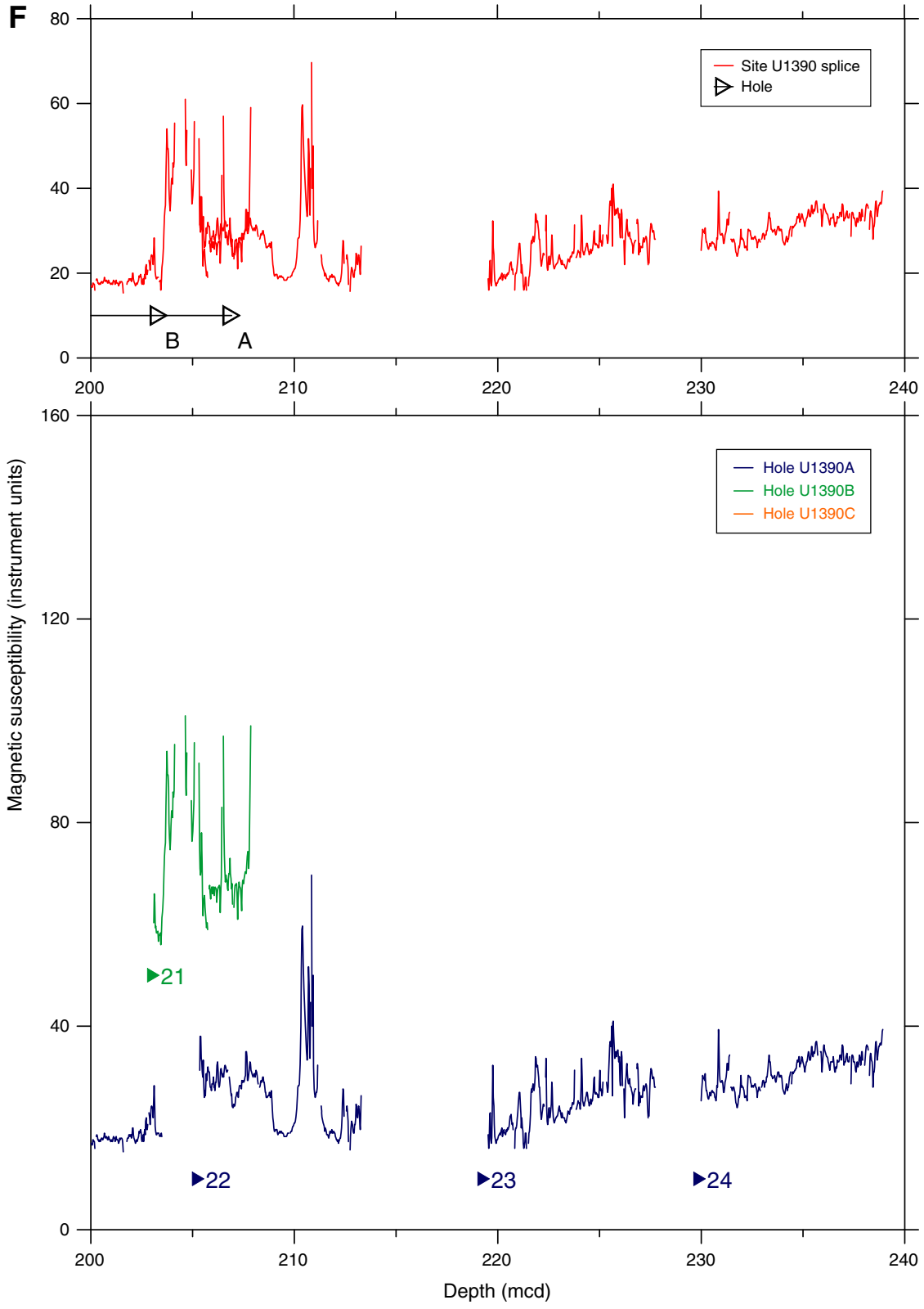

Figure F46 (continued). **G.** 240–280 mcd. (Continued on next page.)

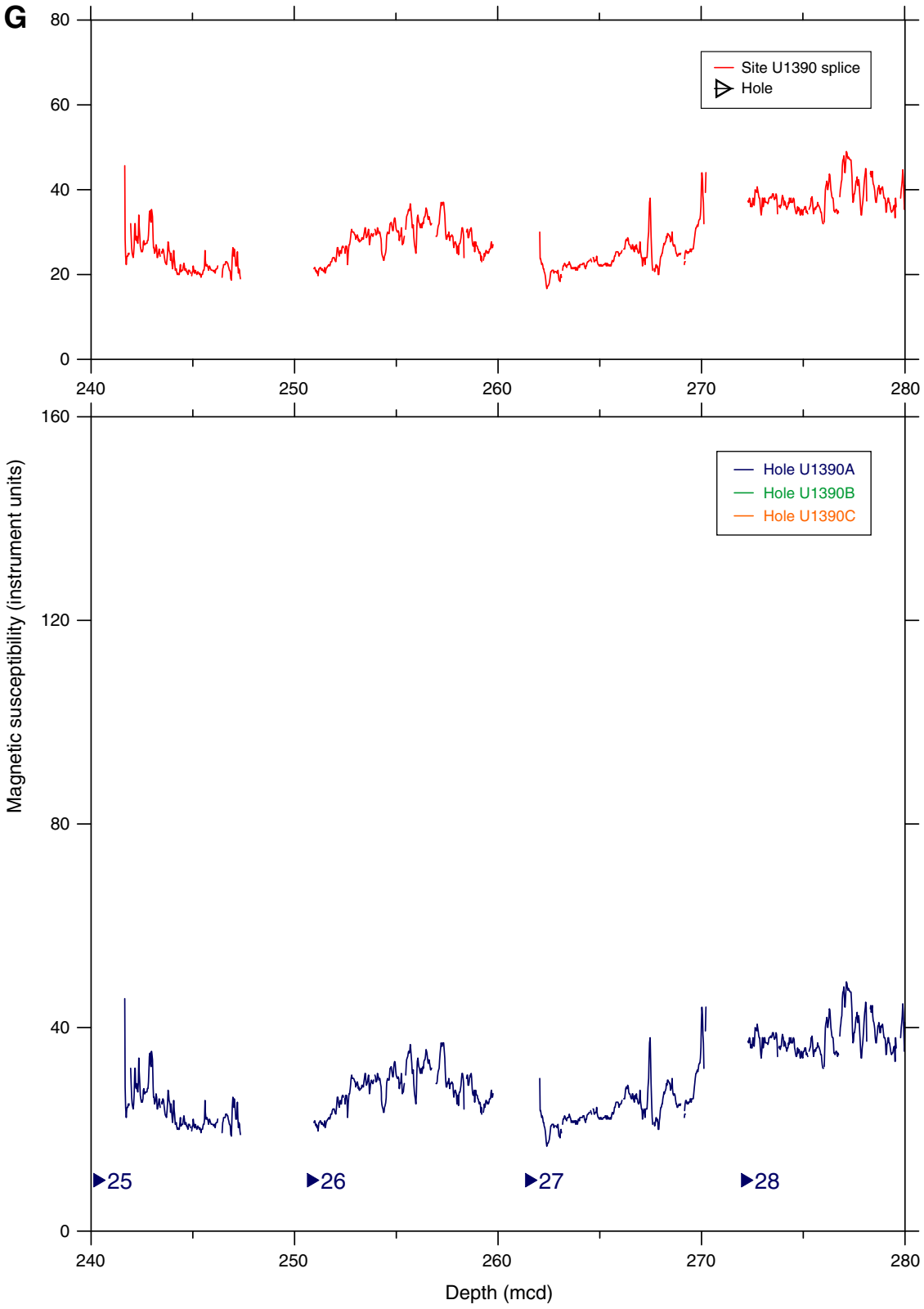

Figure F46 (continued). H. 280–320 mcd. (Continued on next page.)

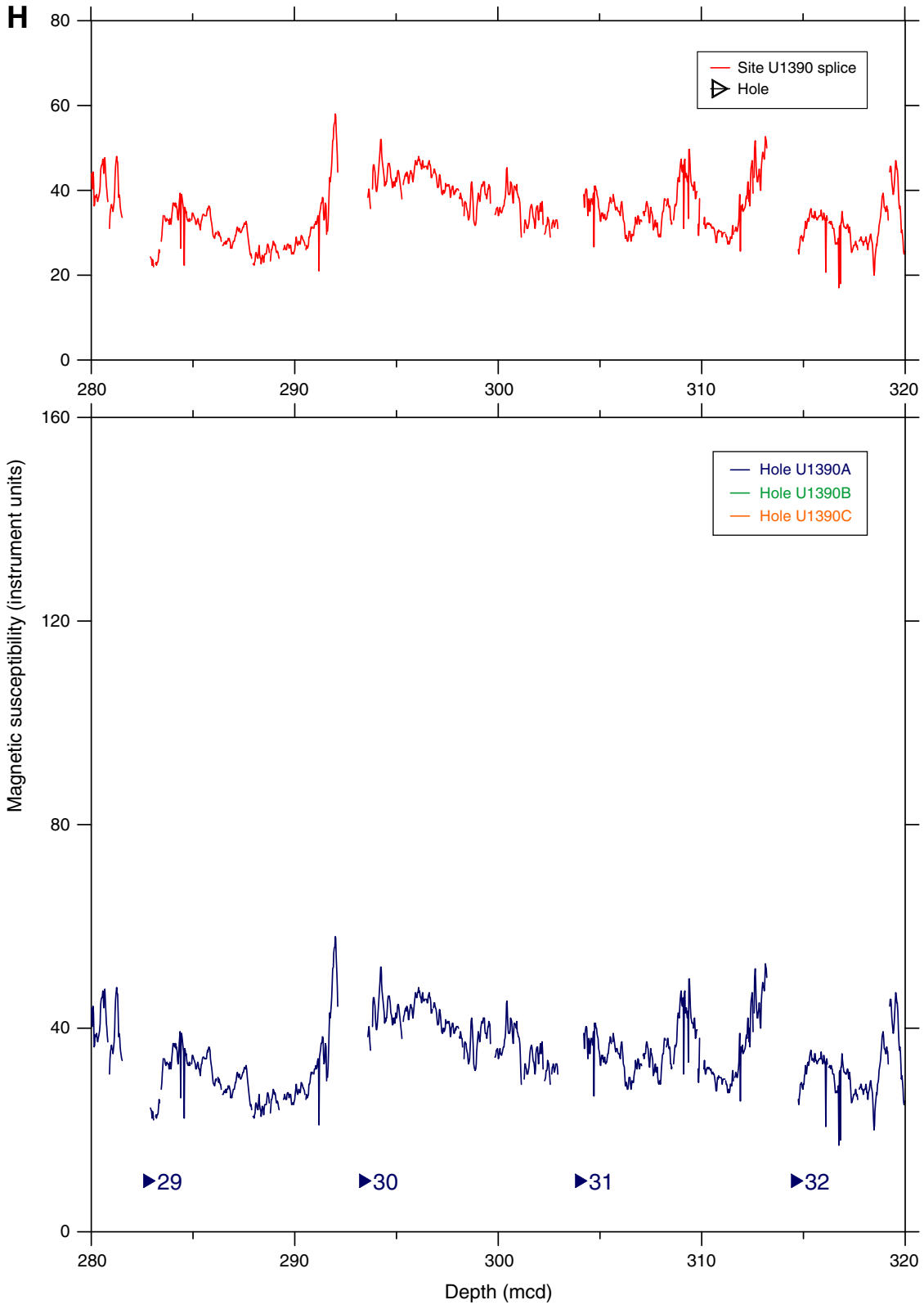

Figure F46 (continued). I. 320–360 mcd. (Continued on next page.)

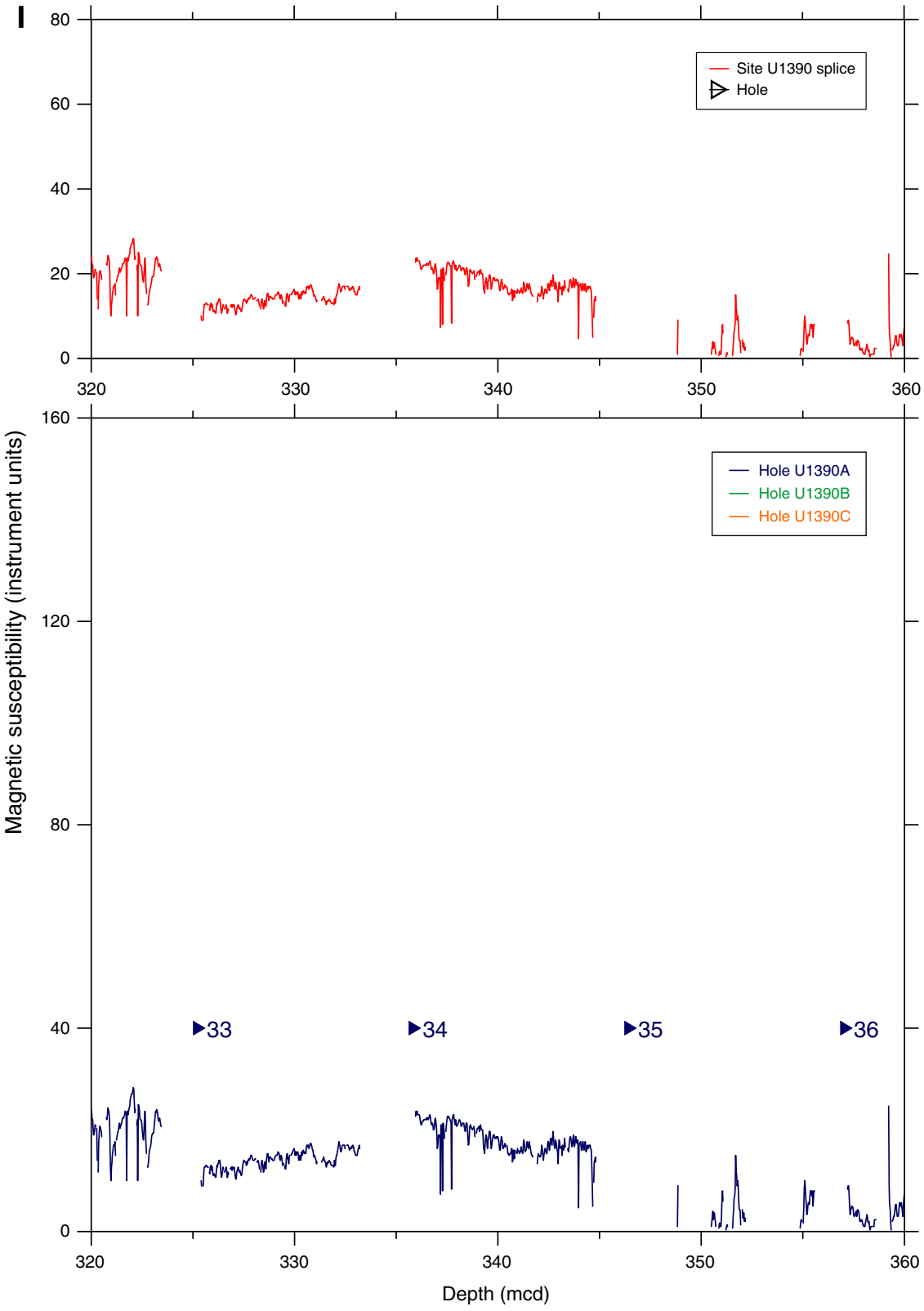

Figure F46 (continued). J. 360–400 mcd.

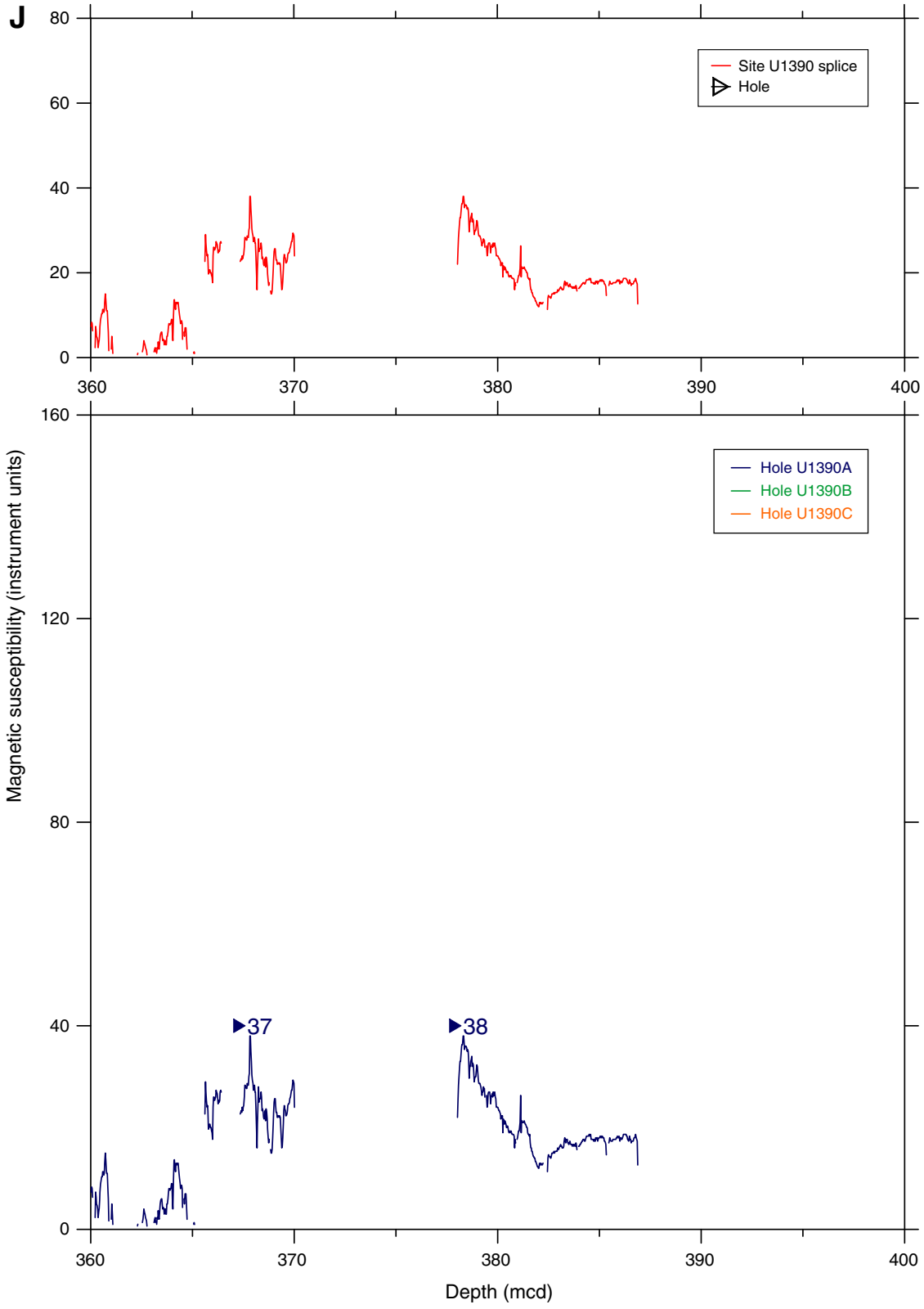

Figure F47. Plot of core top depths for mbsf vs. mcd. The best-fit line (not shown) through all data is for 9.9% expansion, and the expansion for individual Holes U1390A–U1390C are 9.4%, 10.1%, and 12.8%, respectively.

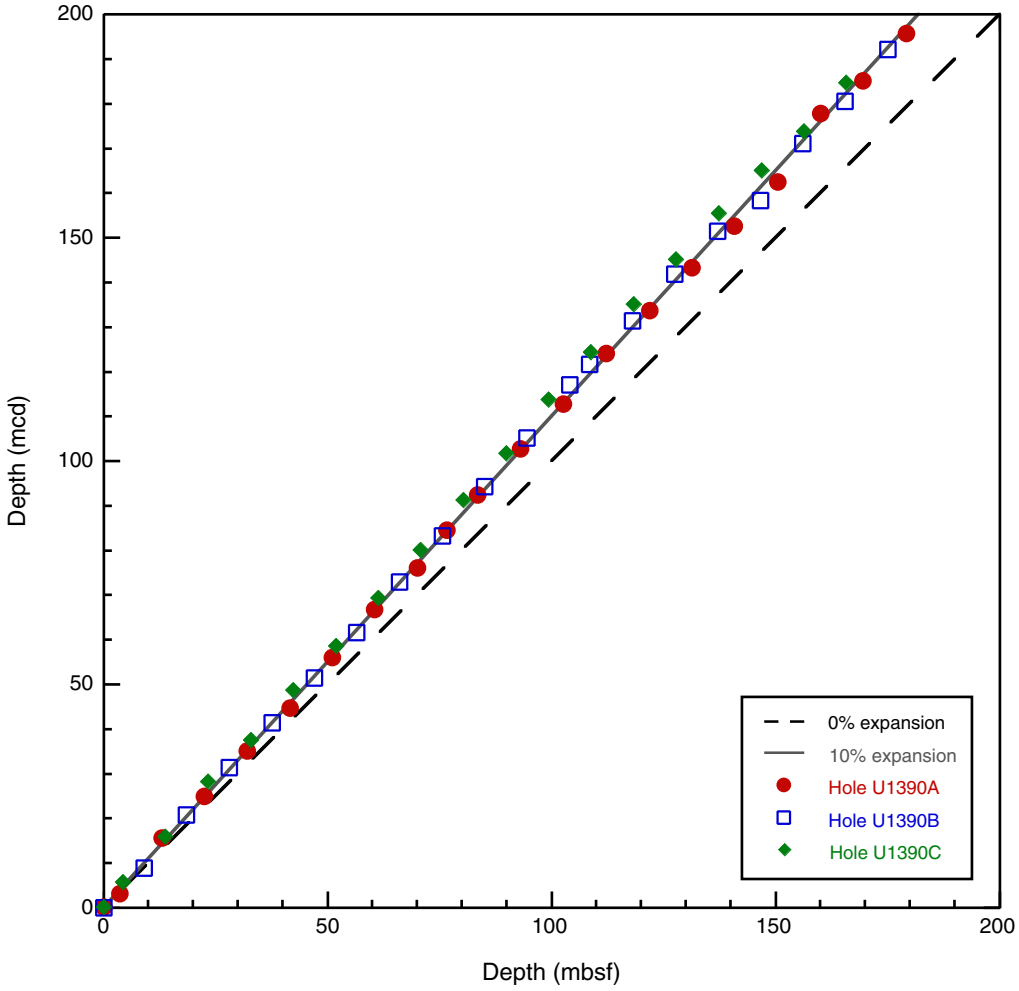

Table T1. Coring summary, Site U1390. (Continued on next page.)

Hole U1390A
Latitude: 36°19.0387′N
Longitude: 7°43.0812′W
Time on hole (d): 2.6
Seafloor (drill pipe measurement below rig floor, m DRF): 1005.1
Distance between rig floor and sea level (m): 11.7
Water depth (drill pipe measurement from sea level, mbsl): 993.4
Total penetration (drilling depth below seafloor, m DSF): 350
Total length of cored section (m): 350
Total core recovered (m): 326.26
Core recovery (%): 93.22
Total number of cores: 38

Hole U1390B
Latitude: 36°19.1460′N
Longitude: 7°43.0815′W
Time on hole (d): 1.4
Seafloor (drill pipe measurement below rig floor, m DRF): 1002.4
Distance between rig floor and sea level (m): 11.7
Water depth (drill pipe measurement from sea level, mbsl): 990.7
Total penetration (drilling depth below seafloor, m DSF): 194.1
Total length of cored section (m): 194.1
Total core recovered (m): 189.93
Core recovery (%): 97.85
Total number of cores: 21

Hole U1390C
Latitude: 36°19.1466′N
Longitude: 7°43.0674′W
Time on hole (d): 1.2
Seafloor (drill pipe measurement below rig floor, m DRF): 1004.1
Distance between rig floor and sea level (m): 11.7
Water depth (drill pipe measurement from sea level, mbsl): 992.4
Total penetration (drilling depth below seafloor, m DSF): 175.4
Total length of cored section (m): 175.4
Total core recovered (m): 170.08
Core recovery (%): 96.97
Total number of cores: 19

Site U1390 totals
Number of cores: 78
Penetration (m): 719.5
Cored (m): 719.5
Recovered (m): 686.27 (95.4%)

Core	Date (2012)	Time (h)	Depth DSF (m) Top of cored interval	Depth DSF (m) Bottom of cored interval	Interval advanced (m)	Depth CSF (m) Top of recovered core	Depth CSF (m) Bottom of recovered core	Length of core recovered (m)	Curated length (m)	Recovery (%)
339-U1390A-										
1H	3 Jan	0525	0.0	3.6	3.6	0.0	3.63	3.63	3.63	101
2H	3 Jan	0640	3.6	13.1	9.5	3.6	13.45	9.83	9.85	103
3H	3 Jan	0720	13.1	22.6	9.5	13.1	22.93	9.83	9.83	103
4H	3 Jan	0820	22.6	32.1	9.5	22.6	32.30	9.63	9.70	101
5H	3 Jan	0900	32.1	41.6	9.5	32.1	41.14	8.97	9.04	94
6H	3 Jan	0945	41.6	51.1	9.5	41.6	51.00	9.35	9.40	98
7H	3 Jan	1035	51.1	60.6	9.5	51.1	61.27	10.17	10.17	107
8H	3 Jan	1120	60.6	70.1	9.5	60.6	70.53	9.93	9.93	105
9H	3 Jan	1200	70.1	76.7	6.6	70.1	76.70	6.60	6.60	100
10X	3 Jan	1630	76.7	83.5	6.8	76.7	84.37	7.67	7.67	113
11X	3 Jan	1710	83.5	93.1	9.6	83.5	92.61	9.11	9.11	95
12X	3 Jan	1755	93.1	102.7	9.6	93.1	101.20	8.10	8.10	84
13X	3 Jan	1840	102.7	112.3	9.6	102.7	110.49	7.79	7.79	81
14X	3 Jan	1925	112.3	121.9	9.6	112.3	121.23	9.08	8.93	95
15X	3 Jan	2000	121.9	131.4	9.5	121.9	129.43	7.53	7.53	79
16X	3 Jan	2045	131.4	140.9	9.5	131.4	140.10	8.70	8.70	92
17X	3 Jan	2130	140.9	150.5	9.6	140.9	149.97	9.07	9.07	94
18X	3 Jan	2210	150.5	160.1	9.6	150.5	159.07	8.57	8.57	89
19X	3 Jan	2300	160.1	169.6	9.5	160.1	165.81	5.71	5.71	60
20X	3 Jan	2335	169.6	179.2	9.6	169.6	178.78	9.18	9.18	96
21X	4 Jan	0035	179.2	188.8	9.6	179.2	187.60	8.40	8.40	88
22X	4 Jan	0125	188.8	198.4	9.6	188.8	197.08	8.28	8.28	86
23X	4 Jan	0215	198.4	208.0	9.6	198.4	207.03	8.63	8.63	90

Table T1 (continued).

Core	Date (2012)	Time (h)	Depth DSF (m) Top of cored interval	Depth DSF (m) Bottom of cored interval	Interval advanced (m)	Depth CSF (m) Top of recovered core	Depth CSF (m) Bottom of recovered core	Length of core recovered (m)	Curated length (m)	Recovery (%)
24X	4 Jan	0320	208.0	217.5	9.5	208.0	217.36	9.36	9.36	99
25X	4 Jan	0415	217.5	227.0	9.5	217.5	224.66	7.16	7.16	75
26X	4 Jan	0505	227.0	236.7	9.7	227.0	236.28	9.28	9.28	96
27X	4 Jan	0550	236.7	246.3	9.6	236.7	246.26	9.56	9.56	100
28X	4 Jan	0640	246.3	255.9	9.6	246.3	256.08	9.78	9.78	102
29X	4 Jan	0735	255.9	265.5	9.6	255.9	265.52	9.62	9.62	100
30X	4 Jan	0830	265.5	275.1	9.6	265.5	275.37	9.87	9.87	103
31X	4 Jan	0925	275.1	284.7	9.6	275.1	284.61	9.51	9.51	99
32X	4 Jan	1020	284.7	294.3	9.6	284.7	293.82	9.12	9.12	95
33X	4 Jan	1115	294.3	303.9	9.6	294.3	302.65	8.35	8.35	87
34X	4 Jan	1220	303.9	313.5	9.6	303.9	313.16	9.26	9.26	96
35X	4 Jan	1320	313.5	323.1	9.6	313.5	323.22	9.72	9.72	101
36X	4 Jan	1415	323.1	332.3	9.2	323.1	332.63	9.53	9.53	104
37X	4 Jan	1535	332.3	341.9	9.6	332.3	335.32	3.02	3.02	31
38X	4 Jan	1650	341.9	350.0	8.1	341.9	351.26	9.36	9.36	116
				Advanced total:	350					
				Total interval cored:	326.26					
339-U1390B-										
1H	5 Jan	1710	0.0	9.1	9.1	0.0	9.12	9.12	9.12	100
2H	5 Jan	1815	9.1	18.6	9.5	9.1	19.12	10.02	10.02	105
3H	5 Jan	1855	18.6	28.1	9.5	18.6	28.35	9.75	9.75	103
4H	5 Jan	1935	28.1	37.6	9.5	28.1	38.26	10.11	10.16	106
5H	5 Jan	2100	37.6	47.1	9.5	37.6	48.14	10.51	10.54	111
6H	5 Jan	2135	47.1	56.6	9.5	47.1	57.58	10.46	10.48	110
7H	5 Jan	2205	56.6	66.1	9.5	56.6	66.96	9.84	10.36	104
8H	5 Jan	2300	66.1	75.6	9.5	66.1	76.11	9.97	10.01	105
9H	5 Jan	2355	75.6	85.1	9.5	75.6	84.79	9.19	9.19	97
10H	6 Jan	0035	85.1	94.6	9.5	85.1	93.66	8.56	8.56	90
11H	6 Jan	0125	94.6	104.1	9.5	94.6	105.03	10.43	10.43	110
12H	6 Jan	0225	104.1	108.6	4.5	104.1	108.98	4.88	4.88	108
13H	6 Jan	0310	108.6	118.1	9.5	108.6	118.93	10.33	10.33	109
14H	6 Jan	0345	118.1	127.6	9.5	118.1	128.68	10.58	10.58	111
15H	6 Jan	0435	127.6	137.1	9.5	127.6	135.58	7.98	7.98	84
16H	6 Jan	0525	137.1	146.6	9.5	137.1	144.82	7.72	7.72	81
17H	6 Jan	0610	146.6	156.1	9.5	146.6	157.65	11.05	11.05	116
18H	6 Jan	0700	156.1	165.6	9.5	156.1	164.67	8.57	8.57	90
19H	6 Jan	0745	165.6	175.1	9.5	165.6	176.08	10.48	10.48	110
20H	6 Jan	0830	175.1	184.6	9.5	175.1	180.38	5.28	5.28	56
21H	6 Jan	1800	184.6	194.1	9.5	184.6	189.70	5.10	5.10	54
				Advanced total:	194.1					
				Total interval cored:	189.93					
339-U1390C-										
1H	7 Jan	0255	0.0	4.4	4.4	0.0	4.40	4.40	4.40	100
2H	7 Jan	0430	4.4	13.9	9.5	4.4	14.36	9.96	9.96	105
3H	7 Jan	0630	13.9	23.4	9.5	13.9	23.52	9.62	9.62	101
4H	7 Jan	0950	23.4	32.9	9.5	23.4	33.44	10.01	10.04	105
5H	7 Jan	1035	32.9	42.4	9.5	32.9	42.76	9.85	9.86	104
6H	7 Jan	1125	42.4	51.9	9.5	42.4	52.71	10.31	10.31	109
7H	7 Jan	1210	51.9	61.4	9.5	51.9	61.87	9.91	9.97	104
8H	7 Jan	1235	61.4	70.9	9.5	61.4	71.71	10.31	10.31	109
9H	7 Jan	1355	70.9	80.4	9.5	70.9	81.68	10.78	10.78	113
10H	7 Jan	1425	80.4	89.9	9.5	80.4	90.74	10.34	10.34	109
11H	7 Jan	1505	89.9	99.4	9.5	89.9	100.28	10.38	10.38	109
12H	7 Jan	1600	99.4	108.9	9.5	99.4	108.93	9.53	9.53	100
13H	7 Jan	1635	108.9	118.4	9.5	108.9	119.85	10.95	10.95	115
14H	7 Jan	1720	118.4	127.9	9.5	118.4	126.48	8.08	8.08	85
15H	7 Jan	1800	127.9	137.4	9.5	127.9	135.10	7.20	7.20	76
16H	7 Jan	1835	137.4	146.9	9.5	137.4	142.57	5.13	5.17	54
17H	7 Jan	2010	146.9	156.4	9.5	146.9	155.01	8.11	8.11	85
18H	7 Jan	2045	156.4	165.9	9.5	156.4	162.51	6.11	6.11	64
19H	7 Jan	2125	165.9	175.4	9.5	165.9	175.00	9.10	9.10	96
				Advanced total:	175.4					
				Total interval cored:	170.08					

DRF = drilling depth below rig floor, DSF = drilling depth below seafloor, CSF = core depth below seafloor. H = advanced piston coring system, X = extended core barrel system. Time is Universal Time Coordinated.

Table T2. XRD peak intensities of minerals from bulk sediment, Hole U1390A.

Hole, core, section, interval (cm)	Depth (mbsf)	Total intensity (counts)	Quartz (counts)	Calcite (counts)	K-feldspar (counts)	Plagioclase (counts)	Dolomite (counts)	Chlorite (counts)	Kaolinite (counts)	Illite (counts)	Smectite (counts)	Hornblende (counts)	Augite (counts)	Pyrite (counts)	Aragonite (counts)
339-U1390A-															
1H-2, 126–127	2.76	54,233	22,980	12,942	639	3,592	1,614	1388	2,947	6,904	627	68	NA	NA	532
2H-6, 122–123	12.35	51,613	31,288	12,182		1075	1,465	634	1,574	2,695	452	248	NA	NA	NA
3H-5, 126–127	20.37	59,923	32,604	13,848	638	1518	4,578	836	2,229	3,066	493	113	NA	NA	NA
4H-6, 84–85	30.98	49,655	26,505	12,011	392	987	1,852	999	2,719	3,387	684	119	NA	NA	NA
5H-6, 130–131	39.19	44,923	24,972	12,269	408	991	1,289	724	1,857	1,862	510	41	NA	NA	NA
6H-6, 129–130	50.52	46,790	26,255	12,563	NA	1,104	2,020	547	1,526	2,204	571	NA	NA	NA	NA
7H-6, 132–133	59.77	46,815	28,562	10,444	510	1,496	1,411	NA	1,683	1,954	559	196	NA	NA	NA
8H-6, 120–121	68.98	49,837	28,478	11,782	424	1,611	1,875	748	1,818	2,063	416	86	NA	NA	536
9H-4, 112–113	75.49	52,225	33,763	8,614	490	1,487	1,284	728	1,841	3,413	461	144	NA	NA	
10X-5, 124–125	83.95	58,777	28,794	14,587	808	1,166	3,725	1,321	2,539	4,407	623	242	NA	NA	565
11X-6, 117–118	92.17	51,661	21,499	13,730	683	1,410	1,634	1,645	3,633	6,551	697	NA	NA	179	NA
12X-5, 97–98	100.07	70,181	36,395	16,287	600	1,900	4,053	1,345	3,069	5,653	718	161	NA	NA	NA
13X-5, 110–111	109.80	47,213	18,452	14,933	708	1,100	1,299	1,319	2,707	,5526	659	143	367	NA	NA
14X-6, 90–91	120.55	45,997	20,344	12,273	487	1,167	2,280	1,142	2,860	4,570	750	124	NA	NA	NA
15X-4, 141–142	127.81	60,598	30,185	14,698	NA	1,376	3,015	1,408	3,063	5,493	671	85	NA	NA	604
16X-6, 50–51	139.40	60,406	31,196	13,547	843	1,633	2,384	1,354	3,646	4,933	664	37	NA	169	NA
17X-6, 91–92	149.31	45,795	27,077	10,456	473	922	1,768	569	1,606	2,248	591	85	NA	NA	NA
18X-5, 137–138	157.46	53,336	25,965	12,585	844	1,481	3,213	1,130	2,634	4,458	490	NA	NA	NA	536
19X-4, 45–46	164.50	41,442	18,300	11,560	566	1,126	1,235	1002	1,772	4,340	523	132	580	306	NA
20X-6, 109–110	178.19	57,382	35,607	13,542	465	1,102	1,021	634	1,659	2,242	410	53	NA	NA	647
21X-6, 62–63	186.92	40,588	19,127	13,226	366	1,104	927	790	1,900	2,604	479	66	NA	NA	NA
22X-6, 72–73	196.77	49,028	24,839	17,118	NA	681	1,747	583	1,179	1,742	325	118	NA	NA	696
23X-6, 81–82	206.71	57,080	31,037	12,176	661	1,437	3,963	945	2,471	3,068	554	103	NA	NA	665
24X-6, 80–81	216.22	45,971	22,655	12,869	501	985	1,793	881	2,475	2,952	726	134	NA	NA	NA
25X-5, 85–86	224.35	53,657	28,361	16,919	595	1,315	2,330	516	1,229	1,481	356	NA	NA	NA	555
26X-6, 120–121	235.70	82,295	36,928	22,734	2,077	2,926	5,822	1,680	3,686	4,997	551	94	NA	NA	799
27X-6, 80–81	245.00	52,220	32,036	11,698	1,785	849	1,313	604	1,644	1,717	574	NA	NA	NA	NA
28X-6, 99–100	254.79	59,164	31,992	11,957	426	1,517	3,906	1,224	3,142	3,805	490	74	NA	NA	631
29X-6, 135–136	263.80	53,281	21,122	15,187	553	3,113	2,225	1,416	3,355	5,400	823	87	NA	NA	NA
30X-6, 135–136	273.17	54,532	31,349	14,147	626	930	1,941	662	1,606	2,194	432	65	NA	NA	580
31X-6, 90–91	283.50	77,251	33,439	16,078	748	5,781	9,260	1,370	3,516	6,368	584	107	NA	NA	NA
32X-6, 117–118	293.37	55,248	26,409	12,094	603	2,075	2,982	1,484	3,780	4,566	795	58	NA	402	NA
33X-6, 59–60	302.10	75,741	44,098	15,460	NA	2,837	5,368	969	2,416	3,208	605	92	NA	NA	687
34X-6, 136–137	312.75	43,638	16,628	18,303	459	685	1,226	860	1,588	2,798	735	143	NA	213	NA
35X-6, 137–138	321.60	51,094	22,453	16,532	466	1,548	2,161	1,184	2,612	3,313	724	101	NA	NA	NA
36X-6, 87–88	331.38	93,793	60,495	13,632	5,977	1,256	5,970	760	1,699	2,509	446	NA	NA	NA	1,049
37X-2, 116–117	334.96	51,438	28,857	12,190	1,407	1,049	2,008	713	2,144	2,473	522	75	NA	NA	NA
38X-6, 136–137	350.76	43,174	23,164	11,970	484	1,025	1,451	838	1,776	1,837	613	17	NA	NA	NA

NA = no peak detected.

Table T3. Lithology and number of beds, Site U1390. (Continued on next page.)

Core	Number of beds			Bed lithology (%)			
	Silty mud	Sandy mud	Silty sand	Silty mud	Sandy mud	Silty sand	Calcareous mud
339-U1390A-							
1H				0	0	0	100
2H	2	1	1	5	1	2	93
3H	1	1		15	0	0	85
4H	2			6	0	0	94
5H	3	3		27	13	0	61
6H	5	5		25	15	0	60
7H	4	4		25	9	0	66
8H	3	3		10	4	0	86
9H	5		2	10	0	3	86
10X	1	3	2	1	17	20	62
11X	2		1	4	0	1	95
12X	1	2		7	9	0	84
13X	2			12	0	0	88
14X	2	1		8	6	0	86
15X	6	4		10	8	0	82
16X	9	5	2	24	10	2	64
17X				0	0	0	100
18X	4	6		19	19	0	62
19X				0	0	0	100
20X	1			5	0	0	95
21X	1			4	0	0	96
22X	3	2	1	9	9	1	80
23X	7	4	1	26	8	8	58
24X	2			1	0	0	99
25X	3	1		9	0	0	90
26X	7	1		33	2	0	65
27X	4	2		13	3	0	84
28X	8	1		22	1	0	77
29X	4	1	1	8	4	1	87
30X	5	1		10	1	0	89
31X		1	1	0	19	3	79
32X	4	5	1	12	12	0	75
33X	2	4	1	8	7	62	24
34X	1		1	44	0	40	16
35X	4	7	1	5	11	8	76
36X	3	5	3	23	7	17	52
37X		2		0	59	0	41
38X	2	2		8	32	0	61
339-U1390B-							
1H		2		0	2	0	98
2H	3	2		83	1	0	16
3H	8			37	0	0	63
4H	8	1		28	1	0	71
5H	3	1	1	9	1	0	90
6H	4	1	1	10	4	1	85
7H		1	1	0	2	2	96
8H	2	5		1	9	0	91
9H	3	4		8	42	0	50
10H	1			3	0	0	97
11H	2	1		11	7	0	81
12H				0	0	0	100
13H	3	1		10	10	0	80
14H	9	2	1	29	3	1	67
15H	7	4	1	42	3	1	54
16H	3			36	0	0	64
17H	7	5	2	66	9	3	22
18H	3	1		9	0	0	90
19H	5			35	0	0	65
20H	1			28	0	0	72
21H				0	0	0	100
339-U1390C-							
1H				0	0	0	100
2H	5	1	1	11	1	1	87
3H	6			28	0	0	72
4H	5			25	0	0	75
5H	4	5		16	6	0	78
6H	9	4	6	32	8	7	53

Table T3 (continued).

Core	Number of beds			Bed lithology (%)			
	Silty mud	Sandy mud	Silty sand	Silty mud	Sandy mud	Silty sand	Calcareous mud
7H	2	3		6	14	0	80
8H	2	4		1	3	0	96
9H	8	3		42	11	0	47
10H	1	1		1	2	0	97
11H	3	2		8	9	0	83
12H	2			5	0	0	95
13H	2	1		16	7	0	78
14H	11	5		36	14	0	50
15H	10	5		21	17	0	62
16H				0	0	0	100
17H	15	9	2	40	14	2	44
18H				0	0	0	100
19H	1			4	0	0	96

Table T4. Results from coulometric and CHNS analysis on whole-round squeezecake samples, Hole U1390A.

Core, section	Depth (mbsf)	Calcium carbonate (wt%)	Inorganic carbon (wt%)	Total carbon (wt%)	Nitrogen (wt%)	Organic carbon (wt%)	C/N
339-U1390A-							
1H-2	2.76	25.33	3.04	3.97	0.10	0.93	9.30
2H-6	12.35	23.23	2.79	3.63	0.07	0.85	12.14
4H-6	30.98	23.94	2.87	3.66	0.09	0.79	8.78
5H-6	39.19	23.73	2.85	3.79	0.10	0.95	9.50
6H-6	50.52	27.64	3.31	4.32	0.10	1.01	10.10
7H-6	59.77	24.15	2.90	3.81	0.10	0.91	9.10
8H-6	68.98	27.12	3.25	4.27	0.10	1.02	10.20
9H-4	75.49	21.15	2.54	2.99	0.06	0.45	7.50
10X-5	83.95	28.74	3.45	4.61	0.10	1.16	11.60
11X-6	92.17	27.05	3.24	4.20	0.11	0.96	8.73
12X-5	100.07	27.84	3.34	4.31	0.08	0.97	12.13
13X-5	109.80	25.80	3.09	4.10	0.11	1.01	9.18
14X-6	120.55	24.30	2.91	3.91	0.12	1.00	8.33
15X-4	127.81	30.23	3.62	4.68	0.10	1.06	10.60
16X-6	139.40	23.70	2.84	3.50	0.08	0.66	8.25
17X-6	149.31	21.99	2.64	3.44	0.08	0.80	10.00
18X-5	157.46	28.45	3.41	4.45	0.10	1.04	10.40
19X-4	164.50	22.84	2.74	3.58	0.09	0.84	9.33
20X-6	178.19	28.68	3.44	4.56	0.11	1.12	10.18
21X-6	186.92	27.39	3.28	4.27	0.11	0.99	9.00
22X-6	196.77	33.32	4.00	5.12	0.11	1.12	10.18
23X-6	206.71	28.79	3.45	4.34	0.08	0.89	11.13
24X-6	216.22	25.42	3.05	3.66	0.08	0.61	7.63
25X-5	224.35	34.51	4.14	5.17	0.09	1.03	11.44
26X-6	235.70	30.50	3.66	4.57	0.08	0.91	11.38
27X-6	245.00	24.20	2.90	3.30	0.06	0.40	6.67
28X-6	254.79	25.73	3.08	3.81	0.09	0.73	8.11
29X-6	263.80	29.69	3.56	4.26	0.09	0.70	7.78
30X-6	273.17	32.14	3.85	4.61	0.08	0.76	9.50
31X-6	283.50	29.69	3.56	4.28	0.06	0.72	12.00
32X-6	293.37	23.39	2.80	3.81	0.08	1.01	12.63
33X-6	302.10	29.26	3.51	4.33	0.08	0.82	10.25
34X-6	312.75	31.54	3.78	4.81	0.11	1.03	9.36
35X-6	321.60	29.78	3.57	4.28	0.10	0.71	7.10
36X-6	331.38	30.36	3.64	4.25	0.05	0.61	12.20
37X-2	334.96	25.09	3.01	3.52	0.07	0.51	7.29
38X-6	350.76	23.68	2.84	3.79	0.09	0.95	10.56

Table T5. Sediment textures, compositions, and lithology names determined by smear slide, Site U1390. (Continued on next two pages.)

Core, section, interval (cm)	Depth (mbsf)	Lithology	Lith. unit	Texture (%)				Composition (%)				Lithology name	Opaque (%)
				Sand	Silt	Clay	Ash	Siliciclastic	Detrital carbonate	Biogenic carbonate	Biogenic silica		
339-U1390A-													
1H-2, 80	2.30	Mud	IA	10	30	60	0	52	28	20	0	Mud with biogenic carbonate	
2H-4, 35	8.47	Sandy mud	IA	67	27	60	0	63	13	20	4	Calcareous silty sand	
2H-5, 75	10.37	Mud	IA	15	30	55	0	55	20	25	0	Calcareous mud	
2H-6, 10	11.23	Sandy mud	IA	40	30	30	0	60	20	20	0	Sandy mud with biogenic carbonate	
3H-1, 54	13.64	Sandy mud	IA	45	28	27	0	50	25	25	0	Sandy mud with biogenic carbonate	
3H-5, 127	20.38	Mud	IA	10	38	52	0	55	20	25	0	Calcareous mud	
4H-3, 85	26.46	Black patch	IA	60	20	20	0	10	15	15	0	Opaque with biogenic carbonate	60
4H-6, 17	30.31	Silty mud	IA	25	35	40	0	50	25	25	0	Calcareous silty mud	
4H-6, 29	30.43	Black shelly patch	IA	70	20	10	0	25	20	20	0	Opaque with biogenic carbonate	35
4H-6, 84	30.98	Mud	IA	15	30	55	0	50	25	25	0	Calcareous mud	
5H-5, 135	37.72	Black sandy mud	IA	40	30	30	0	35	20	20	0	Sandy mud with opaque	25
5H-6, 130	39.19	Mud	IA	15	30	55	0	55	20	25	0	Calcareous mud	
5H-7, 115	40.54	Sandy mud	IA	40	30	30	0	55	25	20	0	Sandy mud with biogenic carbonate	
6H-2, 139	44.49	Mud	IA	10	30	60	0	50	25	25	0	Calcareous mud	
6H-6, 112	50.35	Sandy mud	IA	40	30	30	0	60	20	20	0	Sandy mud with biogenic carbonate	
7H-1, 40	51.50	Sandy mud	IA	45	27	28	0	50	30	20	0	Sandy mud with biogenic carbonate	
8H-6, 100	68.78	Sandy mud	IA	40	30	30	0	30	15	20	0	Opaque sandy mud	
8H-6, 120	68.98	Mud	IA	20	50	30	0	60	20	20	0	Silty mud with biogenic carbonate	
8H-6, 122	69.00	Black patch	IA	35	30	35	0	55	25	20	0	Sandy mud with biogenic carbonate	
9H-4, 112	75.49	Mud	IA	15	30	55	0	55	20	25	0	Calcareous mud	
9H-4, 128	75.65	Silty mud	IA	20	40	40	0	55	20	25	0	Calcareous silty mud	
10X-1, 80	77.50	Sandy mud	IA	55	25	20	0	60	20	20	0	Silty mud with biogenic carbonate	
10X-3, 60	80.30	Mud	IA	15	30	55	0	55	20	25	0	Calcareous mud	
10X-5, 6	82.77	Sandy mud	IA	35	30	35	0	60	22	18	0	Sandy mud with biogenic carbonate	
11X-2, 16	85.16	Silty sand	IA	60	25	15	0	55	25	20	0	Silty mud with biogenic carbonate	
11X-2, 38	85.38	Silty mud	IA	15	45	40	0	55	25	20	0	Silty mud	
11X-2, 96	85.96	Mud	IA	10	30	60	0	50	30	20	0	Calcareous mud	
12X-2, 32	94.92	Sandy mud	IA	52	23	25	0	60	22	18	0	Silty mud with biogenic carbonate	
12X-5, 72	99.82	Mud	IA	10	30	60	0	55	25	20	0	Calcareous mud	
12X-6, 48	100.62	Silty mud	IA	20	45	35	0	60	22	18	0	Silty mud with biogenic carbonate	
13X-4, 85	108.05	Silty mud	IA	10	35	55	0	45	35	20	0	Calcareous silty mud	
13X-5, 70	109.40	Mud	IA	8	37	55	0	60	22	18	0	Mud with biogenic carbonate	
14X-3, 50	115.80	Sandy mud	IA	55	15	30	1	54	25	20	0	Sandy mud with biogenic carbonate	
14X-4, 70	117.35	Mud	IA	10	30	60	0	38	35	27	0	Calcareous mud	
15X-2, 70	124.10	Mud	IA	8	32	60	0	40	35	25	0	Calcareous mud	
15X-2, 92	124.32	Sandy mud	IA	65	10	25	0	60	25	15	0	Silty sand with biogenic carbonate	
15X-3, 115	126.05	Silty mud	IA	35	25	40	0	55	25	20	0	Sandy mud with biogenic carbonate	
16X-5, 18	137.58	Sandy mud	IA	50	25	25	0	60	20	20	0	Sandy mud with biogenic carbonate	
16X-5, 70	138.10	Mud	IA	25	35	40	0	55	23	22	0	Silty mud with biogenic carbonate	
17X-5, 60	147.50	Mud	IA	5	30	65	0	50	25	25	0	Calcareous mud	
18X-2, 120	153.20	Soupy sand	IA	50	25	25	0	60	20	20	0	Sandy mud with biogenic carbonate	
18X-2, 58	152.58	Light greenish mud	IA	10	25	65	0	50	25	25	0	Calcareous mud	
18X-5, 137	157.46	Silty mud	IA	10	40	40	0	55	25	20	0	Silty mud with biogenic carbonate	
18X-5, 24	156.33	Sandy mud	IA	40	30	30	0	55	25	20	0	Sandy mud with biogenic carbonate	
19X-1, 110	161.20	Mud	IA	5	30	65	0	50	20	25	5	Calcareous mud	
19X-1, 5	160.15	Mud	IA	20	40	40	0	60	20	20	0	Silty mud with biogenic carbonate	
19X-2, 102	162.62	Light mud	IA	3	27	70	0	35	28	35	2	Calcareous mud	
19X-3, 108	163.94	Silty mud	IA	10	25	65	0	45	15	18	22	Biogenic mud	

Table T5 (continued). (Continued on next page.)

Core, section, interval (cm)	Depth (mbsf)	Lithology	Lith. unit	Texture (%)				Composition (%)				Lithology name	Opaque (%)
				Sand	Silt	Clay	Ash	Siliciclastic	Detrital carbonate	Biogenic carbonate	Biogenic silica		
19X-4, 10	164.15	Soupy mud	IA	4	18	78	0	40	20	20	0	Biogenic calcareous biosiliceous indurated sediment	20
20X-1, 50	170.10	Mud	IA	15	33	52	0	50	25	25	0	Calcareous mud	
20X-3, 127	173.87	Silty mud	IA	20	40	40	0	55	22	22	1	Calcareous silty mud	
21X-2, 112	181.82	Grayish	IA	5	30	65	0	50	30	20	0	Calcareous mud	
22X-1, 30	189.10	Mottling mud	IA	5	28	67	0	38	32	30	0	Calcareous mud	
22X-3, 113	192.93	Light mud	IA	3	25	72	0	33	32	35	0	Calcareous mud	
22X-6, 16	196.21	Soupy sandy mud	IA	55	25	20	0	58	22	20	0	Silty sand with biogenic carbonate	
22X-6, 9	196.14	Sandy mud	IA	30	25	45	0	55	20	25	0	Sandy mud with biogenic carbonate	
23X-2, 90	200.80	Silty sand	IA	52	28	20	1	55	20	24	0	Silty sand with biogenic carbonate	
23X-5, 100	205.40	Mud	IA	5	30	65	0	55	25	20	0	Mud with biogenic carbonate	
23X-5, 32	204.72	Sandy mud	IA	45	25	30	0	55	20	25	0	Sandy mud with biogenic carbonate	
23X-5, 36	204.76	Sandy mud	IA	27	30	43	0	55	20	25	0	Sandy mud with biogenic carbonate	
24X-1, 88	208.88	Silty mud	IA	15	45	40	0	35	30	35	0	Calcareous silty mud	
24X-2, 70	210.20	Mud	IA	5	30	65	0	45	30	25	0	Calcareous mud	
25X-5, 36	223.86	Silty mud	IA	15	45	40	0	55	20	25	0	Silty mud with biogenic carbonate	
25X-5, 48	223.98	Sandy mud	IA	50	25	30	0	55	20	25	0	Sandy mud with biogenic carbonate	
25X-5, 75	224.25	Mud	IA	10	25	65	0	55	20	25	0	Calcareous mud	
26X-2, 10	228.60	Mud	IA	10	25	65	0	55	20	25	0	Calcareous mud	
26X-2, 24	228.74	Light grey mud	IA	10	20	70	0	38	30	32	0	Calcareous mud	
26X-6, 43	234.93	Sandy mud	IA	55	15	30	0	52	23	25	0	Sandy mud with biogenic carbonate	
27X-6, 40	244.60	Mud	IA	5	30	65	0	42	30	28	0	Calcareous mud	
27X-7, 40	245.61	Silty mud	IA	20	40	40	0	42	28	30	0	Calcareous silty mud	
28X-4, 25	251.05	Sandy mud	IA	35	25	40	0	58	20	22	0	Sandy mud with biogenic carbonate	
28X-5, 50	252.80	Mud	IA	10	30	60	0	40	28	32	0	Calcareous mud	
29X-4, 75	260.20	Mud	IA	30	25	45	0	60	25	15	0	Sandy mud with biogenic carbonate	
29X-7, 90	264.85	Sandy mud	IA	15	25	60	0	40	32	38	0	Calcareous mud	
30X-3, 75	268.07	Mud	IA	5	35	60	0	40	28	32	0	Calcareous mud	
30X-5, 44	270.76	Sandy mud	IA	25	35	40	0	45	23	32	0	Calcareous silty mud	
31X-2, 20	276.80	Greenish mud	IA	10	30	60	0	55	27	18	0	Mud with biogenic carbonate	
31X-4, 131	280.91	Silty sand	IA	50	30	20	0	60	20	20	0	Silty mud with biogenic carbonate	
31X-5, 125	282.35	Light mud	IA	6	21	73	0	45	30	25	0	Calcareous mud	
31X-7, 16	283.73	Sandy mud	IA	40	30	30	0	55	25	20	0	Sandy mud with biogenic carbonate	
32X-1, 123	285.93	Mud	IA	11	38	51	0	55	25	20	0	Mud with biogenic carbonate	
32X-2, 123	287.43	Light mud	IA	10	30	40	0	45	30	25	0	Calcareous mud	
32X-3, 123	288.93	Reddish mud	IA	10	30	58	0	55	20	25	0	Calcareous mud	
33X-1, 100	295.30	Silty sand	IB	35	30	35	0	60	20	20	0	Sandy mud with biogenic carbonate	
33X-3, 100	298.30	Silty sand	IB	35	30	35	0	58	20	20	2	Silty sand with biogenic carbonate	
33X-4, 100	299.80	Light mud	IB	8	22	70	0	40	30	30	0	Calcareous mud	
33X-6, 59	302.10	Silty mud	IB	20	40	40	0	60	20	20	0	Silty sand with biogenic carbonate	
34X-2, 22	305.62	Silty sand	IB	35	30	35	0	60	20	20	0	Sandy mud with biogenic carbonate	
34X-6, 111	312.50	Mud	IB	12	35	53	0	50	25	25	0	Calcareous mud	
35X-3, 24	316.18	Mud	IB	18	30	52	0	55	20	25	0	Calcareous mud	
35X-4, 134	318.78	Silty sand	IB	45	32	23	0	60	20	20	0	Silty sand with biogenic carbonate	
36X-3, 113	327.23	Sandy mud	IB	32	30	38	0	60	20	20	0	Sandy mud with biogenic carbonate	
36X-3, 55	326.65	Mud	IB	12	38	50	0	50	25	25	0	Calcareous mud	
36X-3, 83	326.93	White sand	IB	65	25	10	0	70	20	10	0	Silty sand with biogenic carbonate	
339-U1390B-1H-6, 58	8.08	Sandy mud	IA	55	25	20	0	55	30	15	0	Silty sand with biogenic carbonate	

Table T5 (continued).

Core, section, interval (cm)	Depth (mbsf)	Lithology	Lith. unit	Texture (%)				Composition (%)				Lithology name	Opaque (%)
				Sand	Silt	Clay	Ash	Siliciclastic	Detrital carbonate	Biogenic carbonate	Biogenic silica		
1H-6, 67	8.17	Mud	IA	15	20	65	0	55	24	21	0	Mud with biogenic carbonate	
2H-4, 75	14.35	Mud	IA	15	20	65	0	55	24	21	0	Mud with biogenic carbonate	
3H-5, 75	25.35	Mud	IA	5	30	65	0	55	24	21	0	Mud with biogenic carbonate	
4H-4, 70	33.30	Mud	IA	5	30	65	0	55	24	21	0	Mud with biogenic carbonate	
4H-CC, 3	37.89	Sandy mud	IA	45	20	35	0	55	25	20	0	Sandy mud with biogenic carbonate	
5H-5, 117	44.69	Silty sand	IA	50	30	20	0	55	25	20	0	Silty sand with biogenic carbonate	
5H-7, 50	47.05	Silty mud	IA	10	42	48	1	58	22	20	0	Silty mud with biogenic carbonate	
6H-4, 50	52.02	Sandy mud	IA	45	15	40	0	55	20	25	0	Sandy mud with biogenic carbonate	
6H-5, 50	53.53	Mud	IA	10	25	65	0	42	30	28	0	Calcareous mud	
7H-2, 95	58.95	Sandy mud	IA	40	30	30	0	60	20	20	0	Sandy mud with biogenic carbonate	
7H-3, 104	60.44	Mud	IA	15	35	50	0	55	25	20	0	Mud with biogenic carbonate	
8H-2, 62	68.13	Sandy mud	IA	45	25	30	0	60	20	20	0	Sandy mud with biogenic carbonate	
8H-6, 75	73.99	Mud	IA	5	25	70	0	50	25	25	0	Calcareous mud	
9H-1, 86	76.46	Reddish silty mud	IA	25	40	35	0	60	25	15	0	Silty sand with biogenic carbonate	
12H-1, 79	104.89	Reddish clay	IA	8	24	68	0	40	35	25	0	Calcareous mud	
14H-3, 21	120.12	Sandy mud	IA	55	35	10	0	55	30	15	0	Silty sand with biogenic carbonate	
14H-3, 8	119.99	Mud	IA	10	25	65	0	40	33	27	0	Calcareous mud	
15H-3, 122	131.76	Sandy mud	IA	60	25	15	0	55	30	15	0	Silty sand with biogenic carbonate	
15H-3, 85	131.39	Mud	IA	5	27	68	0	38	32	30	0	Calcareous mud	
16H-4, 75	140.94	Mud	IA	5	28	67	0	38	30	32	0	Calcareous mud with biogenic carbonate	
17H-4, 50	150.69	Mud	IA	10	30	60	0	52	30	18	0	Mud with biogenic carbonate	
17H-4, 68	150.87	Silty sand	IA	52	35	13	0	60	25	15	0	Silty sand with biogenic carbonate	
17H-4, 90	151.09	Sandy mud	IA	62	25	13	0	55	25	20	0	Sandy mud with biogenic carbonate	
18H-3, 75	159.55	Greenish mud	IA	5	25	70	0	33	33	34	0	Calcareous mud	
18H-4, 90	161.25	Greenish mud	IA	5	25	70	0	33	31	34	2	Calcareous mud	
19H-4, 70	169.20	Mud	IA	15	25	60	0	40	32	28	0	Calcareous mud	
19H-5, 110	171.01	Dark mud	IA	10	25	65	0	38	30	32	0	Calcareous mud	
20H-2, 95	177.23	Mud	IA	3	25	72	0	35	31	34	0	Calcareous mud	
339-U1390C-													
1H-1, 140	1.40	Mud	IA	15	35	50	0	58	20	20	2	Mud with biogenic carbonate	
1H-1, 6	0.06	Top mud	IA	15	35	50	0	57	20	20	3	Mud with biogenic carbonate	
2H-2, 80	6.70	Soupy sand	IA	60	30	10	0	65	18	16	1	Silty sand with biogenic carbonate	

Table T6. Biostratigraphic datums, Site U1390.

Event	Reference	Age (Ma)	Hole U1390A depth (mbsf)			Hole U1390B (mbsf)			Hole U1390C (mbsf)		
			Top	Bottom	Mean	Top	Bottom	Mean	Top	Bottom	Mean
LrO *Emiliania huxleyi* (>4 µm)	Flores et al., 2010	0.01	7.37	8.87	8.12	0	9.1	4.55	4.4	13.9	9.150
FO *Emiliania huxleyi*	Raffi et al., 2006	0.26	189.50	190.50	190.00						
LO *Pseudoemiliania lacunosa*	Raffi et al., 2006	0.46	228.65	228.73	228.69						
LO *Gephyrocapsa omega*	Maiorano and Marino, 2004	0.57	228.65	228.73	228.69						
Stilostomella extinction	Hayward, 2002; Kawagata et al., 2005	0.58–0.7	284.61	293.68	289.14						
T paracme *Neogloboquadrina pachyderma* (sin)	Lourens et al., 2004	1.21	284.61	293.68	289.14						
LO large *Gephyrocapsa* (>5.5 µm)	Raffi et al., 2006	1.24	292.08	292.43	292.25						
LO *Helicosphaera sellii*	Raffi et al., 2006	1.25	332.63	333.02	332.82						

LrO = last regular occurrence, FO = first occurrence, LO = last occurrence, T = top, sin = sinistral.

Table T7. Abundance of nannofossils, Site U1390. (Continued on next two pages.)

Core, section	Depth (mbsf)	Preservation	Abundance	*Braarudosphaera bigelowii*	*Calcidiscus leptoporus* (<5 µm)	*Calcidiscus leptoporus* (>8 µm)	*Calcidiscus leptoporus* (5–8 µm)	*Coccolithus pelagicus* spp. *azorinus*	*Coccolithus pelagicus* spp. *braarudii*	*Coccolithus pelagicus* ssp. *pelagicus*	*Emiliania huxleyi* (<4 µm)	*Emiliania huxleyi* (>4 µm)	*Florisphaera profunda*	*Gephyrocapsa caribbeanica*	medium *Gephyrocapsa* group (3–5.5 µm)	*Gephyrocapsa oceanica* (>5 µm)	*Gephyrocapsa oceanica* (<5 µm)	*Gephyrocapsa omega*	small *Gephyrocapsa* (<3 µm)	large *Gephyrocapsa* (>5.5 µm)	*Helicosphaera acuta*	*Helicosphaera carteri*	*Helicosphaera sellii*	*Oolithotus* spp.	*Pontosphaera* spp.	*Pseudoemiliania lacunosa*	*Reticulofenestra asanoi* (>6 µm)	*Reticulofenestra asanoi* (<6 µm)	*Reticulofenestra minuta* (<3 µm)	*Rhabdosphaera* spp.	*Syracosphaera* spp.	*Umbilicosphaera sibogae*
339-U1390A-																																
1H-CC	3.63	G	A	R	F	F	F	R	C	F	C	P	F		F	F	F		A			F		F						F	F	F
2H-CC	13.45	M	A				R		F	C	F	C	F		C				A			F									F	
3H-CC	22.93	M	C				F			F	F	F			F				C			F		R							F	F
4H-CC	32.30	M	A					R	R		C	C			F				C			C			R						F	F
5H-CC	41.14	M	A		R		R	R	F	F	F	C		P	C		F		C			F									R	
6H-CC	51.00	G	VA		F		F		F	C	C	C			A				A			F		R							F	F
7H-CC	61.27	G	A		F		R	F	F	F	C	C		P	C	F	F		C			F									F	R
8H-CC	70.53	G	VA		F		F		F	F	C	R			A		R		A			F		R						R	R	R
9H-CC	76.70	G	VA				R			R	C		R						C			F		R						R	R	R
10X-CC	84.37	G	VA				F		F	F	F						D		C			F				R				F	R	
11X-CC	92.61	G	VA				F			F	R						C		D			R				R				F	F	F
12X-CC	101.20	G	VA				F		F	F	R						C		D			F								F	F	F
13X-CC	110.49	G	VA				R			F	R						C		D			R								F	F	
14X-CC	121.23	M	VA				R				R					F	C		A			F										R
15X-CC	129.43	M	VA				R			R	R				F				C			F								F	F	
16X-CC	140.10	M	VA				R		R	R							C		C											C		
17X-CC	149.97	M	A			R	R			R							C		A			R								C	R	
18X-CC	159.07	G	VA				F	F	F	F							C		D			F				F				D	F	
19X-CC	165.81	M	VA		F		F		F	R	R				C				D	P		R									F	R
20X-CC	178.78	M	VA		F		F	R	R	F	F	R			F	F	F		D			F									F	R
21X-CC	187.60	M	VA		F		F		F	F	R			F	R	F	C		D			F									F	
22X-CC	197.08	G	VA		F		F	F	F	F			F	F	R	C	C		D			F				F					F	F
23X-CC	207.03	M	A		R			R	F	F			F	A	F	F	F		A			F								C	F	R
24X-CC	217.36	M	A				R		R	C				C	C		F		A			F								F		
25X-CC	224.66	G	VA		R	R		R		R				A	A	R	F		D			F								A	F	F
26X-CC	236.28	M	VA	R	F	F	F			F			F	R		F	F	F	D			F				C			F	F	R	
27X-CC	246.26	M	A		R	R	R	R		F				R		R	F	F	D			F				C			F	F	R	
28X-CC	256.08	M	VA		F		F			R				P	F	F	C	R	D			F			R	C			C			R
29X-CC	265.52	M	VA			R	R		R	F				F	F	F	F		D			F	R				P		A	R		
30X-CC	275.37	G	VA		F	F	F			F						F	F	R	D			F			R	F			F		R	F
31X-CC	284.61	M	A				R			F							R	R	A			F			R	C			C	F	R	
32X-CC	293.68	M	A		F		F			F									A			F			F	C		P	C	F	R	R
33X-CC	302.65	M	VA		R		F	R		F									D	P		F			F	C			C	F		
34X-CC	313.16	G	A			F	C												D			R			R	C		P	C			
35X-CC	323.22	G	VA			R		R											C						R	A		P	A	F	F	F
36X-CC	332.63	M	VA						F	F									A	C	R	F				A			C	F	F	F
37X-CC	335.27	G	VA			F	F	F	F	F									D	C						C		P	F	F		

Table T7 (continued). (Continued on next page.)

Core, section	Depth (mbsf)	Preservation	Abundance	*Braarudosphaera bigelowii*	*Calcidiscus leptoporus* (<5 µm)	*Calcidiscus leptoporus* (>8 µm)	*Calcidiscus leptoporus* (5–8 µm)	*Coccolithus pelagicus* spp. *azorinus*	*Coccolithus pelagicus* spp. *braarudii*	*Coccolithus pelagicus* ssp. *pelagicus*	*Emiliania huxleyi* (<4 µm)	*Emiliania huxleyi* (>4 µm)	*Florisphaera profunda*	*Gephyrocapsa caribbeanica*	medium *Gephyrocapsa* group (3–5.5 µm)	*Gephyrocapsa oceanica* (>5 µm)	*Gephyrocapsa oceanica* (<5 µm)	*Gephyrocapsa omega*	small *Gephyrocapsa* (<3 µm)	large *Gephyrocapsa* (>5.5 µm)	*Helicosphaera acuta*	*Helicosphaera carteri*	*Helicosphaera sellii*	*Oolithotus* spp.	*Pontosphaera* spp.	*Pseudoemiliania lacunosa*	*Reticulofenestra asanoi* (>6 µm)	*Reticulofenestra asanoi* (<6 µm)	*Reticulofenestra minuta* (<3 µm)	*Rhabdosphaera* spp.	*Syracosphaera* spp.	*Umbilicosphaera sibogae*
38X-CC	351.26	G	VA			F	F	F	F	F									D	C						C	P	F				
339-U1390B-																																	
1H-CC	9.12	G	VA	F		F	F	F	F	F	C	C	P			R	R		C			R				F			C		R	
2H-CC	19.12	G	VA			F	F	F	F	F	C	C	P	R		R	R		C			F				F			C		R	F
3H-CC	28.35	G	VA			F	F	F	F	F	C	F	P	R		R	R		C			F				F			C		R	F
4H-CC	38.21	G	VA			F	F		F	F	F	C	P	R		P	R		C			F							C	F	F	
5H-CC	48.11	G	VA			F	F		F	F	C	F					R		C										C		F	
6H-CC	57.56	G	VA			F	F		F	F	C	F		F			F		C			F				F			C		F	
7H-CC	66.44	G	VA			F	F		F	F	C	F					F		C			F							C	F	F	
8H-CC	76.07	G	VA			F	F		F	F	C	F							C			F				R			C		R	
9H-CC	84.79	G	VA				F		R	F	C		C		A				D			F							F	F	F	F
10H-CC	93.66	G	VA		F		F		F	F	C		C		A				D			F				R			F		F	F
11H-CC	105.03	G	A		R		F		R	F	F				C				D			F				R			C		C	F
12H-CC	108.98	G	A		R		F		F	F	F				A				D			F				R			A		R	R
13H-CC	118.93	G	A				F			F	F		C		C	F	F		D			F							C	R	F	R
14H-CC	128.68	G	VA				F		R	F	C	F	C	F	A				D			F				R			A		F	
15H-CC	135.58	M	VA		R		F			F	F	R			C		R		D			R							F		F	F
16H-CC	144.82	G	VA				R			R	R		C		C				D			R							F	R	R	
17H-CC	157.65	G	VA		F	F	F		F	F	R		C	F	A		F		D			F							C		F	
18H-CC	164.67	M	VA		R		F	R	R	R	R				A				D			F							A		F	
19H-CC	175.78	G	VA		F		F	R	F	R	F				F	F			D			F							A	R		
20H-CC	180.38	M	A		F		F	R	R	F	R		F	R	F	F	C		D			F							A		R	F
339-U1390C-																																	
1H-CC	4.40	G	A			F	F		F	A	A		C		C	F	F		A			R							F	F	F	F
2H-CC	14.36	M	A				F	R	R	F	F	C	F		C	F	F		A			F							C		R	
3H-CC	23.52	G	A				F	F	F	F	C	F	F		C	F	F		C			F					R		C		F	C
4H-CC	33.44	M	VA		R		F	R	R	R	C	F	R		C				A			R							R		F	C
5H-CC	42.81	G	A		F		F		R	F	C	C	R		C		R		C			F			R				R		R	C
6H-CC	52.71	G	A		F		F		R	F	C	C			C		R		C			F							R		R	
7H-CC	61.87	G	A		F		F		R	F	C	C			C		F		C			F							R		R	
8H-CC	71.71	G	A		F		F		F	F	C	C			C		R		C			F							F		R	R
9H-CC	81.68	G	VA				F		F	F	C	F			C		A		F			F							R	R	R	R
10H-CC	90.74	G	VA		R		R	R	R	R	C	C			C		C		A			F			R				F		R	
11H-CC	100.28	G	VA			F	F		F	F	C	C			F		R		C			F			R				C		F	F
12H-CC	108.93	G	VA				F		F	F	C				C		R		R			F							F	F	F	R
13H-CC	119.85	M	VA				F		F	F	F	R			F		C		C			F							F	F	F	F
14H-CC	126.48	G	VA				F		F	F	F	R			F		R		C			C							F	F	F	F

Table T7 (continued).

Core, section	Depth (mbsf)	Preservation	Abundance	*Braarudosphaera bigelowii*	*Calcidiscus leptoporus* (<5 µm)	*Calcidiscus leptoporus* (>8 µm)	*Calcidiscus leptoporus* (5–8 µm)	*Coccolithus pelagicus* spp. *azorinus*	*Coccolithus pelagicus* spp. *braarudii*	*Coccolithus pelagicus* ssp. *pelagicus*	*Emiliania huxleyi* (<4 µm)	*Emiliania huxleyi* (>4 µm)	*Florisphaera profunda*	*Gephyrocapsa caribbeanica*	medium *Gephyrocapsa* group (3–5.5 µm)	*Gephyrocapsa oceanica* (>5 µm)	*Gephyrocapsa oceanica* (<5 µm)	*Gephyrocapsa omega*	small *Gephyrocapsa* (<3 µm)	large *Gephyrocapsa* (>5.5 µm)	*Helicosphaera acuta*	*Helicosphaera carteri*	*Helicosphaera sellii*	*Oolithotus* spp.	*Pontosphaera* spp.	*Pseudoemiliania lacunosa*	*Reticulofenestra asanoi* (>6 µm)	*Reticulofenestra asanoi* (<6 µm)	*Reticulofenestra minuta* (<3 µm)	*Rhabdosphaera* spp.	*Syracosphaera* spp.	*Umbilicosphaera sibogae*
15H-CC	135.10	M	A				F		R	R	C	F			F		F		F			F							C	F		F
16H-CC	142.53	G	VA				F		F	F	C	R			C		A		A			F							F	F	F	
17H-CC	155.01	G	VA			F	F	F	R	R	C	C			C				C			F							R		F	
18H-CC	162.51	G	VA			F	C		R	R	F	R			R	R	F		C			R							F		R	
19H-CC	175.00	M	VA		F		R		F	F	F			F	F	F	F		D			R							F			F

Preservation: G = good, M = moderate. Abundance: D = dominant, VA = very abundant, A = abundant, C = common, F = few, R = rare, P = present, B = barren. See **"Biostratigraphy"** in the "Methods" chapter (Expedition 339 Scientists, 2013b) for abundance and preservation definitions.

Table T8. Abundance of planktonic foraminifers, Site U1390. (Continued on next two pages.)

Core, section, interval (cm)	Depth (mbsf) Top	Depth (mbsf) Bottom	Pteropod abundance	Planktonic foraminifer abundance	Planktonic foraminifer preservation	*Beella digitata*	*Globigerina apertura*	*Globigerina bulloides*	*Globigerina calida*	*Globigerina falconensis*	*Globigerinella siphonifera*	*Globigerinita glutinata*	*Globigerinoides conglobatus*	*Globigerinoides ruber* (pink)	*Globigerinoides ruber* (white)	*Globigerinoides sacculifer*	*Globigerinoides trilobus*	*Globorotalia crassaformis* s.l. (dex)	*Globorotalia crassaformis* s.l. (sin)	*Globorotalia hirsuta* (dex)	*Globorotalia hirsuta* (sin)	*Globorotalia inflata*	*Globorotalia margaritae*	*Globorotalia menardii* (dex)	*Globorotalia menardii* (sin)	*Globorotalia miotumida*	*Globorotalia puncticulata*	*Globorotalia scitula* (dex)	*Globorotalia scitula* (sin)	*Globoturborotalita rubescens*	*Globoturborotalita tenella*	*Globorotalia truncatulinoides* (dex)	*Globorotalia truncatulinoides* (sin)	*Neogloboquadrina atlantica* (dex)	*Neogloboquadrina atlantica* (sin)	*Neogloboquadrina dutertrei*	*Neogloboquadrina pachyderma* (dex)	*Neogloboquadrina pachyderma* (sin)	*Orbulina universa*	*Pulleniatina obliquiloculata*	*Sphaeroidinellopsis seminulina*	*Turborotalita quinqueloba*	Comment
339-U1390A-																																									
1H-CC	3.58	3.63		D	G	P		P	P		R		P	P	A	F	A	P	P	P	P									P	R	R		P	P					Holocene
2H-CC	13.40	13.45	C	A	VG			A		F		R			A						A						P							A				R	
3H-CC	22.88	22.93		A	G			D	P		R	F			P				P		A						P	P			R			A	P	R			
4H-CC	32.25	32.30		A	G			D				F			B						B						P							A	R	P		F	
5H-CC	41.09	41.14	R	A	G			A				F			A						A						R	P						F	R	P			
6H-CC	50.95	51.00	R	A	G			F			R	R			R						F						R				P	P		D		F		R	
7H-CC	61.22	61.27		A	G			A			R	R			R					P	A						R		P		P	P		F	D	F		P	
8H-CC	70.48	70.53		A	VG	P		A			P	R			R						A						R		P		P			A	P			P	
9H-CC	76.65	76.70		A	VG			D	P	P	P	A									P	P					R		P		P	P		F		R		P	
10X-CC	84.32	84.37		D	VG	P		D			R	R			R						A						R					R		R		R			
11X-CC	92.56	92.61		D	VG			D	P		R	R			R			P			A						R				P	R	D	F	P	F		P	
12X-CC	101.15	101.20	R	A	VG			A	P		R	R	P		R			P			A						R					F	R	A	P	R		P	
13X-CC	110.44	110.49	R	A	VG			D			R	R			R						A						P					P	F	F		R		P	
14X-CC	121.18	121.23	R	D	VG			F				R	P		A	P	R				A						P					P		R		R			
15X-CC	129.38	129.43		A	VG			A	P			R			F			P			F						R					R	P	F		R			
16X-CC	140.05	140.10		A	G			F			P	P			R						R						P					P		D	P	R		F	
17X-CC	149.92	149.97		P	G			A			R				B						R													F	P	R		A	Many grains of black pyrite?
18X-CC	159.02	159.07	R	A	G			A	P		P	P			R						A						P					F		A		R		P	
19X-CC	165.76	165.81		D	G			A			P	P						P			P						P							D		R		R	
20X-CC	178.73	178.78		A	G			A			P	P			R	P	R				A		R				P		P			F		R		R			
21X-CC	187.55	187.60		A	G			F		P	P	P			R			P			D						P					F		R		R		R	
22X-CC	197.03	197.08		A	G			A		R	P	P			P						D						A							R		R		P	
23X-CC	206.98	207.03		A	G			A		P	R	P			R			P			A			P			P					P	R	A		F			
24X-CC	217.31	217.36		A	VG			A		F	P	R			P						P						P							D		R		F	
25X-CC	224.61	224.66		A	G			A				R			R			P			A						P			P			F	A		R		F	
26X-CC	236.23	236.28		A	G			A		R	P	P			F	P	P		P		A						P				P	F	P	F		R			
27X-CC	246.21	246.26		A	G			A	P	R		R			R						F						P			P		R		A		R			
28X-CC	256.03	256.08		A	G			F		R	P	P			R			R	P		F						P			P		A		A		R			
29X-CC	265.47	265.52		A	G			A		F	P	F			P						F						P			P				A	R	R		F	
30X-CC	275.32	275.37		D	G			A		R	P	P			R	P	P				F	P					P	P				R		A		F			Reworked Pliocene species
31X-CC	284.56	284.61		F	G			A		R		F			P				P		F	P				P						P	P		A	R	R		P	Reworked Pliocene species
32X-CC	293.63	293.68		A	G			A	P		P				F						F							R						A	P	R			
33X-CC	302.60	302.65		A	M			A	P			R			F		P		P		R	P						P				P		F	P	R	P		
34X-1, 59–61	304.49	304.51		P	M		P	A				R			F			P	P		R	P		P				P				P		F	P	P		R	Sand; reworked Pliocene species
34X-3, 59–61	307.48	307.50		F	M			A	P		P	R			F				P		R					P		P				F		A		P	P	R	Reworked Miocene species

Table T8 (continued). (Continued on next page.)

Core, section, interval (cm)	Depth (mbsf) Top	Depth (mbsf) Bottom	Pteropod abundance	Planktonic foraminifer abundance	Planktonic foraminifer preservation	*Beella digitata*	*Globigerina apertura*	*Globigerina bulloides*	*Globigerina calida*	*Globigerina falconensis*	*Globigerinella siphonifera*	*Globigerinita glutinata*	*Globigerinoides conglobatus*	*Globigerinoides ruber* (pink)	*Globigerinoides ruber* (white)	*Globigerinoides sacculifer*	*Globigerinoides trilobus*	*Globorotalia crassaformis* s.l. (dex)	*Globorotalia crassaformis* s.l. (sin)	*Globorotalia hirsuta* (dex)	*Globorotalia hirsuta* (sin)	*Globorotalia inflata*	*Globorotalia margaritae*	*Globorotalia menardii* (dex)	*Globorotalia menardii* (sin)	*Globorotalia miotumida*	*Globorotalia puncticulata*	*Globorotalia scitula* (dex)	*Globorotalia scitula* (sin)	*Globoturborotalita rubescens*	*Globoturborotalita tenella*	*Globorotalia truncatulinoides* (dex)	*Globorotalia truncatulinoides* (sin)	*Neogloboquadrina atlantica* (dex)	*Neogloboquadrina atlantica* (sin)	*Neogloboquadrina dutertrei*	*Neogloboquadrina pachyderma* (dex)	*Neogloboquadrina pachyderma* (sin)	*Orbulina universa*	*Pulleniatina obliquiloculata*	*Sphaeroidinellopsis seminulina*	*Turborotalita quinqueloba*	Comment
34X-5, 59–61	310.48	310.50		A	G			A		R	R	R			A				P			P						P								F	P	R	P		F	
34X-CC	313.11	313.16		D	VG			F			P	P			F				P			F						P	P			R				D	P	R				
35X-CC	323.17	323.22		D	G			A		R	P	P			R			P	R			A						P				P				A		R			R	
36X-CC	332.58	332.63		P	G			F				R			A		P		P			A										P	P	P		R	P	P	P			
37X-CC	335.22	335.27		P	G		P	A			P				R							A		P				P				R		R		A	P	R			R	
38X-CC	351.21	351.26		D	G			A	P		P	P			R				R			R						P				P	P			A		R	P			
339-U1390B-																																												
1H-CC	9.07	9.12		D	VG			A		R	R	R			R				P			F						P				R				R		R				
2H-CC	19.07	19.12		A	VG			A			R	R			R				P			F						P				P				R		R			P	
3H-CC	28.30	28.35		D	VG			D	P		R				P							F						P				P				A		R			P	
4H-CC	38.21	38.26		A	VG			A				R			R							R						P					P			D		R			P	
5H-CC	48.09	48.14		A	G			A	P		P	R			P							R						R				P	P			D		R			R	
6H-CC	57.53	57.58	R	A	VG			A	P	R	P	B			R				P			F						P				P				A	P	R			P	
7H-CC	66.89	66.94		A	G			A	P	P	P	P			P				P			A						P				P				A	P	R			P	
8H-CC	76.05	76.10	R	F	G			F		R	P	R			R							R						P				P	P			D	P	R			P	
9H-CC	84.73	84.79		A	G			F		P	R	R			R				P			F		P				R					R			D		P			P	
10H-CC	93.62	93.66		A	G			A		R	P	R			R							A						P		P			P			A		P			P	
11H-CC	104.98	105.03		A	G			A		R	P	R			P					P		A						P					R	P			R		P				
12H-CC	108.93	108.98		D	VG			A	R	P	R	P	P		R				P			A						R		P	P		R			F		R			R	
13H-CC	118.88	118.93	R	D	VG			P	R		R	P	R	R	A	P	R		R		P	F						P		R	R	R	R		P	R		R			P	
14H-CC	128.63	128.68		D	VG			A	R	P	F	P	P		A							A						R		R		P			P	F		F			P	
15H-CC	135.53	135.58		A	G			F	F		F	R			A					P	P	A						P		P	P	P			P	A		R				
16H-CC	144.77	144.82		D	G			D			P	P						P		P		A		P				P							P	D		R			R	
17H-CC	157.60	157.65		D	VG			A		P	P	P			R							R						P		P	P	R	P			A	R	F			R	
18H-CC	164.62	164.67		D	VG			D		R	P	R			R					P		F						P		P	P	R			R	A	R	R			R	
19H-CC	175.72	175.78		D	G			A		P	P	R			R			P				F						R		P	P	R			P	A		R			P	
20H-CC	180.33	180.38		D	G			F	R		R	P			A			P				F										F				F		R				
21H-CC	189.64	189.70		D	G			D				P			P			P				R						P				R	P			F		R			R	
339-U1390C-																																												
1H-CC	4.35	4.40		A	G			R		P	F	P	P		A	F	F		P			F										P	P			P		R				
2H-CC	14.31	14.36	R	F	VG			F	R	R	F	R	P		F							A						P				R				F		R			P	
3H-3, 127–137	18.09	18.19	R	F	VG			R	R	R	R	R										F										P				D		R				
3H-CC	23.47	23.52	R	F	VG			F	P	R	P	R			P							F						P				P				D		R				
4H-CC	33.38	33.44		A	G	P		A	P	R	P	R			P							F						P			P	P				D		P			P	
5H-CC	42.76	42.81		D	VG			F	P		P		R		P							F						R	P			P				A		F			R	
6H-CC	52.66	52.71		A	VG			A		P	P	R			R					P		F						P				R	P			A	P	R				
7H-CC	61.82	61.87		A	G			A		R	P	P			R					P		F						R				P	P			A		R				
8H-CC	71.66	71.71		A	VG			A	P		P	R			R							P						P				P				R	P	P			F	
9H-CC	81.63	81.68		D	VG			D				R			R							R						R				P	P			R		P			R	

Table T8 (continued).

Core, section, interval (cm)	Depth (mbsf)		Pteropod abundance	Planktonic foraminifer abundance	Planktonic foraminifer preservation	*Beella digitata*	*Globigerina apertura*	*Globigerina bulloides*	*Globigerina calida*	*Globigerina falconensis*	*Globigerinella siphonifera*	*Globigerinita glutinata*	*Globigerinoides conglobatus*	*Globigerinoides ruber* (pink)	*Globigerinoides ruber* (white)	*Globigerinoides sacculifer*	*Globigerinoides trilobus*	*Globorotalia crassaformis* s.l. (dex)	*Globorotalia crassaformis* s.l. (sin)	*Globorotalia hirsuta* (dex)	*Globorotalia hirsuta* (sin)	*Globorotalia inflata*	*Globorotalia margaritae*	*Globorotalia menardii* (dex)	*Globorotalia menardii* (sin)	*Globorotalia miotumida*	*Globorotalia puncticulata*	*Globorotalia scitula* (dex)	*Globorotalia scitula* (sin)	*Globoturborotalita rubescens*	*Globoturborotalita tenella*	*Globorotalia truncatulinoides* (dex)	*Globorotalia truncatulinoides* (sin)	*Neogloboquadrina atlantica* (dex)	*Neogloboquadrina atlantica* (sin)	*Neogloboquadrina dutertrei*	*Neogloboquadrina pachyderma* (dex)	*Neogloboquadrina pachyderma* (sin)	*Orbulina universa*	*Pulleniatina obliquiloculata*	*Sphaeroidinellopsis seminulina*	*Turborotalita quinqueloba*	Comment
	Top	Bottom																																									
10H-CC	90.69	90.74		D	VG			A	P	R	R	R			F							F					R	P	P	R	P			R		F				R	
11H-CC	100.23	100.28		A	VG			A	P	R	P	R	P		F							A					P		P	R	R			R		R				R	
12H-CC	108.88	108.93		A	VG	P		A	R		R	R										F					P			P	R			R		F				R	
13H-CC	119.80	119.85		D	VG			R			R	R		P	A	P	R		R	P		F					P			P	R			P		R					
14H-CC	126.43	126.48		F	VG			A				F			F				P			R					P			F	P			A							
15H-CC	135.05	135.10		P	VG			A		R	R	R			P					P	F						P							R		R					
16H-CC	142.48	142.53		P	VG			A			P	R			F							A					P			P				A		R				R	
17H-CC	154.96	155.01		F	G			F	P			R			P					P		A					P			R	P			D	P	R					
18H-CC	162.46	162.51		F	G			A			P	R								P		A					P			R				D	P	F				F	
19H-CC	174.95	175.00		D	G			D			R	R			F			P		P		F					R			A	P			D		F					

Abundance: D = dominant, A = abundant, C = common, F = few, P = present, R = rare. Preservation: VG = very good, G = good, M = moderate. sin = sinistral, dex = dextral. See **"Biostratigraphy"** in the "Methods" chapter (Expedition 339 Scientists, 2013b) for abundance and preservation definitions.

Table T9. Abundance of benthic foraminifers, Hole U1390A. (Continued on next three pages.)

Core, section	Depth (mbsf) Top	Depth (mbsf) Bottom	Preservation	Abundance	Agglutinated spp. (indet.)	*Ammonia beccarii*	*Amphicoryna scalaris*	*Amphicoryna* spp.	*Anomalinoides* spp.	*Asterigerinata* spp.	*Astrononion* spp.	*Bigenerina nodosaria*	*Biloculinella* spp.	*Bolivinita quadrilatera*	*Bolivina subaenariensis*	*Bolivina/Brizalina* spp.	*Brizalina alata*	*Brizalina dilatata*	*Brizalina earlandi*	*Brizalina spathulata*	*Bulimina aculeata*	*Bulimina elongata*	*Bulimina gibba*	*Bulimina marginata*	*Bulimina striata* gr.	*Bulimina* spp.	*Buliminella elegantissima*	*Cassidulina laevigata/teretis*	*Cassidulina* spp.	*Cassidulinoides* spp.	*Chilostomella oolina*	*Chrysalogonium* spp.	*Cibicides lobatulus*	*Cibicides refulgens*	*Cibicides/Cibicidoides* spp.	*Cibicidoides cicatricosus*	*Cibicidoides incrassatus*	*Cibicidoides pachyderma*	*Cibicidoides* cf. *wuellerstorfi*	*Cribromiliolinella* sp.	*Dentalina filiformis*	*Discanomalina coronata*	*Discanomalina semipunctata*	*Discanomalina* spp.
339-U1390A-																																											
1H-CC	3.58	3.63	G	A			P					P						A		R	P			R	R	P		R	P					R			P						
2H-CC	13.40	13.45	G	A									P	R		P	R	A	R						P		P	F	P				P		R								
3H-CC	22.88	22.93	G	A													A	A		R	P		P					R			F				R			R					
4H-CC	32.25	32.30	G	A							P		R			R	R	P								R	D	F			R				F								
5H-CC	41.09	41.14	G	F							P					R	R	R			R		P				A	R			R				R	R			R				
6H-CC	50.95	51.00	G	A										R	A	R	F	A			R				P	R		A		P					R								
7H-CC	61.22	61.27	G	D			P							R	P		F	A			R			P	F			R		P	F				R								
8H-CC	70.48	70.53	G	D												R	F	D							F			F		R	P				R			P					
9X-CC	76.65	76.70	M	F		P					P					A		A		P				P				A	F						F								
10X-CC	84.32	84.37	G	D			P									R	P	F			P				F			F		R	R				R			R					
11X-CC	92.56	92.61	G	D												P		F			P			R	A			R			P				R	P		R	P				
12X-CC	101.15	101.20	G	A				P					P			R	P	A		P				R	F			R							P			P					
13X-CC	110.44	110.49	G	A								P		R			F	A	P	P				P	R										R								
14X-CC	121.18	121.23	G	A			P										P	A					P	P	F			R							P			R					
15X-CC	129.38	129.43	G	F												R		D						P				F			P		P		R								
16X-CC	140.05	140.10	G	F												R	P	D						P			R	R	R						P					R			
17X-CC	149.92	149.97	M	A										R		R		D		P					A	P	R	A							P					P			
18X-CC	159.02	159.07	G	F							P					R		A						R	F	P	P	F	R						R								
19X-CC	165.76	165.81	G	D												P		R			P				F			P							R			R					
20X-CC	178.73	178.78	G	D			P									A	R	D						P	R			R		P					F								
21X-CC	187.55	187.60	G	D												R	R	A			R				F			A	R		R				R			P					
22X-CC	197.03	197.08	G	D							P					R	R	P			F			P	R			R	P	P					R	R		R	R				
23X-CC	206.98	207.03	G	D										F			A	R						F	R		R	R	P				F		R			R		P			
24X-CC	217.31	217.36	G	A		P					P					R		R			R			P			F	A	P				R	R	R			R		P			
25X-CC	224.61	224.66	M	F												R	F	R						R	F		F	F	R		R				R	P			P				
26X-CC	236.23	236.28	G	F												R	P	A			R			P	P			A	P				P		F					P			
27X-CC	246.21	246.26	G	A									P			R		P			F			P	A		R	R	P				P		F			P		P	P		
28X-CC	256.03	256.08	G	A												F		F	P	P	R			P	P	P		P							P		P	R		P		R	R	
29X-CC	265.47	265.52	G	A		P										P		F			F	P		F				A	P				R		R			P					
30X-CC	275.32	275.37	G	A					P							P	P	F					P		R	P		R					P		F		P	P			P		P
31X-CC	284.56	284.61	M	F	P							P				R	P	F						P	R			F					P	P	F	P		F	P		P		
32X-CC	293.63	293.68	G	F												R		F							A			A				P	P		R		P	R			R			
33X-CC	302.60	302.65	M	R		R			R	P						R		P							P			A	F						A								
34X-CC	313.11	313.16	G	A												P					A			F		A	P		P						F			F					
35X-CC	323.17	323.22	G	A									P			R		R			R					F	P	F	R	P					R			A					
36X-CC	332.58	332.63	M	F		R			R							R		R			F					R		R	P			F			A								
37X-CC	335.22	335.27	G	D		F												R							P			R				R	R	A			R					
38X-CC	351.21	351.26	G	A												R	P	D		P					P			F						R								

Preservation: G = good, M = medium. Abundance: D = dominant, A = abundant, C = common, F = few, P = present, R = rare. See **"Biostratigraphy"** in the "Methods" chapter (Expedition 339 Scientists, 2013b) for abundance and preservation definitions.

Table T9 (continued). (Continued on next page.)

Core, section	Depth (mbsf) Top	Depth (mbsf) Bottom	Preservation	Abundance	*Discorbis* spp.	*Dorothia bradyana*	*Dorothia* spp.	*Ehrenbergina* spp.	Elphidiid taxa	*Elphidium crispum*	*Elphidium* cf. *jenseni*	*Elphidium* spp.	*Epistominella* spp.	*Eubuliminella exilis*	*Fissurina* spp.	*Frondicularia* spp.	*Fursenkoina* spp.	*Gavelinopsis* spp.	*Glabratella patelliformis*	*Glandulina ovula*	*Glandulina* spp.	*Globobulimina affinis*	*Globobulimina turgida*	*Globobulimina* spp.	*Globocassidulina globosa*	*Globocassidulina oblonga*	*Globocassidulina* spp.	*Grigelis* spp.	*Gyroidinoides soldanii*	*Gyroidinoides* spp.	*Hanzawaia* spp.	*?Hanzawaia* spp.	*Hoeglundina elegans*	*Hyalinea balthica*	Hyaline indet.	*Hyalinonetrion gracillimum*	*Karreriella bradyi*	*Karreriella* spp.	*Lagena* spp.	*Lenticulina* spp.	*Lingulina seminuda*	*Loxostomina major*	*Marginulina* spp.	*Martinottiella* spp.
339-U1390A-																																											
1H-CC	3.58	3.63	G	A											F			R					R									P	P						P	P			
2H-CC	13.40	13.45	G	A				P									P						P																				
3H-CC	22.88	22.93	G	A								P						P					P					P				R							P				
4H-CC	32.25	32.30	G	A											P														P				R						P				
5H-CC	41.09	41.14	G	F								P			R		P						R						R										R	P			
6H-CC	50.95	51.00	G	A																			R	P								R	R									
7H-CC	61.22	61.27	G	D																			R									P	R									
8H-CC	70.48	70.53	G	D													P	P							P				P			R	R									
9X-CC	76.65	76.70	M	F								F						R							P																		
10X-CC	84.32	84.37	G	D								P						R							P				R			R	R						P	P			
11X-CC	92.56	92.61	G	D			P						P											P									P		P	P	P			P			P
12X-CC	101.15	101.20	G	A											P									P	P				P	R	P		P						R				
13X-CC	110.44	110.49	G	A		P												P									P			P			R						R		P		
14X-CC	121.18	121.23	G	A																				A					P				A						P				
15X-CC	129.38	129.43	G	F											R		P	R								P					P	P										
16X-CC	140.05	140.10	G	F								P	R		R			R											P					P									
17X-CC	149.92	149.97	M	A					P									R											P	R													
18X-CC	159.02	159.07	G	F														R				P	P			P			P														R
19X-CC	165.76	165.81	G	D										D															P										R				
20X-CC	178.73	178.78	G	D														P				R			R					R			P						P				
21X-CC	187.55	187.60	G	D									P		R			A							P				P	R			R						R				
22X-CC	197.03	197.08	G	D														R					P		R								A										
23X-CC	206.98	207.03	G	D							P			P			P	P					R						P														
24X-CC	217.31	217.36	G	A										P	P							R							P														
25X-CC	224.61	224.66	M	F	P										P			F						R	F	P																	
26X-CC	236.23	236.28	G	F					P					P	R		P	R						R			R				P	P	P	R									
27X-CC	246.21	246.26	G	A	P		R								P		P			P		R		P			P		R	R				P								P
28X-CC	256.03	256.08	G	A			R						P		P		P	P				R		P			P			P			F				P					R
29X-CC	265.47	265.52	G	A			R				P								P						P	P	R				P											
30X-CC	275.32	275.37	G	A			R		P			R			R			R							R	R	R		P	F				P								
31X-CC	284.56	284.61	M	F			P					R			P										R	R					P									P			P
32X-CC	293.63	293.68	G	F					P													P			P	P	P			R			P	R				P				P
33X-CC	302.60	302.65	M	R							R	R			R			R							R	R													P				
34X-CC	313.11	313.16	G	A											R						P		P							R					P				R	R			
35X-CC	323.17	323.22	G	A											R														P	R		R										
36X-CC	332.58	332.63	M	F						R	F	R									P					R				R		R							R				
37X-CC	335.22	335.27	G	D							R	R																	R	R	P		P						P				
38X-CC	351.21	351.26	G	A												R							P		P					P									P				

Table T9 (continued). (Continued on next page.)

Core, section	Depth (mbsf) Top	Depth (mbsf) Bottom	Preservation	Abundance	*Melonis barleeanus*	*Melonis pompilioides*	*Melonis* spp.	*?Myllostomella* spp.	*?Neoeponides* spp.	Nodosariidae indet.	*Nonionella* cf. *bradii*	*Nonionella turgida*	*Nonionella* spp.	*Oolina* spp.	*Oridorsalis* spp.	*Orthomorphina* spp.	*Pattelina corrugata*	*Planulina ariminensis*	*Planulina* spp.	*Pleurostomella alternans*	*Proxifrons inaequalis*	*Pseudoclavulina* spp.	*Pseudoglandulina* spp.	*Pullenia bulloides*	*Pullenia quinqueloba*	*Pullenia* spp.	*Pyrgo* spp.	*Quinqueloculina* spp.	*Rhizammina* spp.	*Rosalina bradyi*	*Rosalina* spp.	*Sigmoilopsis schlumbergeri*	*Siphonina tubulosa*	*Siphonodosaria hispidula*	*Siphonodosaria ketienziensis*	*Siphonodosaria* sp. 2	*Siphonodosaria* spp.	*Siphogenerina columellaris*	*Siphogenerina dimorpha*	*Siphogenerina* spp.	*Siphotextularia* spp.	*Siphouvigerina ampullacea*	*Sphaeroidina bulloides*
339-U1390A-																																										
1H-CC	3.58	3.63	G	A	F	R	R			P				P				P										R					P					R				P
2H-CC	13.40	13.45	G	A	P	R																					P	P	P														
3H-CC	22.88	22.93	G	A	P	R	P																				R	R				P										P
4H-CC	32.25	32.30	G	A								A																R														P
5H-CC	41.09	41.14	G	F	A				P				P												P		R	F			R									P	P	P	P
6H-CC	50.95	51.00	G	A	P							P													P		P	R				P										R
7H-CC	61.22	61.27	G	D	A	P									P												R	R															
8H-CC	70.48	70.53	G	D	F																							R				P										
9X-CC	76.65	76.70	M	F	R		P																					F			R											
10X-CC	84.32	84.37	G	D	A	R												R									R	P				R										R
11X-CC	92.56	92.61	G	D	R																							P	A	P													
12X-CC	101.15	101.20	G	A	F	R	P			P																P		F			P							P				
13X-CC	110.44	110.49	G	A	R	R																					P	R	A			P										
14X-CC	121.18	121.23	G	A	R	R											P									P		R														P
15X-CC	129.38	129.43	G	F	P		R						P															F				P						P	P			
16X-CC	140.05	140.10	G	F	P		F			R			P															R			R							P				P
17X-CC	149.92	149.97	M	A																						P	R				R										P
18X-CC	159.02	159.07	G	F									R														R	F	P			P										
19X-CC	165.76	165.81	G	D											P									R	R			R														
20X-CC	178.73	178.78	G	D	A	R												P							P			R			P										R
21X-CC	187.55	187.60	G	D	A																			R	P			P														P
22X-CC	197.03	197.08	G	D	F	R												R									R	R														F
23X-CC	206.98	207.03	G	D	F	R												P	P								R	R														P
24X-CC	217.31	217.36	G	A	A								R								P				P		F	A														P
25X-CC	224.61	224.66	M	F	F	R													R					P				R														P
26X-CC	236.23	236.28	G	F	F	P				P												P						R												P	P	P
27X-CC	246.21	246.26	G	A	R	P																R					R	R				R										F
28X-CC	256.03	256.08	G	A													P						P							P	P					P					F
29X-CC	265.47	265.52	G	A	R	P	R	P		R																	P	P												P		
30X-CC	275.32	275.37	G	A	F	R	R												P	P	P						P	P				P										R
31X-CC	284.56	284.61	M	F	P		R																					F				P					P				P
32X-CC	293.63	293.68	G	F	P					R	P																P	P					R	R		R					P
33X-CC	302.60	302.65	M	R															P								R			P			P								R
34X-CC	313.11	313.16	G	A											R									P	P			R					P	P	R						F
35X-CC	323.17	323.22	G	A						P					R									R				A				P		F	P						R
36X-CC	332.58	332.63	M	F	F														R					F			P	R			R										F
37X-CC	335.22	335.27	G	D	P	R	P																	R			R	A				P									R
38X-CC	351.21	351.26	G	A	R					R						P		P										R			P			R	R	R					R

Table T9 (continued).

Core, section	Depth (mbsf) Top	Depth (mbsf) Bottom	Preservation	Abundance	*Spirillina* spp.	*?Spiroloculina* spp.	*Spiroloculina excavata*	*Spiroloculina* spp.	*Spiroplectammina* spp.	Stillostomellidae indet.	*Stilostomella* spp.	*Textularia pseudogramen*	*Textularia* spp.	*Trifarina angulosa*	*Trifarina bradyi*	*Trifarina* spp.	*Triloculina tricarinata*	*Triloculina* spp.	*Uvigerina auberiana*	*Uvigerina* cf. *auberiana*	*Uvigerina hispida*	*Uvigerina mediterranea*	*Uvigerina peregrina*	*Uvigerina* cf. *proboscidea*	*Uvigerina* spp.	*Vaginulina* spp.	Vaginulinidae indet.	*Valvulineria* spp.	*Vulvulina pennatula*
339-U1390A-																													
1H-CC	3.58	3.63	G	A					P				R		R			P							P		P		
2H-CC	13.40	13.45	G	A		R								R		P	P					P	P				P		
3H-CC	22.88	22.93	G	A				P					R	R		P								P	R			R	
4H-CC	32.25	32.30	G	A				R						F											R				
5H-CC	41.09	41.14	G	F				P				P		P		R		P							A				
6H-CC	50.95	51.00	G	A									R	R	P										A				
7H-CC	61.22	61.27	G	D										R	P										A				
8H-CC	70.48	70.53	G	D			P						F	P											A				
9X-CC	76.65	76.70	M	F										P														P	
10X-CC	84.32	84.37	G	D									R	P					R	P		A			R				
11X-CC	92.56	92.61	G	D												R							P		P				
12X-CC	101.15	101.20	G	A			P									P					P	P	P	R	F			P	
13X-CC	110.44	110.49	G	A				R		P	P					P									R				
14X-CC	121.18	121.23	G	A					P					P		P									A				P
15X-CC	129.38	129.43	G	F		P		P						P		P									R				
16X-CC	140.05	140.10	G	F				R																	P				
17X-CC	149.92	149.97	M	A				P						A		P									R				
18X-CC	159.02	159.07	G	F				R					R	P					R	P					R				
19X-CC	165.76	165.81	G	D												R									R				
20X-CC	178.73	178.78	G	D									P	F	R				F			F			A	P			
21X-CC	187.55	187.60	G	D				R					R										P		A				
22X-CC	197.03	197.08	G	D									A	A					R						A				
23X-CC	206.98	207.03	G	D			P						R	F							P				F				
24X-CC	217.31	217.36	G	A	P								P	F											P	P			
25X-CC	224.61	224.66	M	F									R	A					P						F				
26X-CC	236.23	236.28	G	F									P	P		P						R			F				
27X-CC	246.21	246.26	G	A			P							F		R			P				P						
28X-CC	256.03	256.08	G	A				P					P	R		P			P			P	P		F				P
29X-CC	265.47	265.52	G	A									P	R		R									P				
30X-CC	275.32	275.37	G	A										P					R										
31X-CC	284.56	284.61	M	F	P			P		P	P		P	P							P				R				
32X-CC	293.63	293.68	G	F			P	R	P				P	P	P				R		R		F		R				
33X-CC	302.60	302.65	M	R									R																
34X-CC	313.11	313.16	G	A						P	P								R		R				R				
35X-CC	323.17	323.22	G	A									R	R									P		R				
36X-CC	332.58	332.63	M	F			P	P					R	F		P			P						F				
37X-CC	335.22	335.27	G	D									P	F		R									R				
38X-CC	351.21	351.26	G	A				R						R		R									P				

Table T10. Abundance of pollen and spores, Hole U1390A.

Core, section	Depth (mbsf) Top	Depth (mbsf) Bottom	Preservation	Abundance	Exotic counted	*Alnus*	*Anthemis* type	Apiaceae	*Artemisia*	*Asphodelus*	*Aster* type	*Betula*	Brassicaceae	Caryophyllaceae	*Cedrus*	Chenopodiaceae	Cupressaceae	Cyperaceae	*Ephedra distachya* type	*Ephedra fragilis* type	Ericaceae	*Fraxinus excelsior* type	*Helianthemum*	*Isoetes*	*Olea*	*Pinus*	*Plantago*	Poaceae	*Quercus* deciduous type	*Quercus* evergreen type	*Quercus suber* type	*Tamarix*	*Taraxacum* type	Taxodiaceae/Cupressaceae	Trilete ornamented	*Trilete psilate*	*Ulmus*
339-U1390A-																																					
1H-CC	3.58	3.63	G	A	50		F				C		C		F	C	C	F		F		F		A	F	C	F	C	A	C	C	F	A		F		
6H-CC	50.95	51.00	G	A	24		F	F	A		A	F	C	F	A	A	F			F	A			F	F	A		C	A	F	F		A				
12X-CC	101.15	101.20	G	A	54			F	C		F		C			C				F	F			C	F	C	F	C	C	F			A				F
18X-CC	159.02	159.07	M	A	31	F	C	C	A		F		C		C	A	F				C			F		A	C	C	A	C			A				
24X-CC	217.31	217.36	P	A	26				A		C					A	C	F	C	F						A		A					C				
30X-CC	275.32	275.37	M	A	31		F	C	C	F	C		F		F	C		C			C		F	C	C	C		C	C	C	F		A	F			
36X-CC	332.58	332.63	M	A	104				F		F		F								F			F	F	C			C	F			C			F		

Preservation: G = good, M = moderate, P = poor. Abundance: A = abundant, C = common, F = few. See **"Biostratigraphy"** in the "Methods" chapter (Expedition 339 Scientists, 2013b) for abundance and preservation definitions.

Table T11. FlexIt tool core orientation data, Site U1390.

Core	Orientation angle (°)	Orientation standard deviation (°)
339-U1390B-		
4H	194	0.88
5H	143	0.49
6H	134	0.60
7H	303	0.21
8H	275	1.05
9H	283	0.18
10H	201	0.21
11H	184	0.47
12H	230	0.07
13H	104	0.26
14H	188	0.21
15H	250	0.26
16H	75	0.20
17H	251	0.10
18H	76	0.15
19H	55	0.02
20H	166	1.38
21H	92	0.55
339-U1390C-		
9H	298	0.13
10H	60	0.18
11H	301	0.03
12H	269	0.05
13H	225	0.03
14H	348	0.03
15H	129	0.00
16H	184	0.02
17H	141	0.16
18H	18	0.16
19H	23	0.06

Table T12. Disturbed intervals, Site U1390. (Continued on next two pages.)

Core, section, interval (cm)	Drilling disturbance	
	Intensity	Comment
339-U1390A-		
1H-1	Moderate	Soupy mudline extending downhole to ~30 cm, but do not cull data in this interval.
1H-2, 135–140	High	Whole-round IW sample
2H-1, 0–34	High	Disturbed core top
2H-5, 145–150	High	Whole-round IW sample
2H-6, 136–141	High	MBIO
3H-1, 149–150	Void	Void
3H-5, 145–150	High	Whole-round IW sample
4H-1, 0–22	High	Disturbed core top
4H-5, 145–150	High	Whole-round IW sample
4H-6, 96–103	High	MBIO
4H-6, 96–101	High	IW tube sample
5H-2, 0–22	High	Disturbed
5H-6, 145–150	High	Whole-round IW sample
6H-1, 0–17	High	Disturbed core top
6H-4, 147–152	High	Whole-round IW sample
6H-5, 147–152	High	IW tube sample
6H-5, 146–151	High	MBIO
7H-1, 0–3	High	Disturbed core top
7H-5, 150–155	High	Whole-round IW sample
8H-1, 0–15	Moderate	Disturbed core top
8H-5, 140–146	High	Whole-round IW sample
8H-6, 136–141	High	MBIO
9H-1, 0–150	Moderate	Disturbed core top
9H-2, 0–10	Moderate	Disturbed
9H-2, 141–145	Void	Void
10X-3, 140–151	High	Whole-round IW sample
10X-4, 144–150	High	MBIO
11X-4, 140–150	High	Whole-round IW sample
12X-1, 0–6	Moderate	Disturbed core top
12X-3, 140–150	High	Whole-round IW sample
12X-4, 145–150	High	MBIO
13X-3, 140–150	High	Whole-round IW sample
14X-1, 0–11	Moderate	Disturbed core top
14X-4, 139–150	High	Whole-round IW sample
14X-5, 143–150	High	MBIO
15X-3, 139–150	High	Whole-round IW sample
16X-1, 0–12	Moderate	Disturbed core top
16X-4, 136–150	High	Whole-round IW sample
16X-5, 145–150	High	MBIO
17X-1, 0–2	High	Disturbed core top
17X-3, 140–150	High	Whole-round IW sample
18X-1, 10–13	Void	Void
18X-4, 98–109	High	Whole-round IW sample
18X-5, 144–150	High	MBIO
19X-1, 0–9	High	Disturbed core top
19X-2, 115–126	High	Whole-round IW sample
20X-3, 139–150	High	Whole-round IW sample
21X-4, 139–150	High	Whole-round IW sample
22X-1, 0–7	High	Disturbed core top
22X-4, 140–150	High	Whole-round IW sample
22X-5, 120–125	High	MBIO
23X-1, 0–22	High	Disturbed core top
23X-4, 139–150	High	Whole-round IW sample
23X-5, 87–89	Void	Void
24X-4, 132–142	High	Whole-round IW sample
24X-6, 62–66	Void	Void
25X-1, 0–123	Moderate	Disturbed core top
25X-4, 135–150	High	Whole-round IW sample
26X-1, 0–3	High	Disturbed core top
26X-4, 134–150	High	Whole-round IW sample
26X-5, 143–150	High	MBIO
27X-1, 0–40	Moderate	Disturbed core top
27X-5, 134–150	High	Whole-round IW sample
28X-5, 134–150	High	Whole-round IW sample
29X-1, 0–2	High	Disturbed core top
29X-5, 134–150	High	Whole-round IW sample
30X-1, 0–11	Moderate	Disturbed core top

Table T12 (continued). (Continued on next page.)

Core, section, interval (cm)	Drilling disturbance	
	Intensity	Comment
30X-2, 0–2	Moderate	Disturbed core top
30X-5, 135–150	High	Whole-round IW sample
30X-6, 140–146	High	MBIO
31X-1, 0–11	Moderate	Disturbed core top
31X-4, 134–150	High	Whole-round IW sample
32X-1, 0–5	High	Disturbed core top
32X-4, 134–150	High	Whole-round IW sample
33X-4, 134–150	High	Whole-round IW sample
34X-4, 134–150	High	Whole-round IW sample
34X-5, 144–150	High	MBIO
34X-6, 142–150	Void	Void
35X-3, 135–150	High	Whole-round IW sample
36X-1, 0–5	Moderate	Disturbed core top
36X-4, 134–150	High	Whole-round IW sample
37X-1, 0–0	High	Much of this core is disturbed, but it is the only record of this interval for the site.
38X-1, 0–10	High	Disturbed core top
38X-3, 135–150	High	Whole-round IW sample
38X-5, 144–150	High	MBIO
339-U1390B-		
1H-1, 0–0	Moderate	Soupy mudline extending downhole to ~20 cm, but do not cull data in this interval.
2H-1, 0–27	Moderate	Disturbed core top
4H-4, 18–20	Void	Void
6H-1, 0–7	Moderate	Disturbed core top
7H-1, 0–12	Moderate	Disturbed core top
7H-2, 106–109	Void	Void
7H-3, 111–114	Void	Void
7H-4, 65–69	Void	Void
8H-2, 132–141	Void	Void
8H-7, 83–88	Void	Void
10H-1, 0–6	High	Disturbed core top
11H-2, 61–64	Void	Void
12H-1, 0–34	High	Disturbed core top
12H-2, 71–75	Void	Void
13H-4, 71–74	Void	Void
13H-5, 13–23	High	Disturbed
14H-3, 70–77	Void	Void
15H-1, 0–7	High	Disturbed core top
15H-1, 63–68	Void	Void
16H-1, 0–5	Moderate	Disturbed core top
16H-2, 86–96	Void	Void
17H-3, 91–106	Void	Void
19H-1, 0–18	High	Disturbed core top
19H-2, 0–2	High	Disturbed core top (continued)
19H-2, 131–138	Void	Void
19H-3, 126–133	Void	Void
20H-1, 0–22	High	Disturbed core top
20H-1, 56–78	Void	Void
20H-2, 72–78	Void	Void
20H-2, 107–113	Void	Void
21H-4, 0–2	Void	Void
21H-4, 87–111	High	Stretched
339-U1390C-		
1H-1, 0–0	Moderate	Soupy mudline extending downhole to ~20 cm, but do not cull data in this interval.
2H-1, 0–6	Moderate	Disturbed core top
3H-3, 127–137	High	PAL whole-round sample
4H-1, 0–3	Moderate	Disturbed core top
5H-1, 0–55	Moderate	Disturbed core top
5H-4, 0–20	High	Disturbed
5H-8, 0–32	Moderate	Disturbed
6H-1, 0–5	Moderate	Disturbed core top
7H-1, 0–7	High	Disturbed core top
8H-1, 0–2	High	Disturbed core top
10H-1, 0–10	High	Disturbed core top
10H-7, 121–126	Void	Void
10H-8, 86–93	Void	Void
11H-1, 0–5	Moderate	Disturbed core top
12H-1, 0–4	High	Disturbed core top
12H-3, 11–17	Void	Void

Table T12 (continued).

Core, section, interval (cm)	Drilling disturbance	
	Intensity	Comment
12H-3, 57–62	Void	Void
12H-4, 38–45	Void	Void
12H-5, 21–25	Void	Void
12H-6, 70–79	Void	Void
13H-1, 0–2	High	Disturbed core top
13H-1, 61–64	Void	Void
13H-2, 129–141	Void	Void
14H-1, 0–3	High	Disturbed core top
15H-1, 0–2	High	Disturbed core top
15H-2, 136–141	Void	Void
16H-1, 0–11	High	Disturbed core top
16H-1, 87–90	Void	Void
16H-1, 58–66	Void	Void
17H-1, 0–5	Moderate	Disturbed core top
17H-6, 53–58	Void	Void
18H-1, 0–3	High	Disturbed core top
18H-1, 57–63	High	Disturbed
19H-1, 0–3	High	Disturbed core top
19H-1, 51–59	Void	Void

IW = interstitial water, MBIO = microbiology sample, PAL = paleontology.

Table T13. NRM inclination, declination, and intensity data after 20 mT peak field AF demagnetization, Hole U1390A.

Core, section, interval (cm)	Depth (mbsf)	Inclination (°)	Declination (°)	FlexIt-corrected declination (°)	Intensity (A/m)
339-U1390A-					
1H-1	0.00				
1H-1, 5	0.05				
1H-1, 10	0.10				
1H-1, 15	0.15				
1H-1, 20	0.20				
1H-1, 25	0.25				
1H-1, 30	0.30				
1H-1, 35	0.35	47.5	356.4		0.013872
1H-1, 40	0.40	44.2	358.5		0.015522
1H-1, 45	0.45	42.4	3		0.015575
1H-1, 50	0.50	41.1	7.2		0.015122
1H-1, 55	0.55	43.3	7.4		0.014166
1H-1, 60	0.60	44.6	10		0.015767
1H-1, 65	0.65	45	9.6		0.018397
1H-1, 70	0.70	45.8	8.7		0.019636
1H-1, 75	0.75	45.9	7.5		0.020464
1H-1, 80	0.80	47.3	6.1		0.022225
1H-1, 85	0.85	48	4.3		0.024246
1H-1, 90	0.90	48.9	3.8		0.025496
1H-1, 95	0.95	49.5	6		0.026289
1H-1, 100	1.00	49	7.8		0.027149
1H-1, 105	1.05	49.4	9.9		0.026387
1H-1, 110	1.10	52	11.5		0.024941
1H-1, 115	1.15	52.8	13		0.024402
1H-1, 120	1.20	54.1	13.8		0.024033
1H-1, 125	1.25	53.7	12.6		0.025143
1H-1, 130	1.30	53.8	11.3		0.025206
1H-1, 135	1.35	52.1	9.8		0.024996
1H-1, 140	1.40				
1H-1, 145	1.45				
1H-1, 150	1.50				
1H-2	1.50				
1H-2, 5	1.55				
1H-2, 10	1.60				
1H-2, 15	1.65	53.2	357.7		0.021217
1H-2, 20	1.70	53.8	356.5		0.022312
1H-2, 25	1.75	54.3	358.4		0.023273
1H-2, 30	1.80	52.6	358.5		0.023094
1H-2, 35	1.85	52.7	358.2		0.022306
1H-2, 40	1.90	53.5	0.9		0.021291
1H-2, 45	1.95	53.2	1.1		0.021183
1H-2, 50	2.00	51.7	0.7		0.021908
1H-2, 55	2.05	53.3	359.6		0.019657
1H-2, 60	2.10	55.4	0.2		0.017757
1H-2, 65	2.15	53.2	2.5		0.018055
1H-2, 70	2.20	50.6	3.1		0.019636
1H-2, 75	2.25	49.6	4		0.020442
1H-2, 80	2.30	49.9	3.1		0.020009
1H-2, 85	2.35	50.9	4.2		0.018918
1H-2, 90	2.40	52.5	3.5		0.018246
1H-2, 95	2.45	52.3	1.3		0.018275
1H-2, 100	2.50	49.7	1.4		0.019906
1H-2, 105	2.55	48.2	1.9		0.021962
1H-2, 110	2.60	48.8	359.2		0.022813
1H-2, 115	2.65	49.3	358.7		0.022295
1H-2, 120	2.70	49.5	356.7		0.021147
1H-2, 125	2.75	46.9	355.3		0.020505

Blank cells indicate depth levels where data were either not available (i.e., FlexIt-corrected declination data for nonoriented cores) or removed because of disturbance, voids, or measurement edge effects. Only a portion of this table appears here. The complete table is available in **ASCII.**

Table T14. NRM inclination, declination, and intensity data after 20 mT peak field AF demagnetization, Hole U1390B.

Core, section, interval (cm)	Depth (mbsf)	Inclination (°)	Declination (°)	FlexIt-corrected declination (°)	Intensity (A/m)
339-U1390B-					
1H-1, 5	0.00				
1H-1, 10	0.05				
1H-1, 15	0.10				
1H-1, 20	0.15				
1H-1, 25	0.20				
1H-1, 30	0.25	65.1	289.6		0.013384
1H-1, 35	0.30	65.8	288.7		0.01412
1H-1, 40	0.35	63.1	289.4		0.013994
1H-1, 45	0.40	62.7	290.7		0.013894
1H-1, 50	0.45	65.4	280.9		0.012762
1H-1, 55	0.50	61.8	293.9		0.013707
1H-1, 60	0.55	52.8	298.9		0.016247
1H-1, 65	0.60	51.5	299.6		0.016253
1H-1, 70	0.65	51.3	300.4		0.015495
1H-1, 75	0.70	51.7	303.3		0.014075
1H-1, 80	0.75	52.8	304.1		0.013811
1H-1, 85	0.80	55	307.1		0.01403
1H-1, 90	0.85	57.1	307		0.014722
1H-1, 95	0.90	58.1	304.7		0.015609
1H-1, 100	0.95	56.1	303.2		0.017359
1H-1, 105	1.00	55.6	299.4		0.019414
1H-1, 110	1.05	56.7	297		0.020229
1H-1, 115	1.10	55.9	296		0.020981
1H-1, 120	1.15	55.9	294.5		0.021093
1H-1, 125	1.20	56.9	292.6		0.021522
1H-1, 130	1.25	57.4	289.6		0.021967
1H-1, 135	1.30	55.8	289.4		0.022786
1H-1, 140	1.35	53.5	292.5		0.023647
1H-1, 145	1.40				
1H-1, 150	1.45				
1H-1, 5	1.50				
1H-2, 5	1.50				
1H-2, 10	1.55				
1H-2, 15	1.60				
1H-2, 20	1.65	52.1	302.6		0.025076
1H-2, 25	1.70	59.3	296.1		0.021283
1H-2, 30	1.75	61.9	293.3		0.020281
1H-2, 35	1.80	58.9	297.1		0.022316
1H-2, 40	1.85	56.3	288.2		0.022915
1H-2, 45	1.90	55.3	282.2		0.025253
1H-2, 50	1.95	55.2	283.5		0.026948
1H-2, 55	2.00	56.5	285		0.026805
1H-2, 60	2.05	56.5	283.7		0.025867
1H-2, 65	2.10	56.9	283.1		0.024144
1H-2, 70	2.15	56.1	283.6		0.024061
1H-2, 75	2.20	55.4	283.3		0.023781
1H-2, 80	2.25	54.9	284.4		0.023896
1H-2, 85	2.30	54.9	284.6		0.023037
1H-2, 90	2.35	54.9	283.6		0.022623
1H-2, 95	2.40	53.3	283		0.022836
1H-2, 100	2.45	52.9	283.8		0.022602
1H-2, 105	2.50	52.7	283.4		0.022312
1H-2, 110	2.55	52.7	282.3		0.022364
1H-2, 115	2.60	52.8	279.3		0.022478
1H-2, 120	2.65	53.5	279.7		0.023816

Blank cells indicate depth levels where data were either not available (i.e., FlexIt-corrected declination data for nonoriented cores) or removed because of disturbance, voids, or measurement edge effects. Only a portion of this table appears here. The complete table is available in **ASCII.**

Table T15. NRM inclination, declination, and intensity data after 20 mT peak field AF demagnetization, Hole U1390C.

Core, section, interval (cm)	Depth (mbsf)	Inclination (°)	Declination (°)	FlexIt-corrected declination (°)	Intensity (A/m)
339-U1390C-					
1H-1	0.00				
1H-1, 5	0.05				
1H-1, 10	0.10				
1H-1, 15	0.15				
1H-1, 20	0.20				
1H-1, 25	0.25	58.1	11.9		0.011928
1H-1, 30	0.30	59.7	18		0.013682
1H-1, 35	0.35	58.7	23.1		0.014807
1H-1, 40	0.40	53.7	24		0.016416
1H-1, 45	0.45	49.6	21.7		0.017709
1H-1, 50	0.50	47.8	25.6		0.017972
1H-1, 55	0.55	48.2	28.9		0.016626
1H-1, 60	0.60	50.1	28.3		0.015304
1H-1, 65	0.65	48.7	30.4		0.015979
1H-1, 70	0.70	52.8	30.4		0.015938
1H-1, 75	0.75	55.5	29.2		0.016719
1H-1, 80	0.80	55.5	31.7		0.018416
1H-1, 85	0.85	56.7	28.2		0.018512
1H-1, 90	0.90	53.7	25.2		0.019808
1H-1, 95	0.95	50.2	23.7		0.022601
1H-1, 100	1.00	51.3	22.2		0.021702
1H-1, 105	1.05	53.2	20.9		0.019249
1H-1, 110	1.10	53.6	21.5		0.019411
1H-1, 115	1.15	52.7	22.3		0.021834
1H-1, 120	1.20	51.3	27.7		0.023745
1H-1, 125	1.25	50.8	32.6		0.022148
1H-1, 130	1.30	53.2	33.1		0.017857
1H-1, 135	1.35	55.4	28.9		0.016061
1H-1, 140	1.40				
1H-1, 145	1.45				
1H-1, 150	1.50				
1H-2	1.50				
1H-2, 5	1.55				
1H-2, 10	1.60				
1H-2, 15	1.65	52.5	28		0.024315
1H-2, 20	1.70	53.2	29.8		0.023536
1H-2, 25	1.75	53.6	32		0.022773
1H-2, 30	1.80	53.1	32.1		0.023846
1H-2, 35	1.85	51	29.4		0.025636
1H-2, 40	1.90	50.8	27		0.02621
1H-2, 45	1.95	51.5	25		0.025673
1H-2, 50	2.00	50.9	25.3		0.025022
1H-2, 55	2.05	51	25.7		0.024539
1H-2, 60	2.10	51.6	23.8		0.024092
1H-2, 65	2.15	51.5	22.3		0.024333
1H-2, 70	2.20	51.5	21.6		0.02416
1H-2, 75	2.25	52	17.9		0.022811
1H-2, 80	2.30	51.4	18.4		0.022638
1H-2, 85	2.35	50.9	21.2		0.022447
1H-2, 90	2.40	50.4	22.5		0.022804
1H-2, 95	2.45	51.2	22.7		0.021685
1H-2, 100	2.50	51.9	22.8		0.021641
1H-2, 105	2.55	53.2	23.1		0.022389
1H-2, 110	2.60	53	25.2		0.021864
1H-2, 115	2.65	51.5	25.2		0.021175
1H-2, 120	2.70	51.4	23.8		0.019841

Blank cells indicate depth levels where data were either not available (i.e., FlexIt-corrected declination data for nonoriented cores) or removed because of disturbance, voids, or measurement edge effects. Only a portion of this table appears here. The complete table is available in **ASCII.**

Table T16. Headspace sample hydrocarbon concentrations, Hole U1390A.

Core, section	Depth (mbsf)	Concentration (ppmv)				
		Methane	Ethene	Ethane	Propene	Propane
339-U1390A-						
1H-3	2.90	2.88	—	—	—	—
2H-7	12.54	2.67	—	—	—	0.36
3H-7	21.92	10,035.08	—	—	—	—
4H-7	31.16	30,249.31	0.43	0.52	—	—
5H-7	39.39	26,534.37	0.41	—	—	—
6H-6	49.23	63,991.88	1.28	1.94	1.41	—
7H-7	59.95	25,331.80	0.76	1.43	—	—
8H-7	69.19	9,266.37	—	1.1	—	—
10X-4	81.21	6,192.27	0.68	1.27	—	0.41
11X-5	89.50	5,144.98	0.74	1.69	—	—
12X-4	97.60	6,686.41	0.57	2.29	—	—
13X-4	107.20	8,108.68	—	2.74	—	—
14X-5	118.15	7,466.70	0.51	3.49	—	—
15X-4	126.40	14,170.22	1.04	7.59	—	—
16X-5	137.40	7,982.97	—	4.91	—	—
17X-4	145.40	9,196.75	—	4.04	—	—
18X-5	156.09	5,456.44	—	2.48	—	—
19X-3	162.86	6,748.13	1.58	4.57	—	—
20X-4	174.10	7,080.24	0.43	5.82	—	—
21X-6	186.30	7,407.62	0.48	4.7	—	—
22X-6	196.05	10,894.07	0.42	6.77	—	—
23X-6	206.82	7,504.57	0.82	8.07	—	—
24X-7	216.33	7,337.89	1.49	13.5	—	—
25X-5	223.50	9,447.93	1.20	14.74	—	0.45
26X-6	234.50	4,391.90	—	8.98	—	0.53
27X-7	245.21	3,193.33	0.53	5.13	—	—
28X-7	254.92	3,244.92	—	7.15	—	0.66
29X-7	263.95	3,661.48	—	7.34	0.41	0.34
30X-8	274.27	12,261.30	—	21.66	0.38	—
31X-7	283.57	4,799.19	—	9.63	—	—
32X-6	292.20	4,845.77	—	11.73	—	—
33X-6	301.51	8,235.29	—	16.6	—	—
34X-5	309.89	15,951.64	1.35	41.98	—	0.44
35X-4	317.44	5,984.93	—	11.52	—	—
36X-5	329.01	16,457.88	0.64	29.09	—	0.61
37X-2	335.00	7,959.99	0.75	18.86	—	—
38X-4	346.40	9,830.54	2.48	46.38	—	11.52

— = no data.

Table T17. Interstitial water major and trace elements, Hole U1390A. (Continued on next page.)

Core, section, interval (cm	Depth (mbsf)	B (μM) 208.96 nm ICPAES	Ba (μM) 455.40 nm ICPAES	Fe (μM) 239.56 nm ICPAES	Li (μM) 670.78 nm ICPAES	Mn (μM) 257.61 nm ICPAES	Si (μM) 288.16 nm ICPAES	Sr (μM) 407.77 nm ICPAES	Alkalinity (meq/L) TITRA_AUTO	pH ISE	Salinity (%)	Cl^- (mM) TITRA_AUTO	SO_4^{2-} (mM) IC	Na^+ (mM) IC
339-U1390A-														
1H-2, 135–140	2.85	493.65	1.86	27.39	25.71	7.45	397.05	67.84	11.06	7.69	3.8	586.92	18.84	478.83
2H-5, 145–150	11.07	519.28	2.47	53.90	27.18	1.13	413.41	90.06	15.43	7.73	3.6	584.71	4.82	498.37
3H-5, 145–150	20.56	558.82	27.28	18.52	16.02	0.94	337.75	57.49	9.90	7.85	3.4	579.61	0	465.23
4H-5, 145–150	30.08	556.42	23.85	15.51	16.40	0.81	369.05	66.70	10.89	7.90	3.4	586.65	0	473.76
5H-6, 145–150	39.34	561.88	19.95	9.76	14.23	0.64	353.15	55.05	11.99	7.94	3.5	583.48	0	460.20
6H-4, 147–152	47.64	526.10	18.74	5.23	16.85	0.75	348.52	80.27	14.11	8.02	3.5	592.21	0	492.56
7H-5, 150–155	58.40	473.66	15.44	4.93	19.36	0.74	405.74	72.74	14.79	7.96	3.6	607.01	0	495.24
8H-5, 141–146	67.73	412.77	16.87	2.26	19.41	0.50	270.00	61.20	11.05	7.92	3.7	625.46	0	511.61
10X-3, 141–151	81.11	417.16	13.57	3.68	18.10	1.15	324.02	70.31	8.47	8.04	3.9	660.26	0	567.97
11X-4, 141–150	89.41	379.47	14.06	3.31	17.30	1.45	368.04	97.97	7.74	7.81	4.1	686.62	0	567.52
12X-3, 140–150	97.50	371.32	15.10	3.59	16.50	1.16	268.86	86.52	6.49	7.75	4.2	711.98	0	567.05
13X-3, 140–150	107.10	368.40	22.15	2.60	17.33	1.56	270.78	104.70	5.67	8.04	4.4	749.39	0	598.51
14X-4, 140–150	118.05	346.13	40.90	3.60	22.29	1.22	335.22	113.76	6.31	7.93	4.7	806.39	0	626.90
15X-3, 140–150	126.30	381.75	48.94	4.29	29.10	1.30	368.09	147.29	7.58	7.76	NA	844.87	0	647.72
16X-4, 140–150	137.30	377.70	65.54	2.18	25.98	0.97	306.50	142.88	5.92	7.97	5.4	905.16	0	703.39
17X-3, 140–150	145.30	341.92	67.64	3.49	27.20	1.43	386.03	184.26	5.56	7.83	5.6	956.22	0	737.79
18X-4, 140–150	155.99	394.18	66.78	3.12	35.15	1.27	369.03	241.81	7.51	7.81	6.0	1,025.97	0	778.06
19X-2, 116–126	162.76	372.68	72.78	60.19	38.75	1.75	805.11	320.72	8.53	7.59	6.1	1,068.49	0	822.91
20X-3, 140–150	174.00	321.97	90.76	38.32	44.64	1.48	511.29	547.78	7.76	7.58	6.4	1,139.57	0	842.50
21X-4, 140–150	185.10	287.93	119.69	26.46	48.41	2.13	532.94	846.85	6.54	7.54	6.9	1,206.79	0	844.09
22X-4, 140–150	194.70	329.60	155.52	53.32	47.00	1.86	470.25	1,265.84	6.30	7.49	7.4	1,272.30	0	966.03
23X-4, 140–150	204.30	269.45	212.42	39.25	45.55	2.37	444.25	1,629.94	5.37	7.51	7.6	1,330.94	0	975.24
24X-4, 132–142	213.82	256.51	347.61	3.64	45.87	1.71	307.45	2,043.11	3.66	7.63	8.0	1,396.26	0	1,000.70
25X-4, 135–150	223.35	325.66	478.76	122.35	53.63	2.87	544.90	2,344.84	4.46	7.28	8.3	1,452.89	0	1,079.88
26X-4, 135-140	232.85	305.30	615.68	75.32	60.67	2.69	477.96	2,564.97	4.44	7.42	8.4	1,505.11	0	1,091.88
27X-5, 135–150	244.05	271.52	740.14	38.31	60.11	2.81	356.70	2,621.41	2.78	7.45	8.7	1,520.85	0	1,061.03
28X-5, 135–150	253.65	271.96	989.24	38.62	69.34	3.63	329.70	2,758.98	2.44	7.44	9.0	1,590.00	0	1,103.19
29X-5, 135–150	262.30	294.42	1,042.86	89.56	91.80	3.49	314.37	2,793.18	1.73	7.36	9.2	1,629.08	0	1,131.01
30X-5, 136–150	271.68	273.84	1,097.47	33.43	120.76	3.78	292.57	2,781.83	1.77	7.44	9.3	1,650.90	0	1,168.03
31X-4, 135–150	280.95	275.91	1,196.42	51.06	154.08	3.68	326.48	2,714.81	1.59	7.28	9.7	1,716.33	0	1,210.72
32X-4, 135–150	290.55	281.11	1,131.16	62.33	156.89	3.30	339.85	2,631.73	2.05	7.42	9.9	1,744.76	0	1,248.62
33X-4, 134–150	300.14	261.49	931.38	29.42	154.15	3.07	385.55	2,428.07	1.74	7.41	9.9	1,736.69	0	1,229.26
34X-4, 135–150	309.74	285.20	908.70	31.54	151.84	2.97	414.26	2,260.36	2.09	7.29	10.0	1,754.29	0	1,266.21
35X-3, 135–150	317.29	257.43	686.19	20.67	146.79	2.81	296.49	2,237.74	2.10	7.42	9.8	1,721.58	0	1,229.56
36X-4, 135–150	328.86	251.01	894.61	31.51	134.25	2.78	294.14	2,360.43	1.73	7.32	10.1	1,788.40	0	1,309.32
38X-3, 135–150	346.25	242.34	470.43	31.75	170.12	2.87	561.81	1,925.59	2.47	7.36	9	1,603.56	0	1,168.56

TITRA_AUTO = automatic titration, SPEC = spectrometer, ICPAES = inductively coupled plasma–atomic emission spectrometer, ISE = ion-selective electrode. NA = not available.

Table T17 (continued).

Core, section, interval (cm	Depth (mbsf)	K^+ (mM) IC	Mg^{2+} (mM) IC	Ca^{2+} (mM) IC	Na^+/Cl^-	NH_4^+ (µM) SPEC
339-U1390A-						
1H-2, 135–140	2.85	10.74	51.59	7.71	0.82	1,162
2H-5, 145–150	11.07	10.13	47.10	4.17	0.85	2,932
3H-5, 145–150	20.56	8.89	35.93	3.01	0.80	4,572
4H-5, 145–150	30.08	8.91	35.96	3.03	0.81	5,120
5H-6, 145–150	39.34	8.68	35.20	2.72	0.79	5,641
6H-4, 147–152	47.64	9.75	37.88	2.82	0.83	6,673
7H-5, 150–155	58.40	9.14	38.66	3.29	0.82	7,435
8H-5, 141–146	67.73	10.05	37.47	3.71	0.82	8,439
10X-3, 141–151	81.11	10.15	42.51	5.12	0.86	8,417
11X-4, 141–150	89.41	10.13	43.01	5.51	0.83	8,558
12X-3, 140–150	97.50	9.88	43.02	5.93	0.80	8,055
13X-3, 140–150	107.10	10.57	45.94	6.51	0.80	8,642
14X-4, 140–150	118.05	10.99	50.48	6.48	0.78	9,399
15X-3, 140–150	126.30	11.20	53.89	7.11	0.77	NA
16X-4, 140–150	137.30	11.14	59.34	8.02	0.78	10,759
17X-3, 140–150	145.30	11.09	63.10	9.06	0.77	11,212
18X-4, 140–150	155.99	11.45	67.85	10.68	0.76	13,854
19X-2, 116–126	162.76	11.82	72.20	11.57	0.77	14,432
20X-3, 140–150	174.00	11.73	74.95	12.34	0.74	15,514
21X-4, 140–150	185.10	11.40	75.65	13.65	0.70	14,985
22X-4, 140–150	194.70	12.47	85.10	17.31	0.76	14,901
23X-4, 140–150	204.30	11.90	84.62	19.55	0.73	12,372
24X-4, 132–142	213.82	12.65	83.12	21.48	0.72	14,383
25X-4, 135–150	223.35	12.90	87.41	25.13	0.74	15,321
26X-4, 135-140	232.85	13.03	86.40	26.95	0.73	14,975
27X-5, 135–150	244.05	12.49	80.96	26.93	0.70	13,172
28X-5, 135–150	253.65	12.77	81.75	28.87	0.69	11,842
29X-5, 135–150	262.30	13.12	82.42	29.60	0.69	14,883
30X-5, 136–150	271.68	13.41	83.35	30.60	0.71	13,995
31X-4, 135–150	280.95	13.94	84.28	31.41	0.71	15,164
32X-4, 135–150	290.55	13.61	86.08	31.58	0.72	14,280
33X-4, 134–150	300.14	13.88	82.61	28.87	0.71	16,329
34X-4, 135–150	309.74	14.14	84.09	29.29	0.72	16,853
35X-3, 135–150	317.29	13.75	82.26	28.27	0.71	16,181
36X-4, 135–150	328.86	14.38	86.53	29.17	0.73	16,223
38X-3, 135–150	346.25	14.22	80.53	26.77	0.73	15,809

Table T18. Interstitial water oxygen and hydrogen isotopes, Site U1390.

Core, section, interval (cm)	Depth (mbsf)	$\delta^{18}O$ (‰, VSMOW)	δD (‰, VSMOW)
339-U1390A-			
1H-2, 135–140	2.90	0.89	5.82
2H-5, 145–150	11.13	0.96	5.13
3H-5, 145–150	20.61	0.98	6.27
4H-5, 145–150	30.14	1.06	6.77
5H-6, 145–150	39.39	1.07	6.74
6H-4, 147–152	47.70	0.97	7.89
7H-5, 150–155	58.45	0.82	7.09
8H-5, 141–146	67.78	1.10	7.07
10X-3, 141–146	81.21	1.05	6.18
11X-4, 141–146	89.50	1.33	6.46
12X-3, 140–145	97.60	0.97	6.68
13X-3, 140–145	107.20	0.95	6.56
14X-4, 140–145	118.15	0.65	3.76
15X-3, 140–145	126.40	0.97	3.51
16X-4, 140–145	137.40	0.85	3.25
17X-3, 140–145	145.40	0.93	2.22
18X-4, 99–104	156.09	0.40	–0.34
19X-2, 116–121	162.86	1.09	0.78
20X-3, 140–145	174.10	0.66	–0.46
21X-4, 140–145	185.20	0.76	–0.59
22X-4, 140–145	194.80	0.69	–1.58
24X-4, 132–137	213.92	1.04	–2.36
25X-4, 135–140	223.50	0.82	–2.83
26X-4, 135–140	233.00	0.86	–3.84
27X-5, 135–140	244.20	1.08	–2.78
28X-5, 135–140	253.80	0.84	–4.79
29X-5, 135–140	262.45	0.98	–4.04
30X-5, 136–141	271.82	0.93	–4.45
31X-4, 135–140	281.10	0.89	–6.07
32X-4, 135–140	290.70	1.07	–5.59
33X-4, 135–140	300.30	1.31	–6.47
34X-4, 135–140	309.89	0.94	–5.71
35X-3, 135–140	317.44	1.23	–5.28
36X-4, 135–140	329.01	1.24	–5.50
38X-3, 135–140	346.40	1.39	–4.41

VSMOW = Vienna standard mean ocean water.

Table T19. Results from APCT-3 temperature profiles, Site U1390.

Hole, core	Original depth (mbsf)	Tidal sea level height* (m)	Corrected depth (mbsf)	In situ temperature (°C)	Thermal resistance (m^2K/W)
339-U1390A-					
4H	32.1	0.3	31.55	14.2	26.0
7H	60.6	0.5	59.85	15.12	46.8
339-U1390B-					
2H	18.6	–0.7	19.05	13.56	15.7
5H	47.1	0	46.85	14.51	38.3
8H	75.6	0.6	74.75	15.34	57.8
339-U1390C-					
3H	23.4	–0.8	23.95	13.6	19.2
6H	51.9	0.4	51.25	14.86	41.4
9H	80.4	0.8	79.35	15.42	60.8
12H	108.9	0.1	108.55	16.5	83.9

* = –0.25 m tidal height when mudline Core 339-U1390A-1H was taken. In situ temperatures were determined using TP-Fit software by Martin Heesemann. Thermal resistance was calculated from thermal conductivity data (see **"Physical properties"**) corrected for in situ conditions (see **"Downhole measurements"** in the "Methods" chapter [Expedition 339 Scientists, 2012b]).

Table T20. Splice tie points for Site U1390.

Hole, core, section, interval (cm)	Depth (mbsf)	Depth (mcd)		Hole, core, section, interval (cm)	Depth (mbsf)	Depth (mcd)
339-				339-		
				U1390B-1H-6, 0	0.00	0.00
U1390B-1H-6, 76.30	8.26	8.26	Tie to	U1390C-2H-2, 97.70	6.88	8.26
U1390C-2H-5, 51.10	10.91	12.30	Tie to	U1390B-2H-3, 29.72	12.40	12.30
U1390B-2H-6, 85.38	17.45	17.35	Tie to	U1390A-3H-2, 24.37	14.85	17.35
U1390A-3H-4, 105.56	18.67	21.17	Tie to	U1390B-3H-1, 32.38	18.92	21.17
U1390B-3H-7, 57.54	27.99	30.23	Tie to	U1390A-4H-4, 75.52	27.88	30.23
U1390A-4H-5, 105.35	29.68	32.04	Tie to	U1390B-4H-1, 66.27	28.76	32.04
U1390B-4H-7, 34.15	37.48	40.75	Tie to	U1390A-5H-5, 128.23	37.65	40.75
U1390A-5H-7, 87.71	40.27	43.37	Tie to	U1390B-5H-2, 49.91	39.56	43.37
U1390B-5H-7, 6.65	46.62	50.43	Tie to	U1390C-6H-2, 26.06	44.16	50.43
U1390C-6H-6, 85.12	50.92	57.19	Tie to	U1390A-7H-1, 112.77	52.23	57.19
U1390A-7H-7, 69.19	60.64	65.60	Tie to	U1390B-7H-3, 123.43	60.63	65.60
U1390B-7H-4, 143.55	62.28	67.24	Tie to	U1390A-8H-1, 46.046	61.06	67.24
U1390A-8H-6, 41.53	68.20	74.38	Tie to	U1390B-8H-1, 142.02	67.52	74.38
U1390B-8H-7, 40.756	75.09	81.94	Tie to	U1390C-9H-2, 104.46	72.65	81.94
U1390C-9H-8, 59.17	80.86	90.16	Tie to	U1390B-9H-5, 133.50	82.47	90.16
U1390B-9H-7, 57.48	84.22	91.91	Tie to	U1390C-10H-2, 10.11	80.92	91.91
U1390C-10H-5, 93.30	85.85	96.84	Tie to	U1390B-10H-2, 122.56	87.66	96.84
U1390B-10H-6, 71.31	92.85	102.04	Tie to	U1390C-11H-1, 24.03	90.14	102.04
U1390C-11H-7, 93.08	99.48	111.38	Tie to	U1390B-11H-5, 128.85	100.83	111.38
U1390B-11H-7, 134.84	103.89	114.44	Tie to	U1390C-12H-1, 61.26	100.01	114.44
U1390C-12H-7, 32.68	108.07	122.50	Tie to	U1390B-13H-2, 16.79	109.35	122.50
U1390B-13H-5, 44.64	113.98	127.12	Tie to	U1390C-13H-3, 69.33	111.65	127.12
U1390C-13H-7, 42.06	117.20	132.67	Tie to	U1390B-14H-2, 93.92	119.36	132.67
U1390B-14H-5, 60.79	123.52	136.83	Tie to	U1390C-14H-2, 25.35	120.06	136.83
U1390C-14H-6, 4.37	125.40	142.17	Tie to	U1390B-15H-1, 24.87	127.85	142.17
U1390B-15H-5, 7.72	133.53	147.85	Tie to	U1390C-15H-2, 141.52	130.57	147.85
U1390C-15H-5, 88.41	134.35	151.64	Tie to	U1390B-16H-1, 9.30	137.19	151.64
U1390B-16H-5, 31.77	142.03	156.47	Tie to	U1390C-16H-2, 8.62	138.38	156.47
U1390C-16H-4, 80.54	141.33	159.42	Tie to	U1390B-17H-2, 39.17	147.62	159.42
U1390B-17H-6, 107.50	154.28	166.07	Tie to	U1390C-17H-1, 99.61	147.90	166.07
U1390C-17H-6, 15.55	154.06	172.23	Tie to	U1390B-18H-1, 111.30	157.21	172.23
U1390B-18H-6, 86.82	164.12	179.14	Tie to	U1390A-19X-1, 123.81	161.34	179.14
U1390A-19X-3, 110.86	163.97	181.77	Tie to	U1390B-19H-2, 96.58	166.75	181.77
U1390B-19H-7, 87.19	173.71	188.74	Tie to	U1390C-19H-3, 120.02	169.97	188.74
U1390C-19H-6, 108.68	174.07	192.83	Tie to	U1390B-20H-1, 68.54	175.79	192.83
U1390B-20H-4, 78.74	180.05	197.10	Tie to	U1390A-21X-1, 137.29	180.57	197.10
U1390A-21X-6, 51.85	186.82	203.34	Tie to	U1390B-21H-1, 27.43	184.87	203.34
U1390B-21H-3, 114.78	188.45	206.92	Tie to	U1390A-22X-2, 14.39	190.44	206.92
U1390A-22X-6, 79.29	196.84	213.31	Append to	U1390A-23X-1, 0.26	198.40	219.30
U1390A-23X-6, 95.85	206.86	227.76	Append to	U1390A-24X-1, 0.69	208.01	229.92
U1390A-24X-7, 70.02	217.03	238.94	Append to	U1390A-25X-1, 1.2	217.51	240.43
U1390A-25X-5, 95.19	224.45	247.37	Append to	U1390A-26X-1, 1.39	227.01	250.93
U1390A-26X-6, 136.28	235.86	259.78	Append to	U1390A-27X-1, 0.79	236.71	261.64
U1390A-27X-7, 69.56	245.91	270.84	Append to	U1390A-28X-1, 1.33	246.31	272.26
U1390A-28X-7, 67.71	255.60	281.54	Append to	U1390A-29X-1, 2.5	255.93	282.88
U1390A-29X-7, 123.22	265.18	292.14	Append to	U1390A-30X-1, 0	265.50	293.47
U1390A-30X-8, 71.43	274.98	302.95	Append to	U1390A-31X-1, 0	275.10	304.08
U1390A-31X-7, 67.5	284.25	313.23	Append to	U1390A-32X-1, 0.72	284.71	314.70
U1390A-32X-6, 127.18	293.47	323.46	Append to	U1390A-33X-1, 0	294.30	325.30
U1390A-33X-6, 71.85	302.23	333.23	Append to	U1390A-34X-1, 1.25	303.91	335.93
U1390A-34X-6, 146.1	312.85	344.87	Append to	U1390A-35X-2, 1.82	314.46	347.48
U1390A-35X-7, 93.1	322.57	355.60	Append to	U1390A-36X-1, 1.35	323.11	357.15
U1390A-36X-7, 85	332.40	366.44	Append to	U1390A-37X-1, 1.31	332.31	367.32
U1390A-37X-2, 123.28	335.03	370.04	Append to	U1390A-38X-1, 0.61	341.91	377.92

Table T21. Meters composite depth scale, Site U1390.

Core	Top depth (mbsf)	Top depth (mcd)	Offset (m)
339-U1390A-			
1H	0.00	0.18	0.18
2H	3.60	3.20	–0.40
3H	13.10	15.60	2.50
4H	22.60	24.95	2.35
5H	32.10	35.20	3.10
6H	41.60	44.79	3.19
7H	51.10	56.06	4.96
8H	60.60	66.78	6.18
9H	70.10	76.14	6.04
10X	76.70	84.60	7.90
11X	83.50	92.53	9.03
12X	93.10	102.80	9.70
13X	102.70	112.77	10.07
14X	112.30	124.08	11.78
15X	121.90	133.76	11.86
16X	131.40	143.33	11.93
17X	140.90	152.62	11.72
18X	150.50	162.50	12.00
19X	160.10	177.90	17.80
20X	169.60	185.13	15.53
21X	179.20	195.72	16.52
22X	188.80	205.27	16.47
23X	198.40	219.30	20.90
24X	208.00	229.91	21.91
25X	217.50	240.41	22.91
26X	227.00	250.91	23.91
27X	236.70	261.64	24.94
28X	246.30	272.25	25.95
29X	255.90	282.86	26.96
30X	265.50	293.47	27.97
31X	275.10	304.08	28.98
32X	284.70	314.69	29.99
33X	294.30	325.30	31.00
34X	303.90	335.92	32.02
35X	313.50	346.53	33.03
36X	323.10	357.14	34.04
37X	332.30	367.31	35.01
38X	341.90	377.92	36.02
339-U1390B-			
1H	0.00	0.00	0.00
2H	9.10	9.00	–0.10
3H	18.60	20.84	2.24
4H	28.10	31.37	3.27
5H	37.60	41.41	3.81
6H	47.10	51.55	4.45
7H	56.60	61.57	4.97
8H	66.10	72.96	6.86
9H	75.60	83.29	7.69
10H	85.10	94.29	9.19
11H	94.60	105.15	10.55
12H	104.10	117.11	13.01
13H	108.60	121.75	13.15
14H	118.10	131.41	13.31
15H	127.60	141.92	14.32
16H	137.10	151.54	14.44
17H	146.60	158.40	11.80
18H	156.10	171.12	15.02
19H	165.60	180.62	15.02
20H	175.10	192.15	17.05
21H	184.60	203.07	18.47
339-U1390C-			
1H	0.00	0.08	0.08
2H	4.40	5.79	1.39
3H	13.90	15.92	2.02
4H	23.40	28.23	4.83
5H	32.90	37.66	4.76
6H	42.40	48.67	6.27
7H	51.90	58.59	6.69
8H	61.40	69.38	7.98
9H	70.90	80.20	9.30
10H	80.40	91.39	10.99
11H	89.90	101.80	11.90
12H	99.40	113.83	14.43
13H	108.90	124.37	15.47
14H	118.40	135.17	16.77
15H	127.90	145.18	17.28
16H	137.40	155.49	18.09
17H	146.90	165.08	18.18
18H	156.40	173.83	17.43
19H	165.90	184.67	18.77

Table T22. Magnetic susceptibility splice, Site U1390.

Core, section, interval (cm)	Depth (mbsf)	Depth (mcd)	Offset (m)	Magnetic susceptibility
339-U1390B-				
1H-1, 2.5	0.025	0.025	0.000	31.00
1H-1, 5.0	0.050	0.050	0.000	34.33
1H-1, 7.5	0.075	0.075	0.000	33.67
1H-1, 10.0	0.100	0.100	0.000	31.67
1H-1, 12.5	0.125	0.125	0.000	31.00
1H-1, 15.0	0.150	0.150	0.000	34.00
1H-1, 17.5	0.175	0.175	0.000	36.00
1H-1, 20.0	0.200	0.200	0.000	38.00
1H-1, 22.5	0.225	0.225	0.000	38.00
1H-1, 25.0	0.250	0.250	0.000	39.00
1H-1, 27.5	0.275	0.275	0.000	39.00
1H-1, 30.0	0.300	0.300	0.000	38.33
1H-1, 32.5	0.325	0.325	0.000	38.33
1H-1, 35.0	0.350	0.350	0.000	38.33
1H-1, 37.5	0.375	0.375	0.000	38.67
1H-1, 40.0	0.400	0.400	0.000	38.33
1H-1, 42.5	0.425	0.425	0.000	38.00
1H-1, 45.0	0.450	0.450	0.000	39.00
1H-1, 47.5	0.475	0.475	0.000	41.00
1H-1, 50.0	0.500	0.500	0.000	43.67
1H-1, 52.5	0.525	0.525	0.000	45.67
1H-1, 55.0	0.550	0.550	0.000	46.00
1H-1, 57.5	0.575	0.575	0.000	48.00
1H-1, 60.0	0.600	0.600	0.000	47.00
1H-1, 62.5	0.625	0.625	0.000	47.00
1H-1, 65.0	0.650	0.650	0.000	46.33
1H-1, 67.5	0.675	0.675	0.000	45.00
1H-1, 72.5	0.725	0.725	0.000	45.00
1H-1, 75.0	0.750	0.750	0.000	45.00
1H-1, 77.5	0.775	0.775	0.000	44.00
1H-1, 80.0	0.800	0.800	0.000	44.33
1H-1, 82.5	0.825	0.825	0.000	43.00
1H-1, 85.0	0.850	0.850	0.000	41.33
1H-1, 87.5	0.875	0.875	0.000	40.00
1H-1, 90.0	0.900	0.900	0.000	40.00
1H-1, 92.5	0.925	0.925	0.000	39.00
1H-1, 95.0	0.950	0.950	0.000	38.00
1H-1, 97.5	0.975	0.975	0.000	38.00
1H-1, 100.0	1.000	1.000	0.000	38.00
1H-1, 102.5	1.025	1.025	0.000	37.00
1H-1, 105.0	1.050	1.050	0.000	37.00
1H-1, 107.5	1.075	1.075	0.000	38.00
1H-1, 110.0	1.100	1.100	0.000	38.00
1H-1, 112.5	1.125	1.125	0.000	38.00
1H-1, 115.0	1.150	1.150	0.000	38.33
1H-1, 117.5	1.175	1.175	0.000	38.33
1H-1, 120.0	1.200	1.200	0.000	39.00
1H-1, 122.5	1.225	1.225	0.000	39.33
1H-1, 125.0	1.250	1.250	0.000	40.00
1H-1, 127.5	1.275	1.275	0.000	39.33
1H-1, 130.0	1.300	1.300	0.000	39.00
1H-1, 132.5	1.325	1.325	0.000	39.00
1H-1, 135.0	1.350	1.350	0.000	39.00
1H-1, 137.5	1.375	1.375	0.000	39.00
1H-1, 140.0	1.400	1.400	0.000	39.00
1H-1, 142.5	1.425	1.425	0.000	38.33
1H-1, 145.0	1.450	1.450	0.000	38.00
1H-2, 4.7	1.547	1.547	0.000	38.00
1H-2, 7.2	1.572	1.572	0.000	39.33

Only a portion of this table appears here. The complete table is available in **ASCII.**

Table T23. Interstitial water oxygen and hydrogen isotopes, Site U1390.

Core, section, interval (cm)	Depth (mbsf)	$\delta^{18}O$ (‰, VSMOW)	δD (‰, VSMOW)
339-U1390A-			
1H-2, 135–140	2.90	0.89	5.82
2H-5, 145–150	11.13	0.96	5.13
3H-5, 145–150	20.61	0.98	6.27
4H-5, 145–150	30.14	1.06	6.77
5H-6, 145–150	39.39	1.07	6.74
6H-4, 147–152	47.70	0.97	7.89
7H-5, 150–155	58.45	0.82	7.09
8H-5, 141–146	67.78	1.10	7.07
10X-3, 141–146	81.21	1.05	6.18
11X-4, 141–146	89.50	1.33	6.46
12X-3, 140–145	97.60	0.97	6.68
13X-3, 140–145	107.20	0.95	6.56
14X-4, 140–145	118.15	0.65	3.76
15X-3, 140–145	126.40	0.97	3.51
16X-4, 140–145	137.40	0.85	3.25
17X-3, 140–145	145.40	0.93	2.22
18X-4, 99–104	156.09	0.40	–0.34
19X-2, 116–121	162.86	1.09	0.78
20X-3, 140–145	174.10	0.66	–0.46
21X-4, 140–145	185.20	0.76	–0.59
22X-4, 140–145	194.80	0.69	–1.58
24X-4, 132–137	213.92	1.04	–2.36
25X-4, 135–140	223.50	0.82	–2.83
26X-4, 135–140	233.00	0.86	–3.84
27X-5, 135–140	244.20	1.08	–2.78
28X-5, 135–140	253.80	0.84	–4.79
29X-5, 135–140	262.45	0.98	–4.04
30X-5, 136–141	271.82	0.93	–4.45
31X-4, 135–140	281.10	0.89	–6.07
32X-4, 135–140	290.70	1.07	–5.59
33X-4, 135–140	300.30	1.31	–6.47
34X-4, 135–140	309.89	0.94	–5.71
35X-3, 135–140	317.44	1.23	–5.28
36X-4, 135–140	329.01	1.24	–5.50
38X-3, 135–140	346.40	1.39	–4.41

VSMOW = Vienna standard mean ocean water.

Table T24. Excluded magnetic susceptibility data, Site U1390.

Core, section, interval (cm)	Core, section, interval (cm)	Core, section, interval (cm)	Core, section, interval (cm)	Core, section, interval (cm)
339-U1390A-	4H-1, 2.5	6H-3, 154.17	9H-1, 17.5	9H-3, 122.13
1H-1, 0	4H-1, 5	6H-4, 143.46	9H-1, 20	9H-3, 124.63
1H-1, 2.5	4H-1, 7.5	6H-4, 145.96	9H-1, 22.5	9H-3, 129.63
1H-1, 5	4H-1, 10	6H-5, 145.13	9H-1, 25	9H-3, 132.13
1H-1, 7.5	4H-1, 12.5	6H-5, 147.63	9H-1, 27.5	10X-1, 0
1H-1, 10	4H-1, 15	6H-6, 134.42	9H-1, 30	10X-1, 2.5
1H-1, 147.5	4H-1, 17.5	6H-6, 139.42	9H-1, 32.5	10X-1, 5
1H-1, 150	4H-1, 47.5	6H-6, 141.92	9H-1, 35	10X-1, 7.5
1H-2, 53.85	4H-1, 147.5	7H-1, 0.13	9H-1, 37.5	10X-1, 152.5
1H-2, 131.35	4H-1, 150	7H-1, 127.63	9H-1, 40	10X-1, 155
1H-2, 133.85	4H-2, 127.86	7H-1, 130.13	9H-1, 42.5	10X-2, 145.82
1H-3, 47.01	4H-2, 147.86	7H-2, 145.94	9H-1, 45	10X-2, 148.32
1H-3, 49.51	4H-2, 150.36	7H-2, 148.44	9H-1, 47.5	10X-3, 135.57
1H-3, 49.51	4H-3, 146.98	7H-3, 10.63	9H-1, 50	10X-3, 138.07
2H-1, 0	4H-3, 149.48	7H-3, 145.63	9H-1, 52.5	10X-4, 140.16
2H-1, 2.5	4H-4, 84.68	7H-3, 148.13	9H-1, 55	10X-4, 142.66
2H-1, 5	4H-4, 109.68	7H-4, 145.27	9H-1, 57.5	10X-5, 132.92
2H-1, 7.5	4H-4, 117.18	7H-4, 147.77	9H-1, 60	10X-5, 135.42
2H-1, 10	4H-4, 147.18	7H-5, 147.72	9H-1, 62.5	10X-5, 137.92
2H-1, 12.5	4H-4, 149.68	7H-5, 150.22	9H-1, 65	11X-1, 17.5
2H-1, 15	4H-5, 107.18	7H-5, 152.72	9H-1, 67.5	11X-1, 70
2H-1, 17.5	4H-5, 142.18	7H-5, 155.22	9H-1, 70	11X-1, 147.5
2H-1, 20	4H-5, 144.68	7H-6, 147.3	9H-1, 72.5	11X-1, 150
2H-1, 22.5	4H-6, 37.5	7H-6, 149.8	9H-1, 75	11X-2, 144.84
2H-1, 25	4H-6, 47.5	7H-7, 29.23	9H-1, 77.5	11X-2, 147.34
2H-1, 27.5	4H-6, 95	7H-7, 91.73	9H-1, 80	11X-3, 50.17
2H-1, 30	4H-6, 97.5	7H-7, 94.23	9H-1, 82.5	11X-3, 145.17
2H-1, 150	4H-7, 65	8H-1, 1.59	9H-1, 85	11X-3, 147.67
2H-1, 152.5	4H-7, 67.5	8H-1, 4.09	9H-1, 87.5	11X-4, 42.7
2H-2, 91.55	5H-1, 35	8H-1, 6.59	9H-1, 90	11X-4, 132.7
2H-2, 149.05	5H-1, 80	8H-1, 9.09	9H-1, 92.5	11X-4, 135.2
2H-2, 151.55	5H-1, 82.5	8H-1, 11.59	9H-1, 95	11X-4, 137.7
2H-3, 44.61	5H-2, 0	8H-1, 101.59	9H-1, 97.5	11X-4, 140.2
2H-3, 147.11	5H-2, 2.5	8H-1, 141.59	9H-1, 100	11X-5, 97.2
2H-3, 149.61	5H-2, 5	8H-1, 144.09	9H-1, 102.5	11X-5, 144.7
2H-4, 147.84	5H-2, 7.5	8H-2, 131.87	9H-1, 105	11X-5, 147.2
2H-4, 150.34	5H-2, 10	8H-2, 134.37	9H-1, 107.5	11X-5, 149.7
2H-5, 136.1	5H-2, 12.5	8H-2, 136.87	9H-1, 110	11X-6, 122.5
2H-5, 143.6	5H-2, 15	8H-2, 139.37	9H-1, 112.5	11X-6, 125
2H-5, 146.1	5H-2, 17.5	8H-3, 138.8	9H-1, 115	11X-CC, 12.11
2H-6, 133.49	5H-2, 20	8H-3, 141.3	9H-1, 117.5	11X-CC, 14.61
2H-6, 135.99	5H-2, 37.5	8H-4, 0	9H-1, 120	11X-CC, 17.11
2H-7, 64.12	5H-2, 40	8H-4, 44.78	9H-1, 122.5	11X-CC, 19.61
2H-7, 66.62	5H-3, 147.15	8H-4, 142.28	9H-1, 125	11X-CC, 22.11
3H-1, 0	5H-3, 149.65	8H-4, 142.5	9H-1, 127.5	11X-CC, 24.61
3H-1, 2.5	5H-4, 150.5	8H-4, 144.78	9H-1, 130	11X-CC, 27.11
3H-1, 147.5	5H-4, 153	8H-4, 145	9H-1, 132.5	11X-CC, 29.61
3H-1, 150	5H-5, 148.19	8H-5, 10	9H-1, 135	11X-CC, 32.11
3H-2, 11.58	5H-5, 150.69	8H-5, 62.5	9H-1, 137.5	11X-CC, 34.61
3H-2, 146.58	5H-6, 141.42	8H-5, 137.5	9H-1, 140	12X-1, 0
3H-2, 149.08	5H-6, 143.92	8H-5, 140	9H-1, 142.5	12X-1, 2.5
3H-3, 147.56	5H-7, 143.45	8H-6, 69.33	9H-1, 145	12X-1, 7.5
3H-3, 150.06	5H-7, 145.95	8H-6, 71.83	9H-1, 147.5	12X-1, 10
3H-4, 129.52	6H-1, 1.95	8H-6, 131.83	9H-1, 150	12X-1, 12.5
3H-4, 147.02	6H-1, 4.45	8H-6, 134.33	9H-2, 1.62	12X-1, 15
3H-4, 149.52	6H-1, 6.95	8H-7, 97.5	9H-2, 4.12	12X-1, 17.5
3H-5, 143.14	6H-1, 9.45	8H-7, 100	9H-2, 6.62	12X-1, 20
3H-5, 145.64	6H-1, 11.95	8H-7, 102.5	9H-2, 21.62	12X-1, 147.5
3H-6, 16.95	6H-1, 14.45	9H-1, 0	9H-2, 86.62	12X-1, 150
3H-6, 129.45	6H-1, 146.95	9H-1, 2.5	9H-2, 99.12	12X-2, 14.93
3H-6, 131.95	6H-1, 149.45	9H-1, 5	9H-2, 139.12	12X-2, 17.43
3H-7, 44.73	6H-2, 131.54	9H-1, 7.5	9H-2, 141.62	12X-2, 122.43
3H-7, 67.23	6H-2, 149.04	9H-1, 10	9H-2, 144.12	12X-2, 124.93
3H-7, 69.73	6H-2, 151.54	9H-1, 12.5	9H-3, 109.63	12X-2, 127.43
4H-1, 0	6H-3, 151.67	9H-1, 15	9H-3, 119.63	

Only a portion of this table appears here. The complete table is available in **ASCII.**